ENCAPSULATION OF NANOPARTICLES IN METAL-ORGANIC FRAMEWORKS FOR AIR PURIFICATION

A Dissertation
Presented to
The Academic Faculty

by

Karen R. Tulig

In Partial Fulfillment
of the Requirements for the Degree
Doctor of Philosophy in the
School of Chemical and Biomolecular Engineering

Georgia Institute of Technology
August 2016

ENCAPSULATION OF NANOPARTICLES IN METAL-ORGANIC FRAMEWORKS FOR AIR SEPARATION

Approved by:

Dr. Krista S. Walton, Advisor
School of Chemical & Biomolecular Engineering
Georgia Institute of Technology

Dr. Angus P. Wilkinson
School of Chemistry and Biochemistry
Georgia Institute of Technology

Dr. Christopher W. Jones
School of Chemical & Biomolecular Engineering
Georgia Institute of Technology

Dr. Younan Xia
School of Chemical &Biomolecular Engineering
Georgia Institute of Technology

Dr. David S. Sholl
School of Chemical & Biomolecular Engineering
Georgia Institute of Technology

Date Approved: [May 16, 2016]

ACKNOWLEDGEMENTS

First, I would like to acknowledge my advisor, Dr. Krista Walton, for her constant support and guidance over the last five years. She allowed me to make and learn from my own mistakes, encouraged me to think outside the box, and supported collaboration with others. She also recognized my dislike of writing and public speaking and made sure that I did not dodge opportunities to improve these skills, suggesting that I write-up results I found insufficient and sending me to technical conferences to present my research. With her guidance I gained confidence in my abilities and, although still reluctant, no longer shy away from voicing my thoughts in group discussions or speaking opportunities. The knowledge and opportunities I gained working with Dr. Walton and the Walton group have forever shaped my career and life. It has been quite an adventure, and I greatly appreciate everything she has given me.

I would like to thank my committee members, Drs. Chris Jones, David Sholl, Angus Wilkinson, and Younan Xia for taking the time to help shape this work. In addition, I would like to express my deepest appreciation to Drs. David Sholl and Angus Wilkinson for taking the time to provide me with recommendation letters. Also, I would like to thank the Army Research Office, the Defense Threat Reduction Agency, and TDA Research Inc. for sponsoring this work. I also need to acknowledge Rod Sefton, the Bunger-Henry building manager, for going above and beyond the call of duty.

Most importantly, past and present Walton group members (Dr. Bogna Grabicka, Dr. Chris Murdock, Dr. Cody Morelock, Dr. Yang Cai, Dr. Himanshu Jasuja, Dr. Greg Cmarik, Dr. Mike Mangarella, Will Mounfield, Yang Jiao, Erika Garcia-Gutierrez, Lalit

Durante, Julian Hungerford, Colton Moran, Jacob Deneff, and Jay Joshi) have been extremely influential, providing advice and insight for this work as well as helping me grow as a researcher and creating an enjoyable work environment. I would specifically like to acknowledge Dr. Paul Schoenecker for being instrumental in acclimating me to the lab, having many early morning conversations, and setting a standard for constantly improving the lab to make it efficient for everyone. Dr. Katrina Stults for constant MOF conversations, technical advice, and for asking difficult questions that resulted in the clarification of my thoughts. Michael Dutzer for repeatedly editing my initial manuscripts and constantly asking "why" which forced me to think critically about problems. Nick Burtch for performing all of the computational data in this work and for insightful conversations. I would also like to thank John Ahlfield and Jared Schwartz in the Kohl group for the constant exchange of random Swagelock parts and use of characterization equipment.

Finally, I would like to thank my family and friends for all of the moral support over the years. I couldn't have done it without all of you.

TABLE OF CONTENTS

LIST OF TABLES

LIST OF FIGURES

NOMENCLATURE

Abbreviations

Å	Angstrom
Al_2O_3	Aluminum Oxide
AU	Arbitrary Units
AuNP	Gold Nanoparticles
BDC	1,4-Benzenedicarboxylic Acid
BDC-$(CH_3)_2$	1,4-Benzenedicarboxylic Acid, 2,5-Dimethyl
BDC-$(OH)_2$	1,4-Benzenedicarboxylic Acid, 2,5-Dihydroxy
BDC-Anth	Anthracene-9,10-Dicarboxylic Acid
BDC-Br	1,4-Benzenedicarboxylic Acid, 2-Bromo
BDC-Cl_2	1,4-Benzenedicarboxylic Acid, 2,5-Dichloro
BDC-COOH	1,2,4-Benzenetricarboxylic Acid
BDC-Naph	1,4-Naphthalenedicarboxylic Acid
BDC-NH_2	1,4-Benzenedicarboxylic Acid, 2-Amino
BDC-NO_2	1,4-Benzenedicarboxylic Acid, 2-Nitro
BDC-OH	1,4-Benzenedicarboxylic Acid, 2-Hydroxy
BET	Brunauer, Emmett, and Teller
BTC	1,3,5-Benzenetricarboxylic Acid
cm^3	Cubic Meter
CO	Carbon Monoxide
CO_2	Carbon Dioxide
CUS	Coordinatively Unsaturated Sites

CVD	Chemical Vapor Deposition
CWA	Chemical Warfare Agent
d_{AuNP}	AuNP Diameter
DDT	1-Dodecanethiol
DMF	N,N'-Dimethylformamide
E_{app}	Apparent Activation Energy
EDS	Energy Dispersive Spectroscopy
ENC	Encapsulation
g	Gram
GCMC	Grand Canonical Monte Carlo
h	Hour(s)
H_2	Hydrogen
$HAuCl_4 \cdot 3H_2O$	Gold (III) Chloride Trihydrate
HCl	Hydrochloric Acid
HKUST	Hong Kong University of Science and Technology
IMP	Impregnation
IRMOF	Isoreticular Metal-Organic Framework
K	Kelvin
keV	Kiloelectron Volt
kJ	Kilojoule
m^2	Square Meter per Gram
MeOH	Methanol
MFC	Mass Flow Controller

mg	Milligram
MIL	Material of Institute Lavoisier
min	Minute(s)
mL	Milliliter per min
mmol	Millimole
MOF	Metal-Organic Framework
mol	Mole
MUA	11-Mercaptoundecanoic Acid
$NaBH_4$	Sodium Borohydride
nm	Nanometer
NMR	Nuclear Magnetic Resonance
O_2	Oxygen
OSC	Oxygen Storage Capacity
P/P_0	Relative Pressure
PSM	Post-Synthetic Modification
PVP	Polyvinylpyrrolidone
PXRD	Powder X-Ray Diffraction
s	Second(s)
SAM	Surface Assembled Monolayer
SBU	Secondary Building Unit
SDA	Structure Directing Agent
SPR	Surface Plasmon Resonance
STEM	Scanning Electron Microscopy

$T_{1/2}$	Temperature for 50% Conversion
TEM	Transmission Electron Microscopy
TFA	Trifluoroacetic Acid
TGA	Thermogravimetric Analysis
TIC	Toxic Industrial Chemical
TiO_2	Titanium Dioxide
TOF	Turnover Frequency
TPR	Temperature Programmed Reduction
UFF	Universal Force Field
UiO	University of Oslo
ZIF	Zeolitic Imidazolate Framework
ZnO	Zinc Oxide
Zr(O*n*Pr)	Zirconium (IV) Propoxide Solution of 70% in 1-Propanol
Zr^{4+}	Zirconium (IV) Ions
$ZrCl_4$	Zirconium Chloride
ZrO_2	Zirconium Dioxide

Symbols

a	Cross-Sectional Area of Adsorbate
a_i	Theoretical Constant for Brunauer, Emmett, and Teller Theory
b_i	Theoretical Constant for Brunauer, Emmett, and Teller Theory
c	Physical Constant for Brunauer, Emmett, and Teller Theory
d	Spacing Between Crystal Planes
E_i	Heat of Adsorption of Layer i
m_{sample}	Mass of Sample
N_{av}	Avodadro's Number
P	Pressure
P_c	Critical Pressure
R	Ideal Gas Constant
S_{BET}	Brunauer, Emmett, and Teller Theory Surface Area
S_i	Surface Area of Layer i
T	Temperature
T_c	Critical Temperature
v	Total Volume Adsorbed
V	Volume
v_m	Volume of Adsorbed Monolayer
θ	Angle of Incidence
λ	Wavelength
ω	Gas Constant

SUMMARY

Metal-organic frameworks (MOFs) and nanoparticles in MOFs (NP@MOF) are investigated for carbon monoxide adsorption and catalytic oxidation. In this work, gold nanoparticles (AuNPs) are encapsulated in UiO-66, a zirconium-based MOF. The use of zirconium propoxide (Zr(O*n*Pr)) in place of zirconium chloride ($ZrCl_4$) leads to an alternative synthesis route for producing high-quality crystals of UiO-66 without generating by-product HCl. This new method enables the inclusion of HCl-sensitive gold nanoparticles into the mother solution for encapsulation by UiO-66.

Further investigations examine the effects of the solvent ratio, modulator concentration, AuNP capping agent, and UiO-66(Zr(O*n*Pr)) modulator on the UiO-66(Zr(O*n*Pr)) structure and porosity, AuNP diameter, UiO-66(Zr(O*n*Pr)) particle geometry, and AuNP location. These studies show that the AuNP capping agent and UiO-66(Zr(O*n*Pr)) modulator have the most significant effect on the Au@UiO-66(Zr(O*n*Pr)) properties. Conclusive evidence showing that the AuNPs are completely confined within the UiO-66(Zr(O*n*Pr)) particles is not attained, but the preliminary data will guide future endeavors. Additionally, this HCl-free synthesis is applied to the functional versions of UiO-66 resulting in the preparation of a series of UiO-66-X(Zr(O*n*Pr)), where X = {–H, $–NH_2$, $–NO_2$, –Naph, –Anth, $–Cl_2$, –Br, $–(CH_3)_2$, –COOH, –OH, and –(OH)}.

In addition, the potential of UiO-66 as a catalyst support is probed using CO oxidation as a probe reaction throughout this work. First, preformed AuNPs are deposited onto the surfaces of UiO-66, titanium dioxide (TiO_2), and zirconium dioxide (ZrO_2). This colloidal deposition effectively decouples the AuNP factors such as size, shape, and

oxidation state, from the support effect allowing a systematic study of the key support attributes. This study reveals a correlation between the oxygen storage capacity (OSC) and the catalytic activity of the materials with Au on UiO-66 exhibiting an enhanced OSC, due to the unusual chemistry introduced by the metal-linker interactions.

Lastly, Au@UiO-66 prepared via encapsulation is compared to physical mixtures of Au on UiO-66 prepared with various AuNP diameters to probe the effects of the encapsulation procedure. Au@UiO-66 showed improved activity compared to the corresponding physical mixture. The enhanced catalytic activity suggests that synergism is introduced during the encapsulation procedure. This synergism potentially occurs due to partial confinement within UiO-66 particles and/or aggregates which increases the surface area of contact between the AuNPs and UiO-66. This increased contact area results in more interface sites which are typically believed to be responsible for the catalytic abilities of supported AuNPs.

This dissertation concludes by summarizing the experimental results, determining trends between the chapters, and recommending topics for future research projects. In addition, limitations are acknowledged and possible solutions presented.

CHAPTER 1

INTRODUCTION

1.1 Metal-Organic Frameworks

Metal-organic frameworks (MOFs) are crystalline, nanoporous materials formed by linking metal or metal oxide clusters with organic ligands. The numerous combinations of metal node and organic moiety give MOFs exceptional structural diversity; specifically, there are more than 20,000 known and 120,000 hypothetical structures currently in existence.[1, 2] Advantageous properties include high surface areas and pore volumes, uniform pore size distributions, structural diversity, and chemical tunability.[3, 4] These aspects make MOFs promising materials for applications such as gas storage and separation,[3, 5] drug delivery,[6, 7] biomedical imaging,[6, 8] air purification,[9-11] and catalysis.[12, 13]

1.1.1 Metal-Organic Framework Structures and Properties

Initially, the focus of MOF investigations was to create new compounds and structures with interesting properties. However, the field has matured. Currently, studies probe specific properties and determine the advantages and disadvantages of these characteristics. For instance, instead of creating new structures, multiple series of isostructural MOFs have been developed and used to study the effects of metal center, functional groups, and pore diameter. The most well-known being the IRMOF series;[14, 15] however, other isostructural systems such as zeolite imidazolate frameworks (ZIFs),[16]

University of Oslo (UiO) materials,[17, 18] Materials of Institute Lavoisier (MIL),[19-22] and DMOF-1[23-25] have also been utilized to investigate the effects on MOF properties.

With the abundance of structures, understanding the significance of specific properties and functionalities is paramount. For instance, HKUST-1 (also known as CuBTC or MOF-199)[26] and MOF-74 (also known as CPO-27)[14, 27] contain open metal sites or coordinatively unsaturated metal sites (CUS), which introduce Lewis acid sites which are extremely attractive from an applications perspective. Additionally, acid or base groups, such as $–NH_2$,[28, 29] $–NO_2$,[29-31] and $–SO_3H$[18] have been introduced by incorporating modified linkers.

Typically, isostructural MOFs with varied metals and linker functionalities are prepared by directly introducing various metal centers or functionalized ligands to the synthesis. However, not all materials can be prepared by a direct substitution; occasionally, varying the metal center or organic moiety produces new structures.[31] Alternatively, post-synthetic modification (PSM) has been explored and has been used to prepare isostructural compounds that cannot be synthesized directly.[32-35]

1.1.2 Metal-Organic Framework Limitations

MOFs offer many advantages; however, they are also plagued by several limitations. The most prominent constraint for MOFs is the tendency of many structures to degrade under humid conditions.[36] Kaskel et al. suggested that the combination of the hydrophilic metal centers and hydrophobic organic moiety in many MOFs causes the water molecules to cluster near and hydrolyze the metal-ligand bond.[37] For this reason, structures with CUS are often sensitive to humid environments. The available Lewis acid

sites that make these structures so promising also chemisorb water, which accumulates near the metal-ligand interface and, subsequently hydrolyzes the bond causing the crystal structure to irreparably degrade. Techniques to improve the water stability of MOFs are currently under investigation; in particular, tuning the metal inertness and the hydrophobicity and steric factors of the MOF have shown promise.[36]

Another limitation of MOFs is the ability to obtain large quantities of high-quality MOF materials. BASF has made five MOFs commercially available: ZIF-8 (Basolite® Z1200), MIL-53(Al) (Basolite® A100), HKUST-1 (Basolite® C300), FeBTC (Basolite® F300), and MOF-177 (Basolite® Z377); however, this scope of materials is too limited and expensive to make MOFs competitive compared to cheaper alternatives such as activated carbon. In addition, many other MOFs are prepared in batches that yield less than a gram of material. However, investigations into large-scale preparation methods of MOFs are currently underway. For instance, UiO-66[38] and MIL-100(Fe)[39] have been prepared in scaled-up batch reactors with space-time yields exceeding those of commercially available MOFs.[40] In addition, early reports have shown that continuous processes can be utilized to produce a variety of MOFs including MIL-88B,[41] MOF-5,[42] IRMOF-3,[42] HKUST-1,[42, 43] UiO-66,[42, 43] UiO-66-NH_2,[44] and NOTT-400.[43] These studies have launched the development of techniques for producing a wide range of high-quality MOFs at the industrial scale; however, to date, there are a limited number of MOFs capable of being produced in large quantities.

Lastly, these highly porous MOFs are low density materials which make them promising for gravimetric applications. However, this also means that they have a relatively low density of active sites capable of strong interactions with target molecules.

There are several methods for increasing the active site density in MOFs: (1) using structures with CUS, (2) introducing functional groups via the linker, and (3) incorporating metal or metal oxide nanoparticles in the MOF. This work focuses on the addition of metal nanoparticles to MOFs to increase the active site density in known water-stable MOFs.

1.2 Metal-Organic Framework Composites

The incorporation of metal or metal oxide nanoparticles (NP) in MOFs, denoted in this work as NP@MOF, exploits the unusual chemical and physical properties of the nanoparticles and the MOF to produce composites with unprecedented physical and chemical properties. For example, Huo et al. incorporated a wide range of nanomaterials with magnetic, luminescent, and catalytic properties in ZIF-8, a known stable MOF.[45] The ZIF-8 composites exhibited enhanced magnetic, luminescent, and catalytic capabilities, respective to the nanomaterial, compared to parent ZIF-8. This study shows that incorporating nanomaterials in MOFs is an effective way to tune the material properties while preserving the overall structure and stability. In addition, it allows for the exploitation of knowledge already collected, mainly the stability of MOFs and the nanomaterial properties, to design materials for specific applications. For instance, MOF composites have demonstrated promise for applications such as catalysis,[46] chemical sensing,[47] plasmonics,[48] and drug delivery.[49, 50] Therefore, the modification of stable MOFs with nanomaterials will effectively tune the material properties allowing for well-designed materials.

1.2.1 Preparation Techniques

There are two main synthesis techniques used to incorporate nanomaterials within MOFs: impregnation and encapsulation (illustrated in **Error! Reference source not found.**). Impregnation indicates that the nanoparticles are formed within the MOF pores, whereas encapsulation describes the crystallization of the MOF around preformed nanomaterials. Additionally, several alternative nanomaterial incorporation methods have been reported.

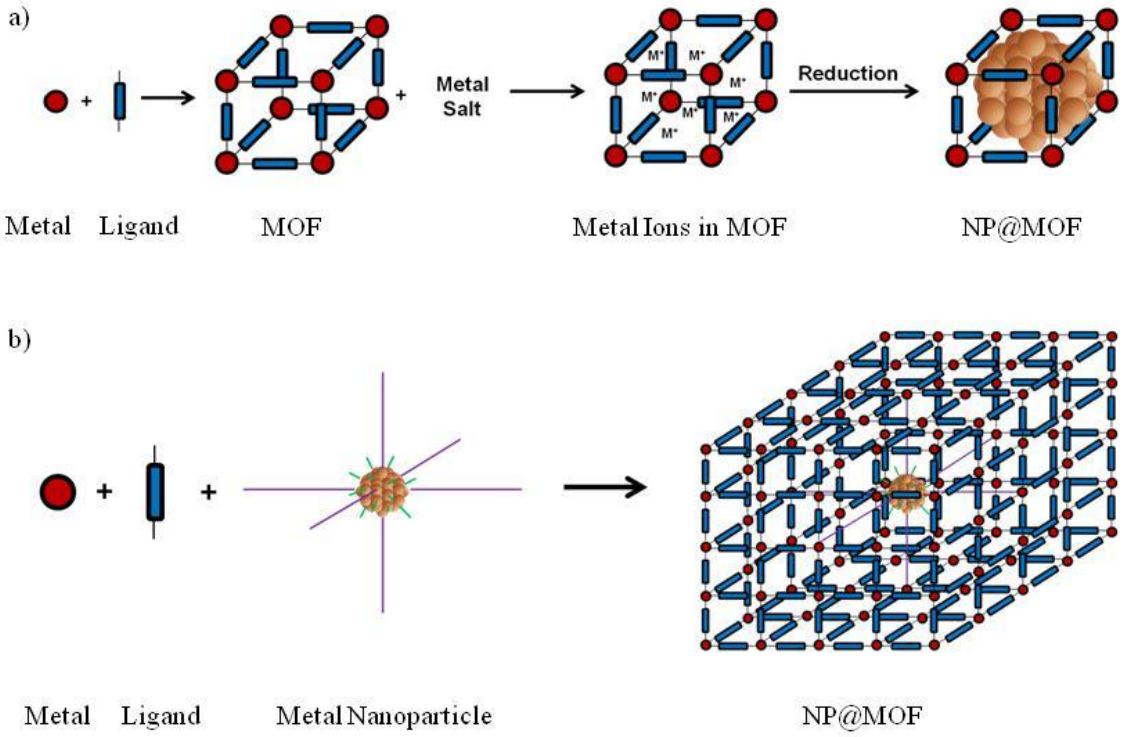

Figure 1.1: Illustration of MOF composite synthesis via (a) impregnation and (b) encapsulation

1.2.1.1 Impregnation

As illustrated in Figure 1.1, the impregnation technique occurs in three steps: (1) the preparation and activation of the MOF; (2) the infiltration of a metal precursor into

the preformed MOF pores; and (3) the reduction, oxidation, or decomposition of the metal precursor. There are several predominant infiltration methods used for preparing NP@MOF via impregnation: solution impregnation,[51-53] the double solvent approach,[54] incipient wetness impregnation,[55] chemical vapor deposition (CVD),[56-58] and solid grinding.[59, 60] After infiltration, the metal precursor is either oxidized[58] or reduced using UV irradiation,[54] redox-active MOFs,[53, 61] or chemical reducing agents such as $NaBH_4$[51] or H_2.[52, 55, 56, 59] Studies have shown that the infiltration method influences NP@MOF properties such as metal loading and nanoparticle location. For instance, solvent-based infiltration methods are limited by the solubility of the metal precursors, competitive incorporation of the metal and solvent in the pore space, and solvent desorption, which causes the precursors to deposit on the surface of the MOF.[62] However, solvent-free methods are also limited; mainly, solvent-free impregnation requires volatile and often moisture- and air-sensitive precursors.

Overall, the impregnation technique offers both advantages and limitations. The most notable advantage is the utilization of the uniform pore size distribution to quench nanoparticle growth, which stabilizes the particles in the MOF pores and yields nanoparticles with the size and shape of the MOF pores. Theoretically, impregnation offers a method for controlling nanoparticle size and shape by exploiting the extensive collection of MOF structures, specifically the various pore structures, to tune the nanoparticle properties. However, there are several limitations. First, strong interactions between the nanoparticles and the MOF are often necessary to control the particle location and limit growth. There are only a limited number of MOFs known to sufficiently interact with the particles in order to limit particle mobility and growth.

Often, functional groups are necessary to sufficiently immobilize the metal nanoparticles within the pores to limit particle aggregation on the surface.[57, 63-65] Second, many MOFs are microporous, which is advantageous for gas separation; however, the metal precursors are often too large to penetrate the micropores limiting the framework selection. Third, the high temperatures and reduction procedures can destroy the MOF structure and porosity.[56, 59] Lastly, the particles block the pores, reducing the available surface area and pore volume.[59, 60]

1.2.1.2 Encapsulation

As depicted in Figure 1.1, encapsulation describes the growth of the MOF on and around preformed nanomaterials. The preformed nanomaterials, either functionalized with a surface-assembled monolayer (SAM)[66, 67] or "naked,"[68-70] are incorporated with the MOF precursors and crystallization proceeds around the nanomaterials. There have been several MOF synthesis procedures used to encapsulate nanomaterials, mainly: solvothermal,[71, 72] microwave,[73, 74] sonochemical or ultrasonic,[75] mechanochemical,[76] and room temperature crystallization.[45, 77]

Encapsulation has the potential to overcome many of the limitations presented by impregnation. Specifically, growing the MOF around the nanomaterial adds the nanomaterial to the framework, rather than trapping it within the pores. The specific surface area of the composite will still be reduced relative to the parent MOF because of the increased density; however, pore blockage will be limited. Also, by starting with preformed, stabilized nanomaterials, the complete collection of MOF structures can, theoretically, be utilized since specific MOF chemistry is not required to quench and

immobilize the NPs. Finally, the greatest advantage of encapsulation is the capability to incorporate nanomaterials that exceed the MOF pore size,[45, 48] which means that nanomaterials designed for specific applications can be coupled with the MOF support.

There are extensive studies of nanomaterials that demonstrate the ability to tune the optic, electric, magnetic, and catalytic properties by controlling the size, shape, composition, and structure (e.g. hollow vs. solid) of the materials.[78] For instance, the optical properties of Ag and Au nanomaterials can be tuned by varying the size and shape of the material.[79, 80] Additionally, magnetic properties are strongly dependent on nanoparticle size; as the size decreases, the ferromagnetic to superparamagnetic transition occurs at lower temperatures.[81] Furthermore, the catalytic activity is strongly dependent on the nanoparticle diameter.[82] The nanomaterial shape is also influential. For instance, Cheon et al. demonstrate an enhanced magnetic coercivity for cobalt nanorods due to shape effects.[83] The crystal surface facets are also controlled by the nanomaterial shape. For example, ceria nanorods predominately expose well-defined {001} and {110} planes, whereas the surface facets for ceria nanoparticles are mostly the {111} planes. The crystal facet, in turn, effects both catalytic activity and selectivity.[84] Lastly, the shape determines the number of atoms at the corners and edges which are essential for catalytic activity.[85]

Realizing the importance of fine tuning nanomaterials, the ability to control the size, shape, composition, and structure of the materials is paramount to designing novel composites. To date, the minute tuning of nanoparticle diameter is possible by varying the ratio of the nanoparticle capping ligand to metal precursor and by seed-mediated synthesis.[86, 87] The nanomaterial shape can also be controlled by altering the synthesis

conditions. For instance, palladium can be shaped into nanocubes,[88] nanorods,[89] and nanoplates.[90] Additionally, synthesis procedures have been developed to tune the size and shape of silver, gold, platinum, and copper nanomaterials.[78] Therefore, the synthetic control and understanding of nanomaterials is available, and by using the encapsulation technique, well designed nanomaterials can be coupled with MOFs to engineer chemically unique nanoporous materials.

1.2.1.3 Alternative MOF Composite Preparation

In addition to impregnation and encapsulation, several other techniques have been utilized to prepare MOF composites. For instance, Zhan et al. incorporated ZnO nanorods in ZIF-8 by using the ZnO nanorods to supply the Zn^{2+} ions for MOF crystallization subsequently growing ZIF-8 from the nanorods.[47] In addition, the nanoparticle metal precursor has been incorporated in UiO-67(bipyridine) by adding the nanoparticle metal precursor to the UiO-67(bipyridine) precursors; the nanoparticle precursor coordinates to the bipyridine functionality on the linker subsequently incorporating it in the structure.[91, 92] Furthermore, Kitagawa et al. have integrated NiNPs in Ni-MOF-74 by partially decomposing Ni-MOF-74 by heating under vacuum.[93] Lastly, MOF composites can be prepared by colloidal deposition creating physical mixtures.[94, 95]

1.2.2 Characterization Techniques

The characterization of NP@MOF is a challenging problem. In particular, conclusively determining the location of the nanomaterials either within the MOF particles or on the surface has proven difficult. Typically, transmission electron

microscopy (TEM) is used to determine the size and shape of the nanoparticles. When impregnation techniques are used, nanoparticle confinement can be elucidated from TEM images when the nanoparticles are smaller than the MOF pores.[96, 97] However, TEM is a two-dimensional technique and, therefore, other techniques are necessary to definitely determine the nanoparticle location. To date, a couple of alternative methods have been employed: TEM tomography[57, 98] and selective catalysis.[45, 99]

TEM tomography is a three-dimensional imaging technique that rotates the sample stage from -70-70° under the electron beam recording images every 1-2°. These images are then aligned, and a three-dimensional reconstruction developed.[100] However, TEM tomography is limited to specific systems because many MOFs degrade upon exposure to the electron beam.[98] Alternatively, selective catalysis exploits the MOF microporosity. Briefly, molecules too cumbersome to permeate into the MOF pores are used either as the reactant[45] or added as a catalyst poison[99] to determine if the nanoparticles are actually confined within the MOF or merely on the particles' surface. The presence or lack of a reaction is used to determine the NP location.

1.3 Objectives and Overview of this Work

The overall goal of this work is to design novel, water-stable MOF composites for the removal of toxic gases for use in one pass filtration devices. This goal will be achieved through the completion of three objectives: (1) development of efficient methods of preparing MOF composites via the self-assembly of the MOF from the surface of preformed functionalized nanoparticles; (2) determination of the effect of the nanoparticle size and the composite preparation method on the structure-property

relationship of the composites; (3) and evaluation of the adsorptive and catalytic capabilities of MOF composites towards toxic gases. Objective 1 is addressed in Chapters 3, 6, and 7 and Appendices A and B using AuNPs in three MOF systems: UiO-66, MIL-125, and ZIF-8. Objective 2 is documented in Chapters 3 and 5 with AuNPs and UiO-66. Lastly, Objective 3 is covered by Chapters 4 and 5 and Appendices A and B utilizing the materials from Objectives 1 and 2.

Chapter 3 is adapted from a peer-reviewed article on the establishment of an alternative UiO-66 synthesis procedure that produces high-quality UiO-66 crystals without generating by-product HCl, which allows for the incorporation of HCl-sensitive materials. Briefly, the conventional synthesis uses zirconium chloride ($ZrCl_4$) as the metal precursor; herein, $ZrCl_4$ is substituted with zirconium propoxide (Zr(O*n*Pr)), which effectively eliminates by-product HCl. Crystallization is dependent upon the inclusion of acetic acid. Further investigation suggests a rapid nucleation rate that requires the addition of a modulator, such as acetic acid, to competitively coordinate with the metal centers to regulate the nucleation rate and enhance crystal growth. In addition, HCl-sensitive AuNPs are added to the reaction slurry to test the compatibility of the UiO-66(Zr(O*n*Pr)) synthesis with HCl-sensitive materials. The resulting Au@UiO-66(Zr(O*n*Pr)) composite reveals AuNPs randomly scattered throughout the material. However, the Au@UiO-66(Zr(O*n*Pr)) composite is not ideal; the AuNPs grow during crystallization and many AuNPs are deposited on the UiO-66(Zr(O*n*Pr)) particles' surfaces. Therefore, optimization of the Au@UiO-66(Zr(O*n*Pr)) procedure is necessary, but the development of this procedure allows for the improved understanding of UiO-66

crystallization and lays the foundation for the development of designed HCl-sensitive UiO-66 composites.

Chapter 4 investigates the practicality of using MOFs as catalyst supports for oxidation reactions. Herein, AuNPs and CO oxidation are used as the catalyst and probe reaction, respectively. AuNPs are deposited on three supports, UiO-66, TiO_2, and ZrO_2, via colloidal deposition, and the physical and catalytic properties are examined. Extensive characterization shows that the AuNP properties were similar; therefore, variations in the catalytic activity are entirely dependent on the support. Further investigation reveals that the key attribute of the support is its oxygen storage capacity (OSC) or the ability to donate oxygen to the reaction. This is concluded by the strong correlation between OSC and catalytic activity. Interestingly, UiO-66 has a larger OSC than commercially available TiO_2 and ZrO_2 showing that there are material attributes other than reducibility, that affect the OSC. To the best of the authors' knowledge, this is the first time that OSC was measured for MOFs, and UiO-66 demonstrates an enhanced OSC compared to commercially available TiO_2 and ZrO_2. Theoretically, the unusual chemistry that evolves from the combination of metal nodes and organic linkers affects the oxygen donation capabilities of MOFs, revealing potential as catalyst supports.

At this point, the author has developed a synthesis procedure capable of using the encapsulation technique to prepare Au@UiO-66, although it is not optimized. In addition, Au on UiO-66 has proven catalytically active for CO oxidation affirming an effective probe reaction for Au@UiO-66 composites. Moving forward, Chapter 5 investigates the impact of the preparation method, specifically, impregnation, encapsulation, and colloidal deposition, on the physical and catalytic properties of UiO-66 composites. The

combination of TEM, STEM tomography, and CO oxidation suggests that the impregnation technique produces an Au@UiO-66(Zr(O*n*Pr)) composite with AuNPs mainly dispersed on the UiO-66(Zr(O*n*Pr)) particles' surfaces. Alternatively, the encapsulation procedure generates a composite that exhibits partial confinement of the AuNPs within either single UiO-66(Zr(O*n*Pr)) particles or an aggregation of UiO-66(Zr(O*n*Pr)) particles. This partial confinement increases the degree of contact between the AuNPs and the UiO-66(Zr(O*n*Pr)) support, enhancing the catalytic capabilities of the composite. This study highlights the advantages of the encapsulation procedure, specifically, showing that, even un-optimized, this technique generates synergistic effects. Therefore, optimization of the Au@UiO-66(Zr(O*n*Pr)) encapsulation method is worthwhile.

After showing that the encapsulation technique generates synergistic effect in Au@UiO-66(Zr(O*n*Pr)), the author proceeds to tune the procedure in Chapter 6. Several synthesis parameters are modified and the effect on the Au@UiO-66(Zr(O*n*Pr)) examined. Specifically, the solvent ratio, modulator concentration, AuNP capping agent, and UiO-66(Zr(O*n*Pr)) modulator are varied and the UiO-66(Zr(O*n*Pr)) crystal structure and porosity, AuNP diameter, UiO-66(Zr(O*n*Pr)) particle geometry, and AuNP location are analyzed to determine the next logical step toward controlling these properties. These studies show that the AuNP capping agent and UiO-66(Zr(O*n*Pr)) modulator have the most prominent effects on the AuNP diameter and location and the UiO-66(Zr(O*n*Pr)) particle size and shape. Specifically, proper selection of both the AuNP capping agent and UiO-66(Zr(O*n*Pr)) modulator controls AuNP aggregation and the propensity of the AuNP capping agent to coordinate to the metal center, respectively. Although conclusive

evidence of completely confined AuNPs in Au@UiO-66(Zr(O*n*Pr)) is not obtained, these preliminary studies guide further optimization.

Chapter 7 explores extending the HCl-free UiO-66(Zr(O*n*Pr)) synthesis procedure to include a multitude of UiO-66 analogues. UiO-66-X(Zr(O*n*Pr)) nucleates rapidly and, therefore, requires the incorporation of an acid in the synthesis to act as a modulating agent. Herein, UiO-66-NH_2(Zr(O*n*Pr)) is used to examine the effects of the acid (acetic acid, benzoic acid, formic acid, trifluoroacetic acid (TFA), and HCl) selected as the modulator and the acid concentration on the UiO-66-NH_2(Zr(O*n*Pr)) properties. These studies suggest that the role of the acid is to regulate the nucleation rate via two-main mechanisms: (1) competitive coordination with the Zr^{4+} sites, and (2) adjustment of the deprotonation equilibrium of 2-aminoterephthalic acid (BDC-NH_2). Based on this analysis, the synthesis procedure is extended to produce high-quality UiO-66-X(Zr(O*n*Pr)), where X = {–H, –NH_2, –NO_2, –Naph, –Anth, –Cl_2, –Br, –$(CH_3)_2$, –COOH, –OH, and –$(OH)_2$}.

Chapter 8 outlines the conclusions from this overall work. Specific topics include the preparation of Au@UiO-66(Zr(O*n*Pr)) via encapsulation, OSC of MOFs, the effect of the preparation methods on the physical and catalytic properties of Au@UiO-66, and the preparation of UiO-66-X(Zr(O*n*Pr)). In addition, recommendations for future work are provided, including suggestions for optimizing the Au@UiO-66(Zr(O*n*Pr)) encapsulation procedure and utilizing the un-optimized Au@UiO-66(Zr(O*n*Pr)) material to explore alternative applications such as plasmonic-assisted photocatalysis.

Appendix A reports a modified synthesis procedure for parent MIL-125, which produces porous, crystalline MIL-125. This is necessary because the previously reported

procedure generates an amorphous powder. In addition, AuNPs are encapsulated in MIL-125, and the physical and catalytic properties of Au@MIL-125 are examined.

Appendix B studies the effects of several synthesis parameters on the physical properties of Au@ZIF-8. In addition, CO oxidation is used to probe the potential of ZIF-8 as an oxidation reaction support. However, Au@ZIF-8 is inactive for temperatures as high as 523K.

Appendix C contains supplemental information for Chapters 3-7, including ^{1}H NMR spectra; nitrogen sorption isotherms at 77K; tables reporting CO conversions, CO conversion rates, and turnover frequencies; and tabulations of CO_2, CO, and O_2 adsorption at 298, 308, and 318K. The information is broken down by chapter. Supplemental TEM images are omitted due to length but are available upon request.

Appendix D contains a tabulated literature review for NP@MOF. It is divided into two tables that review the impregnation and encapsulation reports to date. These tables have been continuously updated throughout the timeframe of this dissertation to include a majority of the NP@MOF literature.

1.4 References

1. The Cambridge Crystallographic Data Centre (CCDC).

2. Wilmer, C. E.; Leaf, M.; Lee, C. Y.; Farha, O. K.; Hauser, B. G.; Hupp, J. T.; Snurr, R. Q., Large-scale screening of hypothetical metal-organic frameworks. *Nature Chemistry* **2012,** *4* (2), 83-89.

3. Ferey, G., Hybrid porous solids: past, present, future. *Chemical Society Reviews* **2008,** *37* (1), 191-214.

4. Furukawa, H.; Cordova, K. E.; O'Keeffe, M.; Yaghi, O. M., The Chemistry and Applications of Metal-Organic Frameworks. *Science* **2013,** *341* (6149), 974-+.

5. Li, J.-R.; Kuppler, R. J.; Zhou, H.-C., Selective gas adsorption and separation in metal-organic frameworks. *Chemical Society Reviews* **2009,** *38* (5), 1477-1504.

6. Horcajada, P.; Chalati, T.; Serre, C.; Gillet, B.; Sebrie, C.; Baati, T.; Eubank, J. F.; Heurtaux, D.; Clayette, P.; Kreuz, C.; Chang, J. S.; Hwang, Y. K.; Marsaud, V.; Bories, P. N.; Cynober, L.; Gil, S.; Ferey, G.; Couvreur, P.; Gref, R., Porous metal-organic-framework nanoscale carriers as a potential platform for drug delivery and imaging. *Nature Materials* **2010,** *9* (2), 172-178.

7. Huxford, R. C.; Della Rocca, J.; Lin, W., Metal-organic frameworks as potential drug carriers. *Current Opinion in Chemical Biology* **2010,** *14* (2), 262-268.

8. Liu, D. M.; Lu, K. D.; Poon, C.; Lin, W. B., Metal-Organic Frameworks as Sensory Materials and Imaging Agents. *Inorganic Chemistry* **2014,** *53* (4), 1916-1924.

9. Britt, D.; Tranchemontagne, D.; Yaghi, O. M., Metal-organic frameworks with high capacity and selectivity for harmful gases. *Proceedings of the National Academy of Sciences of the United States of America* **2008,** *105* (33), 11623-11627.

10. Khan, N. A.; Hasan, Z.; Jhung, S. H., Adsorptive removal of hazardous materials using metal-organic frameworks (MOFs): A review. *Journal of Hazardous Materials* **2013,** *244*, 444-456.

11. DeCoste, J. B.; Peterson, G. W., Metal-Organic Frameworks for Air Purification of Toxic Chemicals. *Chemical Reviews* **2014,** *114* (11), 5695-5727.

12. Lee, J.; Farha, O. K.; Roberts, J.; Scheidt, K. A.; Nguyen, S. T.; Hupp, J. T., Metal-organic framework materials as catalysts. *Chemical Society Reviews* **2009,** *38* (5), 1450-1459.

13. Noei, H.; Amirjalayer, S.; Mueller, M.; Zhang, X.; Schmid, R.; Muhler, M.; Fischer, R. A.; Wang, Y., Low-Temperature CO Oxidation over Cu-Based Metal-Organic Frameworks Monitored by using FTIR Spectroscopy. *Chemcatchem* **2012,** *4* (6), 755-759.

14. Rosi, N. L.; Kim, J.; Eddaoudi, M.; Chen, B. L.; O'Keeffe, M.; Yaghi, O. M., Rod packings and metal-organic frameworks constructed from rod-shaped secondary building units. *Journal of the American Chemical Society* **2005,** *127* (5), 1504-1518.

15. Eddaoudi, M.; Kim, J.; Rosi, N.; Vodak, D.; Wachter, J.; O'Keeffe, M.; Yaghi, O. M., Systematic design of pore size and functionality in isoreticular MOFs and their application in methane storage. *Science* **2002,** *295* (5554), 469-472.

16. Park, K. S.; Ni, Z.; Cote, A. P.; Choi, J. Y.; Huang, R.; Uribe-Romo, F. J.; Chae, H. K.; O'Keeffe, M.; Yaghi, O. M., Exceptional chemical and thermal stability of zeolitic imidazolate frameworks. *Proceedings of the National Academy of Sciences of the United States of America* **2006,** *103* (27), 10186-10191.

17. Cmarik, G. E.; Kim, M.; Cohen, S. M.; Walton, K. S., Tuning the Adsorption Properties of UiO-66 via Ligand Functionalization. *Langmuir* **2012,** *28* (44), 15606-15613.

18. Biswas, S.; Van der Voort, P., A General Strategy for the Synthesis of Functionalised UiO-66 Frameworks: Characterisation, Stability and CO_2 Adsorption Properties. *European Journal of Inorganic Chemistry* **2013,** (12), 2154-2160.

19. Guillerm, V.; Ragon, F.; Dan-Hardi, M.; Devic, T.; Vishnuvarthan, M.; Campo, B.; Vimont, A.; Clet, G.; Yang, Q.; Maurin, G.; Ferey, G.; Vittadini, A.; Gross, S.; Serre, C., A Series of Isoreticular, Highly Stable, Porous Zirconium Oxide Based Metal-Organic Frameworks. *Angewandte Chemie-International Edition* **2012,** *51* (37), 9267-9271.

20. Trung, T. K.; Trens, P.; Tanchoux, N.; Bourrelly, S.; Llewellyn, P. L.; Loera-Serna, S.; Serre, C.; Loiseau, T.; Fajula, F.; Férey, G., Hydrocarbon Adsorption in the Flexible Metal Organic Frameworks MIL-53(Al, Cr). *Journal of the American Chemical Society* **2008,** *130* (50), 16926-16932.

21. Ferey, G.; Mellot-Draznieks, C.; Serre, C.; Millange, F.; Dutour, J.; Surble, S.; Margiolaki, I., A chromium terephthalate-based solid with unusually large pore volumes and surface area. *Science* **2005,** *309* (5743), 2040-2042.

22. Dan-Hardi, M.; Serre, C.; Frot, T.; Rozes, L.; Maurin, G.; Sanchez, C.; Ferey, G., A New Photoactive Crystalline Highly Porous Titanium(IV) Dicarboxylate. *Journal of the American Chemical Society* **2009,** *131* (31), 10857-+.

23. Jasuja, H.; Huang, Y.-g.; Walton, K. S., Adjusting the Stability of Metal-Organic Frameworks under Humid Conditions by Ligand Functionalization. *Langmuir* **2012,** *28* (49), 16874-16880.

24. Jasuja, H.; Burtch, N. C.; Huang, Y.-g.; Cai, Y.; Walton, K. S., Kinetic Water Stability of an Isostructural Family of Zinc-Based Pillared Metal-Organic Frameworks. *Langmuir* **2013,** *29* (2), 633-642.

25. Jasuja, H. Developing Design Criteria and Scale-Up Methods for Water-Stable Metal-Organic Frameworks for Adsorption Applications. Georgia Institute of Technology, 2014.

26. Chui, S. S. Y.; Lo, S. M. F.; Charmant, J. P. H.; Orpen, A. G.; Williams, I. D., A chemically functionalizable nanoporous material $[Cu_3(TMA)_2(H_2O)_3]_n$. *Science* **1999,** *283* (5405), 1148-1150.

27. Caskey, S. R.; Wong-Foy, A. G.; Matzger, A. J., Dramatic tuning of carbon dioxide uptake via metal substitution in a coordination polymer with cylindrical pores. *Journal of the American Chemical Society* **2008,** *130* (33), 10870-+.

28. Hartmann, M.; Fischer, M., Amino-functionalized basic catalysts with MIL-101 structure. *Microporous and Mesoporous Materials* **2012,** *164*, 38-43.

29. Garibay, S. J.; Cohen, S. M., Isoreticular synthesis and modification of frameworks with the UiO-66 topology. *Chemical Communications* **2010,** *46* (41), 7700-7702.

30. Banerjee, R.; Phan, A.; Wang, B.; Knobler, C.; Furukawa, H.; O'Keeffe, M.; Yaghi, O. M., High-Throughput Synthesis of Zeolitic Imidazolate Frameworks and Application to CO_2 Capture. *Science* **2008,** *319* (5865), 939-943.

31. Cai, Y.; Kulkarni, A. R.; Huang, Y.-G.; Sholl, D. S.; Walton, K. S., Control of Metal Organic Framework Crystal Topology by Ligand Functionalization: Functionalized HKUST-1 Derivatives. *Crystal Growth & Design* **2014,** *14* (11), 6122-6128.

32. Karagiaridi, O.; Bury, W.; Sarjeant, A. A.; Stern, C. L.; Farha, O. K.; Hupp, J. T., Synthesis and characterization of isostructural cadmium zeolitic imidazolate frameworks via solvent-assisted linker exchange. *Chemical Science* **2012,** *3* (11), 3256-3260.

33. Karagiaridi, O.; Lalonde, M. B.; Bury, W.; Sarjeant, A. A.; Farha, O. K.; Hupp, J. T., Opening ZIF-8: A Catalytically Active Zeolitic Imidazolate Framework of Sodalite Topology with Unsubstituted Linkers. *Journal of the American Chemical Society* **2012,** *134* (45), 18790-18796.

34. Fei, H. H.; Cahill, J. F.; Prather, K. A.; Cohen, S. M., Tandem Postsynthetic Metal Ion and Ligand Exchange in Zeolitic Imidazolate Frameworks. *Inorganic Chemistry* **2013,** *52* (7), 4011-4016.

35. Kim, M.; Cahill, J. F.; Fei, H.; Prather, K. A.; Cohen, S. M., Postsynthetic Ligand and Cation Exchange in Robust Metal–Organic Frameworks. *Journal of the American Chemical Society* **2012,** *134* (43), 18082-18088.

36. Burtch, N. C.; Jasuja, H.; Walton, K. S., Water Stability and Adsorption in Metal-Organic Frameworks. *Chemical Reviews* **2014,** *114* (20), 10575-10612.

37. Kuesgens, P.; Rose, M.; Senkovska, I.; Froede, H.; Henschel, A.; Siegle, S.; Kaskel, S., Characterization of metal-organic frameworks by water adsorption. *Microporous and Mesoporous Materials* **2009,** *120* (3), 325-330.

38. Jasuja, H. Developing Design Criteria and Scale-Up Methods for Water-Stable Metal-Organic Frameworks for Adsorption Applications. Georgia Institute of Technology, 2014.

39. Seo, Y.-K.; Yoon, J. W.; Lee, J. S.; Lee, U. H.; Hwang, Y. K.; Jun, C.-H.; Horcajada, P.; Serre, C.; Chang, J.-S., Large scale fluorine-free synthesis of hierarchically porous iron(III) trimesate MIL-100(Fe) with a zeolite MTN topology. *Microporous and Mesoporous Materials* **2012,** *157*, 137-145.

40. Stock, N.; Biswas, S., Synthesis of Metal-Organic Frameworks (MOFs): Routes to Various MOF Topologies, Morphologies, and Composites. *Chemical Reviews* **2012,** *112* (2), 933-969.

41. Paseta, L.; Seoane, B.; Julve, D.; Sebastián, V.; Téllez, C.; Coronas, J., Accelerating the Controlled Synthesis of Metal–Organic Frameworks by a Microfluidic Approach: A Nanoliter Continuous Reactor. *ACS Applied Materials & Interfaces* **2013,** *5* (19), 9405-9410.

42. Faustini, M.; Kim, J.; Jeong, G.-Y.; Kim, J. Y.; Moon, H. R.; Ahn, W.-S.; Kim, D.-P., Microfluidic Approach toward Continuous and Ultrafast Synthesis of Metal–Organic Framework Crystals and Hetero Structures in Confined Microdroplets. *Journal of the American Chemical Society* **2013,** *135* (39), 14619-14626.

43. Rubio-Martinez, M.; Batten, M. P.; Polyzos, A.; Carey, K.-C.; Mardel, J. I.; Lim, K.-S.; Hill, M. R., Versatile, High Quality and Scalable Continuous Flow Production of Metal-Organic Frameworks. *Scientific Reports* **2014,** *4*, 5443.

44. Schoenecker, B., Grabicka, and Walton, Kinetics Study and Crystallization Process Design for Scale-Up of UiO-66-NH_2 Synthesis. *AIChE* **2012**.

45. Lu, G.; Li, S.; Guo, Z.; Farha, O. K.; Hauser, B. G.; Qi, X.; Wang, Y.; Wang, X.; Han, S.; Liu, X.; DuChene, J. S.; Zhang, H.; Zhang, Q.; Chen, X.; Ma, J.; Loo, S. C. J.; Wei, W. D.; Yang, Y.; Hupp, J. T.; Huo, F., Imparting functionality to a metal-organic framework material by controlled nanoparticle encapsulation. *Nature Chemistry* **2012,** *4* (4), 310-316.

46. Dhakshinamoorthy, A.; Garcia, H., Catalysis by metal nanoparticles embedded on metal-organic frameworks. *Chemical Society Reviews* **2012,** *41* (15), 5262-5284.

47. Zhan, W.-w.; Kuang, Q.; Zhou, J.-z.; Kong, X.-j.; Xie, Z.-x.; Zheng, L.-s., Semiconductor@Metal-Organic Framework Core-Shell Heterostructures: A Case

of ZnO@ZIF-8 Nanorods with Selective Photoelectrochemical Response. *Journal of the American Chemical Society* **2013,** *135* (5), 1926-1933.

48. Sugikawa, K.; Furukawa, Y.; Sada, K., SERS-Active Metal-Organic Frameworks Embedding Gold Nanorods. *Chemistry of Materials* **2011,** *23* (13), 3132-3134.

49. Deng, K.; Hou, Z.; Li, X.; Li, C.; Zhang, Y.; Deng, X.; Cheng, Z.; Lin, J., Aptamer-Mediated Up-conversion Core/MOF Shell Nanocomposites for Targeted Drug Delivery and Cell Imaging. *Scientific Reports* **2015,** *5*.

50. Falcaro, P.; Ricco, R.; Yazdi, A.; Imaz, I.; Furukawa, S.; Maspoch, D.; Ameloot, R.; Evans, J. D.; Doonan, C. J., Application of metal and metal oxide nanoparticles@MOFs. *Coordination Chemistry Reviews* **2016,** *307*, 237-254.

51. Zhang, D.; Guan, Y.; Hensen, E. J. M.; Chen, L.; Wang, Y., Porous MOFs supported palladium catalysts for phenol hydrogenation: A comparative study on MIL-101 and MIL-53. *Catalysis Communications* **2013,** *41* (0), 47-51.

52. Khajavi, H.; Stil, H. A.; Kuipers, H.; Gascon, J.; Kapteijn, F., Shape and Transition State Selective Hydrogenations Using Egg-Shell Pt-MIL-101(Cr) Catalyst. *Acs Catalysis* **2013,** *3* (11), 2617-2626.

53. Suh, M. P.; Moon, H. R.; Lee, E. Y.; Jang, S. Y., A redox-active two-dimensional coordination polymer: Preparation of silver and gold nanoparticles and crystal dynamics on guest removal. *Journal of the American Chemical Society* **2006,** *128* (14), 4710-4718.

54. Hou, C. T.; Xu, Q.; Wang, Y. J.; Hu, X. Y., Synthesis of Pt@NH_2-MIL-125(Ti) as a photocathode material for photoelectrochemical hydrogen production. *RSC Advances* **2013,** *3* (43), 19820-19823.

55. Sabo, M.; Henschel, A.; Froede, H.; Klemm, E.; Kaskel, S., Solution infiltration of palladium into MOF-5: synthesis, physisorption and catalytic properties. *Journal of Materials Chemistry* **2007,** *17* (36), 3827-3832.

56. Hermes, S.; Schroter, M. K.; Schmid, R.; Khodeir, L.; Muhler, M.; Tissler, A.; Fischer, R. W.; Fischer, R. A., Metal@MOF: Loading of highly porous coordination polymers host lattices by metal organic chemical vapor deposition. *Angewandte Chemie-International Edition* **2005,** *44* (38), 6237-6241.

57. Esken, D.; Turner, S.; Lebedev, O. I.; Van Tendeloo, G.; Fischer, R. A., Au@ZIFs: Stabilization and Encapsulation of Cavity-Size Matching Gold Clusters inside Functionalized Zeolite Imidazolate Frameworks, ZIFs. *Chemistry of Materials* **2010,** *22* (23), 6393-6401.

58. Muller, M.; Zhang, X. N.; Wang, Y. M.; Fischer, R. A., Nanometer-sized titania hosted inside MOF-5. *Chemical Communications* **2009,** (1), 119-121.

59. Ishida, T.; Nagaoka, M.; Akita, T.; Haruta, M., Deposition of Gold Clusters on Porous Coordination Polymers by Solid Grinding and Their Catalytic Activity in Aerobic Oxidation of Alcohols. *Chemistry-a European Journal* **2008,** *14* (28), 8456-8460.

60. Jiang, H. L.; Liu, B.; Akita, T.; Haruta, M.; Sakurai, H.; Xu, Q., Au@ZIF-8: CO Oxidation over Gold Nanoparticles Deposited to Metal-Organic Framework. *Journal of the American Chemical Society* **2009,** *131* (32), 11302-+.

61. Liu, J.; Strachan, D. M.; Thallapally, P. K., Enhanced noble gas adsorption in Ag@MOF-74Ni. *Chemical Communications* **2014,** *50* (4), 466-468.

62. Esken, D.; Zhang, X.; Lebedev, O. I.; Schroder, F.; Fischer, R. A., Pd@MOF-5: limitations of gas-phase infiltration and solution impregnation of $Zn_4O(bdc)_3$ (MOF-5) with metal-organic palladium precursors for loading with Pd nanoparticles. *Journal of Materials Chemistry* **2009,** *19* (9), 1314-1319.

63. Gole, B.; Sanyal, U.; Mukherjee, P. S., A smart approach to achieve an exceptionally high loading of metal nanoparticles supported by functionalized extended frameworks for efficient catalysis. *Chemical Communications* **2015,** *51* (23), 4872-4875.

64. Cheng, X.; Liu, M.; Zhang, A.; Hu, S.; Song, C.; Zhang, G.; Guo, X., Size-controlled silver nanoparticles stabilized on thiol-functionalized MIL-53(Al) frameworks. *Nanoscale* **2015,** *7* (21), 9738-9745.

65. Luan, Y.; Qi, Y.; Gao, H.; Zheng, N.; Wang, G., Synthesis of an amino-functionalized metal-organic framework at a nanoscale level for gold nanoparticle deposition and catalysis. *Journal of Materials Chemistry A* **2014,** *2* (48), 20588-20596.

66. Lu, G.; Li, S. Z.; Guo, Z.; Farha, O. K.; Hauser, B. G.; Qi, X. Y.; Wang, Y.; Wang, X.; Han, S. Y.; Liu, X. G.; DuChene, J. S.; Zhang, H.; Zhang, Q. C.; Chen, X. D.; Ma, J.; Loo, S. C. J.; Wei, W. D.; Yang, Y. H.; Hupp, J. T.; Huo, F. W., Imparting functionality to a metal-organic framework material by controlled nanoparticle encapsulation. *Nature Chemistry* **2012,** *4* (4), 310-316.

67. Tsuruoka, T.; Kawasaki, H.; Nawafune, H.; Akamatsu, K., Controlled Self-Assembly of Metal-Organic Frameworks on Metal Nanoparticles for Efficient Synthesis of Hybrid Nanostructures. *Acs Applied Materials & Interfaces* **2011,** *3* (10), 3788-3791.

68. Falcaro, P.; Hill, A. J.; Nairn, K. M.; Jasieniak, J.; Mardel, J. I.; Bastow, T. J.; Mayo, S. C.; Gimona, M.; Gomez, D.; Whitfield, H. J.; Ricco, R.; Patelli, A.; Marmiroli, B.; Amenitsch, H.; Colson, T.; Villanova, L.; Buso, D., A new method to position and functionalize metal-organic framework crystals. *Nature Communications* **2011,** *2*.

69. Liu, H.; Chang, L.; Chen, L.; Li, Y., In situ one-step synthesis of metal-organic framework encapsulated naked Pt nanoparticles without additional reductants. *Journal of Materials Chemistry A* **2015,** *3* (15), 8028-8033.

70. Petit, C.; Bandosz, T. J., Engineering the surface of a new class of adsorbents: Metal-organic framework/graphite oxide composites. *Journal of Colloid and Interface Science* **2015,** *447*, 139-151.

71. Zhang, W. N.; Lu, G.; Cui, C. L.; Liu, Y. Y.; Li, S. Z.; Yan, W. J.; Xing, C.; Chi, Y. R.; Yang, Y. H.; Huo, F. W., A Family of Metal-Organic Frameworks Exhibiting Size-Selective Catalysis with Encapsulated Noble-Metal Nanoparticles. *Advanced Materials* **2014,** *26* (24), 4056-4060.

72. Zhang, C.-F.; Qiu, L.-G.; Ke, F.; Zhu, Y.-J.; Yuan, Y.-P.; Xu, G.-S.; Jiang, X., A novel magnetic recyclable photocatalyst based on a core-shell metal-organic framework Fe_3O_4@MIL-100(Fe) for the decolorization of methylene blue dye. *Journal of Materials Chemistry A* **2013,** *1* (45), 14329-14334.

73. Khaletskaya, K.; Reboul, J.; Meilikhov, M.; Nakahama, M.; Diring, S.; Tsujimoto, M.; Isoda, S.; Kim, F.; Kamei, K.-i.; Fischer, R. A.; Kitagawa, S.; Furukawa, S., Integration of Porous Coordination Polymers and Gold Nanorods into Core-Shell Mesoscopic Composites toward Light-Induced Molecular Release. *Journal of the American Chemical Society* **2013,** *135* (30), 10998-11005.

74. Ohhashi, T.; Tsuruoka, T.; Matsuyama, T.; Takashima, Y.; Nawafune, H.; Minami, H.; Akamatsu, K., Metal nanocrystal/metal-organic framework core/shell nanostructure from selective self-assembly induced by localization of metal ion precursors on nanocrystal surface. *Journal of Colloid and Interface Science* **2015,** *451*, 212-215.

75. Zheng, J. N.; Lin, Z.; Lin, G.; Yang, H. H.; Zhang, L., Preparation of magnetic metal-organic framework nanocomposites for highly specific separation of histidine-rich proteins. *Journal of Materials Chemistry B* **2015,** *3* (10), 2185-2191.

76. Han, Y.; Qi, P.; Feng, X.; Li, S.; Fu, X.; Li, H.; Chen, Y.; Zhou, J.; Li, X.; Wang, B., In Situ Growth of MOFs on the Surface of Si Nanoparticles for Highly Efficient Lithium Storage: Si@MOF Nanocomposites as Anode Materials for Lithium-Ion Batteries. *Acs Applied Materials & Interfaces* **2015,** *7* (4), 2178-2182.

77. Zhang, N.; Zhu, B.; Peng, F.; Yu, X.; Jia, Y.; Wang, J.; Kong, L.; Jin, Z.; Luo, T.; Liu, J., Synthesis of metal-organic-framework related core-shell heterostructures and their application to ion enrichment in aqueous conditions. *Chemical Communications* **2014,** *50* (57), 7686-7689.

78. Xia, Y.; Xiong, Y.; Lim, B.; Skrabalak, S. E., Shape-Controlled Synthesis of Metal Nanocrystals: Simple Chemistry Meets Complex Physics? *Angewandte Chemie (International ed. in English)* **2009,** *48* (1), 60-103.

79. Eustis, S.; El-Sayed, M. A., Why gold nanoparticles are more precious than pretty gold: Noble metal surface plasmon resonance and its enhancement of the radiative and nonradiative properties of nanocrystals of different shapes. *Chemical Society Reviews* **2006,** *35* (3), 209-217.

80. Wiley, B. J.; Im, S. H.; Li, Z.-Y.; McLellan, J.; Siekkinen, A.; Xia, Y., Maneuvering the surface plasmon resonance of silver nanostructures through shape-controlled synthesis. *Journal of Physical Chemistry B* **2006,** *110* (32), 15666-15675.

81. Jun, Y.-W.; Seo, J.-W.; Cheon, A., Nanoscaling laws of magnetic nanoparticles and their applicabilities in biomedical sciences. *Accounts of Chemical Research* **2008,** *41* (2), 179-189.

82. Haruta, M., Size- and support-dependency in the catalysis of gold. *Catalysis Today* **1997,** *36* (1), 153-166.

83. Park, J. I.; Kang, N. J.; Jun, Y. W.; Oh, S. J.; Ri, H. C.; Cheon, J., Superlattice and magnetism directed by the size and shape of nanocrystals. *Chemphyschem* **2002,** *3* (6), 543-+.

84. Zhou, K.; Li, Y., Catalysis Based on Nanocrystals with Well-Defined Facets. *Angewandte Chemie International Edition* **2012,** *51* (3), 602-613.

85. Narayanan, R.; El-Sayed, M. A., Catalysis with transition metal nanoparticles in colloidal solution: Nanoparticle shape dependence and stability. *Journal of Physical Chemistry B* **2005,** *109* (26), 12663-12676.

86. Hostetler, M. J.; Wingate, J. E.; Zhong, C. J.; Harris, J. E.; Vachet, R. W.; Clark, M. R.; Londono, J. D.; Green, S. J.; Stokes, J. J.; Wignall, G. D.; Glish, G. L.; Porter, M. D.; Evans, N. D.; Murray, R. W., Alkanethiolate gold cluster molecules with core diameters from 1.5 to 5.2 nm: Core and monolayer properties as a function of core size. *Langmuir* **1998,** *14* (1), 17-30.

87. Zheng, Y. Q.; Ma, Y. Y.; Zeng, J.; Zhong, X. L.; Jin, M. S.; Li, Z. Y.; Xia, Y. N., Seed-Mediated Synthesis of Single-Crystal Gold Nanospheres with Controlled

Diameters in the Range 5-30nm and their Self-Assembly upon Dilution. *Chemistry-an Asian Journal* **2013,** *8* (4), 792-799.

88. Xiong, Y. J.; Chen, J. Y.; Wiley, B.; Xia, Y. N.; Yin, Y. D.; Li, Z. Y., Size-dependence of surface plasmon resonance and oxidation for pd nanocubes synthesized via a seed etching process. *Nano Letters* **2005,** *5* (7), 1237-1242.

89. Xiong, Y.; Cai, H.; Wiley, B. J.; Wang, J.; Kim, M. J.; Xia, Y., Synthesis and mechanistic study of palladium nanobars and nanorods. *Journal of the American Chemical Society* **2007,** *129* (12), 3665-3675.

90. Xiong, Y. J.; McLellan, J. M.; Chen, J. Y.; Yin, Y. D.; Li, Z. Y.; Xia, Y. N., Kinetically controlled synthesis of triangular and hexagonal nanoplates of palladium and their SPR/SERS properties. *Journal of the American Chemical Society* **2005,** *127* (48), 17118-17127.

91. Chen, L.; Chen, X.; Liu, H.; Li, Y., Encapsulation of Mono- or Bimetal Nanoparticles Inside Metal-Organic Frameworks via In situ Incorporation of Metal Precursors. *Small* **2015,** *11* (22), 2642-2648.

92. Chen, L.; Huang, B.; Qiu, X.; Wang, X.; Luque, R.; Li, Y., Seed-mediated growth of MOF-encapsulated Pd@Ag core-shell nanoparticles: toward advanced room temperature nanocatalysts. *Chemical Science* **2016,** *7* (1), 228-233.

93. Mukoyoshi, M.; Kobayashi, H.; Kusada, K.; Hayashi, M.; Yamada, T.; Maesato, M.; Taylor, J. M.; Kubota, Y.; Kato, K.; Takata, M.; Yamamoto, T.; Matsumura, S.; Kitagawa, H., Hybrid materials of Ni NP@MOF prepared by a simple synthetic method. *Chemical Communications* **2015,** *51* (62), 12463-12466.

94. Peterson, G. W.; Rossin, J. A.; DeCoste, J. B.; Killops, K. L.; Browe, M.; Valdes, E.; Jones, P., Zirconium Hydroxide-Metal-Organic Framework Composites for Toxic Chemical Removal. *Industrial & Engineering Chemistry Research* **2013,** *52* (15), 5462-5469.

95. Wang, R.; Gu, L.; Zhou, J.; Liu, X.; Teng, F.; Li, C.; Shen, Y.; Yuan, Y., Quasi-Polymeric Metal–Organic Framework UiO-66/g-C_3N_4 Heterojunctions for Enhanced Photocatalytic Hydrogen Evolution under Visible Light Irradiation. *Advanced Materials Interfaces* **2015,** *2* (10).

96. Zlotea, C.; Campesi, R.; Cuevas, F.; Leroy, E.; Dibandjo, P.; Volkringer, C.; Loiseau, T.; Ferey, G.; Latroche, M., Pd Nanoparticles Embedded into a Metal-Organic Framework: Synthesis, Structural Characteristics, and Hydrogen Sorption Properties. *Journal of the American Chemical Society* **2010,** *132* (9), 2991-2997.

97. Li, X.; Guo, Z.; Xiao, C.; Goh, T. W.; Tesfagaber, D.; Huang, W., Tandem Catalysis by Palladium Nanoclusters Encapsulated in Metal-Organic Frameworks. *Acs Catalysis* **2014,** *4* (10), 3490-3497.

98. Turner, S.; Lebedev, O. I.; Schroder, F.; Esken, D.; Fischer, R. A.; Van Tendeloo, G., Direct imaging of loaded metal-organic framework materials (metal@MOF-5). *Chemistry of Materials* **2008,** *20* (17), 5622-5627.

99. Goel, S.; Wu, Z.; Zones, S. I.; Iglesia, E., Synthesis and Catalytic Properties of Metal Clusters Encapsulated within Small-Pore (SOD, GIS, ANA) Zeolites. *Journal of the American Chemical Society* **2012,** *134* (42), 17688-17695.

100. Ding, Y.; Zhang, F.; Wang, Z. L., Deriving the three-dimensional structure of ZnO nanowires/nanobelts by scanning transmission electron microscope tomography. *Nano Research* **2013,** *6* (4), 253-262.

CHAPTER 2

EXPERIMENTAL MATERIALS AND METHODS

2.1 Materials

2.1.1 Gold Nanoparticles (AuNPs)

Gold nanomaterials are widely studied due to their unusual optic and catalytic properties, and extensive studies have led to the preparation of AuNPs with controlled size, shape, and structure. [1-6] For gold nanomaterials, the unusual optical properties occur upon reduction in size into the nanoscale, which causes the electrons in the conduction band to oscillate at a frequency within the visible region. This oscillation gives rise to the surface plasmon resonance (SPR) absorption, which is observed by the red coloration of gold nanomaterials. The SPR can be tuned by varying the size and shape of the gold nanomaterials, as illustrated in Figure 2.1; therefore, the geometric tuning of the AuNPs controls the optical properties of the materials which are useful for sensing and imaging applications.[1, 2] In addition, supported AuNPs have been proven catalytically active for numerous oxidation; selective hydrogenation; C-C coupling; oxophilic, alkyne, and hydrosilane activation; and cyclization reactions.[7-9] Moreover, the AuNP diameter often affects the catalytic activity and selectivity of the materials further highlighting the importance of geometric control of AuNPs for catalytic applications.[10, 11]

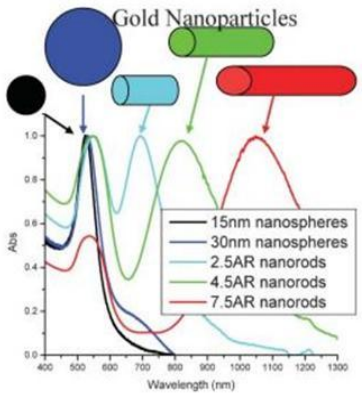

Figure 2.1: Light absorption of gold nanomaterials of various diameters and shapes. Reproduced from El-Sayed et al.[2]

AuNPs with a mixed monolayer of 1-dodecanethiol (DDT) and 11-mercaptoundecanoic acid (MUA), as illustrated in Figure 2.2, are used throughout this work. DDT is necessary to control the AuNP diameter during the nanoparticle synthesis, and MUA adds carboxylic acid functional groups for integration in the MOF. The AuNPs are prepared in two steps: (1) a two-phase reduction reaction followed by (2) a ligand place exchange. The two-phase reduction procedure, known as the "Brust-Schiffrin Two-Phase Approach," is previously reported and illustrated in Figure 2.3.[12] Briefly, gold(III) chloride trihydrate ($HAuCl_4 \cdot 3H_2O$) is transferred from an aqueous solution to an organic medium using the phase transfer agent, tetraoctylammonium bromide. Then, the gold salt is reduced using sodium borohydride ($NaBH_4$) in the presence of DDT, producing DDT protected AuNPs. Multiple studies have examined the various synthesis parameters and shown that the diameter of the DDT capped AuNPs can be tuned by varying the DDT to $HAuCl_4 \cdot 3H_2O$ ratio, where larger ratios yield smaller AuNPs.[5] The DDT-protected AuNPs are then functionalized with MUA using a ligand exchange reaction previously reported and outlined in Eq. 2.1[13]

$$x(MUA)+(DDT)_m\ AuNP \rightarrow x(DDT)+(MUA)_m(DDT)_{m-x}\ AuNP, \quad (2.1)$$

where *x* is the number of ligands place-exchanged and *m* is the original number of DDT molecules on the AuNPs. The resulting DDT/MUA protected AuNPs are used for encapsulation throughout this work.

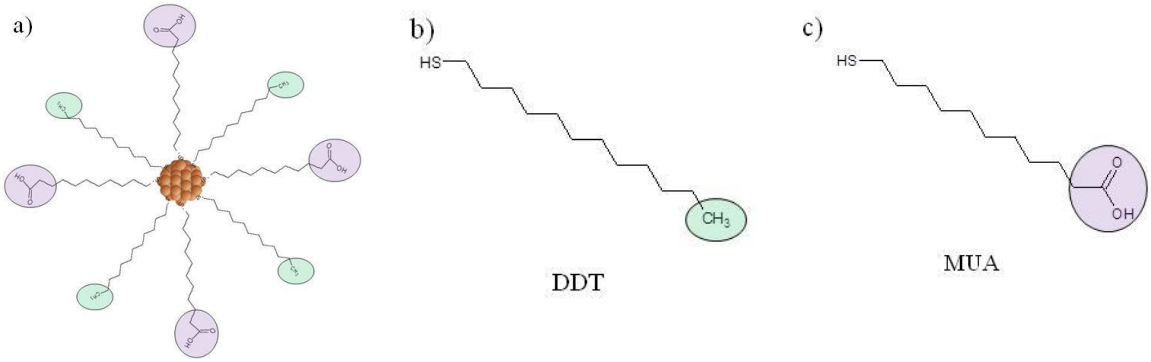

Figure 2.2: Illustration of (a) AuNPs with a mixed monolayer of DDT and MUA; (b) structure of DDT; (c) structure of MUA

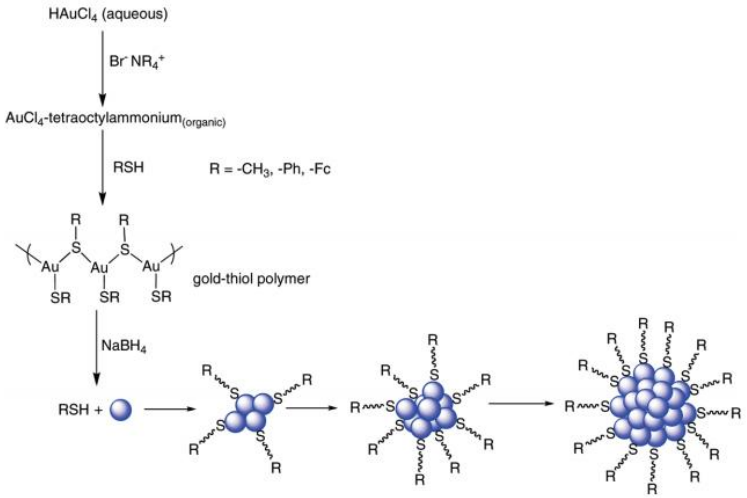

Figure 2.3: Scheme for AuNP synthesis using the Brust-Schiffrin Two-Phase Approach reproduced from Sardar et al.[14]

2.1.2 Metal-Organic Frameworks (MOFs)

2.1.2.1 UiO-66

UiO-66, depicted in Figure 2.4, is a zirconium-based MOF that consists of $Zr_6O_4(OH)_4$ octahedron linked by 1,4-benzenedicarboxylic acid (BDC). UiO-66 is a promising material due to its thermal, mechanical, and chemical resistance and straightforward chemical functionalization.[15-17] UiO-66 and its analogues have been investigated for a multitude of applications including hydrogen storage,[18, 19] carbon capture,[20, 21] gas separation,[22, 23] toxic industrial chemical (TIC) removal,[24-26] drug delivery,[27] heavy metal removal,[28] degradation of chemical warfare agents (CWAs),[29-32] catalysis,[33-35] and photocatalysis.[36, 37] In addition, various methods have been explored to scale-up the synthesis procedure to yield large quantities of UiO-66.[38-41]

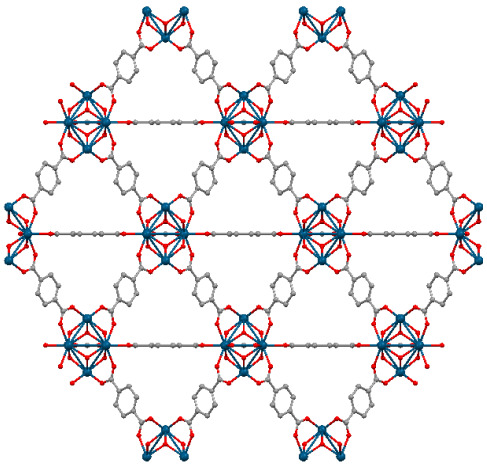

Figure 2.4: Illustration of UiO-66 structure where zirconium atoms are blue, oxygen atoms are red, and carbon atoms are gray

The conventional synthesis of UiO-66 uses zirconium chloride ($ZrCl_4$), which generates hydrochloric acid (HCl) as a by-product during the solvothermal reaction. Unfortunately, HCl dissolves AuNPs, which is problematic for the encapsulation of

AuNPs in UiO-66. Therefore, an alternative synthesis was developed that substitutes $ZrCl_4$ with zirconium propoxide (Zr(O*n*Pr)). This alternative synthesis mixes Zr(O*n*Pr) (0.227 mmol), BDC (0.454 mmol), and acetic acid (6.81 mmol) in methanol and N,N'-dimethylformamide (DMF) at 393 K for 24 h.[42]

2.1.3 MOF Composites

2.1.3.1 Colloidal Deposition

Preformed metal nanoparticles are deposited on the surface of MOFs using a colloidal deposition process. In this work, AuNPs were deposited on the surface of UiO-66. Briefly, 40-50 mg of UiO-66 were sonicated in methanol (9.9 mL) for 5 min. Then, various amounts of AuNPs were added, and the mixture was stirred at room temperature for 24 h.

2.1.3.2 Impregnation

Metal nanoparticles are incorporated in MOFs by adding metal chlorides to the preformed MOF in a process designated as impregnation throughout this work. Herein, AuNPs are incorporated in UiO-66 using $HAuCl_4 \cdot 3H_2O$. Briefly, 170 mg of UiO-66 was degassed at 473 K under vacuum for 16-18 h. The activated UiO-66 was stirred in a solution of g $HAuCl_4 \cdot 3H_2O$ (0.018 mmol) in methanol (40 mL) for 6 h. Then, $NaBH_4$ (0.178 mmol) was added to the slurry and stirred for an additional 1 h. Finally, the product was filtered and rinsed with methanol.

2.1.3.3 Encapsulation

Metal nanoparticles can also be integrated in MOFs using an encapsulation technique by adding preformed metal nanoparticles to the MOF mother solution. Herein, preformed AuNPs, prepared as described above, were added to Zr(O*n*Pr) (0.227 mmol), BDC (0.454 mmol), methanol (86.5 mmol), DMF (45.4 mmol), and glacial acetic acid (6.81 mmol) and stirred in a glass scintillation vial at 393 K for 24 h. Lastly, the resulting material was filtered and washed three times with DMF and three times with methanol.

2.2 Experimental Methods

2.2.1 Material Characterization

Multiple characterization techniques were utilized in this work. Powder X-ray diffraction, nitrogen sorption at 77 K, and thermogravimetric analysis were used to characterize the MOF structures. In addition, microscopic techniques were utilized to determine the size and morphology of the materials; spectroscopic techniques were used to characterize the organic layer on the nanoparticles; and temperature programmed reduction (H_2-TPR) was used to characterize the redox characteristics of the materials.

2.2.1.1 Powder X-ray Diffraction

Powder X-ray Diffraction (PXRD) is a non-destructive characterization technique that reveals the crystalline nature of a material. PXRD measures the constructive interference between the X-rays diffracted by the crystal structure relating the angle of

incidence, Θ, to the spacing between the crystal planes, d, as depicted in Figure 2.5. The incidence angle is related to the d-spacing via Bragg's Equation (Eq. 2.2).[43]

$$2d\sin\theta = n\lambda \tag{2.2}$$

The remaining constants, n and λ, refer to the order of diffraction and the X-ray wavelength, respectively. Destructive interference at specific incidence angles results in systematic absences, which yield information about the lattice geometry.

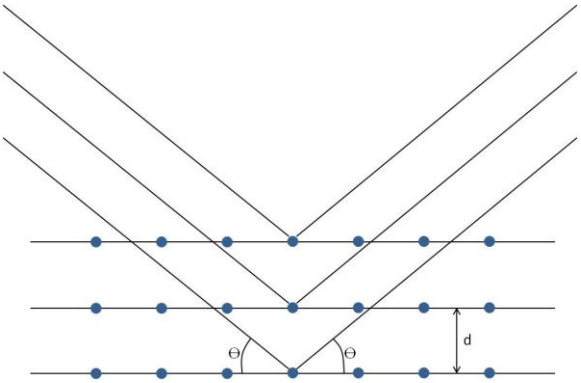

Figure 2.5: Illustration of Bragg's Law

PXRD patterns throughout this work were obtained using the X'Pert Pro PANalytical X-ray diffractometer equipped with the X'Celerator detector. The scan uses a Θ-Θ scan configuration which means that the source and the detector both scan at Θ° relative to the sample pan. In this work, diffractograms were measured from 5-90°, and the peak positions were compared to published MOF structures to ensure the correct material is obtained.

2.2.1.2 Thermogravimetric Analysis

Thermogravimetric analysis (TGA) was used to determine the thermal degradation temperature of all materials. TGA curves were collected using the Netzsch STA 449 Jupiter Simultaneous TG-DSC apparatus under 20 mL/min of air or helium flow. Approximately 5-20 mg of material were placed in an alumina crucible with a lid and placed on a microbalance within the furnace. The temperature was ramped at rates ranging from 1-10 K/min, and the sample mass was recorded. Solvent loss and material degradation were determined from the mass and temperature results.

2.2.1.3 Microscopy

Transmission electron microscopy (TEM) is used to investigate the preformed nanoparticle geometry and the nanoparticle geometry and location within the MOF composites. The MOF composites are analyzed using several microscopic techniques including bright field TEM, scanning transmission electron microscopy-energy dispersive spectroscopy (STEM-EDS), and electron tomography. Figure 2.6 depicts a simple diagram of TEM operation and the various TEM modes. TEM operates by passing an electron beam through a thin sample. Bright field TEM is the most common mode of operation, where the image forms by the blockage and absorbance of the electrons by the sample. This means that thicker regions of the sample and materials with higher atomic numbers appear darker. STEM operates by focusing the beam on a small area and rastering the beam over the sample. The electrons are detected using a high-angle annular dark-field detector, which detects the electrons scattered by the sample. This means that materials with higher atomic numbers appear brighter. Electron tomography is a three-

dimensional technique that operates by rotating the sample from -70° to 70° in STEM mode and acquiring a series of images in 2° intervals. Electron tomography is the most widely accepted technique for determining nanoparticle location for supported nanoparticles. Notably, many MOFs degrade under the electron beam; however, UiO-66 does not have this limitation.[44-47]

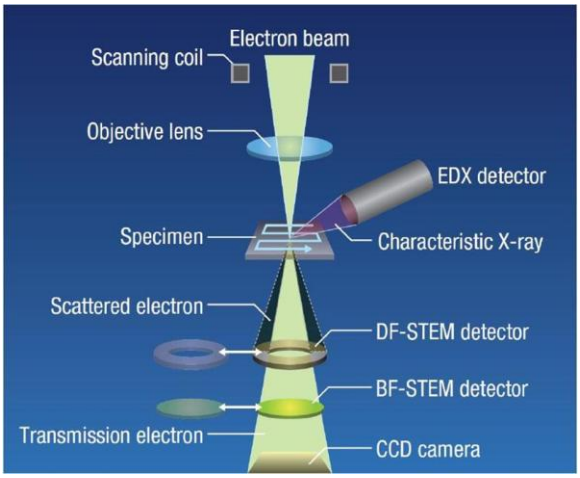

Figure 2.6: Illustration of TEM modes. Reproduced from MATE 6110 notes[48]

TEM samples were prepared by suspending less than a milligram of sample in methanol or chloroform and dropcasting the sample onto a lacy carbon coated copper grid. TEM was conducted using the JEOL 100CX operated at 100 keV, the Hitachi HT7700 operated at 120 keV, and the FEI Tecnai F30 operated at 300 keV. STEM-EDS was run using the FEI Tecnai F30 coupled with the Oxford EDX 6763. The composition was measured at a specified point marked with a red circle and analyzed using TEM Imaging & Analysis (TIA) Software. Finally, TEM tomography was run in STEM mode using the FEI Tecnai F30 with a TEM tomography sample holder and FEI tomography software taking an image every 2°.

2.2.1.4 Proton Nuclear Magnetic Resonance Spectroscopy

Proton nuclear magnetic resonance (^{1}H NMR) spectroscopy is used to characterize the organic monolayer on the AuNPs. ^{1}H NMR spectra were collected using a Varian Mercury Vx 300. Approximately 5-10 mg of AuNPs were suspended in 1 mL of chloroform-d or dimethyl sulfoxide-d_6. The spectrum was an average of 64 scans measured from -2 to 14 ppm. The number of scans necessary was dependent on the amount of sample. The spectra were analyzed using MestReNova Lite software.

2.2.1.5 Temperature Programmed Reduction

Temperature programmed reduction (H_2-TPR) was performed using the Micromeritics AutoChem II 2920. Approximately 30-50 mg of material were loaded into a quartz U-tube reactor. Prior to the H_2-TPR experiment the samples were heated at 473 K for 1 h under helium flow to remove any water and solvent. The H_2-TPR experiment ramped the temperature from 323 K to 673 K at 5 K/min under a stream of 10% H_2 in helium for UiO-66 and subsequent composites. UiO-66 decomposes at temperatures exceeding 673 K under 10% H_2 in helium; therefore, the temperature ramp was terminated in order to protect the detector from the decomposition components. For metal oxides and metal oxide composites, the temperature was ramped from 323 K to 1073 K at 5 K/min. In addition, before the H_2-TPR analysis for some samples, there was a calcination step, which consisted of flowing a stream of 10% oxygen in helium at 523 K for 2 h, then cooling the sample to 323 K under helium before beginning the H_2-TPR experiment.

2.2.2 Adsorption Measurements

2.2.2.1 Nitrogen Sorption at 77 K

Nitrogen sorption measurements at 77 K were obtained using a Quantachrome Quadrasorb SI and a Quantachrome Quadrasorb Evo volumetric analyzer. The isotherms were measured over a range of relative pressures from 0.003 to 0.990 using high purity nitrogen (99.998%) obtained from Airgas. Prior to the measurement, the samples were outgassed in a Quantachrome FloVac Degasser at temperatures ranging from 383-473 K under dynamic vacuum. The sample was backfilled with nitrogen; the activated mass was measured and used to normalize the uptake.

The specific surface area of the materials was modeled using the Brunauer, Emmett, and Teller (BET) theory which models multilayer adsorption of gases on surfaces near the gas condensation temperature.[49] There are five main assumptions used to derive the BET theory. First, it is assumed that the non-dissociative adsorption of a molecule only occurs on well-defined surface sites. Secondly, an adsorbed molecule can act as a single adsorption site for molecules in the upper layers. Third, the uppermost adsorbate layer is at equilibrium with the gas phase meaning that the rate of adsorption is equal to the rate of desorption. This is represented in Eq. 2.3

$$\begin{aligned} a_1 P S_0 &= b_1 S_1 e^{-E_1/RT} \\ a_2 P S_1 &= b_2 S_2 e^{-E_2/RT} \\ a_3 P S_2 &= b_3 S_3 e^{-E_3/RT} \\ &\vdots \\ a_i P S_{i-1} &= b_i S_i e^{-E_i/RT} \end{aligned} \tag{2.3}$$

where P is pressure, S_0, S_1, S_2, S_{i-1}, S_i represent the surface area covered by layer i of adsorbate, E_1, E_2, E_3, E_i is the heat of adsorption of layer i, and a_1, a_2, a_3, a_i and b_1, b_2, b_3, b_i are constants. Fourth, heat is required to activate the adsorption/desorption process. The heat of adsorption for the first layer, represented as E_1, is the heat of adsorption of the adsorbate on the surface. The heats of adsorption for the second and higher layers are similar and assumed to be the same as the condensed phase. This is shown in Eq. 2.4

$$E_2 = E_3 = ... = E_i = E_L \tag{2.4}$$

where E_L represents the heat of liquefaction of the adsorbate. Finally, it is assumed that at the saturation pressure an infinite number of layers exist on the adsorbent surface. Using these assumptions the final isotherm model is calculated and reported in Eq. 2.5:

$$\frac{P}{v\left(P_0 - P\right)} = \frac{1}{v_m c} + \frac{c-1}{v_m c}\frac{P}{P_0} \tag{2.5}$$

where v is the total volume adsorbed, v_m is the volume of the adsorbed monolayer, P/P_0 is the relative pressure of the system, and c is a constant. Eq. 2.5 is fit to experimental data by plotting $P/v\left(P_0 - P\right)$ versus P/P_0 over the relative pressure range of $0.05 \leq P/P_0 \leq 0.3$, and the resulting line has a y-intercept of $1/v_m c$ and a slope of $\left(c-1\right)/v_m c$. From this information, the BET surface area is calculated using Eq. 2.6:

$$S_{BET} = \frac{v_m N_{Av} a}{v m_{sample}}, \tag{2.6}$$

where N_{Av} is Avogadro's number, a is the cross-sectional area of the adsorbate, and m_{sample} is the mass of the sample.

However, layer-by-layer adsorption is not realistic in MOFs, rather it has been suggested that adsorption occurs via a pore-filling mechanism.[50] In order to for the BET model to be applied to MOFs, four consistency criteria must be met: (1) the pressure range used must have a $v\left(P_0 - P\right)$ that increases with P/P_0,[51, 52] (2) the y-intercept of the linear region must be positive to yield a meaningful c value,[51, 52] (3) the monolayer loading, v_m, should correspond to a relative pressure, P/P_0, within the selected range, and (4) $1/\left(\sqrt{c}+1\right)$ should be equal to the relative pressure corresponding to the v_m from criterion 3. Based on these criteria, a relative pressure range of $0.005 \leq P/P_0 \leq 0.03$ is typically valid, but all parameters must be verified.[50] In addition, even when the consistency criteria are satisfied, the BET calculation can overestimate the monolayer loading in MOFs with mesopores (pore diameter ≥ 2 nm) and large micropores (pore diameter = 1-2 nm) due to an overlap of the pore-filling and monolayer regimes. For MOFs with small micropores (pore diameter ≤ 1 nm), BET theory calculates the true monolayer loading because it is equal to the saturation loading.[53]

2.2.2.2 Equilibrium Adsorption Isotherms

Adsorption isotherms at temperatures less than 343 K and at pressures up to 5 bar were collected using a home-built volumetric adsorption system. Figure 2.7 illustrates a single cell of the home-built system. The entire system consists of two cells, so two samples can be run simultaneously.

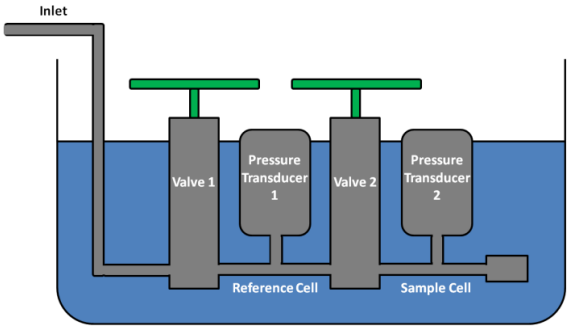

Figure 2.7: Illustration of home-built volumetric adsorption system

Prior to an isotherm measurement, the samples were outgassed in-situ using heat tape that is controlled with a PID controller. During an isotherm measurement, the sample and reference cells were immersed in a water bath to maintain the temperature set point. For each pressure point, the reference cell was dosed with the adsorbate, allowed to reach thermal equilibrium, and the pressure was recorded. Next, the valve to the sample cell was opened, the gas entered the sample cell, and the valve was closed. When the pressure reached equilibrium, the pressure in the reference cell and sample cell was recorded. This procedure was repeated at intervals throughout $0 \leq P \leq 5$ bar. Upon completion of the experiment, the uptake was calculated using a mass balance and the Peng-Robinson equation of state (Eq. 2.7-2.12).

$$P = \frac{RT}{V_m - b} - \frac{a\alpha}{V_m^2 + 2bV_m - b^2} \tag{2.7}$$

$$V_m = \frac{V}{n} \tag{2.8}$$

$$a = \frac{0.45724 R^2 T_c^2}{P_c} \tag{2.9}$$

$$b = \frac{0.07780 RT_c}{P_c} \tag{2.10}$$

$$\alpha = \left[1 + \left(\left(0.37464 + 1.54226\omega - 0.26992\omega^2\right)\left(1 - T_r^2\right)\right)\right] \tag{2.11}$$

$$T_r = \frac{T}{T_c} \tag{2.12}$$

where P is pressure, T is temperature, V is volume, n is moles, ω is a gas constant, and T_c and P_c represent critical temperature and pressure, respectively. Table 2.1 reports the Peng-Robinson constants used herein. For samples that require calcination before the isotherm measurement, the material was outgassed under vacuum at 473 K for 16-18 h to remove excess water and solvent. Next, the temperature was ramped to 523K, air was backfilled into the cells up to approximately 1 bar, and the sample was calcined for 2 h. Finally, the samples were cooled to room temperature under vacuum and transferred to the water bath to begin the isotherm as described previously.

Table 2.1: Peng-Robinson constant values obtained from Smith, Van Ness, and Abbott[54]

Molecule	ω	T_c (K)	P_c (bar)
CO_2	0.224	304.2	73.83
O_2	0.022	154.6	50.43
CO	0.048	132.9	34.99

2.2.3 Catalytic Activity

2.2.3.1 Packed Bed Reactor

CO oxidation experiments were performed using a packed bed reactor with the outlet connected to a Hiden DSMS (Figure 2.8). Approximately 20-40 mg of sample were packed into the stainless steel sample cell and balanced with glass wool to minimize the pressure drop through the bed. There are three mass flow controllers (MFCs); two

have a maximum flow rate of 100 mL/min and are used for air and either helium or nitrogen, and the third has a maximum flow rate of 10 mL/min and controls the CO flow. Before each catalytic experiment, the sample is activated with helium at 473 K for 16-18 h, and then calcined in air at 523 K for 2 h. After cooling to the reaction temperature under air flow, 1% CO in air flowed through the system at a total flow rate of 40 mL/min.

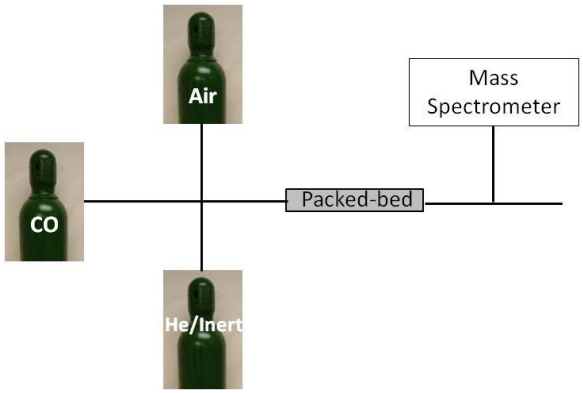

Figure 2.8: Illustration of the packed bed reactor setup

2.3 References

1. Daniel, M. C.; Astruc, D., Gold nanoparticles: Assembly, supramolecular chemistry, quantum-size-related properties, and applications toward biology, catalysis, and nanotechnology. *Chemical Reviews* **2004,** *104* (1), 293-346.

2. Eustis, S.; El-Sayed, M. A., Why gold nanoparticles are more precious than pretty gold: Noble metal surface plasmon resonance and its enhancement of the radiative and nonradiative properties of nanocrystals of different shapes. *Chemical Society Reviews* **2006,** *35* (3), 209-217.

3. Haruta, M., Catalysis of gold nanoparticles deposited on metal oxides. *Cattech* **2002,** *6* (3), 102-115.

4. Frens, G., Controlled Nucleation for the Regulation of Particle Size in Monodisperse Gold Suspensions. *Nature-Physical Science* **1973,** *241* (105), 20-22.

5. Hostetler, M. J.; Wingate, J. E.; Zhong, C. J.; Harris, J. E.; Vachet, R. W.; Clark, M. R.; Londono, J. D.; Green, S. J.; Stokes, J. J.; Wignall, G. D.; Glish, G. L.;

Porter, M. D.; Evans, N. D.; Murray, R. W., Alkanethiolate gold cluster molecules with core diameters from 1.5 to 5.2 nm: Core and monolayer properties as a function of core size. *Langmuir* **1998,** *14* (1), 17-30.

6. Xia, Y.; Xiong, Y.; Lim, B.; Skrabalak, S. E., Shape-Controlled Synthesis of Metal Nanocrystals: Simple Chemistry Meets Complex Physics? *Angewandte Chemie (International ed. in English)* **2009,** *48* (1), 60-103.

7. Corma, A.; Garcia, H., Supported gold nanoparticles as catalysts for organic reactions. *Chemical Society Reviews* **2008,** *37* (9), 2096-2126.

8. Della Pina, C.; Falletta, E.; Rossi, M., Update on selective oxidation using gold. *Chemical Society Reviews* **2012,** *41* (1), 350-369.

9. Stratakis, M.; Garcia, H., Catalysis by Supported Gold Nanoparticles: Beyond Aerobic Oxidative Processes. *Chemical Reviews* **2012,** *112* (8), 4469-4506.

10. Lopez, N.; Janssens, T. V. W.; Clausen, B. S.; Xu, Y.; Mavrikakis, M.; Bligaard, T.; Norskov, J. K., On the origin of the catalytic activity of gold nanoparticles for low-temperature CO oxidation. *Journal of Catalysis* **2004,** *223* (1), 232-235.

11. Noujima, A.; Mitsudome, T.; Mizugaki, T.; Jitsukawa, K.; Kaneda, K., Selective Deoxygenation of Epoxides to Alkenes with Molecular Hydrogen Using a Hydrotalcite-Supported Gold Catalyst: A Concerted Effect between Gold Nanoparticles and Basic Sites on a Support. *Angewandte Chemie-International Edition* **2011,** *50* (13), 2986-2989.

12. Brust, M.; Walker, M.; Bethell, D.; Schiffrin, D. J.; Whyman, R., Synthesis of thiol-derivatised gold nanoparticles in a two-phase Liquid-Liquid system. *Journal of the Chemical Society-Chemical Communications* **1994,** (7), 801-802.

13. Hostetler, M. J.; Templeton, A. C.; Murray, R. W., Dynamics of place-exchange reactions on monolayer-protected gold cluster molecules. *Langmuir* **1999,** *15* (11), 3782-3789.

14. Sardar, R.; Funston, A. M.; Mulvaney, P.; Murray, R. W., Gold Nanoparticles: Past, Present, and Future. *Langmuir* **2009,** *25* (24), 13840-13851.

15. Cavka, J. H.; Jakobsen, S.; Olsbye, U.; Guillou, N.; Lamberti, C.; Bordiga, S.; Lillerud, K. P., A new zirconium inorganic building brick forming metal organic frameworks with exceptional stability. *Journal of the American Chemical Society* **2008,** *130* (42), 13850-13851.

16. Schoenecker, P. M.; Carson, C. G.; Jasuja, H.; Flemming, C. J. J.; Walton, K. S., Effect of Water Adsorption on Retention of Structure and Surface Area of Metal-

Organic Frameworks. *Industrial & Engineering Chemistry Research* **2012,** *51* (18), 6513-6519.

17. Biswas, S.; Van der Voort, P., A General Strategy for the Synthesis of Functionalised UiO-66 Frameworks: Characterisation, Stability and CO_2 Adsorption Properties. *European Journal of Inorganic Chemistry* **2013,** (12), 2154-2160.

18. Zhao, Q.; Yuan, W.; Liang, J. M.; Li, J. P., Synthesis and hydrogen storage studies of metal-organic framework UiO-66. *International Journal of Hydrogen Energy* **2013,** *38* (29), 13104-13109.

19. Ren, J. W.; Langmi, H. W.; North, B. C.; Mathe, M.; Bessarabov, D., Modulated synthesis of zirconium-metal organic framework (Zr-MOF) for hydrogen storage applications. *International Journal of Hydrogen Energy* **2014,** *39* (2), 890-895.

20. Yang, Q.; Vaesen, S.; Ragon, F.; Wiersum, A. D.; Wu, D.; Lago, A.; Devic, T.; Martineau, C.; Taulelle, F.; Llewellyn, P. L.; Jobic, H.; Zhong, C.; Serre, C.; De Weireld, G.; Maurin, G., A Water Stable Metal-Organic Framework with Optimal Features for CO_2 Capture. *Angewandte Chemie-International Edition* **2013,** *52* (39), 10316-10320.

21. Li, L.-J.; Liao, P.-Q.; He, C.-T.; Wei, Y.-S.; Zhou, H.-L.; Lin, J.-M.; Li, X.-Y.; Zhang, J.-P., Grafting alkylamine in UiO-66 by charge-assisted coordination bonds for carbon dioxide capture from high-humidity flue gas. *Journal of Materials Chemistry A* **2015,** *3* (43), 21849-21855.

22. Chevreau, H.; Liang, W.; Kearley, G. J.; Duyker, S. G.; D'Alessandro, D. M.; Peterson, V. K., Concentration-Dependent Binding of CO_2 and CD_4 in UiO-66(Zr). *Journal of Physical Chemistry C* **2015,** *119* (13), 6980-6987.

23. Anjum, M. W.; Vermoortele, F.; Khan, A. L.; Bueken, B.; De Vos, D. E.; Vankelecom, I. F. J., Modulated UiO-66-Based Mixed-Matrix Membranes for CO_2 Separation. *ACS Applied Materials & Interfaces* **2015,** *7* (45), 25193-25201.

24. DeCoste, J. B.; Demasky, T. J.; Katz, M. J.; Farha, O. K.; Hupp, J. T., A UiO-66 analogue with uncoordinated carboxylic acids for the broad-spectrum removal of toxic chemicals. *New Journal of Chemistry* **2015,** *39* (4), 2396-2399.

25. DeCoste, J. B.; Browe, M. A.; Wagner, G. W.; Rossin, J. A.; Peterson, G. W., Removal of chlorine gas by an amine functionalized metal-organic framework via electrophilic aromatic substitution. *Chemical Communications* **2015,** *51* (62), 12474-12477.

26. Peterson, G. W.; DeCoste, J. B.; Fatollahi-Fard, F.; Britt, D. K., Engineering UiO-66-NH_2 for Toxic Gas Removal. *Industrial & Engineering Chemistry Research* **2014,** *53* (2), 701-707.

27. Tai, S.; Zhang, W.; Zhang, J.; Luo, G.; Jia, Y.; Deng, M.; Ling, Y., Facile preparation of UiO-66 nanoparticles with tunable sizes in a continuous flow microreactor and its application in drug delivery. *Microporous and Mesoporous Materials* **2016,** *220*, 148-154.

28. Wang, C. H.; Liu, X. L.; Chen, J. P.; Li, K., Superior removal of arsenic from water with zirconium metal-organic framework UiO-66. *Scientific Reports* **2015,** *5*.

29. Katz, M. J.; Mondloch, J. E.; Totten, R. K.; Park, J. K.; Nguyen, S. T.; Farha, O. K.; Hupp, J. T., Simple and Compelling Biomimetic Metal-Organic Framework Catalyst for the Degradation of Nerve Agent Simulants. *Angewandte Chemie-International Edition* **2014,** *53* (2), 497-501.

30. Katz, M. J.; Klet, R. C.; Moon, S.-Y.; Mondloch, J. E.; Hupp, J. T.; Farha, O. K., One Step Backward Is Two Steps Forward: Enhancing the Hydrolysis Rate of UiO-66 by Decreasing [OH^-]. *ACS Catalysis* **2015,** *5* (8), 4637-4642.

31. Moon, S.-Y.; Wagner, G. W.; Mondloch, J. E.; Peterson, G. W.; DeCoste, J. B.; Hupp, J. T.; Farha, O. K., Effective, Facile, and Selective Hydrolysis of the Chemical Warfare Agent VX Using Zr_6-Based Metal–Organic Frameworks. *Inorganic Chemistry* **2015,** *54* (22), 10829-10833.

32. Peterson, G. W.; Moon, S.-Y.; Wagner, G. W.; Hall, M. G.; DeCoste, J. B.; Hupp, J. T.; Farha, O. K., Tailoring the Pore Size and Functionality of UiO-Type Metal–Organic Frameworks for Optimal Nerve Agent Destruction. *Inorganic Chemistry* **2015,** *54* (20), 9684-9686.

33. Vermoortele, F.; Bueken, B.; Le Bars, G.; Van de Voorde, B.; Vandichel, M.; Houthoofd, K.; Vimont, A.; Daturi, M.; Waroquier, M.; Van Speybroeck, V.; Kirschhock, C.; De Vos, D. E., Synthesis Modulation as a Tool To Increase the Catalytic Activity of Metal-Organic Frameworks: The Unique Case of UiO-66(Zr). *Journal of the American Chemical Society* **2013,** *135* (31), 11465-11468.

34. Granadeiro, C. M.; Ribeiro, S. O.; Karmaoui, M.; Valenca, R.; Ribeiro, J. C.; de Castro, B.; Cunha-Silva, L.; Balula, S. S., Production of ultra-deep sulfur-free diesels using a sustainable catalytic system based on UiO-66(Zr). *Chemical Communications* **2015,** *51* (72), 13818-13821.

35. Arrozi, U. S. F.; Wijaya, H. W.; Patah, A.; Permana, Y., Efficient acetalization of benzaldehydes using UiO-66 and UiO-67: Substrates accessibility or Lewis acidity of zirconium. *Applied Catalysis A: General* **2015,** *506*, 77-84.

36. Long, J.; Wang, S.; Ding, Z.; Wang, S.; Zhou, Y.; Huang, L.; Wang, X., Amine-functionalized zirconium metal-organic framework as efficient visible-light photocatalyst for aerobic organic transformations. *Chemical Communications* **2012,** *48* (95), 11656-11658.

37. Shen, L.; Liang, R.; Luo, M.; Jing, F.; Wu, L., Electronic effects of ligand substitution on metal-organic framework photocatalysts: the case study of UiO-66. *Physical Chemistry Chemical Physics* **2015,** *17* (1), 117-121.

38. Schoenecker, B., Grabicka, and Walton, Kinetics Study and Crystallization Process Design for Scale-Up of UiO-66-NH_2 Synthesis. *AIChE* **2012**.

39. Jasuja, H. Developing Design Criteria and Scale-Up Methods for Water-Stable Metal-Organic Frameworks for Adsorption Applications. Georgia Institute of Technology, 2014.

40. Kim, S.-N.; Lee, Y.-R.; Hong, S.-H.; Jang, M.-S.; Ahn, W.-S., Pilot-scale synthesis of a zirconium-benzenedicarboxylate UiO-66 for CO_2 adsorption and catalysis. *Catalysis Today* **2015,** *245*, 54-60.

41. Taddei, M.; Dau, P. V.; Cohen, S. M.; Ranocchiari, M.; van Bokhoven, J. A.; Costantino, F.; Sabatini, S.; Vivani, R., Efficient microwave assisted synthesis of metal-organic framework UiO-66: optimization and scale up. *Dalton Transactions* **2015,** *44* (31), 14019-14026.

42. Tulig, K.; Walton, K. S., An alternative UiO-66 synthesis for HCl-sensitive nanoparticle encapsulation. *RSC Advances* **2014,** *4* (93), 51080-51083.

43. Bragg, W. L., The structure of some crystals as indicated by their diffraction of x-rays. *Proceedings of the Royal Society of London Series a-Containing Papers of a Mathematical and Physical Character* **1913,** *89* (610), 248-277.

44. Hermes, S.; Schroter, M. K.; Schmid, R.; Khodeir, L.; Muhler, M.; Tissler, A.; Fischer, R. W.; Fischer, R. A., Metal@MOF: Loading of highly porous coordination polymers host lattices by metal organic chemical vapor deposition. *Angewandte Chemie-International Edition* **2005,** *44* (38), 6237-6241.

45. Houk, R. J. T.; Jacobs, B. W.; El Gabaly, F.; Chang, N. N.; Talin, A. A.; Graham, D. D.; House, S. D.; Robertson, I. M.; Allendorf, M. D., Silver Cluster Formation, Dynamics, and Chemistry in Metal-Organic Frameworks. *Nano Letters* **2009,** *9* (10), 3413-3418.

46. Lebedev, O. I.; Millange, F.; Serre, C.; Van Tendeloo, G.; Ferey, G., First direct imaging of giant pores of the metal-organic framework MIL-101. *Chemistry of Materials* **2005,** *17* (26), 6525-6527.

47. Turner, S.; Lebedev, O. I.; Schroder, F.; Esken, D.; Fischer, R. A.; Van Tendeloo, G., Direct imaging of loaded metal-organic framework materials (metal@MOF-5). *Chemistry of Materials* **2008,** *20* (17), 5622-5627.

48. Ding, Y. W., Zhong Lin, STEM [PowerPoint Slides]. **2013**.

49. Brunauer, S.; Emmett, P. H.; Teller, E., Adsorption of gases in multimolecular layers. *Journal of the American Chemical Society* **1938,** *60*, 309-319.

50. Rowsell, J. L. C.; Yaghi, O. M., Effects of functionalization, catenation, and variation of the metal oxide and organic linking units on the low-pressure hydrogen adsorption properties of metal-organic frameworks. *Journal of the American Chemical Society* **2006,** *128* (4), 1304-1315.

51. Walton, K. S.; Snurr, R. Q., Applicability of the BET method for determining surface areas of microporous metal-organic frameworks. *Journal of the American Chemical Society* **2007,** *129* (27), 8552-8556.

52. Rouquerol, J.; Llewellyn, P.; Rouquerol, F., Is the BET equation applicable to microporous adsorbents? In *Studies in Surface Science and Catalysis*, P.L. Llewellyn, F. R.-R. J. R.; Seaton, N., Eds. Elsevier: 2007; Vol. Volume 160, pp 49-56.

53. Gomez-Gualdron, D. A.; Moghadam, P. Z.; Hupp, J. T.; Farha, O. K.; Snurr, R. Q., Application of Consistency Criteria To Calculate BET Areas of Micro- And Mesoporous Metal-Organic Frameworks. *Journal of the American Chemical Society* **2016,** *138* (1), 215-224.

54. Smith, J. M., Van Ness, H.C., and Abbott, M.M, *Introduction to Chemical Engineering Thermodynamics*. 7th ed.; McGraw-Hill: 2005.

CHAPTER 3

AN ALTERNATIVE UIO-66 SYNTHESIS FOR HCl-SENSITIVE NANOPARTICLE ENCAPSULATION

Reproduced (adapted) from Tulig, K.; Walton, K. S., An alternative UiO-66 synthesis for HCl-sensitive nanoparticle encapsulation. *RSC Advances* **2014,** *4* (93), 51080-51083.

3.1 Introduction

Metal and metal oxide nanomaterials are of increasing interest due to their unusual optical, electrical, thermal, magnetic, and catalytic properties that make them advantageous in semiconductors, sensing, imaging, and catalysis.[1-3] Research has led to the tailoring of these properties via controlled synthesis of nanomaterials to manipulate size, shape, composition, and structure.[4-6] However, the high surface-area-to-volume ratio often makes nanomaterials such as metallic nanoparticles unstable, even under ambient conditions. To solve this issue, nanoparticles are often supported either by a polymer shell or on porous materials to retain their size and shape. Typical porous supports limit aggregation, but they do not protect the nanomaterials from poisons that will alter the material properties. For instance, organosulphur compounds strongly bind to many nanoparticle surfaces blocking active catalysis sites. Confinement within microporous supports filters out such poisons and protects the particles.[7]

Metal-organic frameworks (MOFs) are micro-to-mesoporous, crystalline materials consisting of metal or metal oxide clusters connected by organic linkers. Their high surface areas and pore volumes, uniform pore size distributions, and chemical tunability give them potential in applications such as gas storage and separation, drug

delivery, biomedical imaging, air purification, and catalysis.[8, 9] Using MOFs as a support for nanoparticles, specifically confining the nanoparticles within the structure to create MOF composites, allows us to exploit the chemical and physical properties of the nanomaterials and the selectivity of the MOFs. There have been several MOF composites, created by either impregnation or encapsulation of nanoparticles, reported to date.[10, 11] Impregnation describes the production of the nanoparticles within the MOF pores, while encapsulation indicates that the MOF crystallizes around preformed nanoparticles. Huo et. al used encapsulation to successfully incorporate a wide range of nanoparticles in ZIF-8 and demonstrated good spatial control of the nanoparticles, improving the catalytic, magnetic, and photoluminescent properties of the parent structure.[12] Synthetic control over the spatial location of the nanomaterials is paramount for extending the applicability of MOF composites for catalysis, sensing, photovoltaics, and microelectronics.[13-16] The expansion of this controlled encapsulation technique to a wide variety of MOFs will open the door for the creation of designer-specific supports.

UiO-66 is a zirconium-based MOF composed of $Zr_6O_4(OH)_4$ clusters linked by 1,4-benzenedicarboxylic acid. It is thermally stable, mechanically and chemically resistant, and easily tuned.[17-20] Unfortunately, the synthesis of UiO-66 produces hydrochloric acid (HCl), which is problematic when encapsulating metal or metal oxide nanoparticles. For instance, gold nanoparticles are widely studied and have interesting optic and catalytic properties,[21] but they easily dissolve in HCl. In fact, HCl either reacts with, or dissolves, numerous metal or metal oxide nanoparticles with favorable properties.[22-25] Férey et al. have reported an alternative procedure using a zirconium methacrylate secondary building unit (SBU), yielding UiO-66 with reduced crystallinity

and porosity.[26] However, the synthesis of the SBU precursor requires air sensitive materials and is time intensive.[27] Herein, we report an alternative procedure to synthesize UiO-66 with equivalent crystallinity, porosity, thermal stability, and chemical resistance without forming HCl. A demonstration of this new method is also presented for the encapsulation of HCl-sensitive gold nanoparticles.

3.2 Experimental Methods

3.2.1 Synthesis Procedures

3.2.1.1 UiO-66($ZrCl_4$) and UiO-66(Zr(O*n*Pr))

All chemicals were obtained commercially (Sigma-Aldrich and Fisher Scientific) and used as obtained. UiO-66($ZrCl_4$) was synthesized following procedures reported previously.[17] Briefly, zirconium chloride ($ZrCl_4$) (0.227 mmol) and 1,4-benzenedicarboxylic acid (BDC) (0.227 mmol) were dissolved in N,N'-dimethylformamide (DMF) (340 mmol) in a glass scintillation vial. The mixture was then stirred at 393 K for 24 h in a silicone oil bath. The solution was allowed to cool to room temperature, then soaked with fresh DMF overnight three times. Finally, the solution was exchanged with fresh methanol (MeOH) three times. Figure 3.1 shows that when AuNPs were added to the reaction slurry they dissolved within 2 min.

UiO-66(Zr(O*n*Pr)) was synthesized by stirring a mixture of 70% solution of zirconium(IV) propoxide in *n*-propanol (Zr(O*n*Pr)) (0.227 mmol), BDC (0.454 mmol), methanol (86.5 mmol), DMF (45.4 mmol), and glacial acetic acid (6.81 mmol) in a glass scintillation vial at 393 K for 24 h. The material was washed the same as UiO-66($ZrCl_4$).

Several synthesis parameters were varied: (1) temperature, solvent ratio, and time; acetic acid:Zr(O*n*Pr) ratio; and (3) acetic acid was exchanged with nitric acid and benzoic acid. Table 3.1 reports the synthesis procedures used to determine the effect of temperature, solvent ratio, and time. In addition, Table 3.2 reports the synthesis conditions used to probe the effect of the acetic acid:Zr(O*n*Pr) ratio. Lastly, acetic acid was exchanged with nitric acid (0.023 mmol) yielding a mother solution with a pH of 1.5 and with benzoic acid (6.81 mmol) yielding a solution with a pH of 3.6. Both sets of conditions, when coupled with acetic acid (pH of 1.5 and 30:1 ratio of organic acid to Zr(O*n*Pr), yield porous, crystalline UiO-66.

Table 3.1: Temperatures, solvents, and times used to synthesize UiO-66(Zr(O*n*Pr))

Sample	Zr(O*n*Pr) (mmol)	BDC (mmol)	Acetic Acid (mmol)	MeOH (mmol)	DMF (mmol)	T (K)	Time (h)
MeOH, 393K, 24 h	0.227	0.454	6.81	173	0	393	24
MeOH, 393K, 48 h	0.227	0.454	6.81	173	0	393	48
MeOH, 393K, 72 h	0.227	0.454	6.81	173	0	393	72
MeOH:DMF, 393K, 24 h	0.227	0.454	6.81	86.5	45.4	393	24
MeOH:DMF, 393K, 48 h	0.227	0.454	6.81	86.5	45.4	393	48
MeOH:DMF, 393K, 72 h	0.227	0.454	6.81	86.5	45.4	393	72
DMF, 393K, 24 h	0.227	0.454	6.81	0	90.8	393	24
DMF, 393K, 48 h	0.227	0.454	6.81	0	90.8	393	48
DMF, 393K, 72 h	0.227	0.454	6.81	0	90.8	393	72
MeOH, 343K, 24 h	0.227	0.454	6.81	173	0	343	24
MeOH, 343K, 48 h	0.227	0.454	6.81	173	0	343	48
MeOH, 343K, 72 h	0.227	0.454	6.81	173	0	343	72
MeOH:DMF, 343K, 24 h	0.227	0.454	6.81	86.5	45.4	343	24
MeOH:DMF, 343K, 48 h	0.227	0.454	6.81	86.5	45.4	343	48
MeOH:DMF, 343K,72 h	0.227	0.454	6.81	86.5	45.4	343	72
DMF, 343K, 24 h	0.227	0.454	6.81	0	90.8	343	24
DMF, 343K, 48 h	0.227	0.454	6.81	0	90.8	343	48
DMF, 343K,72 h	0.227	0.454	6.81	0	90.8	343	72
MeOH, RT, 24 h	0.227	0.454	6.81	173	0	RT	24
MeOH, RT, 48 h	0.227	0.454	6.81	173	0	RT	48
MeOH, RT, 72 h	0.227	0.454	6.81	173	0	RT	72
MeOH:DMF, RT, 24 h	0.227	0.454	6.81	86.5	45.4	RT	24
MeOH:DMF, RT, 48 h	0.227	0.454	6.81	86.5	45.4	RT	48
MeOH:DMF, RT, 72 h	0.227	0.454	6.81	86.5	45.4	RT	72
DMF, RT, 24 h	0.227	0.454	6.81	0	90.8	RT	24
DMF, RT, 48 h	0.227	0.454	6.81	0	90.8	RT	48
DMF, RT, 72 h	0.227	0.454	6.81	0	90.8	RT	72

Table 3.2: Various acetic acid concentrations used to synthesize UiO-66(Zr(O*n*Pr))

Acetic Acid:Zr(O*n*Pr)	pH	Acetic Acid (mmol)	Zr(O*n*Pr) (mmol)	BDC (mmol)	MeOH (mmol)	DMF (mmol)	Temp (K)	Time (h)
0	8.3	0.000	0.227	0.454	86.5	45.4	393	24
1	6.1	0.227	0.227	0.454	86.5	45.4	393	24
7.5	5.1	1.703	0.227	0.454	86.5	45.4	393	24
15	4.4	3.405	0.227	0.454	86.5	45.4	393	24
30	4.1	6.810	0.227	0.454	86.5	45.4	393	24
60	3.4	13.620	0.227	0.454	86.5	45.4	393	24
120	2.5	27.240	0.227	0.454	86.5	45.4	393	24
240	2.1	54.480	0.227	0.454	86.5	45.4	393	24
480	1.3	108.960	0.227	0.454	86.5	45.4	393	24

3.2.1.2 AuNPs and Au@UiO-66

Gold nanoparticles (AuNPs) capped with 1-dodecanethiol (DDT) were prepared using a previously reported procedure.[28] A solution of tetraoctylammonium bromide (0.728 mmol) in toluene (40 mL) was added to a solution of gold(III) chloride trihydrate (0.314 mmol) in water (20 mL). The mixture was stirred for 30 min. Then, DDT (0.314 mmol) was added, followed by a solution of sodium borohydride ($NaBH_4$) (3.14 mmol) in water (10 mL). The solution was stirred vigorously for 3 h and washed with copious amounts of water. The organic phase was separated and reduced to approximately 10 mL under vacuum at 298K. Next, 100 mL of methanol was added and the particles precipitated overnight. The solvent was decanted and the particles were washed twice more with copious amounts of methanol. Finally, the DDT monolayer was place-exchanged with 11-mercaptoundecanoic acid (MUA) (0.154 mmol) and washed with toluene.[29] The AuNPs were then added to the UiO-66(Zr(O*n*Pr)) mother solution and stirred at 393 K for 24 h. Figure 3.2 shows the color difference between UiO-66(Zr(O*n*Pr)) and Au@UiO-66(Zr(O*n*Pr)) which suggests that AuNPs are present in Au@UiO-66(Zr(O*n*Pr)).

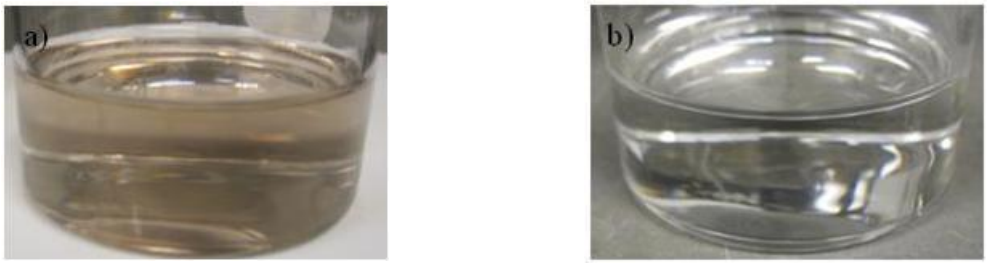

Figure 3.1: Images of AuNP-DDT/MUA in UiO-66($ZrCl_4$) mother solution (a) initially and (b) after 2 min at 393 K

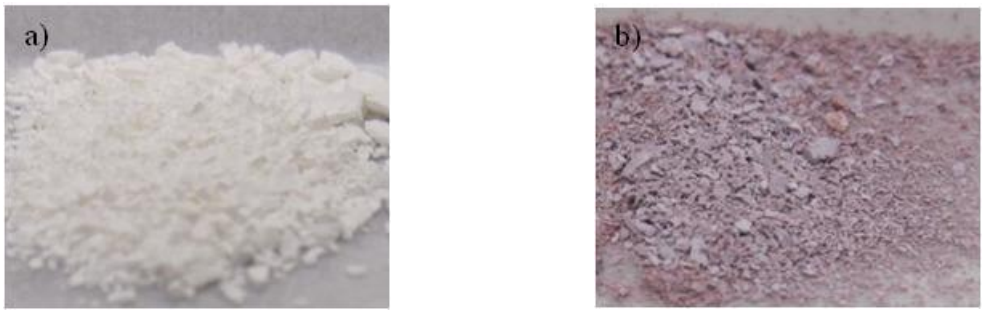

Figure 3.2: Images of (a) UiO-66(Zr(O*n*Pr)) and (b) Au@UiO-66(Zr(O*n*Pr))

3.2.2 Material Characterization

Powder X-ray diffraction (PXRD) patterns were obtained using a PANalytical X-ray diffractometer. Approximately 5 mg of sample were placed on a low background sample holder and scanned from 5-50°. The obtained diffractograms were compared to the simulated pattern to confirm the UiO-66 structure was obtained.

Thermogravimetric analysis (TGA) data were collected using the Netzsch STA 449 Jupiter Simultaneous TG-DSC apparatus. Approximately 10 mg of material were placed in an Al_2O_3 crucible and ramped at 5 K/min to 1073 K under helium flow at 20 mL/min. TGA analysis was used to determine the thermal degradation temperature of the materials.

Nitrogen sorption measurements at 77 K were completed using a Quantachrome Quadrasorb SI volumetric analyzer. The isotherms were measured over a range of

relative pressures from 0.003 to 0.990 using high purity nitrogen (99.998%) obtained from Airgas. Prior to the measurement, the samples were outgassed in a Quantachrome FloVac Degasser at 473 K under dynamic vacuum for approximately 18 h. The surface areas were calculated using the Brunauer, Emmett, and Teller (BET) theory using relative pressures ranging from 0.005-0.03 and the total pore volume was calculated at a relative pressure (P/P_0) of 0.6.

Transmission Electron Microscopy (TEM) and Scanning Transmission Electron Microscopy-Energy Dispersive Spectroscopy (STEM-EDS) were used to analyze the original AuNPs and Au@UiO-66. The samples were prepared by suspending less than 1 mg in solution and drop-casting onto a lacy carbon coated copper grid. The AuNPs were analyzed using the JEOL 100CX II operated at 100 keV. Au@UiO-66 was analyzed using the FEI Tecnai F30 operated at 300 keV and EDS spectra were acquired using the Oxford EDX 6763. The composition was measured at a specified point marked with a red circle and analyzed using TEM Imaging & Analysis (TIA) Software. The FEI Tecnai F30 is supported by funding DMR 0922776.

Proton nuclear magnetic resonance (^{1}H NMR) spectroscopy was measured on a Varian Mercury Vx 300. The samples were prepared by suspending approximately 10 mg of AuNPs in 1 mL of dimethyl sulfoxide-d_6. ^{1}H NMR data were used to determine the composition of the organic monolayer on the AuNPs.

3.3 Results and Discussion

The conventional synthesis of UiO-66($ZrCl_4$) is a solvothermal method whereby a mixture of $ZrCl_4$ and BDC in DMF are heated at 393 K for 24 h. HCl is produced during

the reaction. To avoid this HCl formation, we have developed an alternative synthesis using a mixture of Zr(O*n*Pr), BDC, acetic acid, MeOH, and DMF. A systematic study was performed to evaluate the impact of various MeOH:DMF ratios, synthesis temperatures (298 K – 393 K), and reaction times (24 h – 72 h) on the synthesis of UiO-66 (Tables 3.1 and 3.2). The results of these experiments are shown in Figure 3.3. At room temperature, UiO-66(Zr(O*n*Pr)) crystals do not form. However, at 343 K and 393 K, crystals form in both DMF and a mixture of MeOH:DMF = 1.9 but not in pure methanol. Figure 3.4a shows the PXRD patterns of UiO-66(Zr(O*n*Pr)) for the case of MeOH:DMF = 1.9 and acetic acid:Zr(O*n*Pr) = 30 carried out at 393 K for 24 h. The PXRD patterns match very well the simulated UiO-66 pattern. In addition, the BET surface area, shown in Table 3.3, is comparable to UiO-66($ZrCl_4$). PXRD and BET analysis prove this alternative synthesis yields porous, high-quality UiO-66 crystals. TGA analysis confirms thermal stability of UiO-66(Zr(O*n*Pr)) up to 783 K (Figure 3.5). Finally, the water resistance of UiO-66(Zr(O*n*Pr)) is confirmed by soaking activated samples in water for 24 h. The combination of PXRD (Figure 3.4b) and BET surface area analysis (Table 3.3) shows that the crystal structure and porosity remain intact after water exposure. Therefore, this alternate synthesis using Zr(O*n*Pr) produces UiO-66 crystals with porosity, thermal stability, and water resistance that are comparable to the conventionally synthesized samples.

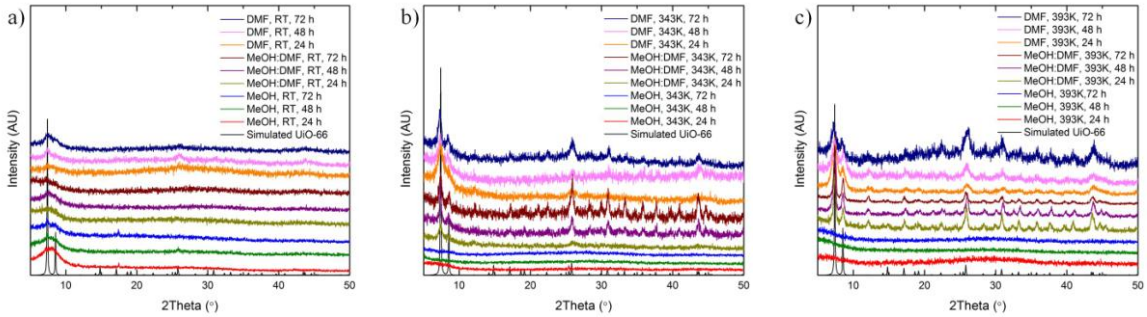

Figure 3.3: PXRD patterns of UiO-66(Zr(O*n*Pr)) with varying solvents and times at (a) room temperature (b) 343 K and (c) 393 K

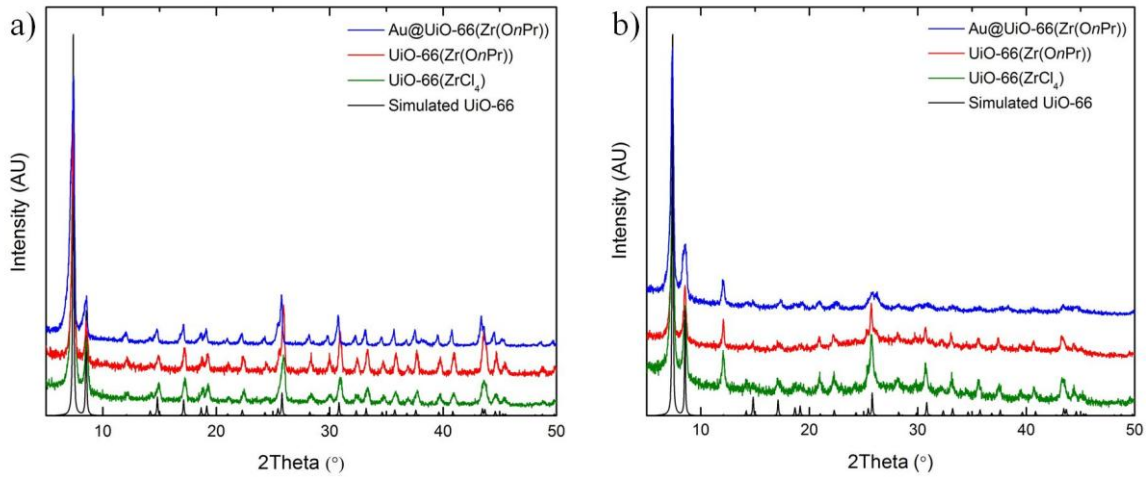

Figure 3.4: PXRD patterns of simulated UiO-66, UiO-66($ZrCl_4$), UiO-66(Zr(O*n*Pr)), and Au@UiO-66(Zr(O*n*Pr)) (a) as-synthesized and (b) after 24 h of exposure to liquid H_2O

Table 3.3: BET Surface Area Comparison

Sample	As-Synthesized		After H_2O Exposure	
	BET Surface Area (m^2/g)	Total Pore Volume (cm^3/g)[a]	BET Surface Area (m^2/g)	Total Pore Volume (cm^3/g)[a]
UiO-66($ZrCl_4$)	1118	0.48	1103	0.48
UiO-66(Zr(O*n*Pr))	1155	0.56	1119	0.47
Au@UiO-66(Zr(O*n*Pr))	1061	0.47	1050	0.46

[a]Measured at $P/P_0 = 0.6$

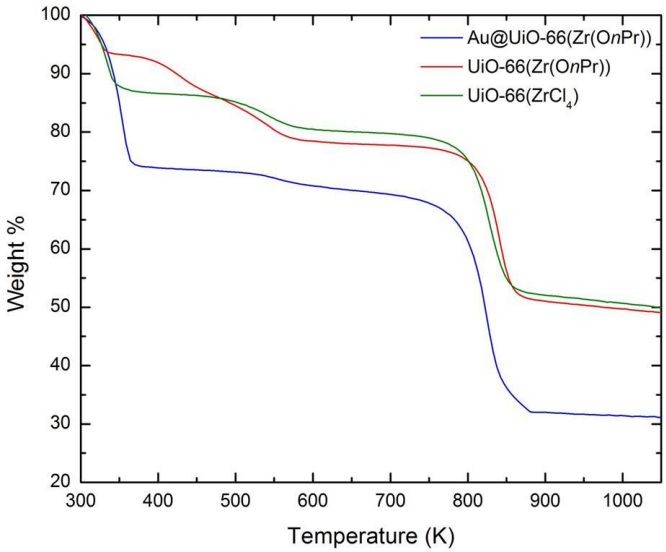

Figure 3.5: TGA curves of UiO-66($ZrCl_4$), UiO-66(Zr(O*n*Pr)), and Au@UiO-66(Zr(O*n*Pr))

Using the MeOH:DMF ratio specified above at 393 K for 24 h, a systematic study of the effect of acetic acid:Zr(O*n*Pr) ratio on crystal formation and porosity was conducted, and acetic acid was found to be critical for UiO-66(Zr(O*n*Pr)) crystallization (Figure 3.6a). An acetic acid:Zr(O*n*Pr) ratio of at least 15:1 is necessary for UiO-66(Zr(O*n*Pr)) crystal formation. Figure 3.7 shows the relationship between the ratio of acetic acid:Zr(O*n*Pr), pH, and BET surface area of UiO-66(Zr(O*n*Pr)). At an acetic acid:Zr(O*n*Pr) ratio of 15:1, UiO-66 crystals form, as shown by PXRD, but the BET surface area is reduced. As the ratio of acetic acid:Zr(O*n*Pr) increases to 30:1, the BET surface area is comparable to UiO-66($ZrCl_4$). There are three possible reasons acetic acid is necessary to drive UiO-66(Zr(O*n*Pr)) crystallization: (1) it creates an acidic environment (pH), (2) it forms a zirconium acetate precursor, or (3) it acts as a modulator, slowing nucleation through competitive coordination and increasing crystal growth. In order to determine the most likely reason acetic acid is required, we performed the same experiments with nitric acid (HNO_3) or benzoic acid instead of acetic acid. The

data in Figure 3.7 show that a pH between 1.3 and 4 yield highly crystalline, high-surface area UiO-66. The substitution of HNO_3 yields a mother solution with a pH of 1.5, well within the successful pH range observed for the acetic acid case, but produces a non-crystalline material after reaction (Figure 3.6b). Therefore, crystallization is not purely dependent on the pH of the mother solution. On the other hand, exchanging acetic acid for benzoic acid, another known modulator,[30] yields crystalline UiO-66 (Figure 3.6b) with a high surface area of 1307 m^2/g (Table 3.4). This suggests that modulation is necessary for the particles to reach the critical size for measurable crystallization. Thus, we can infer that the key role of acetic acid is to modulate the growth. The acetic acid competitively coordinates to zirconium ions in solution, which slows nucleation and increases growth so UiO-66 particles reach a critical diameter with measurable periodicity and significant porosity.

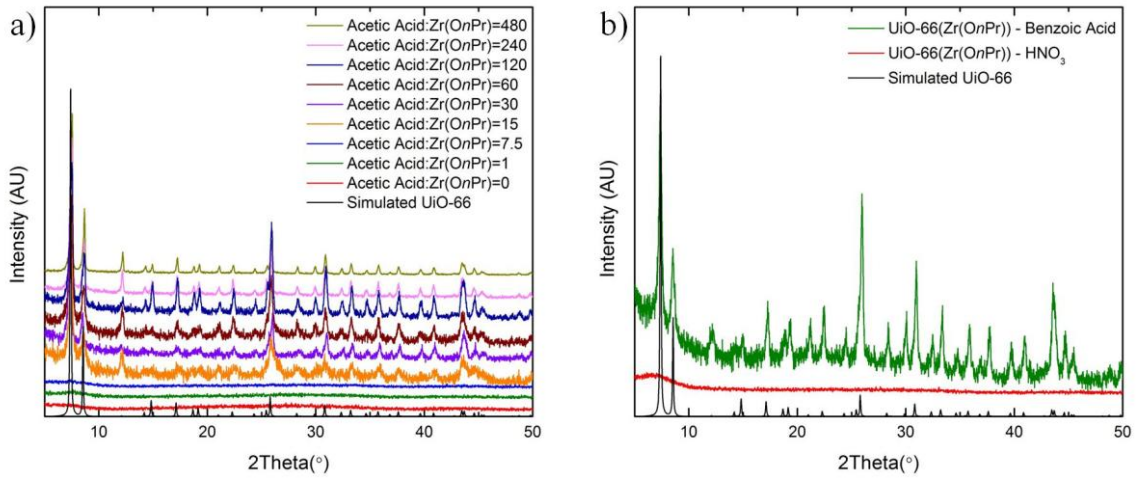

Figure 3.6: PXRD patterns of UiO-66(Zr(O*n*Pr)) prepared by (a) varying acetic acid:Zr(O*n*Pr) ratio and (b) substituting nitric acid and benzoic acid

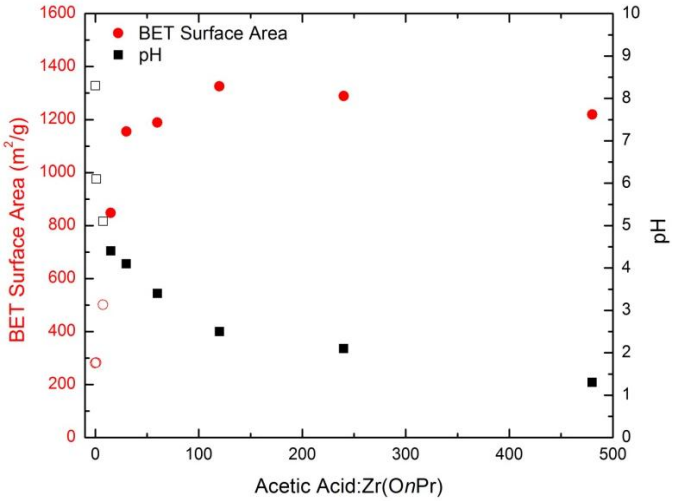

Figure 3.7: Relationship between acetic acid:Zr(O*n*Pr), pH, and BET surface area. The closed and open points represent crystalline and non-crystalline materials, respectively

Table 3.4: BET surface areas using nitric acid and benzoic acid

Acid	BET Surface Area (m^2/g)	Total Pore Volume (cm^3/g)[a]
HNO_3	358	0.22
Benzoic Acid	1307	0.62

[a]Measured at $P/P_0 = 0.6$

To test the capability of this synthesis with HCl-sensitive materials, we encapsulated gold nanoparticles (AuNPs) in UiO-66(Zr(O*n*Pr)). The encapsulation procedure entails growing the MOF from preformed functionalized AuNPs. First, AuNPs 3.1±0.6 nm in diameter are synthesized as previously reported.[28, 29] They are stabilized in solution using a mixed monolayer consisting of MUA:DDT in a 2:1 ratio. TEM is used to determine the AuNP diameter (Figure 3.8a) and ^{1}H NMR confirms and quantifies the mixed monolayer on the AuNPs (Figure 3.8b). In Figure 3.8b, the broad peaks are characteristic of ligands bound to a surface. The T_2 relaxation time accelerates when an organic is bound to a surface.[5] Therefore, the lack of coupling suggests that all of the ligands are bound to the AuNP surface. Additionally, the composition of the monolayer is confirmed by analyzing the characteristic peak positions. DDT has a unique peak at 0.84

ppm associated with $–CH_3$ and MUA has a characteristic peak at 2.13 ppm for $–CH_2COOH$. These preformed AuNPs are then added to the UiO-66(Zr(O*n*Pr)) mother solution and the mixture is heated to 393 K for 24 h.

Figure 3.4a shows that the PXRD pattern of Au@UiO-66(Zr(O*n*Pr)) matches the simulated pattern for UiO-66. Therefore, adding AuNPs to the mother solution does not affect the structure. The BET surface area for the composite, reported in Table 3.3, is also comparable to the parent UiO-66. The slight loss in specific internal surface area is expected with the addition of dense, non-porous materials. Normalizing the surface area by UiO-66, rather than the composite, yields a BET surface area similar to the parent. This suggests that the reduced surface area of the composite is due to the increased material density rather than pore blockage by the AuNPs. Additionally, the composite is thermally stable up to 813 K (Figure 3.5) and retains its structure and porosity after water exposure (Figure 3.4b and Table 3.3). PXRD, nitrogen sorption at 77K, and TGA analysis show that incorporating AuNPs in the synthesis does not affect UiO-66(Zr(O*n*Pr)) structure, porosity, thermal stability, or water resistance.

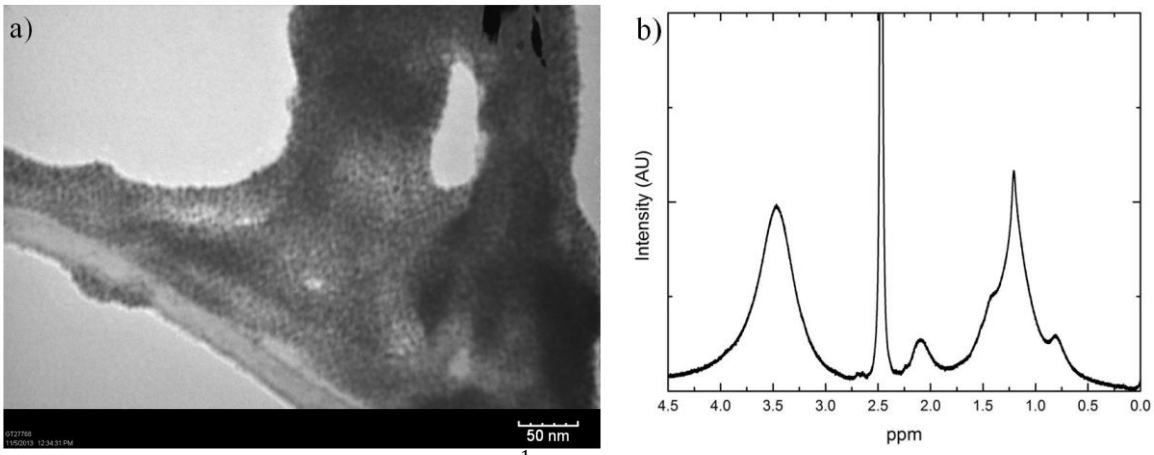

Figure 3.8: (a) TEM image and (b) ^{1}H NMR spectrum of as-synthesized AuNP-DDT/MUA

TEM and STEM-EDS are used to analyze AuNP size, distribution, location, and composition (Table 3.5). Figure 3.9 shows that there are AuNPs 16.2±4.6 nm in diameter scattered non-uniformly throughout the sample, suggesting that the AuNPs grow significantly during the synthesis. Additionally, there are several particles that are clearly anchored to the surface of the support, resting on both the UiO-66 particle and the TEM grid. However, the spatial location of the bulk of the nanoparticles is inconclusive due to the two dimensional nature of TEM. The significant AuNP growth, surface-attached AuNPs, and non-uniform AuNP dispersion suggest a need for an optimized encapsulation procedure.

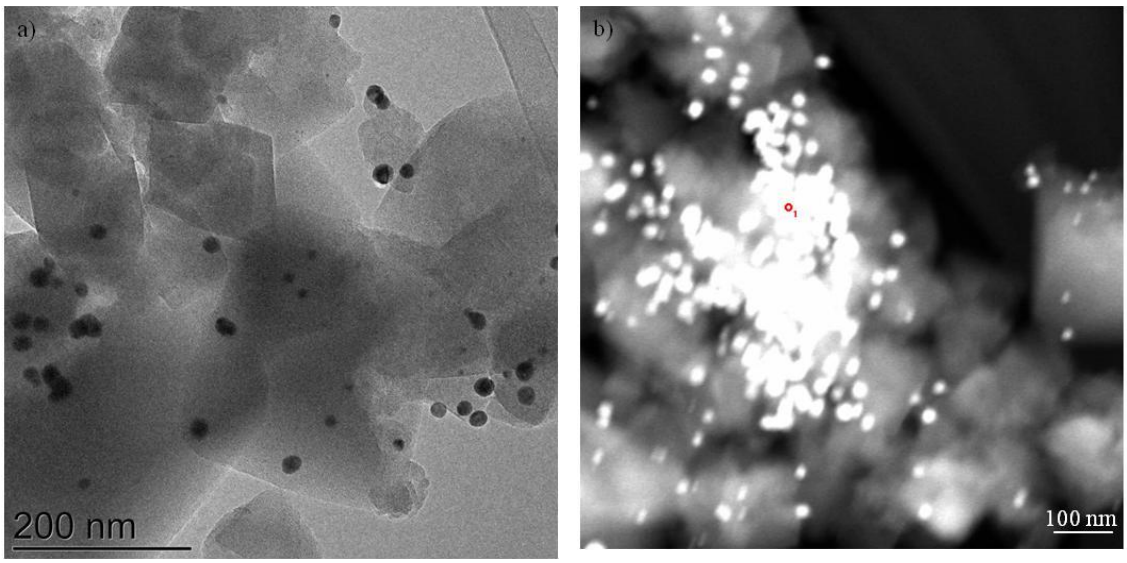

Figure 3.9: (a) TEM and (b) STEM-EDS images of Au@UiO-66(Zr(O*n*Pr))

Table 3.5: EDS analysis of Au@UiO-66(Zr(O*n*Pr)) at red dot in Figure 3.9b

Element	Weight Percentage
C(K)	39.95
O(K)	7.89
Cu(K)	11.03
Zr(K)	14.88
Au(L)	26.22

3.4 Conclusions

In summary, we have demonstrated an alternative UiO-66 synthesis procedure for HCl-sensitive materials for the encapsulation of AuNPs in UiO-66. This alternative procedure yields porous crystals with comparable properties to the conventional synthesis procedure, specifically, porosity, thermal stability and water resistance. We have demonstrated that UiO-66(Zr(O*n*Pr)) crystallization is dependent on the addition of a modulator such as acetic acid. This dependence suggests that crystallization of UiO-66(Zr(O*n*Pr)) is limited by crystal growth yielding insight for further crystallization control. The alternative procedure also allows AuNPs to be included in the mother solution in order to encapsulate them within the framework. This method lays the groundwork for the controlled synthesis of HCl-sensitive UiO-66 composites with potential for catalysis, sensing, gas storage and separation, photovoltaics, and microelectronics.

3.5 References

1. El-Sayed, M. A., Some interesting properties of metals confined in time and nanometer space of different shapes. *Accounts of Chemical Research* **2001,** *34* (4), 257-264.

2. Jain, P. K.; Huang, X.; El-Sayed, I. H.; El-Sayed, M. A., Noble Metals on the Nanoscale: Optical and Photothermal Properties and Some Applications in Imaging, Sensing, Biology, and Medicine. *Accounts of Chemical Research* **2008,** *41* (12), 1578-1586.

3. Haruta, M., Catalysis of gold nanoparticles deposited on metal oxides. *Cattech* **2002,** *6* (3), 102-115.

4. Frens, G., Controlled Nucleation for the Regulation of Particle Size in Monodisperse Gold Suspensions. *Nature-Physical Science* **1973,** *241* (105), 20-22.

5. Hostetler, M. J.; Wingate, J. E.; Zhong, C. J.; Harris, J. E.; Vachet, R. W.; Clark, M. R.; Londono, J. D.; Green, S. J.; Stokes, J. J.; Wignall, G. D.; Glish, G. L.; Porter, M. D.; Evans, N. D.; Murray, R. W., Alkanethiolate gold cluster molecules with core diameters from 1.5 to 5.2 nm: Core and monolayer properties as a function of core size. *Langmuir* **1998,** *14* (1), 17-30.

6. Xia, Y.; Xiong, Y.; Lim, B.; Skrabalak, S. E., Shape-Controlled Synthesis of Metal Nanocrystals: Simple Chemistry Meets Complex Physics? *Angewandte Chemie (International ed. in English)* **2009,** *48* (1), 60-103.

7. Goel, S.; Wu, Z.; Zones, S. I.; Iglesia, E., Synthesis and Catalytic Properties of Metal Clusters Encapsulated within Small-Pore (SOD, GIS, ANA) Zeolites. *Journal of the American Chemical Society* **2012,** *134* (42), 17688-17695.

8. Kitagawa, S.; Kitaura, R.; Noro, S., Functional porous coordination polymers. *Angewandte Chemie-International Edition* **2004,** *43* (18), 2334-2375.

9. Farruseng, D., *Metal Organic Frameworks: Applications from Catalysis to Hydrogen Storage*. First ed.; Wiley-VCH Verlag GmbH & Co.: 2011.

10. Meilikhov, M.; Yusenko, K.; Esken, D.; Turner, S.; Van Tendeloo, G.; Fischer, R. A., Metals@MOFs - Loading MOFs with Metal Nanoparticles for Hybrid Functions. *European Journal of Inorganic Chemistry* **2010,** (24), 3701-3714.

11. Moon, H. R.; Lim, D.-W.; Suh, M. P., Fabrication of metal nanoparticles in metal-organic frameworks. *Chemical Society Reviews* **2013,** *42* (4), 1807-1824.

12. Lu, G.; Li, S.; Guo, Z.; Farha, O. K.; Hauser, B. G.; Qi, X.; Wang, Y.; Wang, X.; Han, S.; Liu, X.; DuChene, J. S.; Zhang, H.; Zhang, Q.; Chen, X.; Ma, J.; Loo, S. C. J.; Wei, W. D.; Yang, Y.; Hupp, J. T.; Huo, F., Imparting functionality to a metal-organic framework material by controlled nanoparticle encapsulation. *Nature Chemistry* **2012,** *4* (4), 310-316.

13. Yin, H. F.; Ma, Z.; Chi, M. F.; Dai, S., Heterostructured catalysts prepared by dispersing $Au@Fe_2O_3$ core-shell structures on supports and their performance in CO oxidation. *Catalysis Today* **2011,** *160* (1), 87-95.

14. Buso, D.; Jasieniak, J.; Lay, M. D. H.; Schiavuta, P.; Scopece, P.; Laird, J.; Amenitsch, H.; Hill, A. J.; Falcaro, P., Highly Luminescent Metal-Organic Frameworks Through Quantum Dot Doping. *Small* **2012,** *8* (1), 80-88.

15. Lee, D. Y.; Shin, C. Y.; Yoon, S. J.; Lee, H. Y.; Lee, W.; Shrestha, N. K.; Lee, J. K.; Han, S. H., Enhanced photovoltaic performance of Cu-based metal-organic frameworks sensitized solar cell by addition of carbon nanotubes. *Scientific Reports* **2014,** *4*, 3930.

16. Lauhon, L. J.; Gudiksen, M. S.; Wang, C. L.; Lieber, C. M., Epitaxial core-shell and core-multishell nanowire heterostructures. *Nature* **2002,** *420* (6911), 57-61.

17. Cavka, J. H.; Jakobsen, S.; Olsbye, U.; Guillou, N.; Lamberti, C.; Bordiga, S.; Lillerud, K. P., A new zirconium inorganic building brick forming metal organic frameworks with exceptional stability. *Journal of the American Chemical Society* **2008,** *130* (42), 13850-13851.

18. Schoenecker, P. M.; Carson, C. G.; Jasuja, H.; Flemming, C. J. J.; Walton, K. S., Effect of Water Adsorption on Retention of Structure and Surface Area of Metal-Organic Frameworks. *Industrial & Engineering Chemistry Research* **2012,** *51* (18), 6513-6519.

19. Garibay, S. J.; Cohen, S. M., Isoreticular synthesis and modification of frameworks with the UiO-66 topology. *Chemical Communications* **2010,** *46* (41), 7700-7702.

20. Biswas, S.; Van der Voort, P., A General Strategy for the Synthesis of Functionalised UiO-66 Frameworks: Characterisation, Stability and CO_2 Adsorption Properties. *European Journal of Inorganic Chemistry* **2013,** (12), 2154-2160.

21. Daniel, M. C.; Astruc, D., Gold nanoparticles: Assembly, supramolecular chemistry, quantum-size-related properties, and applications toward biology, catalysis, and nanotechnology. *Chemical Reviews* **2004,** *104* (1), 293-346.

22. Abbott, A. P.; Capper, G.; Davies, D. L.; McKenzie, K. J.; Obi, S. U., Solubility of metal oxides in deep eutectic solvents based on choline chloride. *Journal of Chemical and Engineering Data* **2006,** *51* (4), 1280-1282.

23. Li, L.; Zhu, Y.-J., High chemical reactivity of silver nanoparticles toward hydrochloric acid. *Journal of Colloid and Interface Science* **2006,** *303* (2), 415-418.

24. Elzey, S.; Grassian, V. H., Nanoparticle Dissolution from the Particle Perspective: Insights from Particle Sizing Measurements. *Langmuir* **2010,** *26* (15), 12505-12508.

25. Shi, H.; Bi, H.; Yao, B.; Zhang, L., Dissolution of Au nanoparticles in hydrochloric acid solution as studied by optical absorption. *Applied Surface Science* **2000,** *161* (1–2), 276-278.

26. Guillerm, V.; Gross, S.; Serre, C.; Devic, T.; Bauer, M.; Ferey, G., A zirconium methacrylate oxocluster as precursor for the low-temperature synthesis of porous zirconium(IV) dicarboxylates. *Chemical Communications* **2010,** *46* (5), 767-769.

27. Kickelbick, G.; Schubert, U., Oxozirconium methacrylate clusters: $Zr_6(OH)_4O_4(OMc)_{12}$ and $Zr_4O_2(OMc)_{12}$(OMc = methacrylate). *Chemische Berichte-Recueil* **1997,** *130* (4), 473-477.

28. Brust, M.; Walker, M.; Bethell, D.; Schiffrin, D. J.; Whyman, R., Synthesis of thiol-derivatised gold nanoparticles in a two-phase Liquid-Liquid system. *Journal of the Chemical Society-Chemical Communications* **1994,** (7), 801-802.

29. Hostetler, M. J.; Templeton, A. C.; Murray, R. W., Dynamics of place-exchange reactions on monolayer-protected gold cluster molecules. *Langmuir* **1999,** *15* (11), 3782-3789.

30. Schaate, A.; Roy, P.; Godt, A.; Lippke, J.; Waltz, F.; Wiebcke, M.; Behrens, P., Modulated Synthesis of Zr-Based Metal-Organic Frameworks: From Nano to Single Crystals. *Chemistry-a European Journal* **2011,** *17* (24), 6643-6651.

CHAPTER 4

STATIC OXYGEN STORAGE CAPACITY AND CATALYTIC ACTIVITY OF METAL-ORGANIC FRAMEWORK SUPPORTED GOLD NANOPARTICLES

4.1 Introduction

Supported gold nanoparticles (AuNPs) have garnered a lot of attention due to their enhanced catalytic abilities for many reactions such as hydrogenation, oxidation, and reduction reactions.[1-3] Specifically, supported AuNPs catalysts are exceptionally active for carbon monoxide (CO) oxidation at temperatures well below ambient temperature.[4, 5] CO is an odorless, toxic gas that is hazardous to human health and the environment at low concentrations. Catalysts capable of low-temperature selective oxidation of CO are ideal for filtration devices including gas masks, air purification systems, and fuel cells, where CO is a common poison.[6] Extensive studies have probed the catalytic activity for CO oxidation over AuNPs supported on metal oxides. There are several key factors that contribute to the catalytic activity including AuNP size, shape, and oxidation state; metal-support interactions; activation conditions; support reducibility; and the oxygen storage capacity of the support.[7-13] Many other studies have shown catalytic abilities of AuNPs supported on or in porous materials including zeolites, carbon nanotubes, and metal-organic frameworks (MOFs).[14-16] However, aside from common metal oxides, there is a dearth of studies that focus on determining the importance of the specific support.

MOFs are crystalline, nanoporous materials that consist of metal oxide centers connected via organic linkers. Advantages of MOFs include high surface areas and pore volumes, uniform pore sizes, and chemical tunability.[17-19] MOFs are currently being explored as catalyst supports for hydrogenation, oxidation, and photocatalytic reactions.[20-22] Several MOF systems have been explored as catalyst supports for CO oxidation including ZIF-8, ZIF-67, MOF-5, CPL-2, MIL-101, Al-MIL-53, and UiO-66.[21, 23-27] Among these, AuNPs were supported by ZIF-8, CPL-2, and UiO-66, and CO oxidation was probed.[21, 25, 26] Interestingly, Au@CPL-2, under the conditions used, did not oxidize CO or H_2, possibly due to a lack of oxygen vacancy sites at the AuNP-CPL-2 interface.[26] However, both Au@ZIF-8 and Au@UiO-66 proved active for CO oxidation suggesting that not all MOFs lack oxygen vacancy sites.[21, 25] In this work, the catalytic activity of the AuNPs on UiO-66 is further probed to determine the specific effect that the UiO-66 support has on CO oxidation. Extensive characterization and catalytic studies are performed to determine the fundamental role that the support plays in CO oxidation.

UiO-66 is a zirconium-based MOF consisting of $Zr_6O_4(OH)_4$ centers connected by 1,4-benzenedicarboxylic acid linkers.[28] Its potential stems from its thermal stability up to 813 K, mechanical resistance, acid and base resistance, stability in humid environments, and straightforward functionalization.[28-31] In this work, we use UiO-66 to determine the potential of MOFs as catalyst supports for CO oxidation. By comparing AuNPs supported on UiO-66 to AuNPs supported on titanium dioxide (TiO_2) and zirconium dioxide (ZrO_2), we can probe the effect of the support and determine the support attributes necessary to promote CO oxidation. Additionally, this information gives insight into the reaction mechanism for CO oxidation over MOF-supported AuNPs.

Iijima et al. showed that the support plays an important role in catalytic CO oxidation and subsequent studies have examined this effect in depth.[5, 13, 32, 33] The enhanced catalytic activity of AuNPs on various supports is often attributed to the reducibility and oxygen storage capacity (OSC) of the support.[12, 13] Furthermore, improved OSC is attributed to the support reducibility, oxygen vacancy sites, structural distortion and coordination environment alterations, and crystal structure.[13, 34-36]

In the present study, preformed AuNPs are deposited on UiO-66, TiO_2, and ZrO_2, and the CO oxidation capabilities are analyzed. The supported AuNPs are characterized using transmission electron microscopy (TEM), inductively coupled plasma (ICP) emission spectroscopy, and temperature programmed reduction (H_2-TPR) to show that the AuNPs are comparable across the various supports, which equalizes the AuNP effect and allows an accurate assessment of the support effect. The composites and parent supports are also probed to determine the controlling attributes of the supports.

4.2 Experimental Methods

All chemicals were obtained commercially (Sigma Aldrich, VWR, Fisher Scientific, and City Chemical) and used without further purification. AuNPs capped with 1-dodecanethiol (DDT) and 11-mercaptoundecanoic acid (MUA) were prepared using a two-step process: (1) the synthesis of DDT capped gold nanoparticles (AuNP-DDT) followed by (2) a ligand exchange with MUA. AuNP-DDT were prepared using a previously reported procedure.[37] A solution of tetraoctylammonium bromide (0.728 mmol) in toluene (40 mL) was mixed with a solution of gold(III) chloride trihydrate (0.314 mmol) in water (20 mL) and stirred for 30 min. Next, DDT (0.314 mmol) was

added, and the mixture was stirred for 30 min. Finally, a solution of sodium borohydride ($NaBH_4$) (3.14 mmol) in water (10 mL) was added and the mixture was rigorously stirred for 3 h. The product was washed with de-ionized water, the organic phase separated, and the AuNP-DDT were precipitated from methanol three times. The ligand exchange entailed stirring AuNP-DDT (3 mg/mL) and MUA (0.154 mmol) in toluene for 72 h and washing the product three times with toluene.[38] The resulting mixed ligand product will be referred to as AuNP throughout this work.

UiO-66 was synthesized as previously reported.[39] Briefly, zirconium(IV) propoxide (0.227 mmol), 1,4-benzenedicarboxylic acid (0.454 mmol), methanol (86.5 mmol), N,N'-dimethylformamide (45.4 mmol), and glacial acetic acid (6.81 mmol) were stirred in a glass scintillation vial at 393 K for 24 h in a silicone oil bath. The resulting material was filtered and washed three times with DMF and three times with methanol.

The physical mixtures, denoted throughout this work as Au on UiO-66 and Au on TiO_2, were prepared by sonicating 40-50 mg of the support in methanol (9.9 mL) in a sonication bath for 5 min. Then, 1-1.5 mg of AuNPs 2.1±0.5 nm in diameter were added and the suspension was stirred for 24 h. Au on ZrO_2 was prepared similarly, 40-50 mg of ZrO_2 was sonicated in 9.5 mL of methanol and 0.4 mL of acetic acid, which is necessary to lower the pH below the isoelectric point, for 5 min. Then, 1-1.5 mg of the AuNPs were added and stirred for 24 h. A fresh physical mixture was used for every CO oxidation run and characterization technique and repeated twice to confirm the consistency of the preparation method.

Proton nuclear magnetic resonance (^{1}H NMR) spectroscopy was measured using the Varian Mercury Vx 300. Samples were prepared by suspending approximately 5-10

mg of AuNPs in 1 mL of dimethyl sulfoxide-d_6. Powder X-ray diffraction (PXRD) patterns were measured using a PANalytical X-ray diffractometer. Approximately 5-10 mg of samples was loaded onto a low background silica sample holder and scanned from 5-90°. Nitrogen sorption measurements were run using the Quantachrome Quadrasorb Evo volumetric analyzer. The isotherms were measured over a range of relative pressures (P/P_0) from 0.001-0.990 with high purity nitrogen (99.998%) obtained from Airgas. Prior to the measurement, the sample was outgassed at 473 K under dynamic vacuum overnight using a Quantachrome FloVac Degasser. The surface areas were calculated using the Brunauer, Emmett, and Teller (BET) theory using $0.005 \leq P/P_0 \leq 0.03$ and the total pore volume was calculated at $P/P_0 = 0.6$. Inductively coupled plasma (ICP) emission spectroscopy was run using the Perkin Elmer Optima 3000 DV ICP Emission Spectrometer. Transmission electron microscopy (TEM) images were obtained using the Hitachi HT7700 operated at 120 keV. The samples were deposited on a lacy carbon copper grid by suspending less than 1 mg of material in methanol and dropcasting it on the grid. Temperature programmed reduction (H_2-TPR) was performed using the Micromeritics AutoChem II 2920. Prior to each H_2-TPR experiment, the sample underwent a 1 h water bakeoff under He flow at 473 K, a 2 h calcination under 10% O_2 in helium at 523 K, and a 30 min helium purge. Finally, H_2-TPR measurement ramped the temperature from 323 K to 1073 K (673 K for UiO-66) at 5 K/min under 10% H_2 in helium flow. The static oxygen storage capacity (OSC) of the materials was measured using a CO step experiment in a packed-bed reactor. The materials were purged with nitrogen at 473 K overnight, calcined in air at 523 K for 2 h, purged with nitrogen for 30 min at 523 K, and, finally, 1% CO in nitrogen was run through the sample bed at a total

flow rate of 40 mL/min. The static OSC was calculated by integrating the CO_2 curve from 0-45 min.

CO oxidation experiments were performed using a packed bed reactor with the outlet connected to a Hiden DSMS. Approximately 25-40 mg of sample were packed into the sample cell with glass wool. Before the catalytic measurement, the material was purged with He at 473 K for 16-18 h, and then calcined in air at 523 K for 2 h to remove the capping agents on the AuNPs. CO_2 evolves during the calcination process and is completely depleted after 2 h suggesting that the capping ligands were completely removed. After cooling to the reaction temperature under air flow, 1% CO in air was passed through the system at a total flow rate of 40 mL/min.

Adsorption isotherms were collected using a home-built volumetric adsorption system and the Peng-Robinson equation of state was used to calculate the gas uptake. Before each measurement, the samples were outgassed at 473 K under dynamic vacuum for 16-18 h. Then, the sample was backfilled with air to approximately 1 bar and heated at 523 K for 2 h in order to combust the organic capping agents on the AuNPs. Vacuum was then used to remove the air to begin the adsorption isotherms.

4.3 Results and Discussion

There are many factors that influence catalytic activity for CO oxidation including AuNP size and oxidation state, support, preparation method, and activation conditions.[5, 8, 9, 11, 12, 32, 40-43] In order to probe the support effect on CO oxidation without inadvertently including other variables, preformed AuNPs 2.1±0.5 nm in diameter are deposited on the surface of the support and thoroughly characterized to prove that the support is the only

manipulated variable in order to ascertain the key contributing factor(s) of the supports. The catalyst characterization includes: powder X-ray diffraction (PXRD), nitrogen sorption at 77K, inductively coupled plasma atomic emission spectroscopy (ICP-AES), transmission electron microscopy (TEM), temperature programmed reduction (H_2-TPR), and a CO step experiment to probe the static oxygen storage capacity (OSC).

The AuNPs were characterized with ^{1}H NMR, TGA, and TEM to confirm the presence and composition of the surface-assembled monolayer (SAM), the combustion temperature of the SAM, and the AuNP diameter. Figure 4.1a shows the ^{1}H NMR spectrum for the AuNPs with a mixed monolayer of DDT and MUA. There are broad peaks observed at 0.81 ppm, 1.22 ppm, 2.14 ppm, 2.5 ppm, and 3.3 ppm. The peaks at 2.5 ppm and 3.3 ppm are due to dimethyl sulfoxide-d_6 and H_2O in dimethyl sulfoxide-d_6, respectively. The peak at 1.22 ppm encompasses the $–CH_2$ protons in the long chains of both DDT and MUA. DDT has a unique peak at 0.81 ppm characteristic of the protons on the $–CH_3$ group and MUA has a unique peak at 2.14 ppm associated with the protons on the $–CH_2COOH$ group. The lack of coupling for these characteristic peaks is informative; both DDT and MUA are bound to the surface of the AuNPs instead of excess ligand in the solvent.[44] In addition, Figure 4.1b shows the AuNP capping ligands are removed, under air flow, at temperatures exceeding 500K. Figure 4.2 exhibits TEM images of the AuNPs. The AuNP diameter of 2.1±0.5 nm was measured from thirteen different grid locations.

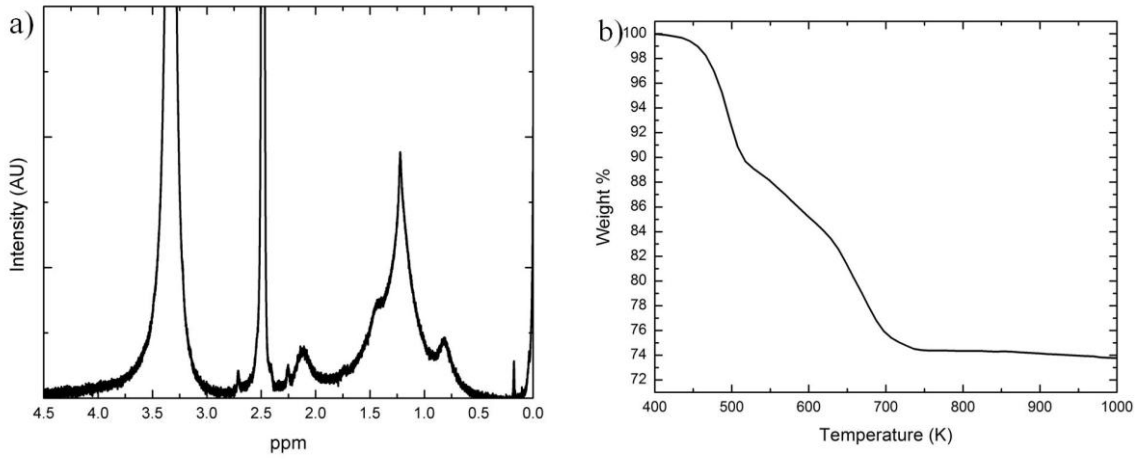

Figure 4.1: (a) ^{1}H NMR of AuNP-DDT/MUA and (b) TGA data for AuNP-DDT/MUA heated under air flow

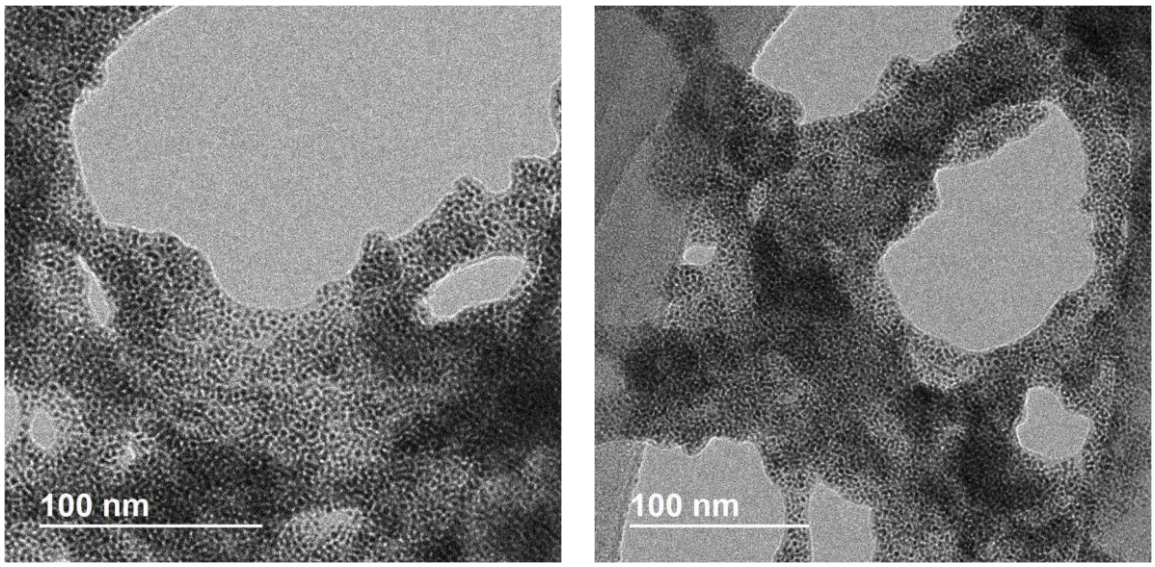

Figure 4.2: TEM images of as-synthesized AuNP-DDT/MUA

The PXRD patterns for UiO-66 and Au on UiO-66 before and after CO oxidation, depicted in Figure 4.3a, match the simulated pattern. This confirms that the UiO-66 structure is initially obtained, remains after depositing AuNPs on the surface, and remains after CO oxidation up to a maximum oxidation temperature of 523K. The retention of UiO-66 after CO oxidation at 523 K is notable because it allows for a direct comparison to TiO_2 and ZrO_2. Also, there are no gold peaks observed, suggesting the AuNPs are too

small to be detected by PXRD. Both Au on ZrO_2 and Au on TiO_2 retain their structures after AuNP deposition and CO oxidation up to 523 K, and they also lack gold peaks (Figure 4.3b).

Table 4.1 shows the results from ICP, TEM, and nitrogen sorption at 77 K data for the various catalysts. Nitrogen sorption at 77 K shows that the supports retain their porosity after AuNP deposition. Specifically, the BET surface area for Au on UiO-66 is comparable but slightly lower than the parent material. This is due to the addition of the non-porous AuNPs to porous UiO-66 which increases the overall material density. Nitrogen sorption at 77 K shows that high quality Au on UiO-66 is used throughout this work. Conversely, TiO_2 and ZrO_2 are non-porous, and the addition of non-porous AuNPs does not significantly affect the BET surface area.

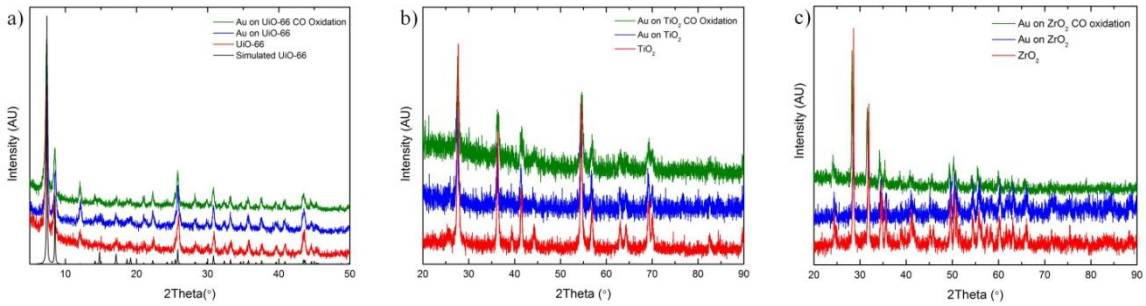

Figure 4.3: PXRD patterns for the (a) UiO-66, (b) TiO_2, and (c) ZrO_2 materials before and after CO oxidation

Table 4.1: Characterization of UiO-66, TiO_2, and ZrO_2 materials

Material	Au wt%	As-synthesize d_{AuNP} (nm)	d_{AuNP} Post CO at 523 K (nm)	BET Surface Area (m^2/g)	Pore Volume[a] (cm^3/g)
UiO-66	-----	-----	-----	1069±28	0.45±0.01
TiO_2	-----	-----	-----	30±1	0.03±0.00
ZrO_2	-----	-----	-----	5±1	0.01±0.00
Au on UiO-66	1.2	2.7±1.0	4.4±1.7	951±75	0.39±0.03
Au on TiO_2	1.2	2.7±0.8	3.5±1.5	16±10	0.009±0.00
Au on ZrO_2	1.2	2.3±0.5	4.6±2.4	27±4	0.04±0.01

[a]Measured at $P/P_0 = 0.6$

Figure 4.4 shows the TEM images of the as-synthesized catalysts and the catalysts after CO oxidation at 523K, and Table 4.1 reports the average AuNP diameter for the catalysts. TEM after CO oxidation at 523 K is representative because AuNP sintering occurs more extensively at elevated temperatures.[45] The average AuNP diameter, both before and after CO oxidation at 523 K, is comparable for all of the supports. The AuNPs measured after CO oxidation at 523 K for all of the catalysts show a slight increase in diameter due to AuNP sintering. However, the AuNPs remain smaller than 5 nm in diameter and similar for all of the catalysts. The AuNPs on ZrO_2 and UiO-66 grow approximately 1 nm larger than the AuNPs supported on TiO_2 during CO oxidation at 523K, which could suggest that the AuNPs are more stable on TiO_2. However, the AuNPs on the three catalysts have diameters within a standard deviation of each other both before and after CO oxidation at 523K, suggesting that the AuNP size is constant across the supports and is not a factor for divergent catalytic activity.

Figure 4.5 shows the H_2-TPR curves for the catalysts after calcination in 10% O_2 in helium at 523K. The lack of peaks ranging from 373-398 K suggests that the AuNPs are in the reduced form.[46, 47] For Au on TiO_2 and Au on ZrO_2, the absence of a peak between 573-1073 K suggests that the addition of AuNPs does not destabilize the surface oxygen from the support.[46, 48] H_2-TPR suggests that the AuNPs are in the reduced form when deposited on all three supports and that the AuNPs, deposited via colloidal deposition, do not observably affect the redox capabilities of the supports by H_2.

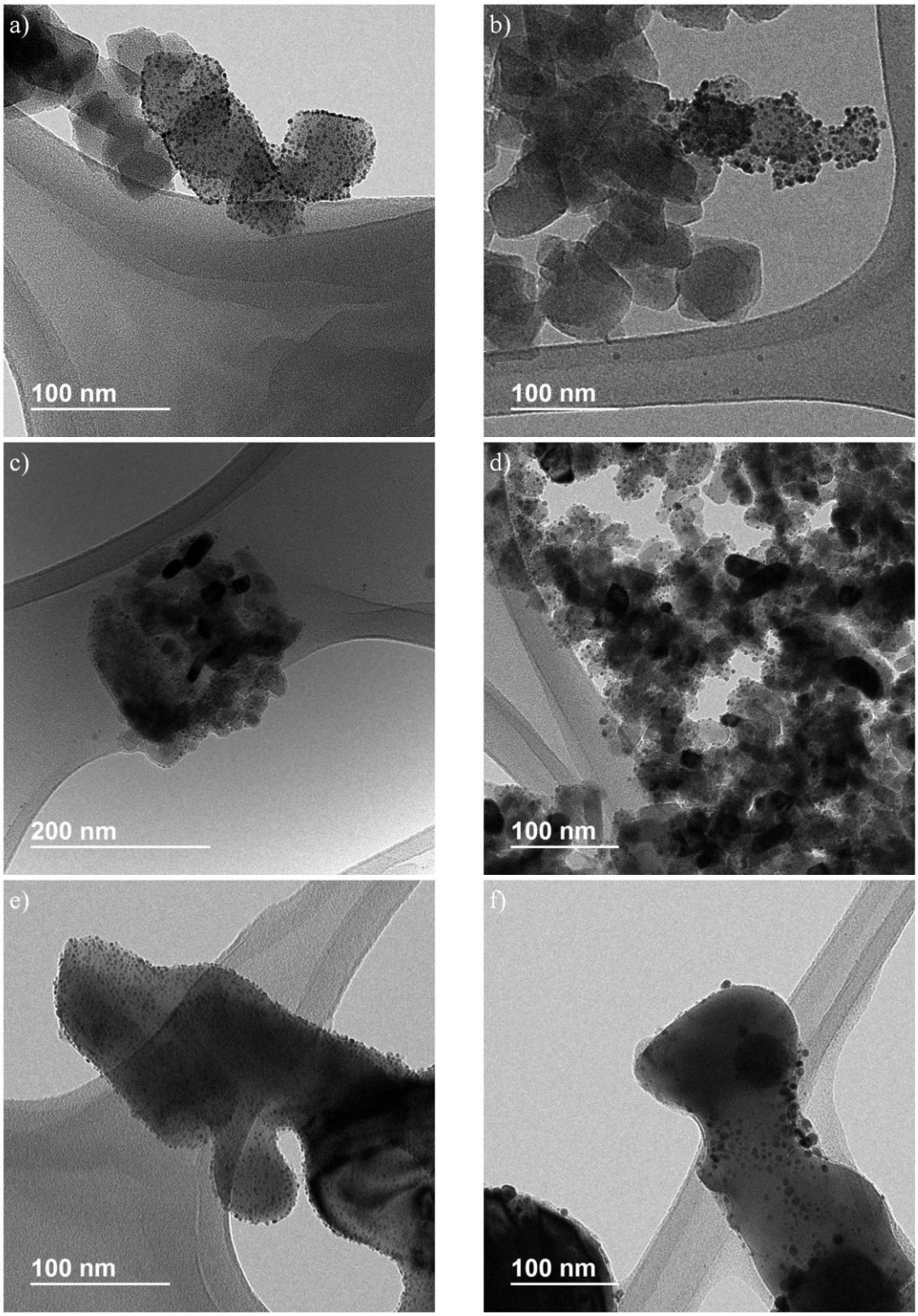

Figure 4.4: TEM images of (a) as-synthesized Au on UiO-66, (b) Au on UiO-66 after CO oxidation at 523K, (c) as-synthesized Au on TiO_2, (d) Au on TiO_2 after CO oxidation at 523K, (e) as-synthesized Au on ZrO_2, (f) Au on ZrO_2 after CO oxidation at 523K

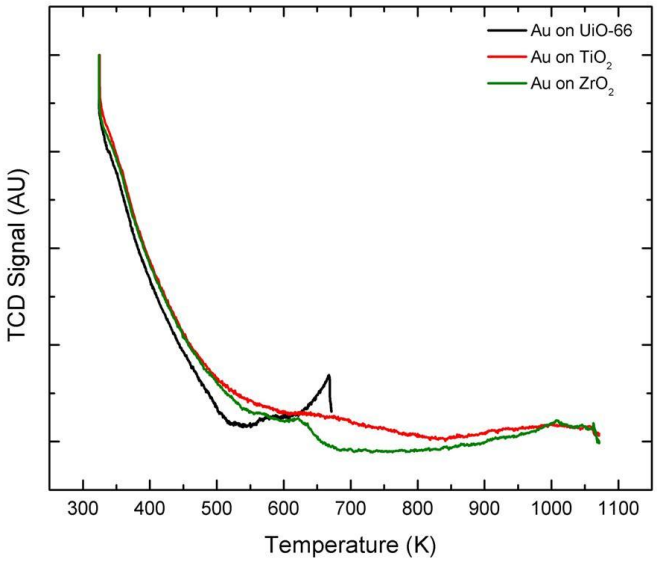

Figure 4.5: H_2-TPR curves ranging from 323-673 K for Au on UiO-66 and from 323-1073 K for Au on TiO_2 and Au on ZrO_2

Oxygen storage capacity (OSC) is a measure of the reducible oxygen stored by a support, either via adsorption or contained within the lattice structure, which is capable of being donated for oxidation purposes. This is determined by calcining the sample in air, purging the system with nitrogen to remove any physisorbed oxygen, then running a CO oxidation experiment with 1% CO in nitrogen. Table 4.2 reports the static OSCs measured using a CO step experiment at 523K, while Figure 4.6 depicts the OSC curves. The static OSC is largest for Au on UiO-66, while Au on ZrO_2 has the smallest static OSC. To the best of the authors' knowledge, this is the first time static OSCs have been reported for MOFs. The same OSC experiment was performed on the parent supports without AuNPs. There is no measureable CO_2 evolution during the experiments on any of the parent supports, which shows that AuNPs are necessary for the evolution of CO_2 under these reaction conditions. The need for AuNPs for CO_2 evolution during the OSC experiment is due to one of four possible reasons: (1) to adsorb CO which is then

oxidized at the interface between the AuNPs and the support with oxygen stored by the support; (2) to destabilize adjacent lattice surface oxygen; (3) to adsorb oxygen that is then reduced by CO; or (4) to create an interface site with the support to adsorb and activate oxygen that subsequently reacts with CO.[1, 49-51]

Table 4.2: CO oxidation results for Au on UiO-66, Au on TiO_2, and Au on ZrO_2

Material	Au on UiO-66	Au on TiO_2	Au on ZrO_2
OSC (mol CO_2/g_{sample})	$3.5x10^{-3}$	$1.6x10^{-3}$	$7.0x10^{-4}$
$T_{1/2}$ (K)	368	454	569
Reaction Rate (mol/g_{sample} s)	$3.7x10^{-7}$	$1.5x10^{-7}$	-----
Reaction Rate (mol/g_{Au} s)	$3.0x10^{-5}$	$1.2x10^{-5}$	-----
TOF (s^{-1})	0.7	0.2	-----
CO Conversion at 298 K (%)	3	2	-----
CO Conversion at 523 K (%)	99	74	22
E_{app} (kJ/mol)	17	29	17

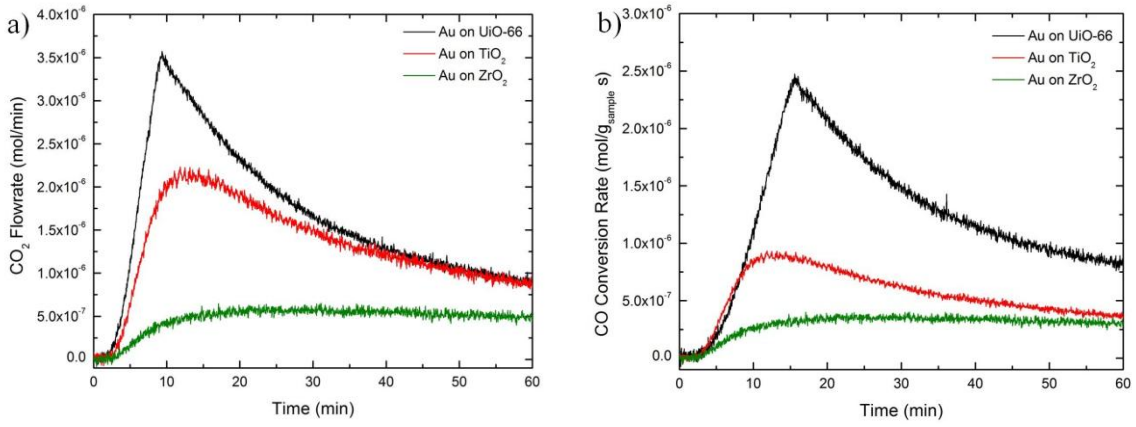

Figure 4.6: (a) CO_2 evolution and (b) CO_2 production rate during a 1% CO in nitrogen experiment used to determine OSC for Au on UiO-66, Au on TiO_2, and Au on ZrO_2

The colloidal deposition and pretreatment used in this work successfully equalize the AuNP effects for the three materials. Specifically, the AuNPs are comparable in size

and in the reduced state across the three supports. The crystal structure is retained for all three supports after both AuNP deposition and CO oxidation at temperatures as high as 523 K for Au on UiO-66 and Au on TiO_2 and as high as 573 K for Au on ZrO_2. The key difference between the three materials is the support attributes, specifically the support porosity and static OSC. Therefore, the support effect can effectively be probed for CO oxidation over supported AuNPs.

Consistent activation procedures are necessary to directly compare the CO oxidation results.[11] In this work, the sample pretreatment consists of water and solvent removal by heating the catalyst at 473 K under helium flow for 16-18 h, followed by calcination in air at 523 K for 2 h. During calcination on samples with AuNPs, CO_2 evolves as the samples are heated at 523 K in air and is completely depleted after 2 h. However, the parent supports do not yield CO_2 when calcined at 523 K. Figure 4.1b depicts the TGA curve for the AuNPs under air flow. At temperatures exceeding 500 K, the organic capping ligands are removed from the AuNP surface. The combination of TGA and CO_2 evolution during calcination suggests that the AuNP capping ligands are combusted at 523 K, freeing active AuNP sites for catalysis.

Figure 4.7 compares the catalytic ability of the materials at various reaction temperatures and highlights the importance of the AuNPs for CO oxidation within the temperature range of 298-573K. Without the addition of AuNPs, UiO-66 and TiO_2 are inactive for CO oxidation at 523 K and ZrO_2 at 573 K. The addition of AuNPs significantly improves the catalytic activity of these supports. Table 4.2 reports the turnover frequency (TOF), which is the reaction rate over a single surface atom per second, at 298 K, the approximate temperature necessary for 50% conversion of CO

($T_{1/2}$), and the apparent activation energy (E_{app}) for the supported AuNPs. Notably, the $T_{1/2}$ for Au on UiO-66 of 368 K compares well with CO oxidation over Au@UiO-66, Au@ZIF-8, and Ag@MIL-53 which convert 50% CO at approximately 428 K,[21] 443 K,[25] and 396 K,[27] respectively. Likewise, the $T_{1/2}$ for Au on TiO_2 and Au on ZrO_2 in this work are similar to the previously reported ranges of 262-477 K and 347-523 K for Au on TiO_2 and Au on ZrO_2, respectively, which are highly dependent on preparation method and activation conditions.[1, 32, 42, 52]

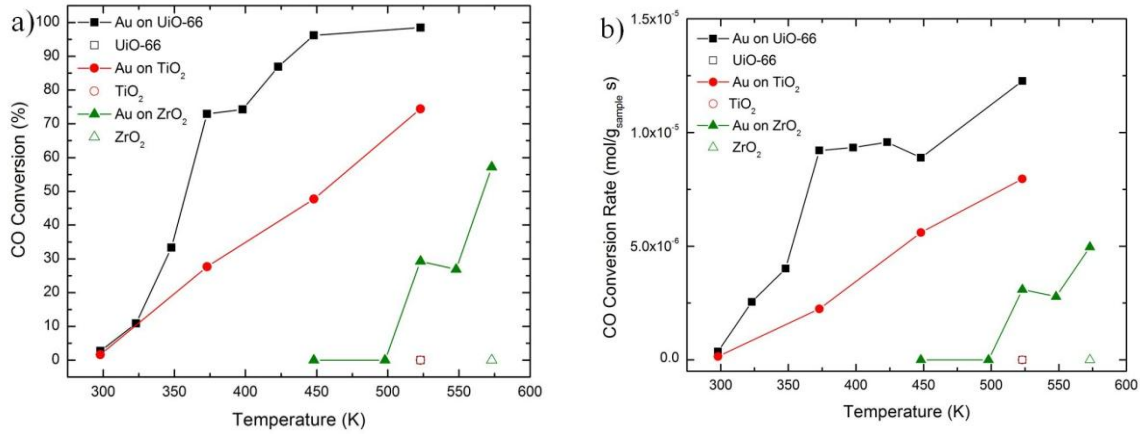

Figure 4.7: (a) CO conversion and (b) reaction rate vs. temperature for Au on UiO-66, Au on TiO_2, and Au on ZrO_2. The lines are to guide the eye only

Furthermore, the apparent activation energies for Au on TiO_2 and Au on ZrO_2 in this work agree well with previously reported values. Figure 4.8 shows the Arrhenius plots for these catalysts. Specifically, Au on TiO_2 has reported apparent activation energies ranging from approximately 2-56 kJ/mol[1, 41, 42] and Au on ZrO_2 has apparent activation energy of approximately 18 kJ/mol.[53] Lastly, the TOF for Au on UiO-66 is similar to Au on TiO_2; and the TOF for Au on TiO_2 is comparable to previously reported values.[42]

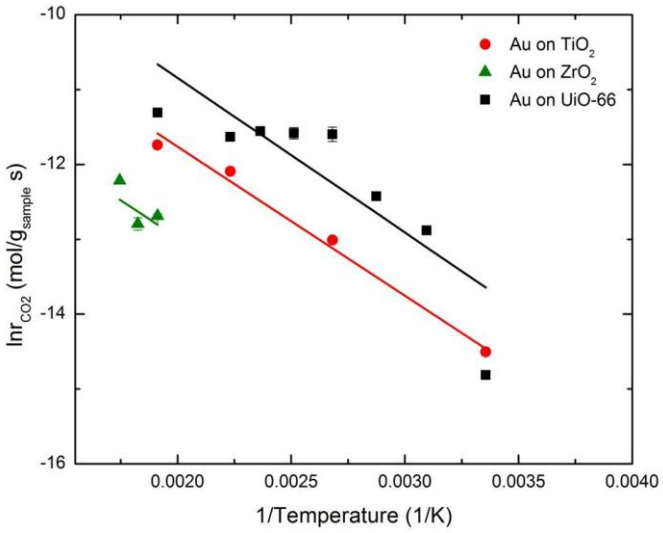

Figure 4.8: Arrhenius plots of Au on UiO-66, Au on TiO_2, and Au on ZrO_2

Based on an extensive catalyst characterization, which suggests that the AuNP effects have been decoupled from those of the support, the support effect on CO oxidation activity was probed. As previously stated, there are two divergent support characteristics: porosity and OSC. UiO-66 is porous, and the metal oxides are not. However, Figure 4.9 and Table 4.2 show a correlation between OSC and CO conversion rate at 523 K of the catalysts. Therefore, the key attribute of the support for CO oxidation is the OSC of the material. The differences in the OSC for the various supports are related to the ability of the support to store and release oxygen via either adsorption or as a part of the lattice structure. For metal oxides this is attributed largely to the reducibility of the support, which defines the ability of the metal to change its oxidation state.[13] This work supports this idea by comparing Au on TiO_2 and Au on ZrO_2. TiO_2 is more reducible relative to ZrO_2; therefore, the larger OSC and subsequently higher CO oxidation activity for Au on TiO_2 follows this reducibility trend compared to Au on ZrO_2. However, there are no data available that directly compare the reducibility of UiO-66 with TiO_2 and

ZrO_2. However, UiO-66 is zirconium-based, and the reducibility of the material should be similar to ZrO_2 since zirconium does not easily change its oxidation state. This suggests that the OSC for MOFs is not only dependent on the reducibility of the metal.

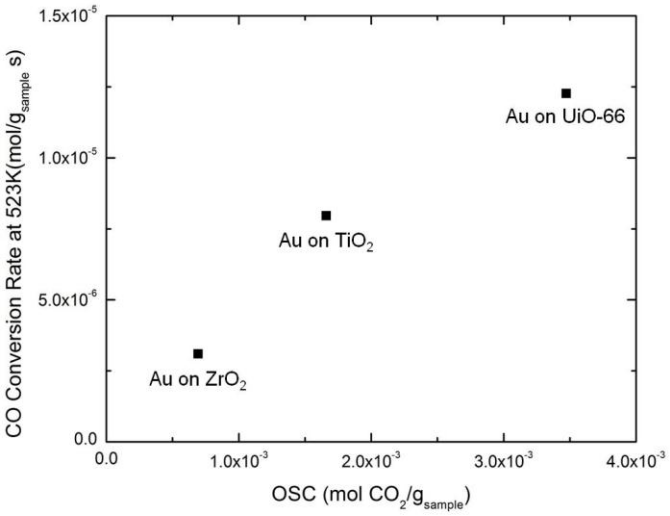

Figure 4.9: Correlation between OSC and activity

There are several unique aspects of UiO-66. First, UiO-66 is a complex coordination material with twelve BDC linkers per $Zr_6O_4(OH)_4$ node. Upon dehydration, the -OH groups are removed, changing the zirconium atoms from 8- to 7-fold coordination, which results in a distorted Zr_6O_6 node.[54] Distortion of the metal center has the potential to alter the reducibility of the material; however, H_2-TPR suggests that this distorted structure does not measurably affect the reducibility of UiO-66 at temperatures below 673K. Notably, there is interest in designing mixed metal oxides in order to distort the coordination environment to create oxygen vacancies and enhance the OSC of metal oxides;[35, 55] whereas UiO-66 has a built-in distortion mechanism that is completely reversible via dehydration/hydration. Second, the dehydrated structure shows an electronic rearrangement with identified preferential sorption sites. Unfortunately, there is

close packing that occurs by linking the $Zr_6O_4(OH)_4$ and Zr_6O_6 units with 12 BDC ligands, which prevents access to the metal centers. However, it is common for linker vacancies to occur; specifically, the absence of approximately one in twelve BDC linkers is known to occur randomly throughout the material allowing more access to the metal centers.[54] These defects can be controlled through the addition of modulators such as trifluoroacetic acid (TFA), which incorporate themselves into the structure and can be removed through heating. The removal results in only eight carboxylic acid groups surrounding the metal nodes and creates extra Lewis acid sites thereby providing access for gas molecules to the metal centers.[56] In this work, acetic acid is used as a modulator in order to create quality UiO-66 crystals. However, the BET surface area and CO_2 uptake (Figure 4.12a) are similar to UiO-66 prepared by the conventional synthesis suggesting that defects introduced by modulation is minimal.[57] Third, the band gap energy (E_g) measured and calculated for UiO-66 is lower than ZrO_2 due to the presence of the organic ligand.[54] This shows that the linker plays a significant role in the overall chemistry of the material. Lastly, a larger BET surface area potentially yields more accessible oxygen donation sites. The combination of structural distortion, accessible Lewis acid sites, unusual chemistry introduced by the addition of the organic ligand, and a large surface area result in an enhanced OSC for Au on UiO-66 relative to Au on TiO_2 and Au on ZrO_2. This suggests that the OSC capacity relies on more than material reducibility when extended to MOFs and can potentially be improved upon by tuning the organic linker. Additionally, for MOFs and metal oxides alike, the OSC correlates to the CO oxidation showing the potential for MOFs as oxidation supports.

Static OSC measurements were also run on the parent supports. The lack of CO_2 evolved reveals the necessity of the AuNPs for oxygen donation. This could suggest that the reaction occurs completely on the AuNPs and the role of the support is to control the AuNP properties; however, other mechanisms are possible. AuNPs could be necessary because they create a charge transfer between the support and the AuNPs, they create an interface site for reaction to proceed, or they destabilize the support to create active defect sites.[1, 50, 51, 58-61] The exact mechanism cannot be determined from the current measurements. However, the dependence on the support for enhanced catalytic activity suggests that the 'gold only' mechanism is unlikely; otherwise, the three materials would have similar activities because the AuNP properties are comparable for all three materials. The AuNP dependence on OSC measurements coupled with the correlation between OSC and CO oxidation activities suggests that the support provides a critical function in CO oxidation. Adsorption equilibrium isotherms are measured to further probe the role of the AuNPs and the support.

Figure 4.10 shows that Au on UiO-66 reaches a steady-state conversion at temperatures exceeding 373K. However, for temperatures of 348 K and less, there is significant catalyst deactivation within 50 min on-stream. There are several potential mechanisms of catalyst deactivation that are categorized as chemical, thermal, and mechanical deactivation.[62] AuNPs on metal oxides are often plagued by both chemical and thermal deactivation, specifically, the accumulation of carbonate species on active sites and thermally triggered sintering of the AuNPs.[63] Figure 4.11 depicts a cyclic study performed on Au on UiO-66 at 348 K to probe the potential deactivation mechanisms. First, CO oxidation was run on a fresh sample resulting in 44% conversion followed by

the rapid deactivation of the catalyst. The sample was regenerated twice: (1) helium regeneration at 348 K for 16-18 h and air pretreatment at 348 K for 2 h and (2) helium regeneration at 473 K for 16-18 h and air pretreatment at 348 K for 2 h. The resulting maximum CO conversions are 19% and 40% before deactivation, respectively. These studies suggest that there is a combination of deactivation mechanisms: (1) readsorbed product CO_2, (2) formation and adsorption of reaction intermediates or carbonates which requires regeneration at 473K, and (3) sintering of AuNPs which is further suggested by TEM. These results agree well with studies performed on Au on TiO_2, Au on ZrO_2, and Au on other metal oxides, which suggest the formation of a surface carbonate layer that blocks oxygen sorption sites and can be removed by heating.[11, 53, 63, 64] Furthermore, there is less catalyst deactivation after helium regeneration at 473K, which could suggest that there are impurities, such as surface sulfates formed by the degradation of the AuNP capping agents, in the fresh sample.

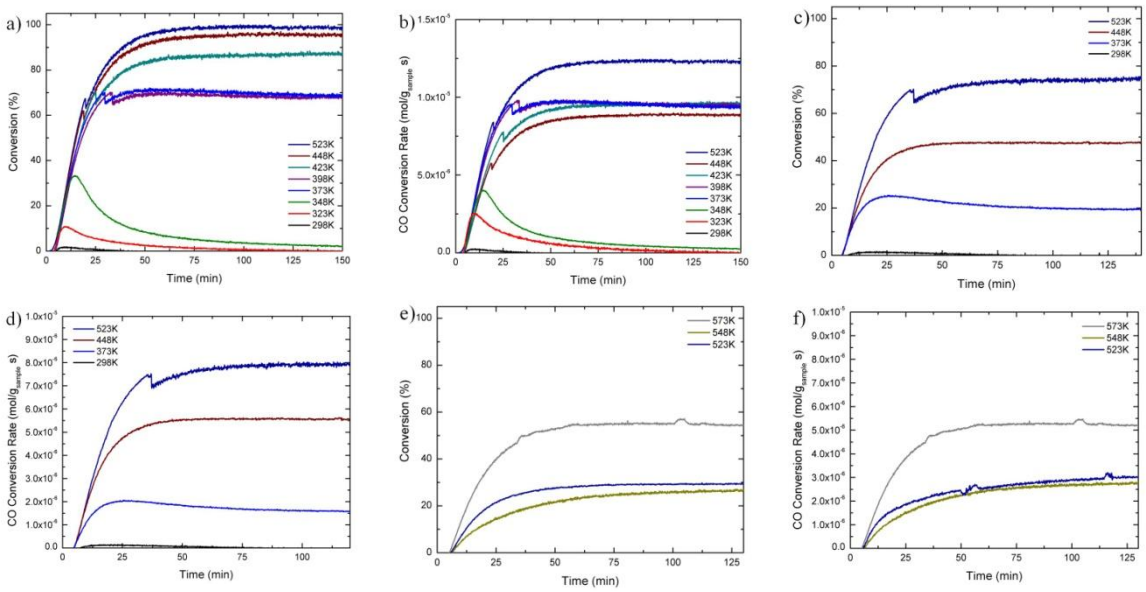

Figure 4.10: Catalytic activity over time in the temperature range of 298-523 K for (a,b) Au on UiO-66, (c,d) Au on TiO_2, and (e,f) Au on ZrO_2

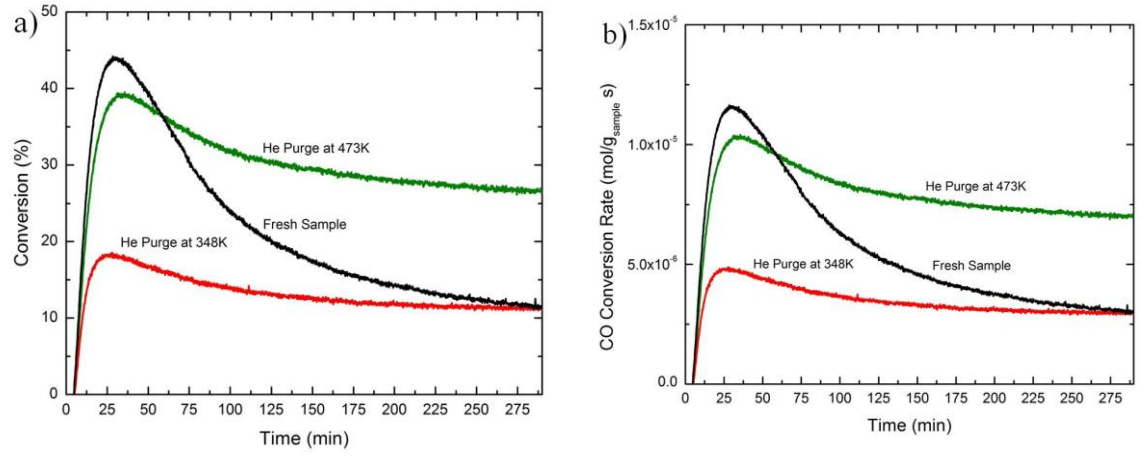

Figure 4.11: (a) CO conversion and (b) reaction rate over time for Au on UiO-66 at 348 K for a fresh sample, the same sample regenerated in a He stream at 348 K overnight, and the same sample regenerated in a He stream at 473 K overnight

Single-component adsorption isotherms are measured to probe the adsorptive capabilities of the different materials for both the reactants and products. Figure 4.12 shows the CO_2, O_2, and CO isotherms for the various supported catalysts and parent supports at 298K, respectively. Figure 4.12 show the CO_2, O_2, and CO isotherms at 298 K from 0-1 bar. UiO-66 adsorbs more CO_2, O_2, and CO at high pressures compared to both TiO_2 and ZrO_2; this is due to the increased porosity of UiO-66. UiO-66 also adsorbs more CO_2 at low pressures. The sharp slope in the low pressure region suggests strong interactions between UiO-66 and CO_2 which can contribute to catalyst deactivation at low temperatures via readsorbed CO_2, which will block active sorption sites. Similarly, Au on UiO-66 exhibits a similar CO_2 curve with a slight reduction in uptake due to the density increase of the material with the addition of AuNPs (Figure 4.12a). This suggests that the AuNPs do not contain active CO_2 sorption sites. The nearly linear O_2 isotherms, as seen in Figure 4.12b, for the three supports suggest weak interactions between O_2 and the supports. The addition of AuNPs does not significantly improve the O_2 uptake. The CO isotherms, depicted in Figure 4.12c, are also nearly linear which describes weak CO interactions with the supports and the addition of AuNPs does not significantly improve CO uptake.

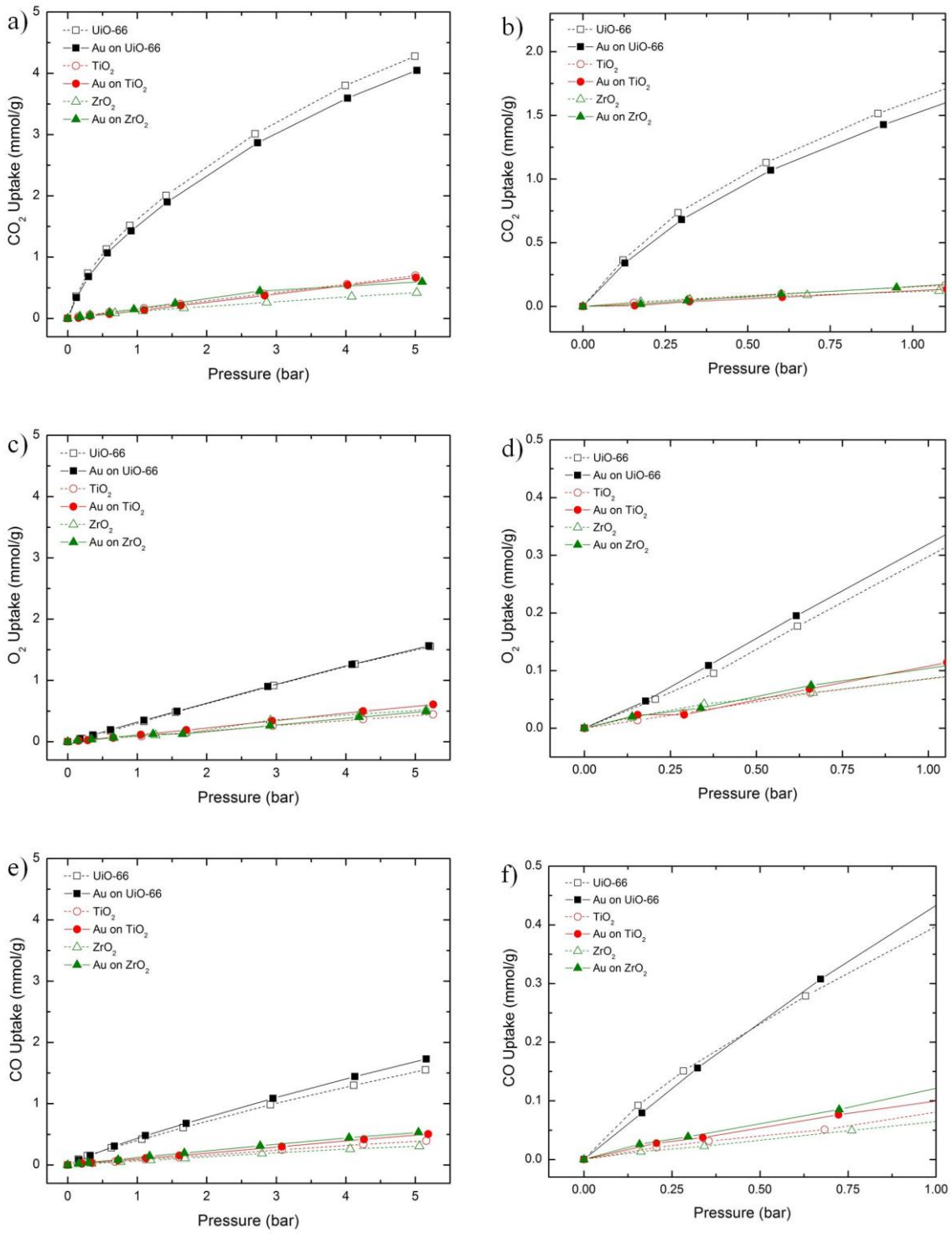

Figure 4.12: Static adsorption isotherms at 298 K of (a,b) CO_2, (c,d) O_2, and (e,f) CO on UiO-66, Au on UiO-66, TiO_2, Au on TiO_2, ZrO_2, and Au on ZrO_2. The lines are to guide the eye only.

4.4 Conclusions

An effective study on the support contribution towards catalytic activity for CO oxidation has extended from metal oxides to include MOFs, specifically zirconium-based UiO-66. A colloidal deposition is successfully employed to decouple the AuNP variables from the support effect. A multitude of characterization techniques showed that the AuNPs are the same size and oxidation state on the three supports and that the introduction of the AuNPs did not affect the support reducibility. From this study, it is concluded that the crucial support attribute for UiO-66 and the metal oxides tested is the static OSC. Importantly, UiO-66 has a larger static OSC compared to TiO_2 and ZrO_2, showing that there are other material attributes, not merely reducibility, which impact the OSC of a support. This is the first time that static OSCs have been measured for any MOF, and the enhanced OSC is promising for extending MOF applicability to catalyst supports for oxidation reactions. Overall, static OSC for MOFs are measured for the first time exceeding that of common, industrial grade TiO_2 and ZrO_2 due to the unprecedented chemistry that evolves from the combination of metal nodes and organic linkers and the potential defect sites. The ease of tuning MOF chemistry by a simple ligand functionalization conveys the overall potential of MOFs as supports for oxidation reactions.

4.5 References

1. Haruta, M., Catalysis of gold nanoparticles deposited on metal oxides. *Cattech* **2002,** *6* (3), 102-115.

2. Liu, X.; He, L.; Liu, Y. M.; Cao, Y., Supported Gold Catalysis: From Small Molecule Activation to Green Chemical Synthesis. *Accounts of Chemical Research* **2014,** *47* (3), 793-804.

3. Lang, X. J.; Chen, X. D.; Zhao, J. C., Heterogeneous visible light photocatalysis for selective organic transformations. *Chemical Society Reviews* **2014,** *43* (1), 473-486.

4. Haruta, M.; Kobayashi, T.; Sano, H.; Yamada, N., Novel gold catalysts for the oxidation of carbon monoxide at a temperature far below 0^{o}C. *Chemistry Letters* **1987,** (2), 405-408.

5. Haruta, M.; Yamada, N.; Kobayashi, T.; Iijima, S., Gold catalysts prepared by coprecipitation for low-temperature oxidation of hydrogen and of carbon monoxide. *Journal of Catalysis* **1989,** *115* (2), 301-309.

6. Oetjen, H. F.; Schmidt, V. M.; Stimming, U.; Trila, F., Performance data of a proton exchange membrane fuel cell using H_2/CO as fuel gas. *Journal of the Electrochemical Society* **1996,** *143* (12), 3838-3842.

7. Haruta, M., Size- and support-dependency in the catalysis of gold. *Catalysis Today* **1997,** *36* (1), 153-166.

8. Valden, M.; Lai, X.; Goodman, D. W., Onset of catalytic activity of gold clusters on titania with the appearance of nonmetallic properties. *Science* **1998,** *281* (5383), 1647-1650.

9. Guzman, J.; Gates, B. C., Catalysis by supported gold: Correlation between catalytic activity for CO oxidation and oxidation states of gold. *Journal of the American Chemical Society* **2004,** *126* (9), 2672-2673.

10. Liu, X. Y.; Wang, A. Q.; Zhang, T.; Mou, C. Y., Catalysis by gold: New insights into the support effect. *Nano Today* **2013,** *8* (4), 403-416.

11. Saavedra, J.; Powell, C.; Panthi, B.; Pursell, C. J.; Chandler, B. D., CO oxidation over Au/TiO_2 catalyst: Pretreatment effects, catalyst deactivation, and carbonates production. *Journal of Catalysis* **2013,** *307*, 37-47.

12. Schubert, M. M.; Hackenberg, S.; van Veen, A. C.; Muhler, M.; Plzak, V.; Behm, R. J., CO oxidation over supported gold catalysts-"inert" and "active" support materials and their role for the oxygen supply during reaction. *Journal of Catalysis* **2001,** *197* (1), 113-122.

13. Widmann, D.; Liu, Y.; Schuth, F.; Behm, R. J., Support effects in the Au-catalyzed CO oxidation - Correlation between activity, oxygen storage capacity, and support reducibility. *Journal of Catalysis* **2010,** *276* (2), 292-305.

14. Chen, J. H.; Lin, J. N.; Kang, Y. M.; Yu, W. Y.; Kuo, C. N.; Wan, B. Z., Preparation of nano-gold in zeolites for CO oxidation: Effects of structures and

number of ion exchange sites of zeolites. *Applied Catalysis a-General* **2005,** *291* (1-2), 162-169.

15. Gil, S.; Munoz, L.; Sanchez-Silva, L.; Romero, A.; Valverde, J. L., Synthesis and characterization of Au supported on carbonaceous material-based catalysts for the selective oxidation of glycerol. *Chemical Engineering Journal* **2011,** *172* (1), 418-429.

16. Dhakshinamoorthy, A.; Garcia, H., Catalysis by metal nanoparticles embedded on metal-organic frameworks. *Chemical Society Reviews* **2012,** *41* (15), 5262-5284.

17. Ferey, G., Hybrid porous solids: past, present, future. *Chemical Society Reviews* **2008,** *37* (1), 191-214.

18. Furukawa, H.; Cordova, K. E.; O'Keeffe, M.; Yaghi, O. M., The Chemistry and Applications of Metal-Organic Frameworks. *Science* **2013,** *341* (6149), 974-+.

19. Coudert, F.-X., Responsive Metal–Organic Frameworks and Framework Materials: Under Pressure, Taking the Heat, in the Spotlight, with Friends. *Chemistry of Materials* **2015,** *27* (6), 1905-1916.

20. Khajavi, H.; Stil, H. A.; Kuipers, H.; Gascon, J.; Kapteijn, F., Shape and Transition State Selective Hydrogenations Using Egg-Shell Pt-MIL-101(Cr) Catalyst. *Acs Catalysis* **2013,** *3* (11), 2617-2626.

21. Wu, R.; Qian, X.; Zhou, K.; Liu, H.; Yadian, B.; Wei, J.; Zhu, H.; Huang, Y., Highly dispersed Au nanoparticles immobilized on Zr-based metal-organic frameworks as heterostructured catalyst for CO oxidation. *Journal of Materials Chemistry A* **2013,** *1* (45), 14294-14299.

22. Shen, L.; Wu, W.; Liang, R.; Lin, R.; Wu, L., Highly dispersed palladium nanoparticles anchored on UiO-66(NH_2) metal-organic framework as a reusable and dual functional visible-light-driven photocatalyst. *Nanoscale* **2013,** *5* (19), 9374-9382.

23. Aijaz, A.; Akita, T.; Tsumori, N.; Xu, Q., Metal-Organic Framework-Immobilized Polyhedral Metal Nanocrystals: Reduction at Solid-Gas Interface, Metal Segregation, Core-Shell Structure, and High Catalytic Activity. *Journal of the American Chemical Society* **2013,** *135* (44), 16356-16359.

24. Wang, W. X.; Li, Y. W.; Zhang, R. J.; He, D. H.; Liu, H. L.; Liao, S. J., Metal-organic framework as a host for synthesis of nanoscale Co_3O_4 as an active catalyst for CO oxidation. *Catalysis Communications* **2011,** *12* (10), 875-879.

25. Jiang, H.-L.; Liu, B.; Akita, T.; Haruta, M.; Sakurai, H.; Xu, Q., Au@ZIF-8: CO Oxidation over Gold Nanoparticles Deposited to Metal-Organic Framework. *Journal of the American Chemical Society* **2009,** *131* (32), 11302-+.

26. Ishida, T.; Nagaoka, M.; Akita, T.; Haruta, M., Deposition of Gold Clusters on Porous Coordination Polymers by Solid Grinding and Their Catalytic Activity in Aerobic Oxidation of Alcohols. *Chemistry-a European Journal* **2008,** *14* (28), 8456-8460.

27. Qian, X.; Zhong, Z.; Yadian, B.; Wu, J.; Zhou, K.; Teo, J. S.-k.; Chen, L.; Long, Y.; Huang, Y., Loading MIL-53(Al) with Ag nanoparticles: Synthesis, structural stability and catalytic properties. *International Journal of Hydrogen Energy* **2014,** *39* (26), 14496-14502.

28. Cavka, J. H.; Jakobsen, S.; Olsbye, U.; Guillou, N.; Lamberti, C.; Bordiga, S.; Lillerud, K. P., A new zirconium inorganic building brick forming metal organic frameworks with exceptional stability. *Journal of the American Chemical Society* **2008,** *130* (42), 13850-13851.

29. Schoenecker, P. M.; Carson, C. G.; Jasuja, H.; Flemming, C. J. J.; Walton, K. S., Effect of Water Adsorption on Retention of Structure and Surface Area of Metal-Organic Frameworks. *Industrial & Engineering Chemistry Research* **2012,** *51* (18), 6513-6519.

30. Biswas, S.; Van der Voort, P., A General Strategy for the Synthesis of Functionalised UiO-66 Frameworks: Characterisation, Stability and CO_2 Adsorption Properties. *European Journal of Inorganic Chemistry* **2013,** (12), 2154-2160.

31. Kandiah, M.; Nilsen, M. H.; Usseglio, S.; Jakobsen, S.; Olsbye, U.; Tilset, M.; Larabi, C.; Quadrelli, E. A.; Bonino, F.; Lillerud, K. P., Synthesis and Stability of Tagged UiO-66 Zr-MOFs. *Chemistry of Materials* **2010,** *22* (24), 6632-6640.

32. Comotti, M.; Li, W. C.; Spliethoff, B.; Schuth, F., Support effect in high activity gold catalysts for CO oxidation. *Journal of the American Chemical Society* **2006,** *128* (3), 917-924.

33. Janssens, T. V. W.; Carlsson, A.; Puig-Molina, A.; Clausen, B. S., Relation between nanoscale Au particle structure and activity for CO oxidation on supported gold catalysts. *Journal of Catalysis* **2006,** *240* (2), 108-113.

34. Mamontov, E.; Egami, T.; Brezny, R.; Koranne, M.; Tyagi, S., Lattice defects and oxygen storage capacity of nanocrystalline ceria and ceria-zirconia. *Journal of Physical Chemistry B* **2000,** *104* (47), 11110-11116.

35. Gupta, A.; Waghmare, U. V.; Hegde, M. S., Correlation of Oxygen Storage Capacity and Structural Distortion in Transition-Metal-, Noble-Metal-, and Rare-Earth-Ion-Substituted CeO_2 from First Principles Calculation. *Chemistry of Materials* **2010,** *22* (18), 5184-5198.

36. Zhang, J.; Kumagai, H.; Yamamura, K.; Ohara, S.; Takami, S.; Morikawa, A.; Shinjoh, H.; Kaneko, K.; Adschiri, T.; Suda, A., Extra-Low-Temperature Oxygen Storage Capacity of CeO_2 Nanocrystals with Cubic Facets. *Nano Letters* **2011,** *11* (2), 361-364.

37. Brust, M.; Walker, M.; Bethell, D.; Schiffrin, D. J.; Whyman, R., Synthesis of thiol-derivatised gold nanoparticles in a two-phase Liquid-Liquid system. *Journal of the Chemical Society-Chemical Communications* **1994,** (7), 801-802.

38. Hostetler, M. J.; Templeton, A. C.; Murray, R. W., Dynamics of place-exchange reactions on monolayer-protected gold cluster molecules. *Langmuir* **1999,** *15* (11), 3782-3789.

39. Tulig, K.; Walton, K. S., An alternative UiO-66 synthesis for HCl-sensitive nanoparticle encapsulation. *RSC Advances* **2014,** *4* (93), 51080-51083.

40. Kung, M. C.; Davis, R. J.; Kung, H. H., Understanding Au-catalyzed low-temperature CO oxidation. *Journal of Physical Chemistry C* **2007,** *111* (32), 11767-11775.

41. Overbury, S. H.; Schwartz, V.; Mullins, D. R.; Yan, W.; Dai, S., Evaluation of the Au size effect: CO oxidation catalyzed by Au/TiO_2. *Journal of Catalysis* **2006,** *241* (1), 56-65.

42. Bamwenda, G. R.; Tsubota, S.; Nakamura, T.; Haruta, M., The influence of the preparation methods on the catalytic activity of platinum and gold supported on TiO_2 for CO oxidation. *Catalysis Letters* **1997,** *44* (1-2), 83-87.

43. Schimpf, S.; Lucas, M.; Mohr, C.; Rodemerck, U.; Brückner, A.; Radnik, J.; Hofmeister, H.; Claus, P., Supported gold nanoparticles: in-depth catalyst characterization and application in hydrogenation and oxidation reactions. *Catalysis Today* **2002,** *72* (1–2), 63-78.

44. Hostetler, M. J.; Wingate, J. E.; Zhong, C. J.; Harris, J. E.; Vachet, R. W.; Clark, M. R.; Londono, J. D.; Green, S. J.; Stokes, J. J.; Wignall, G. D.; Glish, G. L.; Porter, M. D.; Evans, N. D.; Murray, R. W., Alkanethiolate gold cluster molecules with core diameters from 1.5 to 5.2 nm: Core and monolayer properties as a function of core size. *Langmuir* **1998,** *14* (1), 17-30.

45. Boccuzzi, F.; Chiorino, A.; Manzoli, M.; Lu, P.; Akita, T.; Ichikawa, S.; Haruta, M., Au/TiO_2 nanosized samples: A catalytic, TEM, and FTIR study of the effect

of calcination temperature on the CO oxidation. *Journal of Catalysis* **2001,** *202* (2), 256-267.

46. Neri, G.; Visco, A. M.; Galvagno, S.; Donato, A.; Panzalorto, M., Au iron oxide catalysts: temperature programmed reduction and X-ray diffraction characterization. *Thermochimica Acta* **1999,** *329* (1), 39-46.

47. Kang, Y. M.; Wan, B. Z., Gold and iron supported on Y-type zeolite for carbon monoxide oxidation. *Catalysis Today* **1997,** *35* (4), 379-392.

48. Zhang, C. B.; He, H.; Tanaka, K., Catalytic performance and mechanism of a Pt/TiO_2 catalyst for the oxidation of formaldehyde at room temperature. *Applied Catalysis B-Environmental* **2006,** *65* (1-2), 37-43.

49. Kotobuki, M.; Leppelt, R.; Hansgen, D. A.; Widmann, D.; Behm, R. J., Reactive oxygen on a Au/TiO_2 supported catalyst. *Journal of Catalysis* **2009,** *264* (1), 67-76.

50. Wang, Y.-G.; Yoon, Y.; Glezakou, V.-A.; Li, J.; Rousseau, R., The Role of Reducible Oxide–Metal Cluster Charge Transfer in Catalytic Processes: New Insights on the Catalytic Mechanism of CO Oxidation on Au/TiO_2 from ab Initio Molecular Dynamics. *Journal of the American Chemical Society* **2013,** *135* (29), 10673-10683.

51. Yoon, B.; Häkkinen, H.; Landman, U.; Wörz, A. S.; Antonietti, J.-M.; Abbet, S.; Judai, K.; Heiz, U., Charging Effects on Bonding and Catalyzed Oxidation of CO on Au_8 Clusters on MgO. *Science* **2005,** *307* (5708), 403-407.

52. Maciejewski, M.; Fabrizioli, P.; Grunwaldt, J. D.; Beckert, O. S.; Baiker, A., Supported gold catalysts for CO oxidation: Effect of calcination on structure, adsorption and catalytic behaviour. *Physical Chemistry Chemical Physics* **2001,** *3* (17), 3846-3855.

53. Konova, P.; Naydenov, A.; Tabakova, T.; Mehandjiev, D., Deactivation of nanosize gold supported on zirconia in CO oxidation. *Catalysis Communications* **2004,** *5* (9), 537-542.

54. Valenzano, L.; Civalleri, B.; Chavan, S.; Bordiga, S.; Nilsen, M. H.; Jakobsen, S.; Lillerud, K. P.; Lamberti, C., Disclosing the Complex Structure of UiO-66 Metal Organic Framework: A Synergic Combination of Experiment and Theory. *Chemistry of Materials* **2011,** *23* (7), 1700-1718.

55. Paier, J.; Penschke, C.; Sauer, J., Oxygen Defects and Surface Chemistry of Ceria: Quantum Chemical Studies Compared to Experiment. *Chemical Reviews* **2013,** *113* (6), 3949-3985.

56. Vermoortele, F.; Bueken, B.; Le Bars, G.; Van de Voorde, B.; Vandichel, M.; Houthoofd, K.; Vimont, A.; Daturi, M.; Waroquier, M.; Van Speybroeck, V.; Kirschhock, C.; De Vos, D. E., Synthesis Modulation as a Tool To Increase the Catalytic Activity of Metal-Organic Frameworks: The Unique Case of UiO-66(Zr). *Journal of the American Chemical Society* **2013,** *135* (31), 11465-11468.

57. Cmarik, G. E.; Kim, M.; Cohen, S. M.; Walton, K. S., Tuning the Adsorption Properties of UiO-66 via Ligand Functionalization. *Langmuir* **2012,** *28* (44), 15606-15613.

58. Remediakis, I. N.; Lopez, N.; Norskov, J. K., CO oxidation on gold nanoparticles: Theoretical studies. *Applied Catalysis a-General* **2005,** *291* (1-2), 13-20.

59. Widmann, D.; Behm, R. J., Active Oxygen on a Au/TiO_2 Catalyst: Formation, Stability, and CO Oxidation Activity. *Angewandte Chemie-International Edition* **2011,** *50* (43), 10241-10245.

60. Kim, H. Y.; Lee, H. M.; Henkelman, G., CO Oxidation Mechanism on CeO_2-Supported Au Nanoparticles. *Journal of the American Chemical Society* **2012,** *134* (3), 1560-1570.

61. Molina, L. M.; Rasmussen, M. D.; Hammer, B., Adsorption of O_2 and oxidation of CO at Au nanoparticles supported by TiO_2(110). *Journal of Chemical Physics* **2004,** *120* (16), 7673-7680.

62. Bartholomew, C. H., Mechanisms of catalyst deactivation. *Applied Catalysis a-General* **2001,** *212* (1-2), 17-60.

63. Konova, P.; Naydenov, A.; Venkov, C.; Mehandjiev, D.; Andreeva, D.; Tabakova, T., Activity and deactivation of Au/TiO_2 catalyst in CO oxidation. *Journal of Molecular Catalysis a-Chemical* **2004,** *213* (2), 235-240.

64. Schubert, M. M.; Plzak, V.; Garche, J.; Behm, R. J., Activity, selectivity, and long-term stability of different metal oxide supported gold catalysts for the preferential CO oxidation in H_2-rich gas. *Catalysis Letters* **2001,** *76* (3-4), 143-150.

CHAPTER 5

EVALUATING THE EFFECT OF PREPARATION METHOD ON AU@UIO-66 PROPERTIES

5.1 Introduction

Metal-organic frameworks (MOFs) are nanoporous, crystalline materials composed of metal or metal oxide nodes linked by organic moieties. MOFs offer numerous advantages such as high surface areas and pore volumes, uniform pore size distributions, structural diversity, and chemical tunabilty; properties that make them promising materials for applications such as gas storage and separation, drug delivery, imaging, air purification, and catalysis.[1, 2] Unfortunately, many promising MOFs degrade when exposed to humid conditions considerably limiting the applicability. However, there are other MOFs that have been shown to be stable in humid environments.[3] Often these water stable MOFs are limited by a low density of active sorption sites. Fortunately, the active site density can be increased by doping MOFs with metal nanoparticles, subsequently enhancing the sorptive and catalytic capabilities.[4]

There are two techniques for incorporating metal nanoparticles in microporous materials designated in this work as impregnation and encapsulation. Impregnation describes the diffusion of a metal precursor into the pores of a preformed MOF followed by the reduction, oxidation, or decomposition of the metal, forming nanoparticles within the pores. Theoretically, nanoparticle growth is quenched by the pores producing a composite with randomly distributed nanoparticles the size and shape of the MOF pores. This potential control of the nanoparticle size and shape, based on the support, is a

notable advantage of the impregnation technique. There are several methods for introducing the metal precursor into the MOF pore space: solution impregnation, incipient wetness impregnation, the double solvents method, chemical vapor deposition (CVD), and solid grinding. In addition, metal nanoparticle formation has been achieved via various reduction techniques: in solution with chemical reducing agents such as sodium borohydride or hydrazine, under hydrogen flow, by UV and microwave irradiation, and the autoreduction of the metal by the MOF.[5-12] Alternatively, encapsulation specifies the formation of the MOF around preformed nanoparticles; the nanoparticles are added to the MOF mother solution, and the MOF crystallizes around the particles. The most prominent advantage of encapsulation is the ability to design the nanomaterial that is coupled with the MOF support. The nanomaterial size and shape are not limited by the MOF pores which allows for the incorporation of nanomaterials exceeding the MOF pore size.[13] There have been several investigations probing the effects of the various impregnation methods;[14, 15] however, there is a dearth of analysis comparing impregnation and encapsulation for incorporating metal nanoparticles.

UiO-66 is a zirconium-based MOF with $Zr_6O_4(OH)_4$ nodes connected via 1,4-benzenedicarboxylic acid (BDC). Its significant application potential arises from its thermal stability up to 813K; mechanical, acid, and base resistance; stability in humid environments; and straightforward chemical tunability.[16-19] In addition, UiO-66 and its analogues have previously been supplemented with metal nanoparticles via both impregnation and encapsulation techniques.[5, 20-23] Gold nanoparticles (AuNPs) are ideal for doping MOFs because they are well studied and known for pinpoint synthetic control, unusual chemical properties, and unprecedented catalytic capabilities.[24-26] Moreover,

supported AuNPs are well developed as catalysts for CO oxidation. For instance, Au@UiO-66 and Au@ZIF-8 demonstrate improved catalytic capabilities compared to the parent materials.[20, 27] AuNPs deposited on metal oxides have also been extensively probed. These investigations discovered several controlling factors, namely the AuNP diameter and oxidation state, the type of support, the preparation method, and the activation conditions.[28-34] Herein, Au@UiO-66 composites are prepared via impregnation and encapsulation, and the physical and catalytic properties are evaluated.

5.2 Experimental Methods

5.2.1 Material Synthesis

All chemicals were obtained commercially (Sigma Aldrich, VWR, and Fisher Scientific) and used without further purification. AuNPs of varying diameters, capped with a mixture of 1-dodecanethiol (DDT) and 11-mercaptoundecanoic acid (MUA) were prepared in two-steps: (1) the synthesis of DDT capped AuNPs, then (2) a ligand exchange between DDT on the AuNP surface with MUA. AuNPs with a diameter of 2.4 nm were prepared using a previously reported procedure.[35] Briefly, a solution of gold(III) chloride trihydrate ($HAuCl_4 \cdot 3H_2O$) (0.314 mmol) in water (20 mL) was combined with a solution of tetraoctylammonium bromide (0.728 mmol) in toluene (40 mL) and stirred for 30 min. Then, DDT (0.314 mmol) was added and the mixture was stirred for an additional 30 min. Finally, sodium borohydride ($NaBH_4$) (3.14 mmol) in water (10 mL) was added and rigorously stirred for 3 h. The product was washed with copious amounts of de-ionized water, the organic phase was separated, and the AuNPs were precipitated from solution with methanol. MUA was added to the AuNPs' surface by stirring AuNP-

DDT (3 mg/mL) and MUA (0.154 mmol) in toluene for 72 h and washing the resulting AuNPs with toluene.[36] The AuNPs with diameters of 4.5 and 10.9 nm were prepared similarly. A solution of $HAuCl_4 \cdot 3H_2O$ (0.314 mmol) in water (20 mL) was mixed with tetraoctylammonium bromide (0.728 mmol) in toluene (40 mL) for 30 min. Next, $NaBH_4$ (3.14 mmol) in water (10 mL) was added and the mixture was stirred for 3 h. Then, DDT (3.14 mmol) was added and the solution was stirred for 72 h and washed with de-ionized water and methanol. Finally, MUA (0.179 mmol) was added to AuNP-DDT (3 mg/mL) suspended in toluene, stirred for 72 h, and washed with toluene. These AuNPs are separated into two diameter groups by centrifuging the AuNPs from methanol.

All UiO-66 samples herein were prepared by stirring zirconium(IV) propoxide (Zr(O*n*Pr)) (0.227 mmol), 1,4-benzenedicarboxylic acid (BDC) (0.454 mmol), methanol (86.5 mmol), N,N'-dimethylformamide (DMF) (45.4 mmol), and glacial acetic acid (6.81 mmol) in a glass scintillation vial at 393 K for 24 h in a silicone oil bath. The product was filtered and washed three times with DMF and three times with methanol. Au@UiO-66(ENC) was prepared by adding various concentrations of AuNPs to the UiO-66 mother solution. The mixture was stirred in a glass scintillation vial at 393 K for 24 h in a silicone oil bath, and the product was filtered and washed three times with DMF and three times with methanol.[23] Au@UiO-66(IMP) was synthesized as previously reported.[5] Approximately, 170 mg of UiO-66 was degassed at 473 K under vacuum overnight. The activated UiO-66 was stirred in a solution of gold(III) chloride trihydrate (0.018 mmol) in methanol (40 mL) for 6 h. Then, $NaBH_4$ (0.178 mmol) was added to the slurry and stirred for an additional 1 h. Finally, the product was filtered and rinsed with methanol. The composites prepared by colloidal mixing, denoted throughout this work as Au on UiO-66,

were prepared by sonicating 40-50 mg of UiO-66, synthesized as previously described, in methanol (9.9 mL) for 5 min. Then, varying amounts of AuNPs were added, and the mixture was stirred at room temperature for 24 h.

5.2.2 Characterization

Proton nuclear magnetic resonance (^{1}H NMR) spectroscopy was measured on a Varian Mercury Vx 300. The samples were prepared by suspending approximately 10 mg of AuNPs in 1 mL of dimethyl sulfoxide-d_6. ^{1}H NMR data were used to determine the composition of the organic monolayer on the AuNPs. Thermogravimetric analysis (TGA) data were obtained using the Netzsch STA 449 Jupiter Simultaneous TG-DSC apparatus. Approximately 5 mg of AuNP were dropped into an Al_2O_3 crucible and ramped at 1 K/min to 1000 K under helium or air flow at 20 mL/min to determine the degradation temperature of the organic layer.

Powder X-ray diffraction (PXRD) patterns were obtained using a PANalytical X-ray diffractometer. Approximately 10 mg of sample were deposited on a low background silica sample holder and scanned from 5-50°. A Quantachrome Quadrasorb Evo volumetric analyzer collected nitrogen sorption data at 77 K. The isotherms were measured over a relative pressure (P/P_0) range of 0.001-0.990 with high purity nitrogen (Airgas 99.998%). Prior to the measurement, the samples were heated at 473 K overnight under vacuum using a Quantachrome FloVac Degasser. The specific surface areas were calculated using the Brunauer, Emmett, and Teller (BET) Theory using $0.005 \leq P/P_0 \leq 0.03$, and the total pore volume was calculated at $P/P_0 = 0.6$. Inductively coupled plasma

(ICP) emission spectroscopy data were obtained using the Perkin Elmer Optima 3000 DV ICP Emission Spectrometer.

Transmission electron microscopy (TEM) images were acquired using the Hitachi HT7700 operated at 120 keV and scanning transmission electron microscopy (STEM) tomography was performed using the FEI Tecnai F30 run at 300 keV. For the STEM tomography experiment, the sample was rotated from -70-60° and images were acquired every 2°. The FEI Tecnai F30 is supported by funding DMR 0922776. The samples were prepared by suspending less than 1 mg of sample in methanol and dropcasting it on a lacy carbon copper grid.

Temperature programmed reduction (H_2-TPR) was performed using the Micromeritics AutoChem II 2920. Prior to each H_2-TPR experiment, the sample underwent a 1 h water bakeoff under He flow at 473K, a 2 h calcination under 10% O_2 in helium at 523K, and a 30 min helium purge. Finally, H_2-TPR measurement ramped the temperature from 323 K to 1073 K (673 K for UiO-66) at 5 K/min under 10% H_2 in helium flow. The static oxygen storage capacity (OSC) was measured in a lab-built packed-bed reactor. The sample was purged with nitrogen at 473 K overnight, calcined in air at 523 K for 2 h, purged with nitrogen for 30 min at 523 K, and finally 1% CO in nitrogen was run through the sample bed at a total flow rate of 40 mL/min. The static OSC was calculated by integrating the CO_2 curve from 0-45 min.

5.2.3 CO Oxidation

CO oxidation experiments were run in a packed bed reactor with the outlet connected to a Hiden DSMS. Approximately 25-40 mg of material were packed into the

sample cell balanced with glass wool to minimize the pressure drop. Prior to the oxidation experiment, the sample was purged with helium at 473 K overnight to remove the solvent from the pores, then calcined in air at 523 K for 2 h to remove the capping ligands on the AuNPs. The sample was cooled to the desired reaction temperature under air flow, then 1% CO in air was passed through the sample at a total flow rate of 40 mL/min.

5.3 Results and Discussion

5.3.1 Characterization

AuNP and UiO-66 composites were prepared using three methods: encapsulation, impregnation, and colloidal mixing, denoted Au@UiO-66(ENC), Au@UiO-66(IMP), and Au on UiO-66, respectively. For Au@UiO-66(ENC) and Au on UiO-66, preformed AuNPs are necessary. Four batches of AuNPs were prepared as previously reported:[35-37] AuNPs 1.8 nm in diameter were used for encapsulation and AuNPs 2.0, 4.2, and 10.9 nm were used for colloidal deposition. Figure 5.1 depicts the TEM images of the preformed AuNPs used to prepare Au@UiO-66(ENC), 2.7 nm Au on UiO-66, 4.9 nm Au on UiO-66, and 7.2 nm Au on UiO-66. In addition, Table 5.1 reports the average AuNP diameter calculated from at least 10 TEM images. The ^{1}H NMR spectra in Figure 5.2 confirm that there is a mixed monolayer on the AuNP surface. In Figure 5.2, the broad peaks are characteristic of ligands bound to a surface. The T_2 relaxation time accelerates when an organic is bound to a surface.[37] Therefore, the lack of coupling suggests that all of the ligands are bound to the AuNP surface. Additionally, the composition of the monolayer is confirmed by analyzing the characteristic peak positions. DDT has a unique peak at 0.84

ppm associated with $–CH_3$, and MUA has a characteristic peak at 2.13 ppm for $–CH_2COOH$. Lastly, the TGA data in Figure 5.3 show that the DDT and MUA is removed from the AuNP surface starting at temperatures less than 523 K under both helium and air flow.

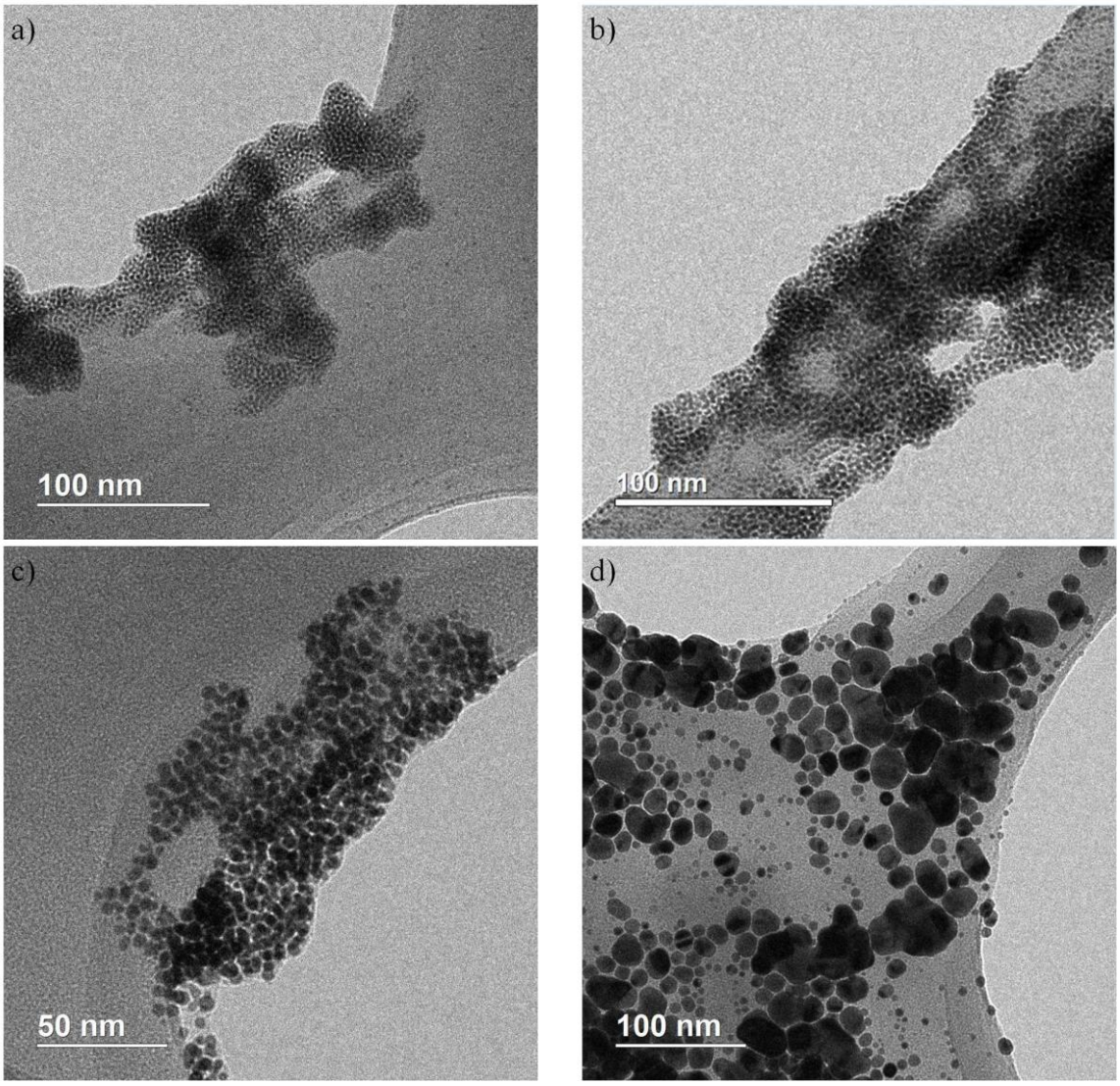

Figure 5.1: TEM images of the preformed AuNPs used to prepare (a) Au@UiO-66(ENC); (b) 2.7 nm Au on UiO-66; (c) 4.9 nm Au on UiO-66; (d) 7.2 nm Au on UiO-66

Table 5.1: Preformed AuNPs

Composite	d_{AuNP} Preformed AuNPs (nm)
8.2 nm Au@UiO-66(ENC)	1.8±0.4
2.7 nm Au on UiO-66	2.0±0.4
4.9 nm Au on UiO-66	4.2±0.9
7.2 nm Au on UiO-66	10.9±5.5

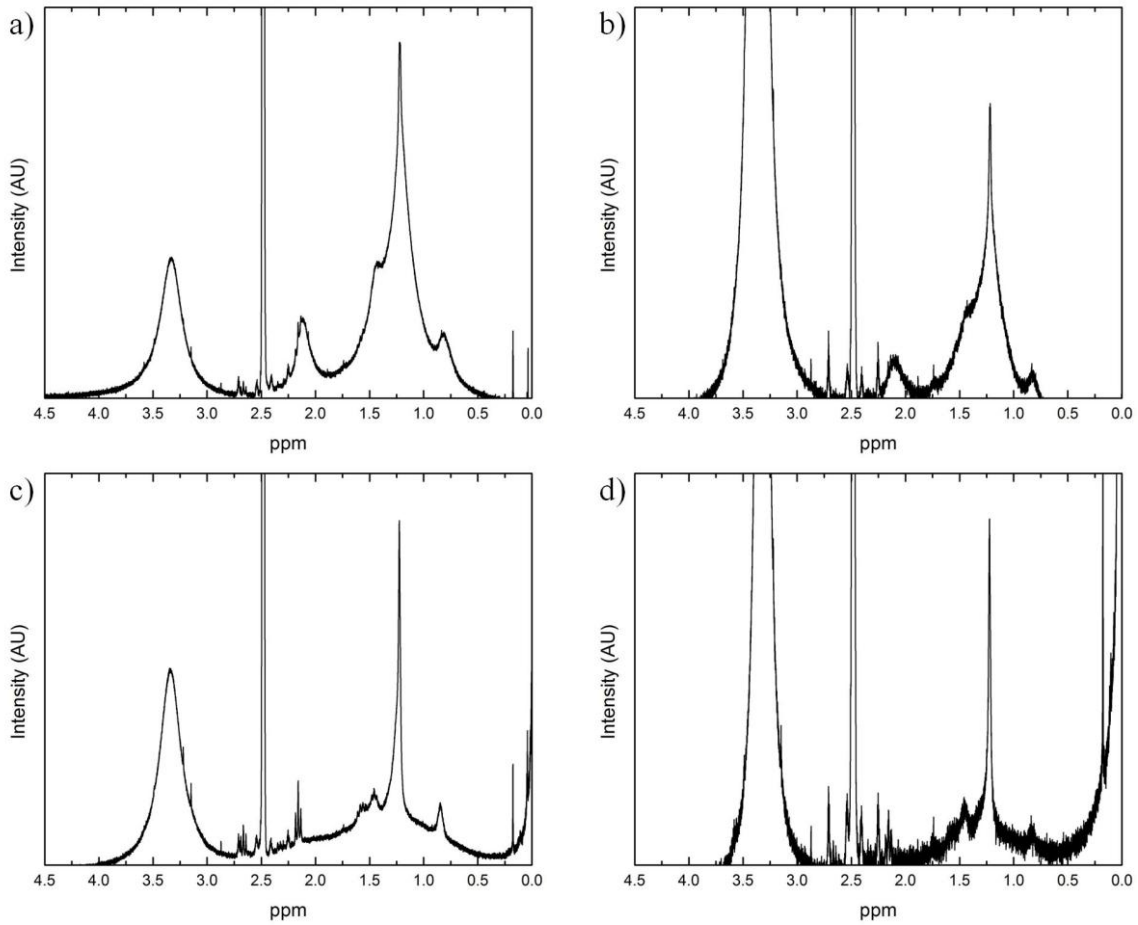

Figure 5.2: ^{1}H NMR spectra of (a) 1.8 nm, (b) 2.0 nm, (c) 4.2 nm, and (d) 10.9 nm AuNP-DDT/MUA

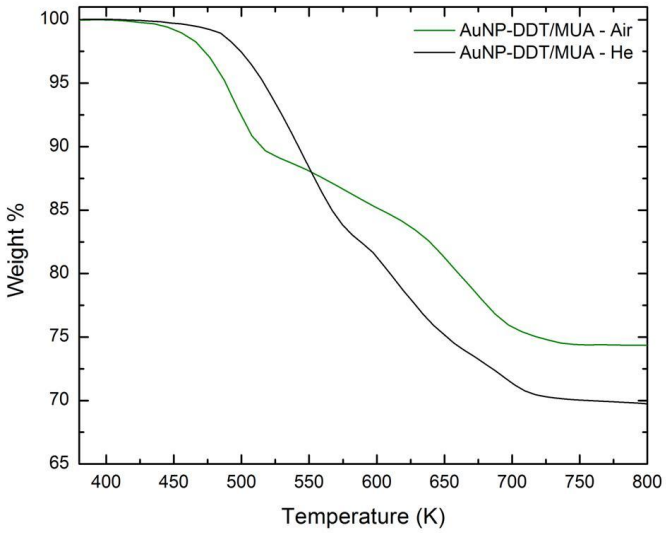

Figure 5.3: TGA curves of AuNP-DDT/MUA under helium flow and air flow

Figure 5.4 depicts the PXRD patterns for Au@UiO-66(ENC), Au@UiO-66(IMP), and Au on UiO-66. The UiO-66 structure is obtained for all of the composites and is retained after CO oxidation at temperatures ranging from 298-523K. Retention of the UiO-66 structure after CO oxidation proves that UiO-66 is stable for catalysis at elevated temperatures under reducing conditions. The stability also suggests that the catalytically active materials are AuNP and UiO-66 composites, instead of AuNP and ZrO_2, formed during the degradation of UiO-66. Additionally, Table 5.2 shows that the porosities for the composites are similar and comparable to parent UiO-66.[23]

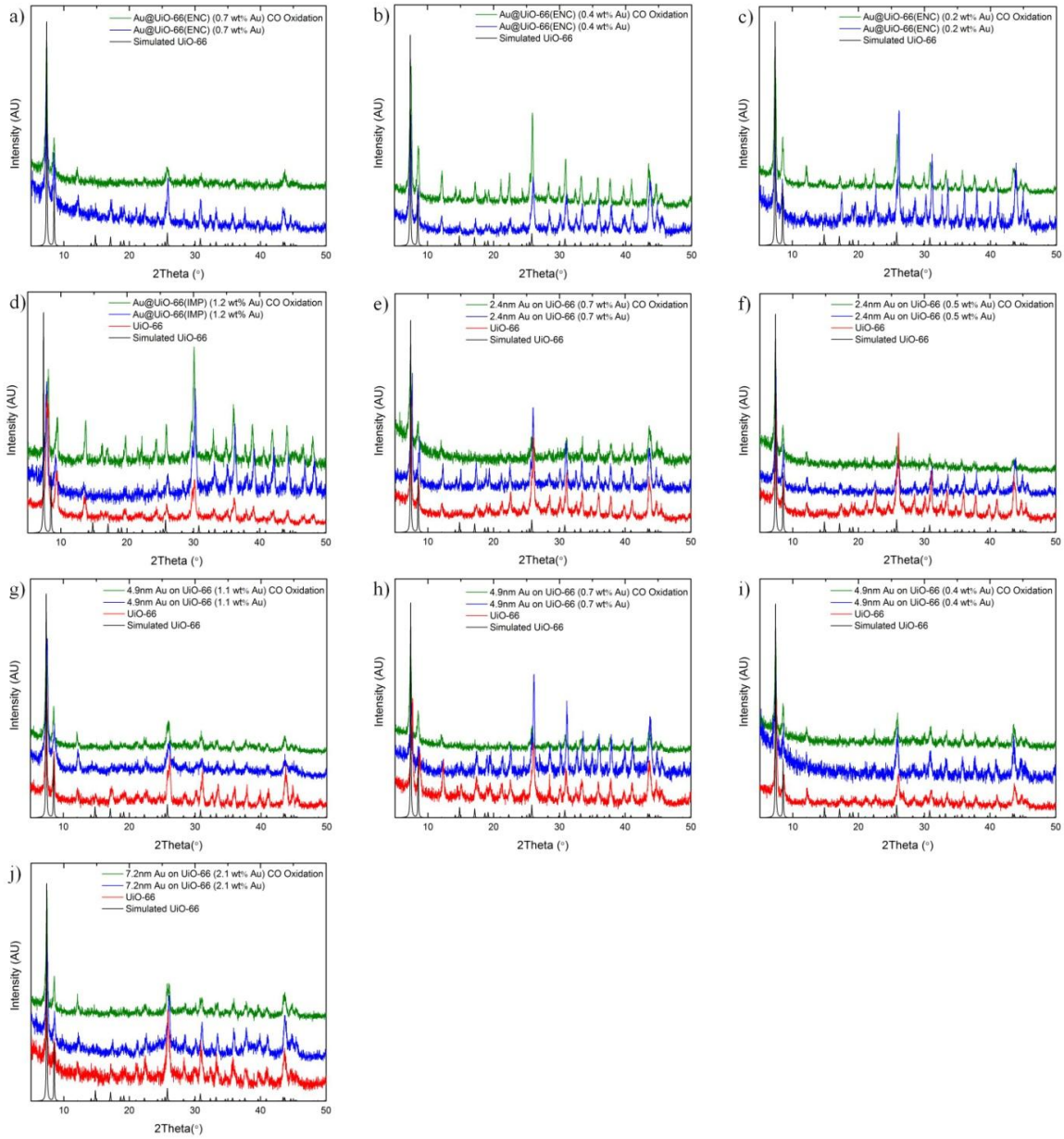

Figure 5.4: PXRD patterns for (a,b,c) Au@UiO-66(ENC); (d) Au@UiO-66(IMP); (e,f) 2.4 nm Au on UiO-66; (g,h,i) 4.9 nm Au on UiO-66; and (j) 7.2 nm Au on UiO-66

Table 5.2: Characterization of Au@UiO-66and Au on UiO-66 composites

Material	Au wt %	BET Surface Area (m^2/g)	Total Pore Volume[a] (cm^3/g)	As-synthesized AuNP Diameter (nm)	After AuNP Diameter[b] (nm)
UiO-66[23]	-----	1155	0.56	-----	-----
Au@UiO-66(ENC)	0.7	1142	0.46	8.2±3.1	10.0±4.0
	0.4	1091	0.44	8.4±3.7	8.9±4.2
	0.2	1098	0.44	9.1±5.0	8.7±3.9
Au@UiO-66(IMP)	1.2	1001	0.41	5.4±2.8	5.9±3.1
2.4 nm Au on UiO-66	0.7	986	0.41	2.4±0.7	4.8±2.2
	0.5	1091	0.45	2.3±0.8	4.1±1.6
4.9 nm Au on UiO-66	1.1	1139	0.48	4.9±2.3	7.1±2.7
	0.7	1135	0.48	4.9±1.8	5.5±2.5
	0.4	1152	0.48	4.5±1.9	5.8±2.6
7.2 nm Au on UiO-66	2.1	1135	0.48	7.2±3.9	7.9±4.4

[a]Measured at $P/P_0 = 0.6$; [b]After CO oxidation at 523K

Figure 5.5 presents TEM images of as-synthesized Au@UiO-66(ENC) and Au@UiO-66(IMP), and Table 5.2 reports the average AuNP diameter of the materials before and after CO oxidation at 523K. TEM images of materials before and after CO oxidation are depicted in Figures 5.6 and 5.7. The AuNP diameter after CO oxidation at 523 K is representative for all temperatures because AuNP sintering occurs more readily at higher temperatures.[38] Figures 5.6 and 5.7 and Table 5.2 show that there is AuNP growth after CO oxidation at 523 K for all of the composites; however, the AuNP growth is similar for all of the materials (1-2 nm), so trends dependent on AuNP diameter can still be evaluated.

In addition, TEM suggests that both the impregnation and encapsulation techniques used in this work are not optimized for two key reasons: (1) there are several distinctly surface AuNPs observed, revealing that the AuNPs are not completely confined within the UiO-66 particles and (2) the AuNPs are larger than expected for both

preparation techniques. The impregnation technique is utilized to control the nanoparticle size and shape; theoretically, nanoparticle growth is quenched by the pores yielding particles the size and shape of the pores. Therefore, the AuNPs should be approximately 6 Å in diameter to match the UiO-66 pores; however, the AuNPs formed herein via impregnation in UiO-66 are approximately 4.9 nm in diameter. This suggests that the AuNPs are deposited either (1) within the pores causing significant structural deformation during growth, which is not observed in PXRD, or (2) on the outer surface of the UiO-66 particles. Additionally, during encapsulation, the AuNPs grew from 1.8 nm to 8.2 nm in diameter, which indicates that the encapsulation procedure must be tuned to control aggregation to utilize the full extent of the technique. However, the key advantage of encapsulation is the potential to incorporate nanomaterials larger than the pores within the MOF particles. Therefore, many of the AuNPs scattered through UiO-66 can be either on the surface or incorporated in the UiO-66 particles. Based on TEM, neither technique completely confined AuNPs within UiO-66; however, it is possible that there are AuNPs partially embedded. Therefore, further characterization and catalytic studies were performed to establish the potential of both preparation techniques.

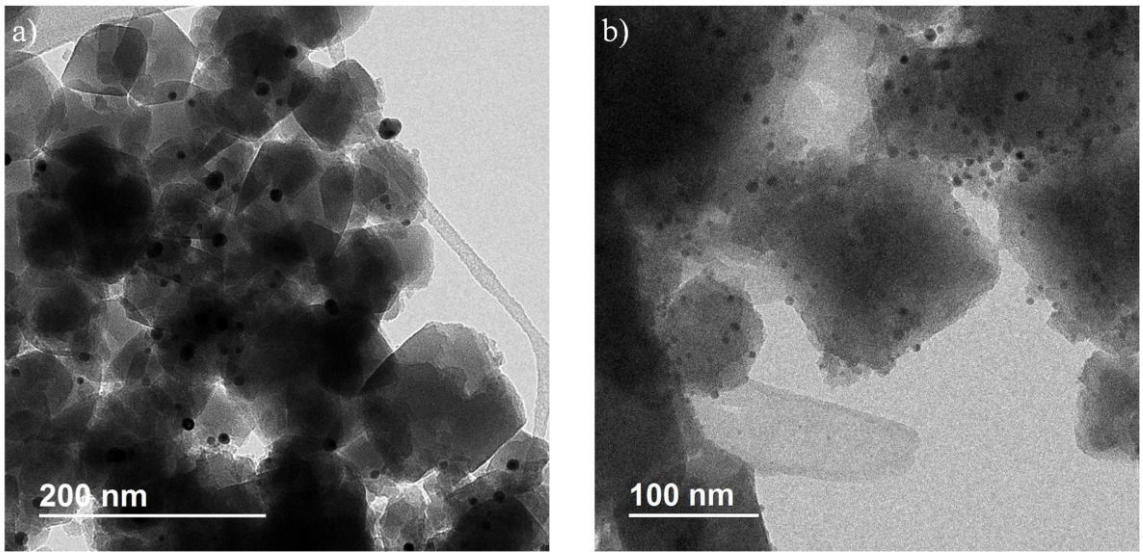

Figure 5.5: TEM images of as-synthesized (a) Au@UiO-66(ENC) (0.7 wt% Au) and (b) Au@UiO-66(IMP) (1.2 wt% Au)

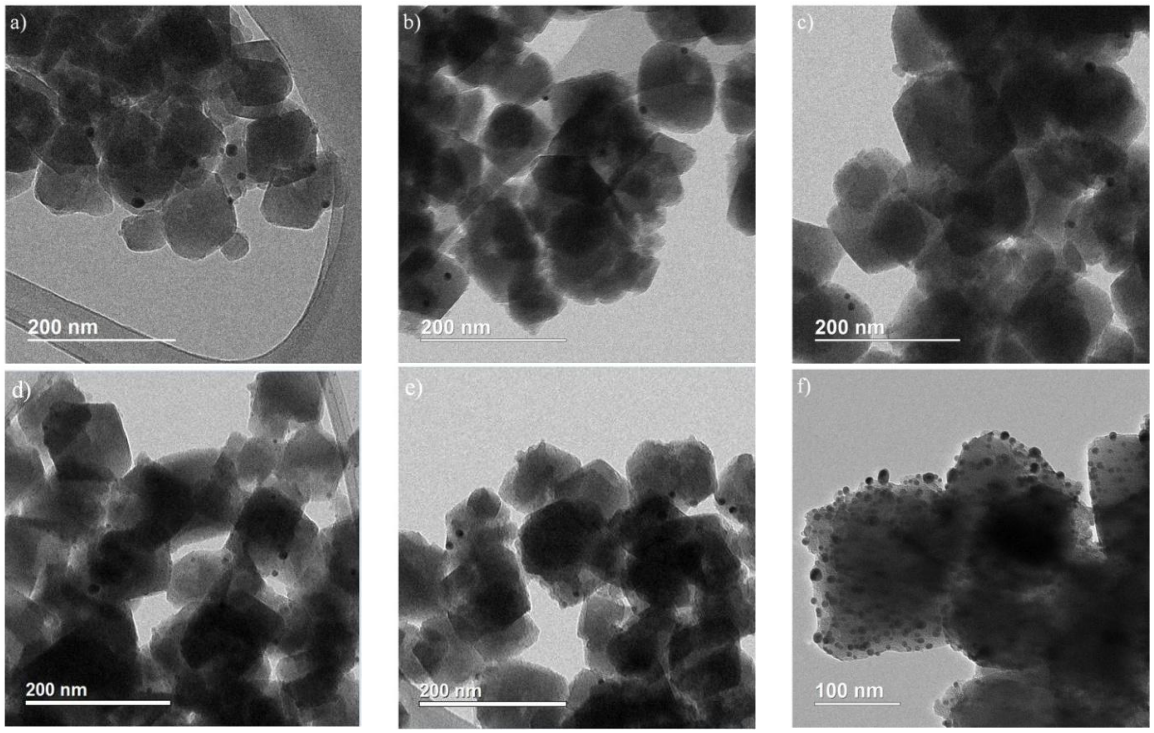

Figure 5.6: TEM images for Au@UiO-66(ENC) (a) 0.7 wt % Au after CO oxidation at 523K, (b) 0.4 wt % Au as-synthesized, (c) 0.4 wt % Au after CO oxidation at 523K, (d) 0.2 wt % Au as-synthesized, and (e) 0.2 wt % Au after CO oxidation at 523K; and (f) Au@UiO-66(IMP) (1.2 wt % Au) after CO oxidation at 523K

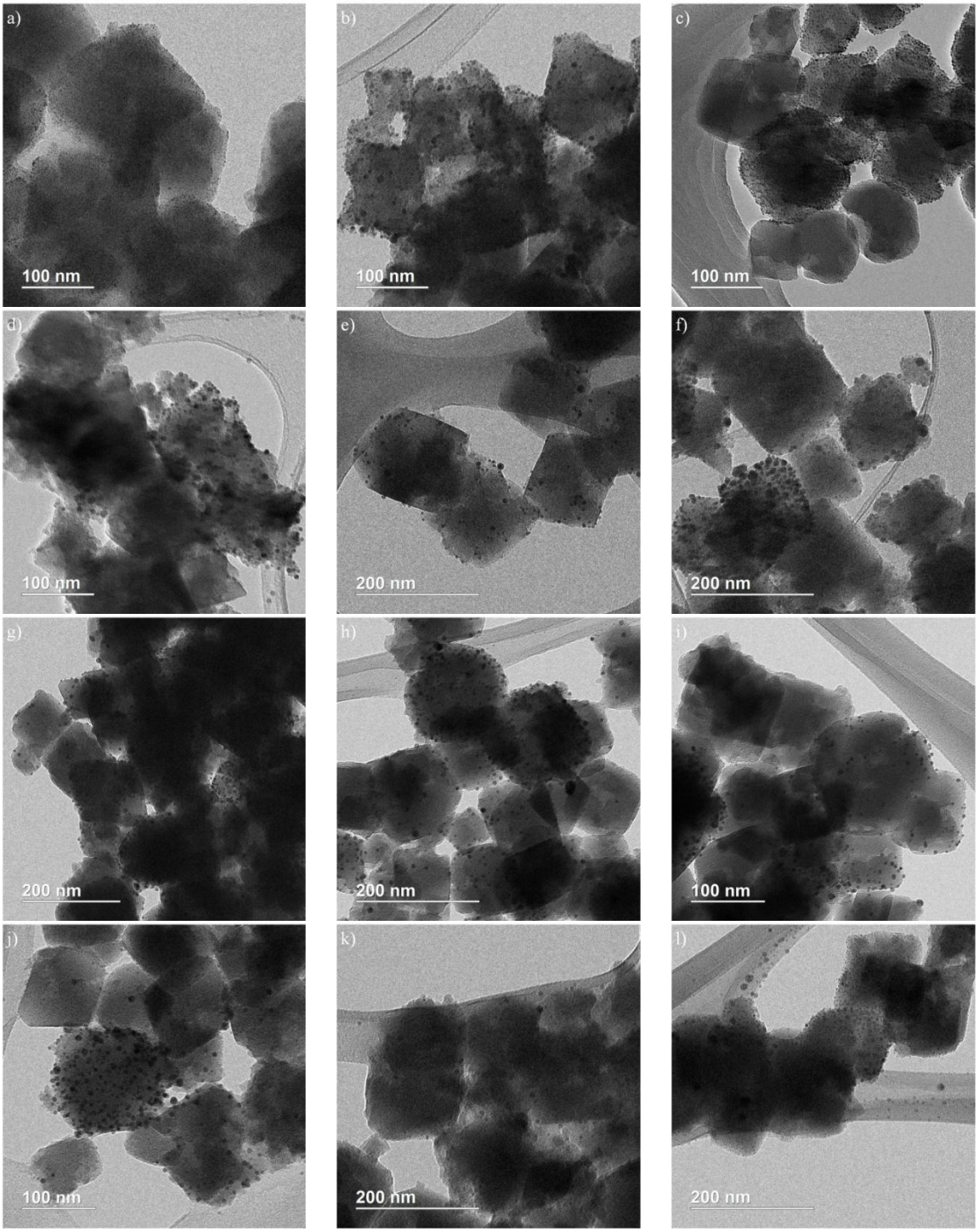

Figure 5.7: TEM images for 2.4 nm Au on UiO-66 (a) 0.7 wt % Au as-synthesized; (b) 0.7 wt % Au after CO oxidation at 523K; (c) 0.5 wt % Au as-synthesized; (d) 0.5 wt % Au after CO oxidation at 523K; 4.9 nm Au on UiO-66 (e) 1.1 wt % Au as-synthesized; (f) 1.1 wt % Au after CO oxidation at 523K; (g) 0.7 wt % Au as-synthesized; (h) 0.7 wt % Au after CO oxidation at 523K; (i) 0.4 wt % Au as-synthesized; and (j) 0.4 wt % Au after CO oxidation at 523K; and 7.2 nm Au on UiO-66 (k) 2.1 wt % Au as-synthesized and (l) 2.1 wt % Au after CO oxidation at 523K

To further probe the AuNP location, STEM tomography was performed on Au@UiO-66(ENC). Figure 5.8 shows several frames at various angles of rotation with AuNPs scattered throughout the UiO-66 particles. Many AuNPs are deposited on the surface of UiO-66. However, the two highlighted AuNPs, designated with red circles and orange hexagons, appear consistently encased in the MOF support upon rotation, which suggests that those AuNPs are confined either within UiO-66 or the UiO-66 cluster, as illustrated in Figure 5.9. The AuNP in Figure 5.8c highlighted by the blue box, demonstrates the latter. Although the AuNP highlighted in blue is definitely a surface-based particle, the degree of contact between the AuNP and support is increased, which subsequently enhances the number of AuNP-support interface sites. However, additional experiments are necessary to determine the AuNP location effects. In addition, CO oxidation was used as a probe to investigate the potential synergistic effects introduced by the various preparation methods.

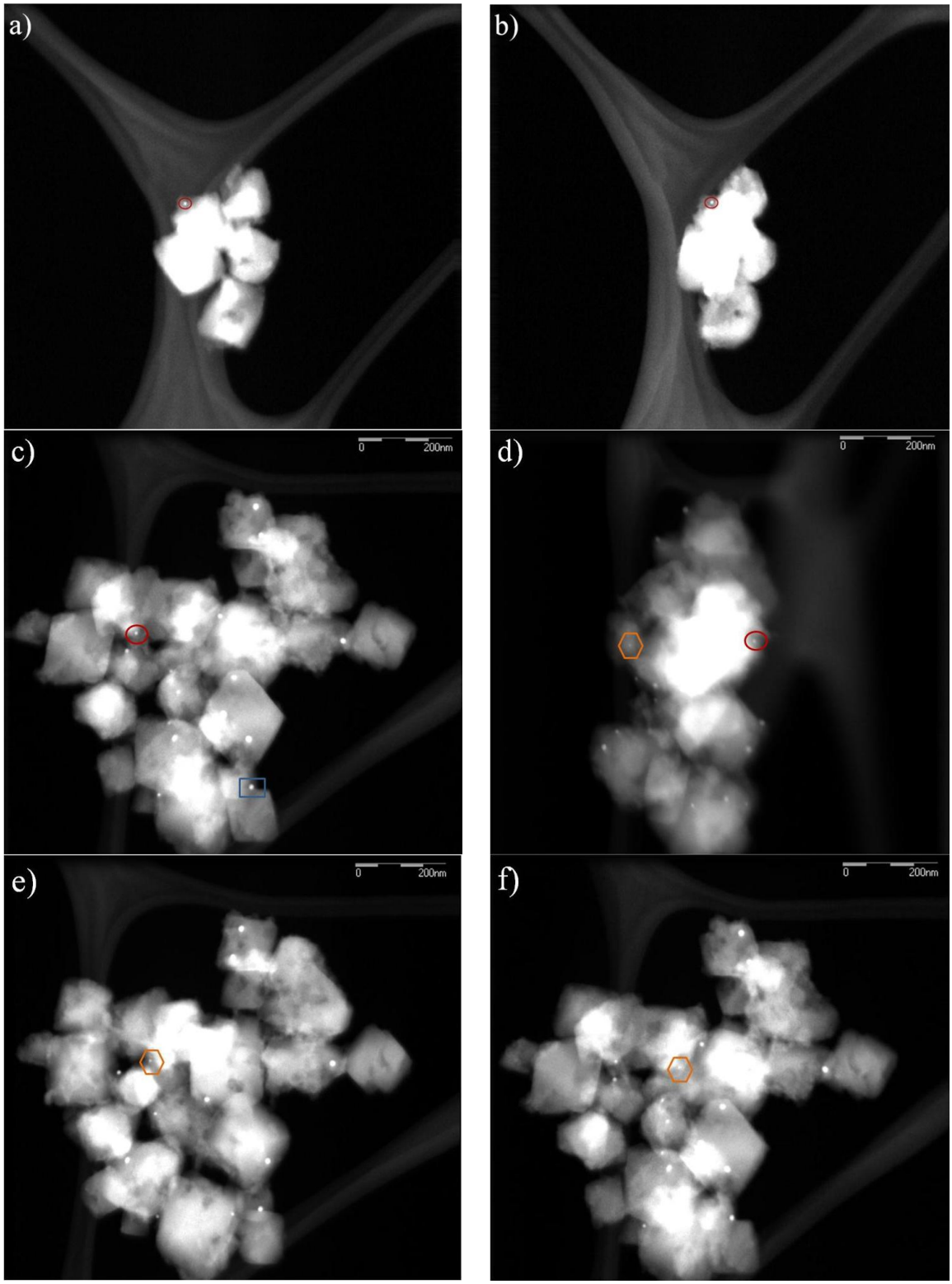

Figure 5.8: STEM images at various angles of rotation during STEM tomography measurements

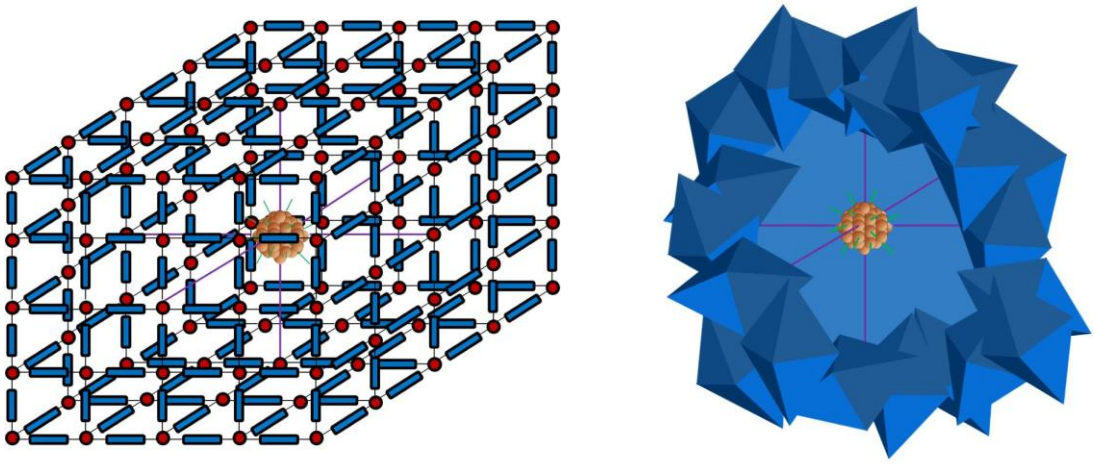

Figure 5.9: Illustration of an AuNP confined within a single UiO-66 particle as a part of the structure (left) and an AuNP encased in an aggregation of UiO-66 particles (right)

Previous studies have reported a significant effect of the AuNP oxidation state on the catalytic activity of supported AuNPs for CO oxidation.[30, 39] Therefore, H_2-TPR was performed on 2.4 nm Au on UiO-66, Au@UiO-66(ENC), and Au@UiO-66(IMP) to determine the AuNP oxidation state and redox capabilities of the materials. Figure 5.10a depicts the H_2-TPR curves after calcination in 10% O_2 in helium at 523 K for 2 h for the samples prepared via various methods. The absence of peaks ranging from 373-398 K suggests that the AuNPs are in the reduced form.[40, 41] In addition, the absence of peaks throughout the entire scan for parent UiO-66 and the UiO-66 composites suggests that the AuNPs do not significantly interact with the support in order to facilitate dissociative H_2 adsorption and spillover, which would promote the reduction of surface oxygen from the support at reduced temperatures. Figure 5.10b reports the H_2-TPR curves for Au@UiO-66(ENC) after calcination in 10% O_2 in helium for 2 h at 448 K and 523 K. Calcination in air at elevated temperatures is a typical pretreatment technique for AuNPs, and the specific calcination temperature affects the oxidation state of the AuNPs. This effect can occur via two potential paths: (1) the onset of Au oxidation at 573 K under air flow or (2)

the conversion of cationic, Au^{3+} or Au^{+}, to metallic, Au^{0}, gold at elevated temperatures under air flow.[39, 42, 43] Figure 5.10b also reveals an absence of peaks ranging from 373-398 K for calcination at 448 K and 523 K suggesting that the calcination temperature has no effect on the AuNP oxidation state in this work.

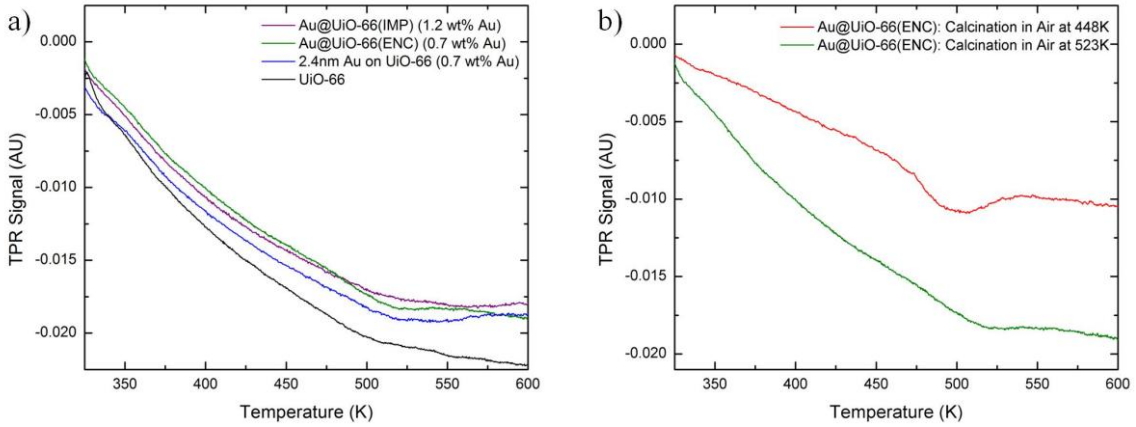

Figure 5.10: H_2-TPR curves of (a) the preparation methods and (b) Au@UiO-66(ENC) calcined at 448 K and 623 K

The oxygen storage capacity (OSC) is the amount of reducible oxygen that can be stored by a material, either as a part of the lattice structure or by adsorption, and donated for oxidation purposes. The OSC is measured by calcining the material in air at 523 K for 2 h, purging the sample with nitrogen for 30 min to remove physisorbed oxygen, then exposing the material to 1% CO in nitrogen and measuring the CO_2 evolution over time. Table 5.3 reports the OSC of parent UiO-66 and the composites, and Figure 5.11 depicts the CO_2 evolution over time during the OSC experiments. Notably, parent UiO-66 does not produce CO_2 during the OSC experiment, whereas all of the composites show CO_2 evolution, suggesting that the AuNPs are necessary for CO_2 evolution. The AuNP requirement for the evolution of CO_2 suggests that the AuNPs play a role in the activation and donation of oxygen for CO oxidation over AuNPs supported in or on UiO-66. There

are four potential theories explaining the specific function of the AuNPs towards oxygen donation: (1) the AuNPs alone adsorb and activate oxygen; (2) the AuNPs destabilize the adjacent lattice surface oxygen, which is then more easily reduced by CO; (3) oxygen is stored by the support and the AuNPs are necessary to adsorb CO; or (4) the AuNPs create an AuNP-support interface site that adsorbs and activates oxygen which is subsequently reduced by CO.[42, 44-46] Several theories are more likely than others. There are numerous studies that demonstrate a support effect on the catalytic activity of supported AuNPs; therefore, it is unlikely that the AuNPs are solely responsible for adsorbing and activating oxygen.[31, 32, 47] Also, the destabilization of surface oxygen by the AuNPs can be probed using H_2-TPR,[43] and there are no peaks in Figure 5.10a correlating to the reduction of surface oxygen.

In addition, the samples can be divided into two distinct sets based on the OSC; Au@UiO-66(ENC) and 7.2 nm Au on UiO-66 have comparable OSCs and Au@UiO-66(IMP), 2.4 nm Au on UiO-66, and 4.9 nm Au on UiO-66 have similar OSCs, but there is an order of magnitude difference between the two sample sets. OSC depends upon the specific support; therefore, an order of magnitude difference between catalysts with the same support is unexpected. Figure 5.12 shows that the OSC is dependent on the AuNP diameter; when the AuNPs are greater than 5.5 nm in diameter, the OSC is significantly reduced. This combination of AuNPs being necessary for CO_2 evolution and the AuNP diameter dependence suggests that the OSC evolves from synergistic effects between the AuNPs and the support.

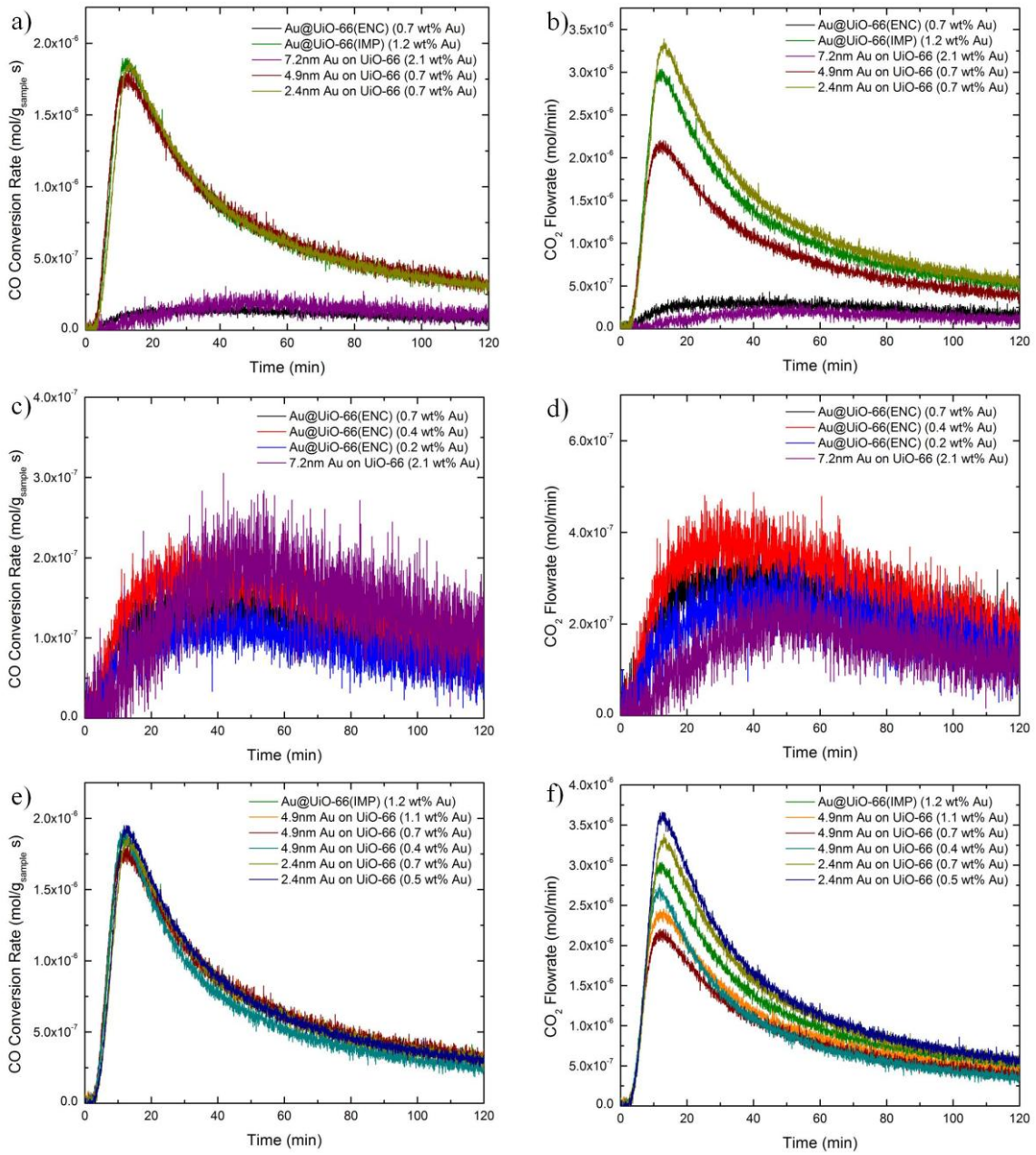

Figure 5.11: CO conversion rate and CO_2 flowrate curves from OSC experiments

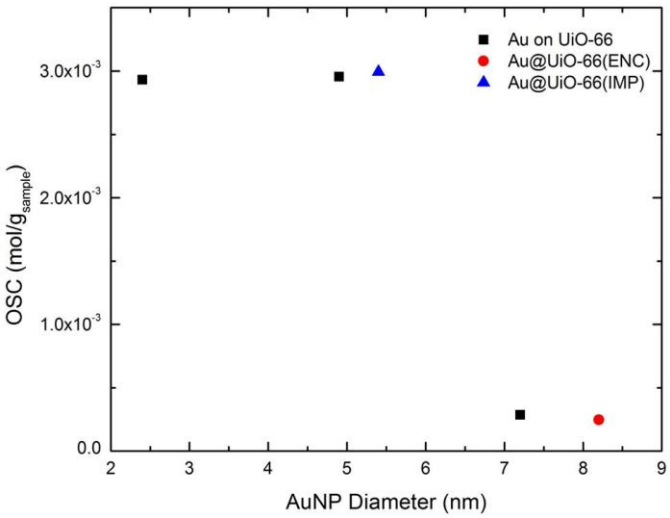

Figure 5.12: AuNP diameter effect on OSC

5.3.2 CO Oxidation

5.3.2.1 Activation

The samples denoted Au@UiO-66(ENC) and Au on UiO-66 were all prepared using AuNPs with a mixed surface assemble monolayer (SAM) of DDT and MUA, as previously shown. Removing this SAM is paramount for catalytic activity; the Au sites must be accessible. CO oxidation at 448 K was used to probe the activation conditions necessary to remove the SAM from the AuNPs. Briefly, the sample was heated under helium flow at 473 K for 16-18 h to remove the water and solvent trapped within the UiO-66 pores. Then, the sample was pretreated in either air or helium at various temperatures for 2 h. Finally 1% CO in air was exposed to the sample at 448 K until the reaction reached steady-state. Figure 5.13 reports the steady-state activity for Au@UiO-66(ENC) under different pretreatment conditions. The hypothesis is that O_2 is necessary to combust the SAM to create accessible CO oxidation sites on the AuNPs and that, without combustion, there will be minimal CO oxidation. To test this hypothesis, various

samples were pretreated under air flow at 448 K, 523 K, and 623 K, while one sample was pretreated under helium flow at 523 K in order to show that the linkers cannot be removed by merely heating at 523 K.

Figure 5.13 depicts the relationship between the pretreatment temperature and catalytic activity of the materials. For Au@UiO-66(ENC), the catalytic activity is significantly reduced when heated, in air, at 448 K compared to 523 K and 623 K. Likewise, the catalytic capabilities of Au@UiO-66(ENC) pretreated at 523 K and 623 K are similar. Additionally, Au@UiO-66(ENC) was pretreated in helium at 523 K for 2 h. Pretreatment in helium at 523 K shows a significant reduction in the catalytic activity compared to Au@UiO-66(ENC) calcined in air at 523K. Therefore, calcination at 523 K in air is required, for Au@UiO-66(ENC), to combust the AuNP capping ligands to ensure that the AuNP active sites are accessible.

Pretreatment conditions for 2.7 nm Au on UiO-66 were simplified by applying the results from Au@UiO-66(ENC). Au on UiO-66 was pretreated with air at 448 K and 523 K and with He at 473 K. Contrary to Au@UiO-66(ENC), calcination in air at 448 K results in comparable steady-state CO oxidation with Au on UiO-66 calcined in air at 523K. However, Figure 5.14 shows that, although calcination in air at both 448 K and 523 K results in similar steady-state catalytic activity, the material calcined at 448 K, designated by the dark red curve, reaches steady-state significantly more slowly. One possibility for this is that a longer calcination time at 448 K is necessary to completely combust the capping ligands. TGA data in Figure 5.3 supports this theory; the combustion of the SAM in air begins at 448K; therefore, complete removal will require a longer period of time at this temperature. Another possibility is that the CO_2 measured is

actually the SAM combusting. However, CO_2 would not be constantly produced if that were the case, and the catalyst would appear to deactivate, which it does not. Additionally, to determine if Au on UiO-66 requires air or merely sufficient heat to vaporize the linkers, the material is heated in helium at 473K, the temperature used for solvent removal. In contrast to the Au@UiO-66(ENC) samples, heating at 473 K under helium results in steady-state activity similar to heating in air. However, the material heated under helium requires approximately 2 h longer to reach steady-state than the materials calcined in air at any temperature. This supports the theory that a longer time period is necessary in order to completely remove the SAM at 448 K.

To summarize, the 2.7 nm Au on UiO-66 samples are active for CO oxidation at 448 K with a limited dependence on the pretreatment for steady-state activity, whereas, Au@UiO-66(ENC) requires calcination in air at 523 K or greater. This suggests that the SAM can be removed from the AuNP surface at temperatures as low as 448 K under air flow. Therefore, the necessity of elevated calcination temperature for Au@UiO-66(ENC) implies that the SAM must combust into fragments capable of diffusing through UiO-66 at reasonable rates to effectively remove the capping ligands, which subsequently releases the active sites. These differences in sufficient pretreatment conditions imply that the AuNPs are confined either within single UiO-66 particles or within an aggregation of UiO-66 particles for Au@UiO-66(ENC) and located on the MOF surface for Au on UiO-66. For consistency, all samples are pretreated in air at 523 K for 2 h for subsequent CO oxidation measurements.

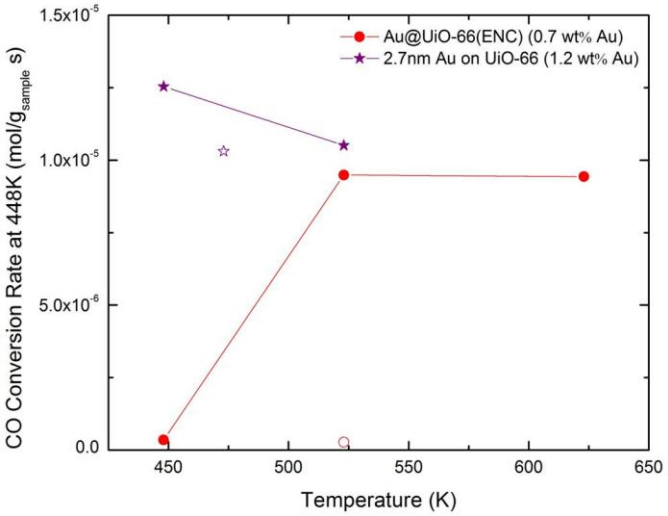

Figure 5.13: Dependence of CO conversion rate on calcination temperature. Closed symbols represent calcination in air and open symbols represent calcination in helium. The lines are only to guide the eye

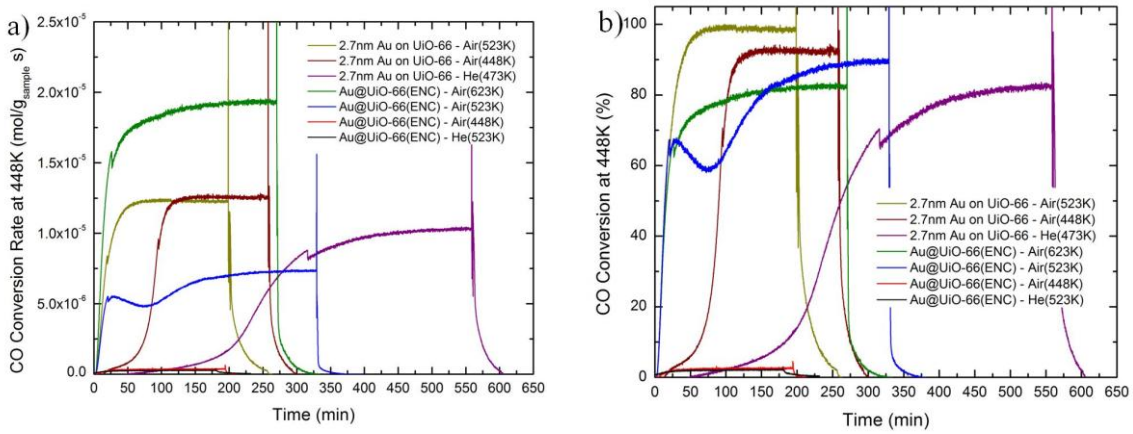

Figure 5.14: (a) CO oxidation activity at 448 K vs. time and (b) CO conversion at 448 K for Au@UiO-66(ENC) (0.7wt% Au) and 2.7 nm Au on UiO-66(1.2 wt% Au) exposed to various pretreatment conditions

5.3.2.2 AuNP and Preparation Method Effect

Once an effective activation procedure was determined, the catalytic capabilities of the materials were probed to ascertain the effects of AuNP concentration and size. Table 5.3 reports the catalytic activities of the materials including the approximate temperature for 50% conversion ($T_{1/2}$); apparent activation energy (E_{app}); and reaction

rate, CO conversion, and turnover frequency (TOF) at 423K. The material activity is compared for CO oxidation at 423 K because it is the lowest temperature that the catalytic capabilities can be compared for all of the materials prepared in this work. Additionally, Figure 5.15 depicts the temperature dependence of catalytic activity and the Arrhenius plots used to calculate E_{app}. The $T_{1/2}$ of 426 K and 428 K for Au@UiO-66(ENC) and Au@UiO-66(IMP), respectively, are similar to previously reported MOF systems. The previously reported $T_{1/2}$ for Au@UiO-66, Au@ZIF-8, and Ag@MIL-53 are 428K,[20] 443K,[27] and 396K,[48] respectively. This is notable because the AuNP diameters for Au@UiO-66(ENC) and Au@UiO-66(IMP) in this work are significantly larger than the 2.8 nm[20] and 3.4 nm[27] AuNPs reported for Au@UiO-66 and Au@ZIF-8, respectively. Likewise, Au on TiO_2 and Au on ZrO_2 report $T_{1/2}$ ranging from 262-477 K and 347-523 K, respectively, dependent on the preparation method and activation conditions.[32, 33, 42, 49]

Table 5.3: Catalytic properties of Au@UiO-66 and Au on UiO-66 composites

Material	Au wt %	OSC (mol CO_2/g_{sample})	$T_{1/2}$ (K)	Reaction Rate[a] (mol/g_{sample} s)	Reaction Rate[a] (mol/g_{Au} s)	TOF[a] (s^{-1})	CO Conv[a] (%)	E_{app} (kJ/mol)
UiO-66	0	0	-----	0	0	0	0	-----
Au@UiO-66(ENC)	0.7	$2.5x10^{-4}$	426	$4.5x10^{-6}$	$6.4x10^{-4}$	27.0	46	30
	0.4	$3.3x10^{-4}$	454	$2.2x10^{-7}$	$5.5x10^{-5}$	2.1	2	63
	0.2	$2.0x10^{-4}$	485	0	0	0	0	-----
Au@UiO-66(IMP)	1.2	$3.0x10^{-3}$	428	$5.0x10^{-6}$	$4.5x10^{-4}$	11.3	47	26
2.4 nm Au on UiO-66	0.7	$2.9x10^{-3}$	360	$9.7x10^{-6}$	$1.4x10^{-3}$	24.5	86	16
	0.5	$3.0x10^{-3}$	399	$8.8x10^{-6}$	$2.2x10^{-4}$	45.1	67	23
4.9 nm Au on UiO-66	1.1	$3.0x10^{-3}$	397	$9.7x10^{-6}$	$8.8x10^{-4}$	30.6	72	20
	0.7	$3.0x10^{-3}$	416	$6.8x10^{-6}$	$9.7x10^{-4}$	40.3	43	26
	0.4	$2.8x10^{-3}$	429	$7.2x10^{-6}$	$1.8x10^{-3}$	73.5	45	27
7.2 nm Au on UiO-66	2.1	$2.9x10^{-4}$	510	0	0	0	0	-----

[a]Measured at 423 K

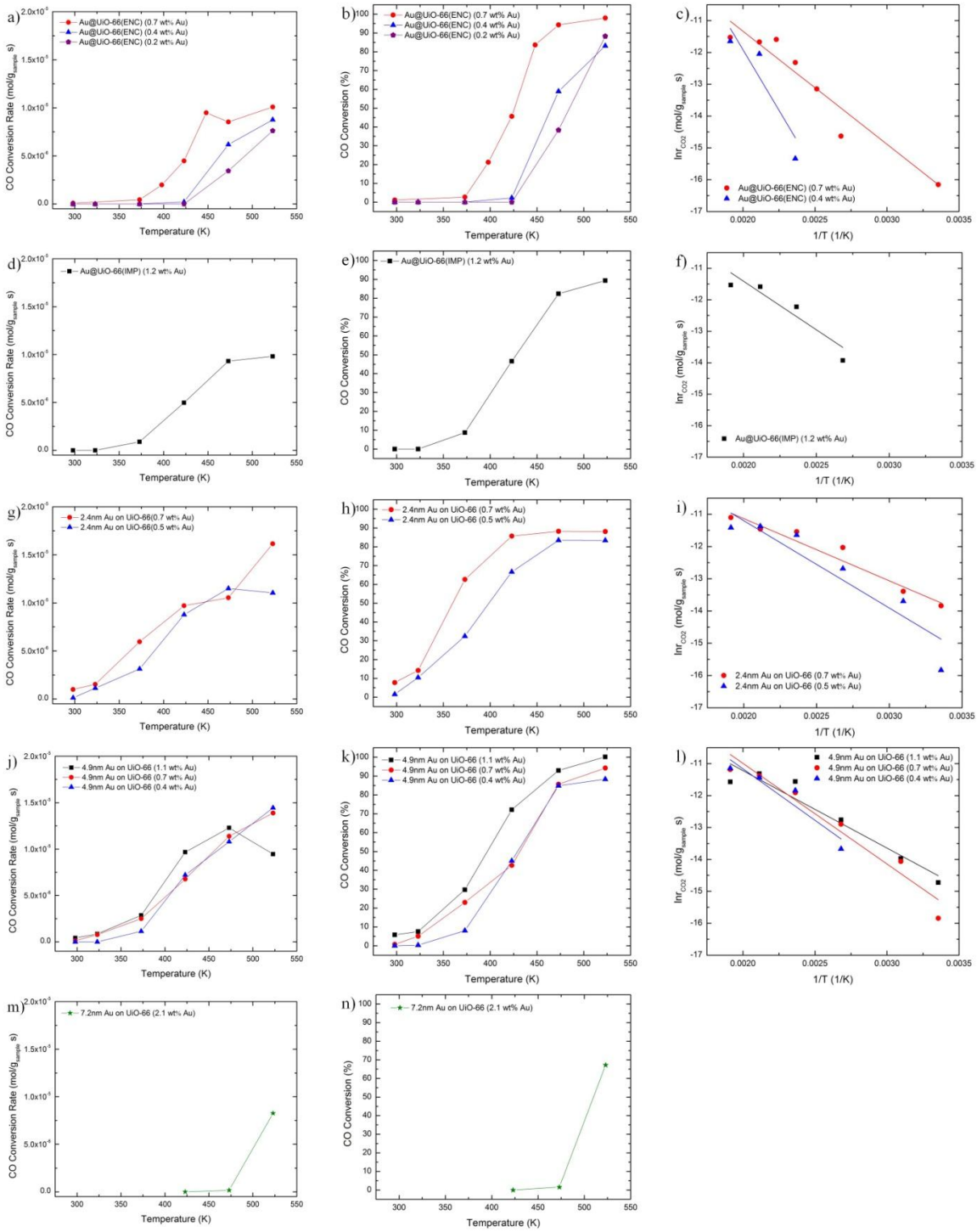

Figure 5.15: Temperature dependence of CO conversion rate (left column), CO conversion (middle column), and Arrhenius plots (right column) for (a,b,c) Au@UiO-66(ENC), (d,e,f) Au@UiO-66(IMP), (g,h,i) 2.4 nm Au on UiO-66, (j,k,l) 4.9 nm Au on UiO-66, and (m,n) 7.2 nm Au on UiO-66

In addition, studies investigating the activity of supported AuNPs for CO oxidation report E_{app} of 2-56 kJ/mol[33, 42, 50] and 18 kJ/mol for Au on TiO_2 and Au on ZrO_2,[51] respectively. Lastly, Behm et al. reported reaction rates at 393 K of $5.7x10^{-7}$, $4.1x10^{-6}$, $7.7x10^{-6}$, and $1.1x10^{-4}$ mol/(g_{cat}·s) for 3 nm AuNPs deposited on Al_2O_3, ZnO, ZrO_2, and TiO_2, respectively.[31] Essentially, the catalytic properties measured for Au@UiO-66 and Au on UiO-66 are similar to previously reported studies that investigate AuNPs supported on MOFs and metal oxides. Moving forward, CO oxidation will be used as a probe reaction to determine the effect of the preparation method on synergism within the material. The Au@UiO-66 materials will be compared to Au on UiO-66 samples as a control to differentiate between catalytic activities introduced by AuNPs deposited on the UiO-66 surface and synergistic effects introduced by incorporation in the UiO-66 particles.

Figure 5.16 depicts the dependence of AuNP concentration and diameter on catalytic activity for the materials prepared via encapsulation, impregnation, and colloidal deposition. Figure 5.16a shows that the catalytic activity of the materials increases as the AuNP concentration increases, specifically for 2.4 nm Au on UiO-66, 4.9 nm Au on UiO-66, and Au@UiO-66(ENC), due to an increased number of active catalytic sites.[20, 27] Figure 5.16b shows that, for the physical mixtures, the activity decreases as the AuNP diameter increases, which is consistent with AuNPs supported on metal oxides.[28, 29] Herein, the physical mixtures, denoted as Au on UiO-66, act as a control to determine the activity of surface based AuNPs of various diameters. The catalytic capabilities of these materials are compared to Au@UiO-66 to determine the effect of the preparation method on the introduction of synergist effects towards CO oxidation. Figure 5.16b shows that

UiO-66 impregnated with AuNPs 5.4 nm in diameter (Au@UiO-66(IMP)) demonstrates similar catalytic capabilities with 4.9 nm Au on UiO-66. This suggests that the impregnation technique introduces minimal synergism. However, Au@UiO-66(ENC) shows a significant enhancement in catalytic activity compared to the corresponding 7.2 nm Au on UiO-66. This improved activity indicates that the encapsulation procedure introduces synergistic effects between the AuNPs and UiO-66. Additionally, Au@UiO-66(ENC) is more active than Au@UiO-66(IMP), which is significant since impregnation yields smaller AuNPs.

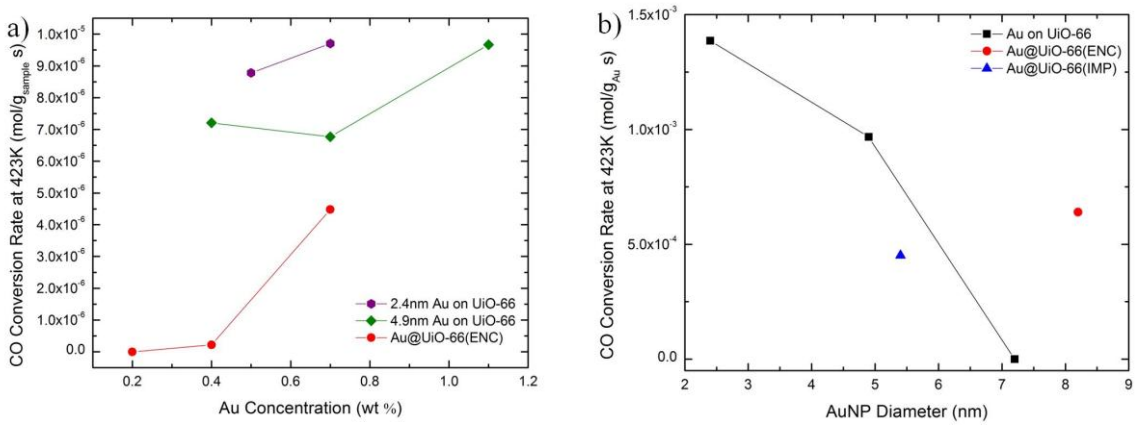

Figure 5.16: Effect of (a) AuNP concentration and (b) AuNP diameter on catalytic activity. The lines are to guide the eyes only

The UiO-66 composite prepared using the encapsulation technique has proven to be more catalytically active than material prepared via impregnation. Based on the combination of TEM and CO oxidation, Au@UiO-66(IMP) most likely consists of AuNPs deposited on the UiO-66 surface. Therefore, the Au precursor is either too large to efficiently diffuse into the pore space or the AuNPs are not anchored within the pores and migrate to the surface during growth. However, the encapsulation procedure yields a material with enhanced catalytic capabilities compared to physical mixtures and the

impregnation technique. The collective microscopy and CO oxidation data suggest that the AuNPs are partially confined within either the UiO-66 particles or UiO-66 aggregates. This confinement increases the degree of contact between the AuNPs and UiO-66 presenting more interface sites active for catalysis. Therefore, the encapsulation method overcomes the limitations of the impregnation technique, specifically diffusional constraints and AuNP migration. Additionally, the enhanced catalytic activity of Au@UiO-66(ENC) could occur due to (1) the introduction of more edge or corner sites due to the aggregation of the AuNPs during UiO-66 crystallization or (2) improved dispersion of the AuNPs throughout the UiO-66 particles. It is well established that as nanoparticle diameters increase, the number of edge and corner sites is reduced; therefore, it is unlikely that AuNP growth would produce more catalytically active sites. However, the TEM images depicted in Figures 5.5-5.7 suggest that the encapsulation procedure distributes the AuNPs more randomly throughout the UiO-66 particles compared to the impregnation technique and colloidal deposition. This random dispersion will also improve the degree of interactions between the AuNPs and UiO-66 and will potentially enhance catalytic activity. Overall, the encapsulation of AuNPs in UiO-66 produce composites that are catalytically active for CO oxidation and perform better than the physical mixtures demonstrating the synergistic effect introduced via the encapsulation method. In addition, Au@UiO-66(ENC) is more catalytically active than Au@UiO-66(IMP) highlighting the advantages of the encapsulation technique for the preparation of UiO-66 composites.

5.3.2.3 Oxygen Storage Capacity Effect

The catalytic activity of supported AuNPs on metal oxides has been shown to be dependent on the supporting material, and the key attribute of the support is the OSC.[31] Additionally, for AuNPs deposited on TiO_2, Kotobuki et al. probed the effect of the AuNP diameter on OSC, and the interface perimeter length was shown to correlate well with OSC and CO conversion rate.[44] However, for Au on UiO-66, this correlation between AuNP diameter and OSC is not observed. In addition, Table 5.3 demonstrates that there is not a correlation between the OSC and the catalytic activity when the supporting material is UiO-66. It is interesting that, although all of the materials are active for CO oxidation at 523 K with conversions ranging from 67-100% (Figure 5.15), there is a significant AuNP diameter dependence on the anaerobic oxidation of CO at 523 K (Figure 5.11). This can potentially be explained by the occurrence of two different reaction paths for the materials. Huang et al. demonstrate an AuNP diameter dependence on reaction path for Au on CeO_2. Briefly, for AuNPs 1.7-3.7 nm in diameter deposited on CeO_2, CO is adsorbed and oxidized; at the same time, carbonate, bicarbonate, and formate species form upon CO adsorption and block the active sites resulting in catalyst deactivation. However, as the AuNP diameter increases, an additional decomposition reaction pathway opens where the carbonate, bicarbonate, and formate species undergo oxygen assisted decomposition subsequently reactivating the catalytic sites.[52] Based on the data herein, an oxygen assisted decomposition pathway is plausible for the 7.2 nm Au on UiO-66 and Au@UiO-66(ENC) composites with AuNPs 8.2 nm in diameter. It explains why the materials are active during the CO oxidation experiments at 523 K in air, but significantly less active during the anaerobic experiments.

Figures 5.17 and 5.18 further support this dual reaction path theory. Figure 5.17 depicts the time dependent reaction rates for Au@UiO-66(ENC). The interesting thing about this data is that the material starts to deactivate, then, appears to reactivate the catalytic sites resulting in an increase in the oxidation rate which eventually reaches steady-state. This delayed increase in oxidation rate could occur due to the reactivation of the catalytic sites via oxygen assisted decomposition of carbonates, bicarbonates, and formates. Additionally, Figure 5.18 depicts the time dependence of the 7.2 nm Au on UiO-66 conversion rates. At 473K, there is a delay in CO conversion; CO_2 is first measured after 80 min. This delay could be attributed to a slow oxygen assisted decomposition of carbonate species. Notably, Au@UiO-66(ENC) and 7.2 nm Au on UiO-66 behave differently than Au@UiO-66(IMP), 2.4 nm Au on UiO-66, and 4.9 nm Au on UiO-66. For the materials with AuNPs smaller than 5.5 nm, the time dependent reaction rates perform similar to AuNPs supported on metal oxides: CO is converted, a maximum rate is attained, and the catalyst deactivates; this deactivation typically occurs due to the deposition of carbonate species on the active sites.[34, 51, 53, 54] In summary, the UiO-66 composites with AuNPs greater than 5.5 nm in diameter demonstrate reduced CO oxidation capabilities under anaerobic conditions and an apparent in-situ reactivation of catalyst sites. These observations suggest that, for AuNPs supported by UiO-66, AuNP diameters greater than 5.5 nm enhance the oxygen assisted decomposition of carbonate species.

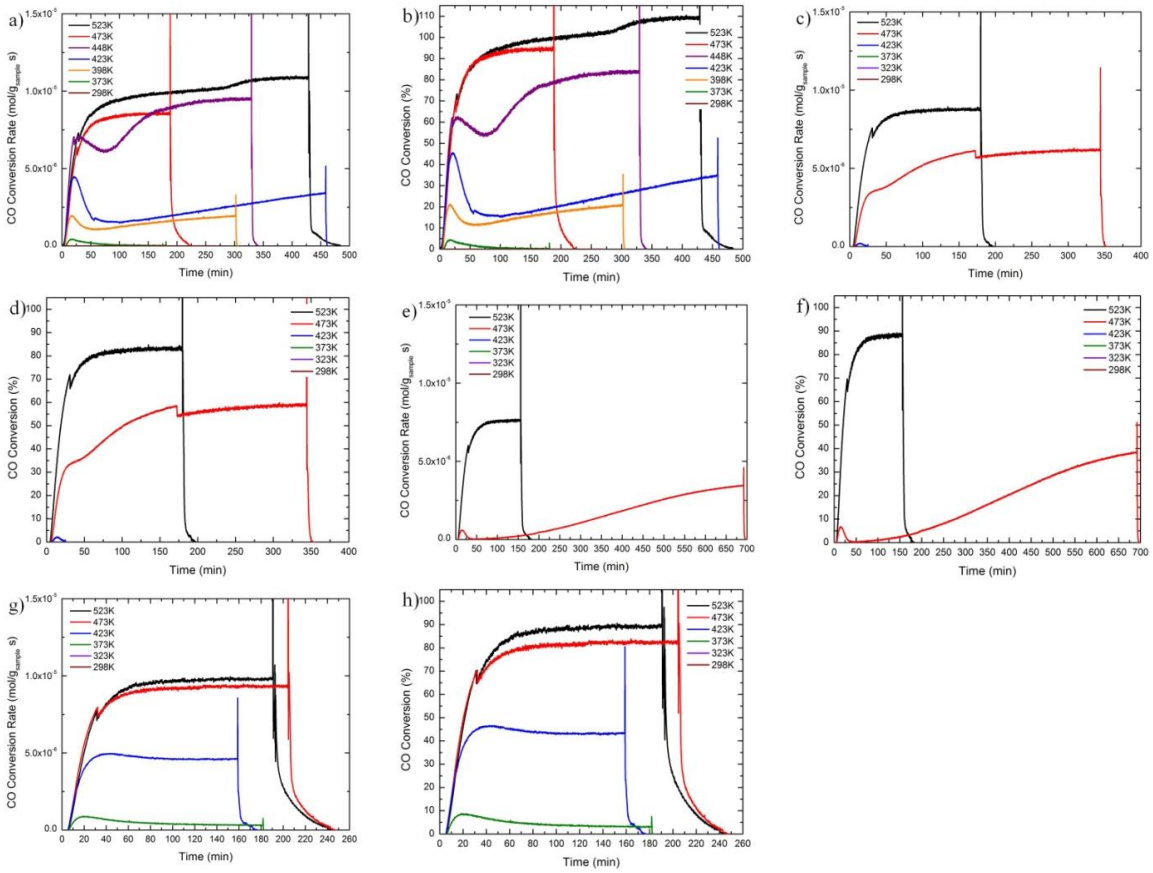

Figure 5.17: Activity vs. time for (a,b) Au@UiO-66(ENC) (0.7 wt% Au); (c,d) Au@UiO-66(ENC) (0.4 wt% Au); (e,f) Au@UiO-66(ENC) (0.2 wt% Au); and (g,h) Au@UiO-66(IMP) (1.2 wt% Au)

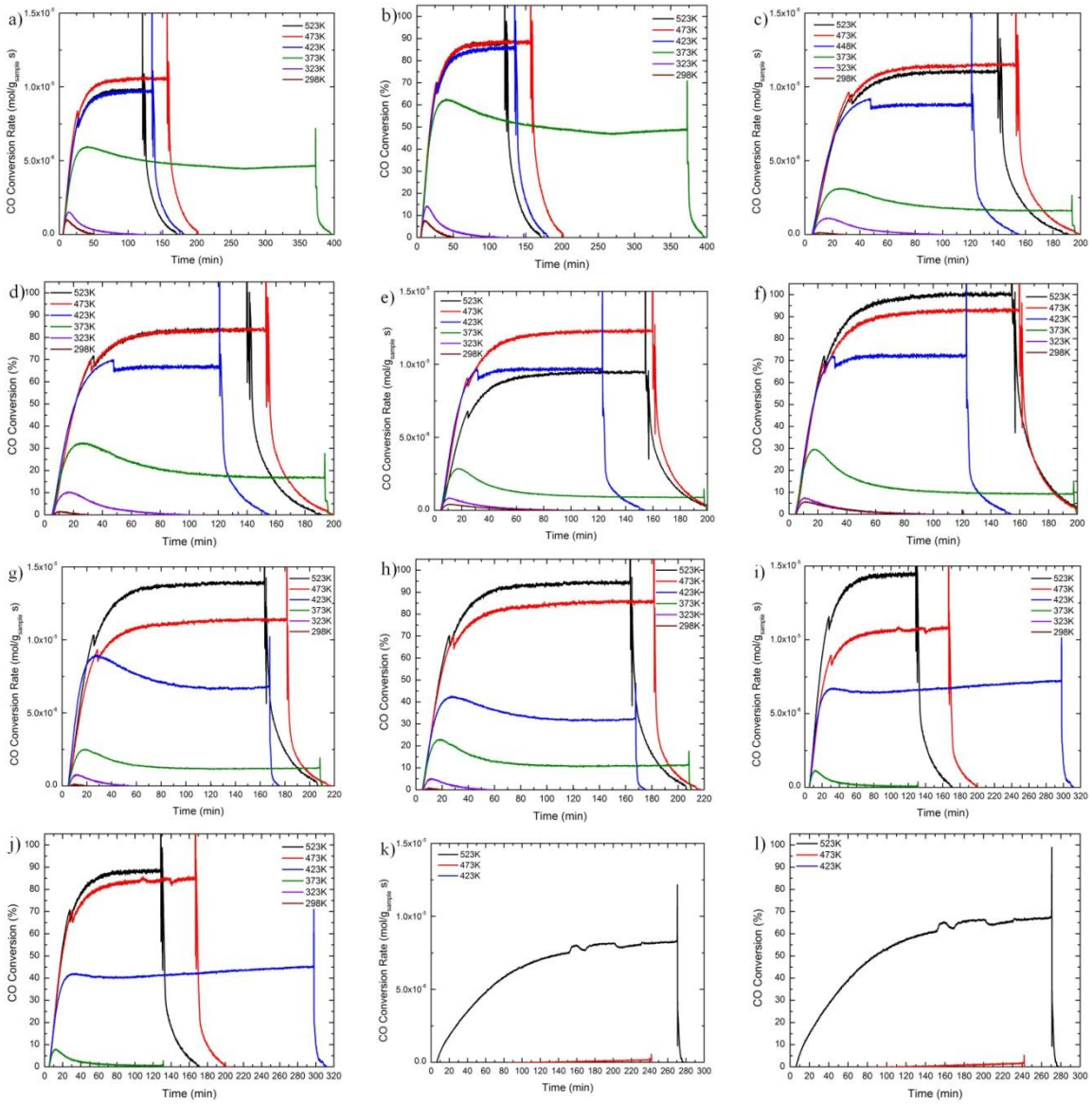

Figure 5.18: Activity vs. time for (a,b) 2.4 nm Au on UiO-66 (0.7 wt% Au); (c,d) 2.4 nm Au on UiO-66 (0.5 wt% Au); (e,f) 4.9 nm Au on UiO-66 (1.1 wt% Au); (g,h) 4.9 nm Au on UiO-66 (0.7 wt% Au); (i,j) 4.9 nm Au on UiO-66 (0.4 wt% Au); and (k,l) 7.2 nm Au on UiO-66 (0.4 wt% Au)

5.4 Conclusions

Au@UiO-66 composites were prepared via impregnation and encapsulation to probe the effect of the preparation method on the UiO-66 properties. Physical mixtures of 2.4 nm Au on UiO-66, 4.9 nm Au on UiO-66, and 7.2 nm Au on UiO-66 were also

prepared to act as a control system. The materials were extensively characterized using PXRD, nitrogen sorption at 77K, TEM, STEM tomography, and H_2-TPR. PXRD and nitrogen sorption at 77 K prove that the UiO-66 structure and porosity are obtained for all of the materials. TEM confirms the AuNP diameter for the physical mixtures and shows that the AuNPs distributed throughout Au@UiO-66(ENC) and Au@UiO-66(IMP) are, on average, 8.2 nm and 5.4 nm, respectively. TEM also shows that both preparation methods result in AuNPs that are definitively on the UiO-66 surface, proving that neither preparation method completely confines the AuNPs within UiO-66. STEM tomography on Au@UiO-66(ENC) suggests that there are AuNPs confined either within individual UiO-66 particles or within aggregates of UiO-66 particles. Lastly, H_2-TPR suggests that the AuNPs in all of the materials are metallic Au and the addition of the nanoparticles does not promote the reduction of surface oxygen from the support.

Next, CO oxidation was used to probe the potential confinement and synergistic effects introduced by the various preparation methods. Au@UiO-66(IMP) demonstrates catalytic capabilities similar to the analogous physical mixture. This lack of synergism coupled with TEM suggests that the AuNPs, incorporated via impregnation, are mainly deposited on the surface of the UiO-66 particles. Therefore, the impregnation technique is limited by either diffusional constraints or the migration of the AuNPs during growth due to inadequate anchoring of the AuNPs within the pores. Alternatively, Au@UiO-66(ENC) shows improved activity compared to the corresponding physical mixtures indicating that synergistic effects are introduced via the encapsulation procedure. The combination of STEM tomography and CO oxidation suggests that the AuNPs are partially confined within individual UiO-66 particles and/or UiO-66 aggregates. This

suggested confinement will increase the degree of contact between the AuNPs and UiO-66, which will introduce more AuNP-support interface sites and enhance the catalytic activity of the materials. In addition, Au@UiO-66(ENC) demonstrates improved catalytic activity over Au@UiO-66(IMP) highlighting the advantages of the encapsulation technique for preparing UiO-66 composites.

5.5 References

1. Ferey, G., Hybrid porous solids: past, present, future. *Chemical Society Reviews* **2008,** *37* (1), 191-214.

2. Furukawa, H.; Cordova, K. E.; O'Keeffe, M.; Yaghi, O. M., The Chemistry and Applications of Metal-Organic Frameworks. *Science* **2013,** *341* (6149), 974-+.

3. Burtch, N. C.; Jasuja, H.; Walton, K. S., Water Stability and Adsorption in Metal-Organic Frameworks. *Chemical Reviews* **2014,** *114* (20), 10575-10612.

4. Meilikhov, M.; Yusenko, K.; Esken, D.; Turner, S.; Van Tendeloo, G.; Fischer, R. A., Metals@MOFs - Loading MOFs with Metal Nanoparticles for Hybrid Functions. *European Journal of Inorganic Chemistry* **2010,** (24), 3701-3714.

5. Leus, K.; Concepcion, P.; Vandichel, M.; Meledina, M.; Grirrane, A.; Esquivel, D.; Turner, S.; Poelman, D.; Waroquier, M.; Van Speybroeck, V.; Van Tendeloo, G.; Garcia, H.; Van Der Voort, P., Au@UiO-66: a base free oxidation catalyst. *RSC Advances* **2015,** *5* (29), 22334-22342.

6. Aijaz, A.; Akita, T.; Tsumori, N.; Xu, Q., Metal-Organic Framework-Immobilized Polyhedral Metal Nanocrystals: Reduction at Solid-Gas Interface, Metal Segregation, Core-Shell Structure, and High Catalytic Activity. *Journal of the American Chemical Society* **2013,** *135* (44), 16356-16359.

7. Hou, C. T.; Xu, Q.; Wang, Y. J.; Hu, X. Y., Synthesis of Pt@NH_2-MIL-125(Ti) as a photocathode material for photoelectrochemical hydrogen production. *RSC Advances* **2013,** *3* (43), 19820-19823.

8. Hermes, S.; Schroter, M. K.; Schmid, R.; Khodeir, L.; Muhler, M.; Tissler, A.; Fischer, R. W.; Fischer, R. A., Metal@MOF: Loading of highly porous coordination polymers host lattices by metal organic chemical vapor deposition. *Angewandte Chemie-International Edition* **2005,** *44* (38), 6237-6241.

9. Jiang, H.-L.; Liu, B.; Akita, T.; Haruta, M.; Sakurai, H.; Xu, Q., Au@ZIF-8: CO Oxidation over Gold Nanoparticles Deposited to Metal-Organic Framework. *Journal of the American Chemical Society* **2009,** *131* (32), 11302-+.

10. Puthiaraj, P.; Ahn, W.-S., Highly active palladium nanoparticles immobilized on NH_2-MIL-125 as efficient and recyclable catalysts for Suzuki-Miyaura cross coupling reaction. *Catalysis Communications* **2015,** *65*, 91-95.

11. Wu, F.; Qiu, L. G.; Ke, F.; Jiang, X., Copper nanoparticles embedded in metal-organic framework MIL-101(Cr) as a high performance catalyst for reduction of aromatic nitro compounds. *Inorganic Chemistry Communications* **2013,** *32*, 5-8.

12. Moon, H. R.; Kim, J. H.; Suh, M. P., Redox-active porous metal-organic framework producing silver nanoparticles from Ag^I ions at room temperature. *Angewandte Chemie-International Edition* **2005,** *44* (8), 1261-1265.

13. Lu, G.; Li, S.; Guo, Z.; Farha, O. K.; Hauser, B. G.; Qi, X.; Wang, Y.; Wang, X.; Han, S.; Liu, X.; DuChene, J. S.; Zhang, H.; Zhang, Q.; Chen, X.; Ma, J.; Loo, S. C. J.; Wei, W. D.; Yang, Y.; Hupp, J. T.; Huo, F., Imparting functionality to a metal-organic framework material by controlled nanoparticle encapsulation. *Nature Chemistry* **2012,** *4* (4), 310-316.

14. Esken, D.; Zhang, X.; Lebedev, O. I.; Schroder, F.; Fischer, R. A., Pd@MOF-5: limitations of gas-phase infiltration and solution impregnation of $Zn_4O(bdc)_3$ (MOF-5) with metal-organic palladium precursors for loading with Pd nanoparticles. *Journal of Materials Chemistry* **2009,** *19* (9), 1314-1319.

15. Ishida, T.; Nagaoka, M.; Akita, T.; Haruta, M., Deposition of Gold Clusters on Porous Coordination Polymers by Solid Grinding and Their Catalytic Activity in Aerobic Oxidation of Alcohols. *Chemistry-a European Journal* **2008,** *14* (28), 8456-8460.

16. Cavka, J. H.; Jakobsen, S.; Olsbye, U.; Guillou, N.; Lamberti, C.; Bordiga, S.; Lillerud, K. P., A new zirconium inorganic building brick forming metal organic frameworks with exceptional stability. *Journal of the American Chemical Society* **2008,** *130* (42), 13850-13851.

17. Piscopo, C. G.; Polyzoidis, A.; Schwarzer, M.; Loebbecke, S., Stability of UiO-66 under acidic treatment: Opportunities and limitations for post-synthetic modifications. *Microporous and Mesoporous Materials* **2015,** *208*, 30-35.

18. Schoenecker, P. M.; Carson, C. G.; Jasuja, H.; Flemming, C. J. J.; Walton, K. S., Effect of Water Adsorption on Retention of Structure and Surface Area of Metal-Organic Frameworks. *Industrial & Engineering Chemistry Research* **2012,** *51* (18), 6513-6519.

19. Biswas, S.; Van der Voort, P., A General Strategy for the Synthesis of Functionalised UiO-66 Frameworks: Characterisation, Stability and CO_2 Adsorption Properties. *European Journal of Inorganic Chemistry* **2013,** (12), 2154-2160.

20. Wu, R.; Qian, X.; Zhou, K.; Liu, H.; Yadian, B.; Wei, J.; Zhu, H.; Huang, Y., Highly dispersed Au nanoparticles immobilized on Zr-based metal-organic frameworks as heterostructured catalyst for CO oxidation. *Journal of Materials Chemistry A* **2013,** *1* (45), 14294-14299.

21. Guo, Z. Y.; Xiao, C. X.; Maligal-Ganesh, R. V.; Zhou, L.; Goh, T. W.; Li, X. L.; Tesfagaber, D.; Thiel, A.; Huang, W. Y., Pt Nanoclusters Confined within Metal Organic Framework Cavities for Chemoselective Cinnamaldehyde Hydrogenation. *Acs Catalysis* **2014,** *4* (5), 1340-1348.

22. Zhang, W. N.; Lu, G.; Cui, C. L.; Liu, Y. Y.; Li, S. Z.; Yan, W. J.; Xing, C.; Chi, Y. R.; Yang, Y. H.; Huo, F. W., A Family of Metal-Organic Frameworks Exhibiting Size-Selective Catalysis with Encapsulated Noble-Metal Nanoparticles. *Advanced Materials* **2014,** *26* (24), 4056-4060.

23. Tulig, K.; Walton, K. S., An alternative UiO-66 synthesis for HCl-sensitive nanoparticle encapsulation. *RSC Advances* **2014,** *4* (93), 51080-51083.

24. Xia, Y.; Xiong, Y.; Lim, B.; Skrabalak, S. E., Shape-Controlled Synthesis of Metal Nanocrystals: Simple Chemistry Meets Complex Physics? *Angewandte Chemie (International ed. in English)* **2009,** *48* (1), 60-103.

25. Eustis, S.; El-Sayed, M. A., Why gold nanoparticles are more precious than pretty gold: Noble metal surface plasmon resonance and its enhancement of the radiative and nonradiative properties of nanocrystals of different shapes. *Chemical Society Reviews* **2006,** *35* (3), 209-217.

26. Liu, X.; He, L.; Liu, Y. M.; Cao, Y., Supported Gold Catalysis: From Small Molecule Activation to Green Chemical Synthesis. *Accounts of Chemical Research* **2014,** *47* (3), 793-804.

27. Jiang, H. L.; Liu, B.; Akita, T.; Haruta, M.; Sakurai, H.; Xu, Q., Au@ZIF-8: CO Oxidation over Gold Nanoparticles Deposited to Metal-Organic Framework. *Journal of the American Chemical Society* **2009,** *131* (32), 11302-+.

28. Lopez, N.; Janssens, T. V. W.; Clausen, B. S.; Xu, Y.; Mavrikakis, M.; Bligaard, T.; Norskov, J. K., On the origin of the catalytic activity of gold nanoparticles for low-temperature CO oxidation. *Journal of Catalysis* **2004,** *223* (1), 232-235.

29. Valden, M.; Lai, X.; Goodman, D. W., Onset of catalytic activity of gold clusters on titania with the appearance of nonmetallic properties. *Science* **1998,** *281* (5383), 1647-1650.

30. Guzman, J.; Gates, B. C., Catalysis by supported gold: Correlation between catalytic activity for CO oxidation and oxidation states of gold. *Journal of the American Chemical Society* **2004,** *126* (9), 2672-2673.

31. Widmann, D.; Liu, Y.; Schuth, F.; Behm, R. J., Support effects in the Au-catalyzed CO oxidation - Correlation between activity, oxygen storage capacity, and support reducibility. *Journal of Catalysis* **2010,** *276* (2), 292-305.

32. Comotti, M.; Li, W. C.; Spliethoff, B.; Schuth, F., Support effect in high activity gold catalysts for CO oxidation. *Journal of the American Chemical Society* **2006,** *128* (3), 917-924.

33. Bamwenda, G. R.; Tsubota, S.; Nakamura, T.; Haruta, M., The influence of the preparation methods on the catalytic activity of platinum and gold supported on TiO_2 for CO oxidation. *Catalysis Letters* **1997,** *44* (1-2), 83-87.

34. Saavedra, J.; Powell, C.; Panthi, B.; Pursell, C. J.; Chandler, B. D., CO oxidation over Au/TiO_2 catalyst: Pretreatment effects, catalyst deactivation, and carbonates production. *Journal of Catalysis* **2013,** *307*, 37-47.

35. Brust, M.; Walker, M.; Bethell, D.; Schiffrin, D. J.; Whyman, R., Synthesis of thiol-derivatised gold nanoparticles in a two-phase Liquid-Liquid system. *Journal of the Chemical Society-Chemical Communications* **1994,** (7), 801-802.

36. Hostetler, M. J.; Templeton, A. C.; Murray, R. W., Dynamics of place-exchange reactions on monolayer-protected gold cluster molecules. *Langmuir* **1999,** *15* (11), 3782-3789.

37. Hostetler, M. J.; Wingate, J. E.; Zhong, C. J.; Harris, J. E.; Vachet, R. W.; Clark, M. R.; Londono, J. D.; Green, S. J.; Stokes, J. J.; Wignall, G. D.; Glish, G. L.; Porter, M. D.; Evans, N. D.; Murray, R. W., Alkanethiolate gold cluster molecules with core diameters from 1.5 to 5.2 nm: Core and monolayer properties as a function of core size. *Langmuir* **1998,** *14* (1), 17-30.

38. Boccuzzi, F.; Chiorino, A.; Manzoli, M.; Lu, P.; Akita, T.; Ichikawa, S.; Haruta, M., Au/TiO_2 nanosized samples: A catalytic, TEM, and FTIR study of the effect of calcination temperature on the CO oxidation. *Journal of Catalysis* **2001,** *202* (2), 256-267.

39. Park, E. D.; Lee, J. S., Effects of pretreatment conditions on CO oxidation over supported Au catalysts. *Journal of Catalysis* **1999,** *186* (1), 1-11.

40. Neri, G.; Visco, A. M.; Galvagno, S.; Donato, A.; Panzalorto, M., Au iron oxide catalysts: temperature programmed reduction and X-ray diffraction characterization. *Thermochimica Acta* **1999,** *329* (1), 39-46.

41. Kang, Y. M.; Wan, B. Z., Gold and iron supported on Y-type zeolite for carbon monoxide oxidation. *Catalysis Today* **1997,** *35* (4), 379-392.

42. Haruta, M., Catalysis of gold nanoparticles deposited on metal oxides. *Cattech* **2002,** *6* (3), 102-115.

43. Ying, F.; Wang, S.; Au, C.-T.; Lai, S.-Y., Effect of the oxidation state of gold on the complete oxidation of isobutane on Au/CeO_2 catalysts. *Gold Bulletin* **2010,** *43* (4), 241-251.

44. Kotobuki, M.; Leppelt, R.; Hansgen, D. A.; Widmann, D.; Behm, R. J., Reactive oxygen on a Au/TiO_2 supported catalyst. *Journal of Catalysis* **2009,** *264* (1), 67-76.

45. Wang, Y.-G.; Yoon, Y.; Glezakou, V.-A.; Li, J.; Rousseau, R., The Role of Reducible Oxide–Metal Cluster Charge Transfer in Catalytic Processes: New Insights on the Catalytic Mechanism of CO Oxidation on Au/TiO_2 from ab Initio Molecular Dynamics. *Journal of the American Chemical Society* **2013,** *135* (29), 10673-10683.

46. Yoon, B.; Häkkinen, H.; Landman, U.; Wörz, A. S.; Antonietti, J.-M.; Abbet, S.; Judai, K.; Heiz, U., Charging Effects on Bonding and Catalyzed Oxidation of CO on Au_8 Clusters on MgO. *Science* **2005,** *307* (5708), 403-407.

47. Haruta, M.; Yamada, N.; Kobayashi, T.; Iijima, S., Gold catalysts prepared by coprecipitation for low-temperature oxidation of hydrogen and of carbon monoxide. *Journal of Catalysis* **1989,** *115* (2), 301-309.

48. Qian, X.; Zhong, Z.; Yadian, B.; Wu, J.; Zhou, K.; Teo, J. S.-k.; Chen, L.; Long, Y.; Huang, Y., Loading MIL-53(Al) with Ag nanoparticles: Synthesis, structural stability and catalytic properties. *International Journal of Hydrogen Energy* **2014,** *39* (26), 14496-14502.

49. Maciejewski, M.; Fabrizioli, P.; Grunwaldt, J. D.; Beckert, O. S.; Baiker, A., Supported gold catalysts for CO oxidation: Effect of calcination on structure, adsorption and catalytic behaviour. *Physical Chemistry Chemical Physics* **2001,** *3* (17), 3846-3855.

50. Overbury, S. H.; Schwartz, V.; Mullins, D. R.; Yan, W.; Dai, S., Evaluation of the Au size effect: CO oxidation catalyzed by Au/TiO_2. *Journal of Catalysis* **2006,** *241* (1), 56-65.

51. Konova, P.; Naydenov, A.; Tabakova, T.; Mehandjiev, D., Deactivation of nanosize gold supported on zirconia in CO oxidation. *Catalysis Communications* **2004,** *5* (9), 537-542.

52. Chen, S.; Luo, L.; Jiang, Z.; Huang, W., Size-Dependent Reaction Pathways of Low-Temperature CO Oxidation on Au/CeO_2 Catalysts. *Acs Catalysis* **2015,** *5* (3), 1653-1662.

53. Konova, P.; Naydenov, A.; Venkov, C.; Mehandjiev, D.; Andreeva, D.; Tabakova, T., Activity and deactivation of Au/TiO_2 catalyst in CO oxidation. *Journal of Molecular Catalysis a-Chemical* **2004,** *213* (2), 235-240.

54. Schubert, M. M.; Plzak, V.; Garche, J.; Behm, R. J., Activity, selectivity, and long-term stability of different metal oxide supported gold catalysts for the preferential CO oxidation in H_2-rich gas. *Catalysis Letters* **2001,** *76* (3-4), 143-150.

CHAPTER 6

TUNING THE AU@UIO-66 ENCAPSULATION PROCEDURE FOR HCl-SENSITIVE NANPARTICLES

6.1 Introduction

Metal-organic frameworks (MOFs) are nanoporous, crystalline materials constructed of metal or metal oxide nodes connected via organic linkers. The nearly infinite combinations of metal centers and organic moieties provide MOFs with exceptional structural diversity. In addition, MOFs have high surface areas and pore volumes, uniform pore size distributions, and chemical tunability.[1, 2] These capabilities can be further improved through the incorporation of metal and metal oxide nanoparticles. This combination exploits the tailorable porosity and chemistry of MOFs with the unusual chemical and physical properties of the nanoparticles, generating MOF composites with enhanced performance towards gas storage and separation, drug delivery, catalysis, and sensing.[3]

MOF composites are conventionally prepared via either impregnation or encapsulation. Impregnation specifies the formation of nanoparticles within preformed MOFs and encapsulation indicates that the MOF crystallizes around preformed nanoparticles. Huo et al. utilized the encapsulation technique to incorporate a wide range of nanomaterials in ZIF-8.[4] Notably, they integrated nanomaterials of various sizes and shapes, many larger than the ZIF-8 pores, and demonstrated impeccable spatial control of the nanomaterials in the ZIF-8 particles highlighting the advantages of the encapsulation

method. The extension of this controlled incorporation of nanomaterials in a variety of MOFs will facilitate the capability to design MOF composites for specific applications.

UiO-66 is a zirconium-based MOF consisting of $Zr_6O_4(OH)_4$ clusters linked by 1,4-benzenedicarboxylic acid (BDC). Notably, it is thermally stable up to 813K, mechanically and chemically resistant, stable in humid environments, and easily tuned.[5-7] The incorporation of gold nanoparticles (AuNPs) will combine these advantages with the unusual optic and catalytic properties of AuNPs.[8] Tulig et al. reported an alternative UiO-66 synthesis procedure capable of encapsulating HCl-sensitive nanoparticles, such as AuNPs, in UiO-66.[9] However, during UiO-66 crystallization, the AuNPs aggregate and grow in diameter from approximately 2 nm to 16 nm. In addition, instead of complete confinement within the UiO-66 particles, the procedure produces some UiO-66 particles devoid of AuNPs and others with AuNPs definitively on the surface of the UiO-66 particles. Therefore, the procedure must be tuned to control the AuNP aggregation and spatial location. Herein, the UiO-66 synthesis parameters are varied to determine their effects on the UiO-66 properties as well as the AuNP diameter and location within the UiO-66 particles.

6.2 Experimental Methods

6.2.1 Materials

All chemicals were obtained commercially (Sigma-Aldrich and Fisher Scientific) and used as obtained. AuNPs capped with 1-dodecanethiol (DDT) and 11-mercaptoundecanoic acid (MUA) were prepared using a two-step process: (1) the synthesis of DDT capped gold nanoparticles (AuNP-DDT) followed by (2) a ligand

exchange with MUA. AuNP-DDT were prepared using a previously reported procedure.[10] A solution of tetraoctylammonium bromide (0.728 mmol) in toluene (40 mL) was mixed with a solution of gold(III) chloride trihydrate ($HAuCl_4 \cdot 3H_2O$) (0.314 mmol) in water (20 mL) and stirred for 30 min. Next, DDT (0.314 mmol) was added, and the mixture was stirred for 30 min. Finally, a solution of sodium borohydride ($NaBH_4$) (3.14 mmol) in water (10 mL) was added, and the mixture was rigorously stirred for 3 h. The product was washed with de-ionized water, the organic phase separated, and AuNP-DDT were precipitated three times from methanol (MeOH). The ligand exchange entailed stirring AuNP-DDT (3 mg AuNP/mL toluene) and MUA (0.154 mmol) in toluene for 72 h and washing the product three times with toluene.[11] The resulting mixed-ligand product will be referred to as AuNP-DDT/MUA herein.

AuNPs capped with polyvinylpyrrolidone (PVP) were prepared as previously reported.[12, 13] An aqueous solution (210 mL) of $HAuCl_4 \cdot 3H_2O$ (0.15 mmol) and PVP (MW 30k, 8.48 mmol) was vigorously stirred for 1 h. Then, an aqueous solution (11 mL) of $NaBH_4$ (1.54 mmol) was added, and the mixture was stirred for 3 h. Finally, the materials were precipitated and washed three times with an acetone and water (15:1 v:v) mixture.

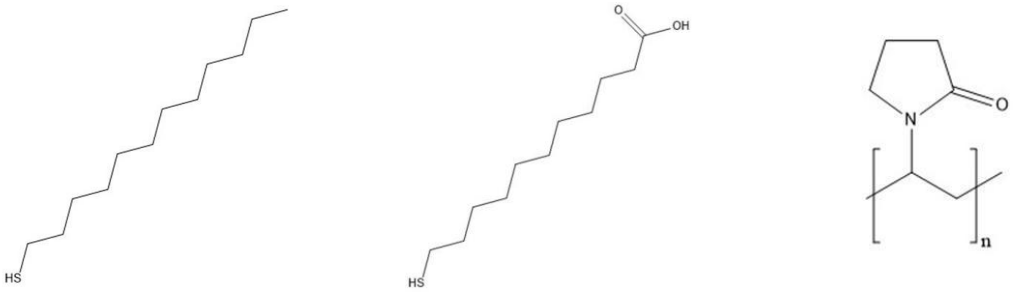

DDT MUA PVP

Figure 6.1: Illustration of AuNP capping agents: DDT/MUA and PVP

Au@UiO-66(Zr(O*n*Pr)) was prepared by stirring zirconium propoxide (Zr(O*n*Pr)) (0.227 mmol) and BDC (0.454 mmol) in solution at 393 K for 24 h. The synthesis was tuned by varying several parameters: the solvent ratio, acetic acid concentration, modulator, and AuNP capping agent. Table 6.1 details the synthetic parameters used to probe the effect of varying the MeOH:DMF ratio, acetic acid:Zr(O*n*Pr) ratio, and AuNP capping agent and UiO-66(Zr(O*n*Pr)) modulator on Au@UiO-66 properties.

Table 6.1: Synthesis parameters for Au@UiO-66(Zr(O*n*Pr)) with various MeOH:DMF ratios, acetic acid:Zr(O*n*Pr) ratios, and capping agents and UiO-66(Zr(O*n*Pr)) modulator. The sections differentiate between the parameters utilized to study the various parameters

Au@UiO-66(Zr(O*n*Pr))	AuNP Capping Agent	MeOH (mmol)	DMF (mmol)	Acetic Acid (mmol)	Benzoic Acid (mmol)
MeOH:DMF = 0.0, acetic acid:Zr(O*n*Pr)=30, and AuNP-DDT/MUA	DDT/MUA	0.00	90.80	6.81	0.00
MeOH:DMF = 0.3, acetic acid:Zr(O*n*Pr)=30, and AuNP-DDT/MUA	DDT/MUA	24.72	77.49	6.81	0.00
MeOH:DMF = 1.9, acetic acid:Zr(O*n*Pr)=30, and AuNP-DDT/MUA	DDT/MUA	86.50	45.40	6.81	0.00
MeOH:DMF = 4.8, acetic acid:Zr(O*n*Pr)=30, and AuNP-DDT/MUA	DDT/MUA	123.67	25.83	6.81	0.00
MeOH:DMF = 1.9, acetic acid:Zr(O*n*Pr)=15, and AuNP-DDT/MUA	DDT/MUA	86.50	45.40	3.41	0.00
MeOH:DMF = 1.9, acetic acid:Zr(O*n*Pr)=20, and AuNP-DDT/MUA	DDT/MUA	86.50	45.40	4.55	0.00
MeOH:DMF = 1.9, acetic acid:Zr(O*n*Pr)=25, and AuNP-DDT/MUA	DDT/MUA	86.50	45.40	5.60	0.00
MeOH:DMF = 1.9, acetic acid:Zr(O*n*Pr)=60, and AuNP-DDT/MUA	DDT/MUA	86.50	45.40	13.62	0.00
MeOH:DMF = 1.9, acetic acid:Zr(O*n*Pr)=120, and AuNP-DDT/MUA	DDT/MUA	86.50	45.40	27.24	0.00
MeOH:DMF = 1.9, acetic acid:Zr(O*n*Pr)=180, and AuNP-DDT/MUA	DDT/MUA	86.50	45.40	41.09	0.00
MeOH:DMF = 1.9, acetic acid:Zr(O*n*Pr)=240, and AuNP-DDT/MUA	DDT/MUA	86.50	45.40	54.48	0.00
MeOH:DMF = 1.9, acetic acid:Zr(O*n*Pr)=480, and AuNP-DDT/MUA	DDT/MUA	86.50	45.40	108.96	0.00
MeOH:DMF=1.9, benzoic acid:Zr(O*n*Pr)=30, and AuNP-DDT/MUA	DDT/MUA	86.50	45.40	0.00	6.81
MeOH:DMF=1.9, acetic acid:Zr(O*n*Pr)=30, and AuNP-PVP	PVP	86.50	45.40	6.81	0.00
MeOH:DMF=1.9, benzoic acid:Zr(O*n*Pr)=30, and AuNP-PVP	PVP	86.50	45.40	0.00	6.81

6.2.2 Characterization

Powder X-ray diffraction (PXRD) patterns were obtained using a PANalytical X-ray diffractometer. Approximately 10 mg of sample were deposited on a low background silica sample holder and scanned from 5-50°. A Quantachrome Quadrasorb Evo volumetric analyzer collected nitrogen sorption data at 77K. The isotherms were measured over a relative pressure (P/P_0) range of 0.001-0.990 with high purity nitrogen (Airgas 99.998%). Prior to the measurement, the samples were heated at 473 K for 16-18 h under vacuum using a Quantachrome FloVac Degasser. The specific surface areas were calculated using the Brunauer, Emmett, and Teller (BET) Theory using $0.005 \leq P/P_0 \leq 0.03$, and the total pore volume was calculated at $P/P_0 = 0.6$. Transmission electron microscopy (TEM) images were acquired using the Hitachi HT7700 operated at 120 keV. The samples were prepared by suspending less than 1 mg of sample in MeOH and dropcasting it on a lacy carbon copper grid. Proton nuclear magnetic resonance (^{1}H NMR) spectroscopy data were collected on a Varian Mercury Vx 300 and used to determine the composition of the organic monolayer on the AuNPs. The samples were prepared by suspending approximately 10 mg of AuNP-DDT/MUA or AuNP-PVP in 1 mL of dimethyl sulfoxide-d_6 or deuterium oxide, respectively.

6.3 Results

6.3.1 Gold Nanoparticles (AuNPs)

For the encapsulation of AuNPs in UiO-66, preformed AuNPs are prepared and added to the UiO-66 mother solution. Herein, two sets of AuNPs were prepared: AuNP-DDT/MUA and AuNP-PVP. The capping agents are illustrated in Figure 6.1. Figure 6.2

depicts the ^{1}H NMR spectra and TEM images for AuNP-DDT/MUA and AuNP-PVP. The ^{1}H NMR spectrum for AuNP-DDT/MUA, depicted in Figure 6.2a, confirms that there is a mixed monolayer of DDT and MUA in a MUA:DDT ratio of 3:1. The broad peaks and lack of coupling in Figure 6.2a are characteristic of ligands bound to a surface, confirming that all of the ligands are bound to the AuNP surface.[14] Additionally, the composition of the monolayer is confirmed by analyzing the characteristic peak positions. DDT has a unique peak at 0.84 ppm associated with $–CH_3$, and MUA has a characteristic peak at 2.13 ppm for $–CH_2COOH$. Additionally, the TEM image of AuNP-DDT/MUA depicted in Figure 6.2b shows that the AuNP-DDT/MUA diameter is 1.8±0.4 nm. The ^{1}H NMR spectrum for AuNP-PVP presented in Figure 6.2c confirms that there is PVP present, and the TEM image of AuNP-PVP represented in Figure 6.2d confirms an AuNP-PVP diameter of 2.2±0.9 nm. These AuNPs are used herein to study the key synthesis parameters for controlling the AuNP size and location when encapsulated in UiO-66(Zr(O*n*Pr)).

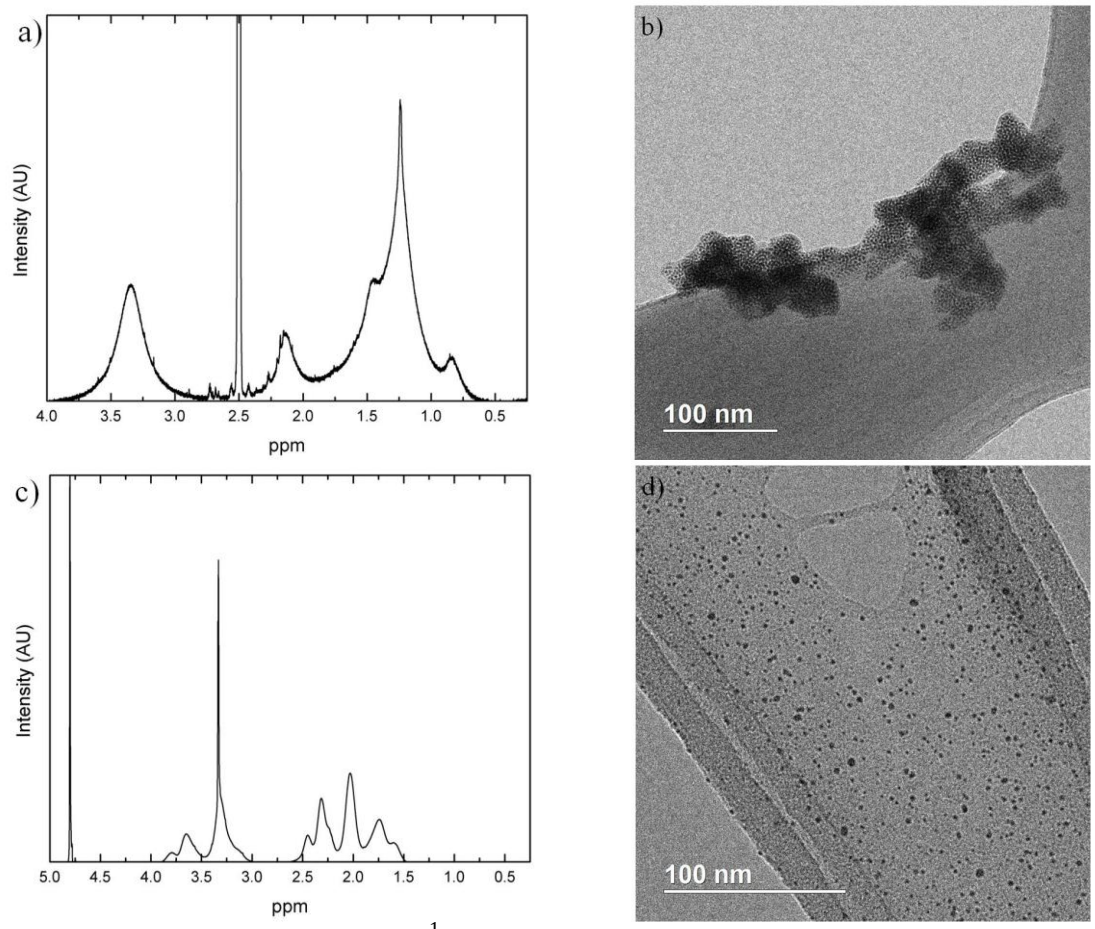

Figure 6.2: AuNP-DDT/MUA (a) ^{1}H NMR spectra and (b) TEM image and AuNP-PVP (c) ^{1}H NMR spectra and (d) TEM image

6.3.2 UiO-66 Crystal Structure and Porosity

Table 6.1 reports the synthesis parameters used to study the effects of MeOH:DMF ratio, acetic acid:Zr(O*n*Pr) ratio, AuNP capping agent, and UiO-66(Zr(O*n*Pr)) modulator on the physical properties of Au@UiO-66(Zr(O*n*Pr)). The MeOH:DMF and acetic acid:Zr(O*n*Pr) ratios were varied from 0-4.8 and 15-480, respectively. These bounds were selected to maximize the ratio ranges capable of producing highly porous, crystalline UiO-66(Zr(O*n*Pr)) as previously discovered by Tulig et al.[9] Additionally, the AuNP capping agent was varied to probe the effect of AuNP-DDT/MUA and AuNP-PVP. AuNP-DDT/MUA was chosen because the AuNP diameter

can be easily manipulated using the original AuNP-DDT synthesis procedure.[14] In addition, the ligand exchange procedure is a straightforward technique used to introduce functional sites, such as –COOH, to the AuNP surface. Therefore, this well-established, two-step procedure produces AuNPs that limit aggregation under ambient conditions due to DDT while also containing –COOH sites, from MUA, that can coordinate with the MOF metal centers during crystallization. Alternatively, AuNP-PVP was selected because PVP capped nanomaterials have effectively been incorporated in many MOFs including ZIF-8, UiO-66, and MIL-53.[4, 15] It has been suggested that PVP has two functions: (1) to stabilize the nanomaterials in solution and (2) to coordinate with the metal centers via weak interactions between the pyrrolidone ring (C=O) and the metal centers. Therefore, AuNP-PVP was chosen as an alternative system to probe the effect of the AuNP capping agent on Au@UiO-66(Zr(O*n*Pr)) properties. Lastly, the effect of UiO-66(Zr(O*n*Pr)) modulator was investigated using acetic acid and benzoic acid. These modulators were selected because they have both been previously used as UiO-66 modulators.[16] In addition, acetic acid and benzoic acid have significantly different geometries; and modulator geometry has been shown to effect MOF crystallization[17] and the introduction of defect sites.[18] Therefore, investigating the effect of acetic acid and benzoic acid on Au@UiO-66(Zr(O*n*Pr)) properties will also yield insight into the effect of defect sites.

Figure 6.3 shows the optical differences between UiO-66(Zr(O*n*Pr)) and as-synthesized Au@UiO-66(Zr(O*n*Pr)) prepared with various synthesis parameters. Although the optical differences are interesting to note, only limited conclusions can be drawn. Mainly, the resulting pink and brown powders strongly suggest that there are

AuNPs present since parent UiO-66 without AuNPs is a white powder. In addition, PXRD patterns, depicted in Figure 6.4, show that the UiO-66 structure is obtained for all of the synthesis conditions tested and nitrogen sorption at 77 K data, reported in Table 6.2, demonstrate that the porosity of all Au@UiO-66(Zr(O*n*Pr)) composites prepared herein are similar to parent UiO-66 synthesized with Zr(O*n*Pr).[9] Notably, the Au@UiO-66(Zr(O*n*Pr)) composites prepared with acetic acid:Zr(O*n*Pr) ratios of 240 and 480 and with a benzoic acid:Zr(O*n*Pr) ratio of 30 exhibit an increased porosity, which suggests that high acetic acid:Zr(O*n*Pr) ratios and a moderate benzoic acid:Zr(O*n*Pr) ratio introduce missing linker sites.[19] Whereas, for Au@UiO-66(Zr(O*n*Pr)) prepared with acetic acid:Zr(O*n*Pr) ratios less than 240, there is competitive coordination between acetic acid and BDC. However, the authors' speculate that the majority of the acetic acid molecules that coordinate with the Zr^{4+} ions to reduce the nucleation rate are exchanged with BDC during crystal growth, resulting in minimal missing linker sites.

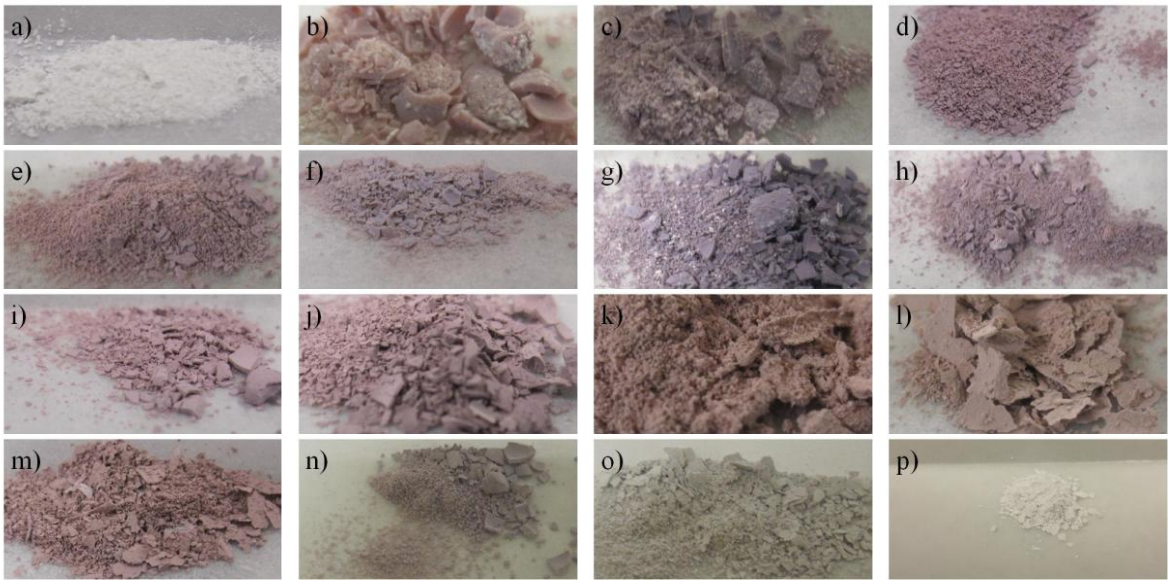

Figure 6.3: Images of (a) UiO-66(Zr(O*n*Pr)) and Au@UiO-66(Zr(O*n*Pr)) prepared by varying (a-e) the MeOH:DMF ratio from 0.0-4.8; (f-m) the acetic acid:Zr(O*n*Pr) ratio from 15-480; and (n-p) the AuNP capping agent and UiO-66 modulator

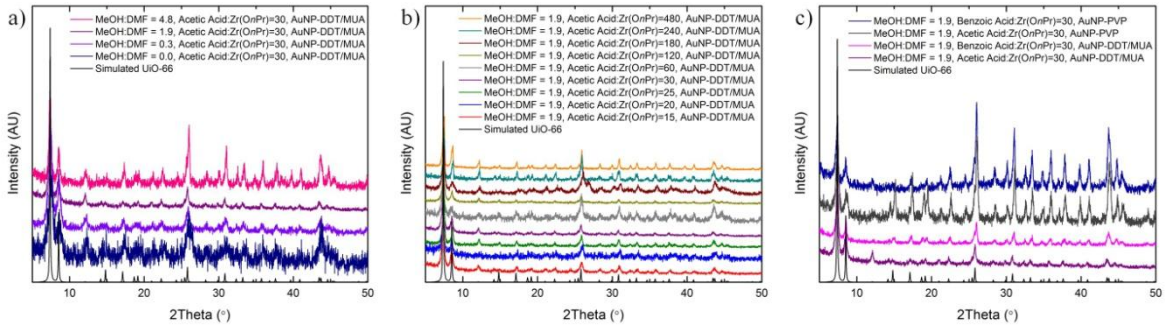

Figure 6.4: PXRD patterns for Au@UiO-66(Zr(O*n*Pr)) prepared by varying (a) the MeOH:DMF ratio, (b) acetic acid:Zr(O*n*Pr) ratio, and (c) AuNP capping agent and UiO-66(Zr(O*n*Pr)) modulator

Table 6.2: Porosity and AuNP diameters measured for Au@UiO-66(Zr(O*n*Pr)) prepared with various synthesis parameters

Au@UiO-66(Zr(O*n*Pr))	BET Surface Area (m^2/g)	Total Pore Volume (cm^3/g)[a]	AuNP Diameter (nm)
UiO-66(Zr(O*n*Pr))[9]	1155	0.56	-----
MeOH:DMF=0.0, acetic acid:Zr(O*n*Pr)=30, and AuNP-DDT/MUA	1120	0.52	11.6±3.6
MeOH:DMF=0.3, acetic acid:Zr(O*n*Pr)=30, and AuNP-DDT/MUA	1146	0.52	15.7±11.1
MeOH:DMF=1.9, acetic acid:Zr(O*n*Pr)=30, and AuNP-DDT/MUA	1142	0.46	8.2±3.1
MeOH:DMF=4.8, acetic acid:Zr(O*n*Pr)=30, and AuNP-DDT/MUA	1257	0.50	10.7±5.0
MeOH:DMF=1.9, acetic acid:Zr(O*n*Pr)=15, and AuNP-DDT/MUA	1173	0.51	3.0±1.5
MeOH:DMF=1.9, acetic acid:Zr(O*n*Pr)=20, and AuNP-DDT/MUA	936	0.40	6.5±4.8
MeOH:DMF=1.9, acetic acid:Zr(O*n*Pr)=25, and AuNP-DDT/MUA	1170	0.47	9.9±3.6
MeOH:DMF=1.9, acetic acid:Zr(O*n*Pr)=60, and AuNP-DDT/MUA	1198	0.48	8.9±3.1
MeOH:DMF=1.9, acetic acid:Zr(O*n*Pr)=120, and AuNP-DDT/MUA	1191	0.47	7.1±3.2
MeOH:DMF=1.9, acetic acid:Zr(O*n*Pr)=180, and AuNP-DDT/MUA	1179	0.45	5.8±2.9
MeOH:DMF=1.9, acetic acid:Zr(O*n*Pr)=240, and AuNP-DDT/MUA	1259	0.48	7.7±7.5
MeOH:DMF=1.9, acetic acid:Zr(O*n*Pr)=480, and AuNP-DDT/MUA	1319	0.53	14.8±11.1
MeOH:DMF=1.9, benzoic acid:Zr(O*n*Pr)=30, and AuNP-DDT/MUA	1405	0.60	3.2±1.1
MeOH:DMF=1.9, acetic acid:Zr(O*n*Pr)=30, and AuNP-PVP	1146	0.47	3.4±1.3
MeOH:DMF=1.9, benzoic acid:Zr(O*n*Pr)=30, and AuNP-PVP	1412	0.61	3.6±1.1

[a]Measured at $P/P_0 = 0.6$

6.3.3 Gold Nanoparticle (AuNP) Diameter

Table 6.2 reports the AuNP diameters for Au@UiO-66(Zr(O*n*Pr)) prepared utilizing various MeOH:DMF and acetic acid:Zr(O*n*Pr) ratios, AuNP capping agents, and UiO-66(Zr(O*n*Pr)) modulators. The MeOH:DMF ratio has an insignificant effect on the AuNP diameter; however, the acetic acid:Zr(O*n*Pr) ratio, AuNP capping agent, and UiO-66(Zr(O*n*Pr)) modulator substantially affect AuNP aggregation and growth. Figure 6.5 illustrates the relationship between the AuNP diameter and the acetic acid:Zr(O*n*Pr) ratio for Au@UiO-66(Zr(O*n*Pr)) prepared with a MeOH:DMF ratio of 1.9 and AuNP-DDT/MUA. At an acetic acid:Zr(O*n*Pr) ratio of 15, there is minimal AuNP growth; however, as the acetic acid:Zr(O*n*Pr) ratio increases, the AuNPs aggregate, resulting in significant particle growth and a considerably wider particle size distribution. A plausible explanation is that AuNP growth is promoted by the pH of the reaction medium. These AuNPs are capped with MUA, which functionalizes the AuNPs with –COOH groups that can be used to coordinate with MOF metal centers during crystallization. However, AuNPs capped with –COOH have the propensity to form hydrogen bonds resulting in AuNP aggregation and growth.[20, 21]

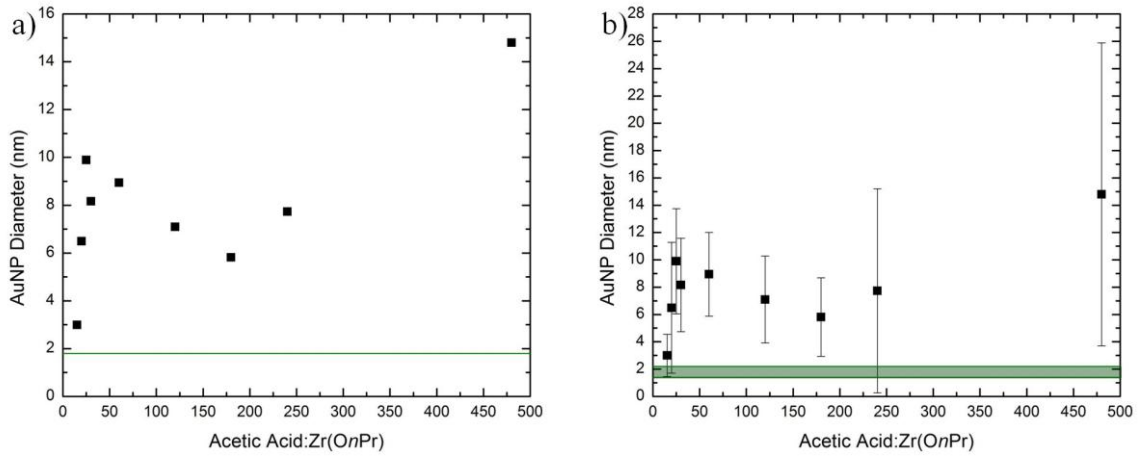

Figure 6.5: Relationship between acetic acid:Zr(O*n*Pr) and AuNP diameter. The green area represents the AuNP diameter of the preformed AuNPs

To confirm that the acetic acid concentration, and subsequent pH, is the main factor causing AuNP aggregation and growth, two experiments were conducted: (1) AuNP-DDT/MUA were stirred in a MeOH:DMF ratio of 1.9 (pH = 7.8) at 393 K for 24 h and (2) AuNP-DDT/MUA were stirred in MeOH:DMF ratio of 1.9, and acetic acid:Zr(O*n*Pr) ratio of 30 (pH = 4.4) at 393 K for 24 h. Figure 6.6 shows that under acidic conditions, AuNP aggregates form; whereas without acetic acid, the AuNPs remain suspended in solution suggesting that the pH is the decisive factor driving AuNP growth during Au@UiO-66(Zr(O*n*Pr)) crystallization. Conversely, when Au@UiO-66(Zr(O*n*Pr)) is prepared with AuNP-DDT/MUA and a benzoic acid:Zr(O*n*Pr) ratio of 30, AuNP growth is minimal. As previously stated, preparation with a benzoic acid:Zr(O*n*Pr) ratio of 30 introduces missing linker defect sites on the Zr^{4+} ions, onto which the –COOH functionalization of AuNP-DDT/MUA can coordinate. This retards AuNP-DDT/MUA aggregation. The authors' speculate that the AuNP-DDT/MUA coordinate to missing linker defects in UiO-66 before hydrogen bonding occurs, therefore, incorporating the AuNPs in the UiO-66(Zr(O*n*Pr)) structure while limiting AuNP growth.

Lastly, when Au@UiO-66(Zr(O*n*Pr)) is prepared with AuNP-PVP, neither modulator generates AuNP-PVP growth. AuNP-PVP stability towards growth likely stems from the lack of hydrogen bonding. AuNP-PVP is suspended in the polar solution by the pyrrolidone (C=O) ring which is incapable of forming hydrogen bonds, therefore, limiting AuNP aggregation under acidic conditions.

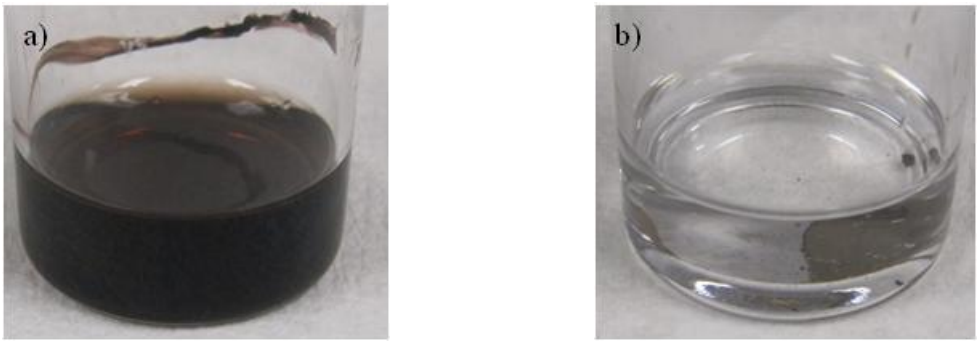

Figure 6.6: (a) AuNP-DDT/MUA stirred in MeOH and DMF (pH = 7.8) at 393 K for 24 h and (b) AuNP-DDT/MUA stirred in MeOH, DMF, and acetic acid (pH = 4.4) at 393 K for 24 h

6.3.4 UiO-66(Zr(O*n*Pr)) Particle Geometry

MOF formation is often extremely sensitive to the synthesis parameters employed.[22] Specifically, the particle geometry can be controlled by altering the reaction medium and tuning the modulation effect.[16, 23-25] Figures 6.7-6.21 demonstrate that the MeOH:DMF and acetic acid:Zr(O*n*Pr) ratios have a significant effect on the UiO-66(Zr(O*n*Pr)) particle geometry; however, exchanging benzoic acid for acetic acid has a minimal effect on MOF geometry. Figures 6.7-6.10 show the MeOH:DMF ratio effect on the UiO-66(Zr(O*n*Pr)) particle diameter and shape. Specifically, as the MeOH:DMF ratio is increased, the UiO-66 particle diameter increases. The addition of MeOH to the mother solution enhances UiO-66(Zr(O*n*Pr)) particle growth. This could occur via two potential

mechanisms: (1) MeOH acts as a modulator competing with BDC for coordination sites or (2) the reduced solubility of BDC in MeOH affects the nucleation rate. The modulation effect would occur when MeOH dissociates into MeO^- and H^+ ions; then the MeO^- anions competitively coordinate with Zr^{4+}. However, MeOH dissociation requires elevated temperatures exceeding 433K[26] suggesting that this is unlikely. Alternatively, BDC is less soluble in MeOH than in DMF; therefore, the supersaturation concentration is decreased, which subsequently reduces nucleation. Additionally, a MeOH:DMF ratio of 0.3 produces two UiO-66 particle shapes: the conventional cubic UiO-66 particles and unexpected spindle-shaped particles, depicted in Figure 6.8. At low concentrations, MeOH has structure directing properties, which are related to the solvent polarity and hydrogen bond donation properties.[23, 27] Therefore, varying the MeOH:DMF ratio affects the reaction medium properties, such as polarity and hydrogen bond donation, which subsequently introduces structure directing properties and enhances the crystal growth of UiO-66(Zr(O*n*Pr)).

Additionally, the acetic acid:Zr(O*n*Pr) ratio has a significant effect on the UiO-66(Zr(O*n*Pr)) particle diameter and morphology. Figures 6.11-6.18 show that as the acetic acid:Zr(O*n*Pr) ratio increases, the UiO-66 particle diameter increases. This occurs due to a modulation effect; acetic acid competes with BDC to coordinate with Zr^{4+} sites to regulate nucleation, then exchanges with BDC during crystal growth.[9, 16] Additionally, Figures 6.16-6.18 reveal the formation of a secondary phase or impurity, identified as wire- or rod-shaped particles. In addition to controlling MOF particle size, the modulation technique has also been utilized to control the morphology.[24, 25, 28] Therefore, the rod-shaped UiO-66(Zr(O*n*Pr)) particles are potentially formed when acetic acid

inhibits crystallization in a specific direction that cannot be discerned by the available data.

6.3.5 AuNP Location

Control over the AuNP location within the UiO-66(Zr(O*n*Pr)) particles is paramount for the controlled preparation of HCl-sensitive UiO-66(Zr(O*n*Pr)) composites designed for specific applications. Therefore, understanding the key synthesis factors for AuNP location is necessary. TEM was used to investigate the AuNP location in Au@UiO-66(Zr(O*n*Pr)) prepared with various synthesis parameters. Figures 6.7-6.21 show that the acetic acid:Zr(O*n*Pr), AuNP capping agents, and UiO-66(Zr(O*n*Pr)) modulator potentially affect the AuNP location, whereas the MeOH:DMF ratio does not. Briefly, Figures 6.7-6.10 show that the AuNPs for all MeOH:DMF ratios results in Au@UiO-66(Zr(O*n*Pr)) composites with AuNPs randomly distributed throughout the material with many AuNPs definitively located on the surface of the UiO-66(Zr(O*n*Pr)) particles. The TEM images show that many of the AuNPs are on either both the UiO-66(Zr(O*n*Pr)) particles and the TEM grid or on two UiO-66(Zr(O*n*Pr)) particles.

Alternatively, Figures 6.11-6.18 show that the acetic acid:Zr(O*n*Pr) ratio potentially affects the AuNP location within the UiO-66(Zr(O*n*Pr)) particles. For Au@UiO-66(Zr(O*n*Pr)) synthesized with an acetic acid:Zr(O*n*Pr) ratio of 15, AuNPs were observed in the filtrate after crystallization suggesting that there was incomplete retention of AuNPs, which will result in a lower concentration of particles in the composite. Figure 6.11 reveals AuNPs approximately 3.0 nm in diameter dispersed in or on the UiO-66(Zr(O*n*Pr)) particles without any definitive surface based AuNPs.

However, merely seventeen AuNPs were located from 34 various grid locations using TEM. Therefore, due to statistical limitations, broader conclusions about the AuNP diameter and location cannot be drawn. Figures 6.12-6.18 depict the TEM images for composites prepared with the acetic acid:Zr(O*n*Pr) ratio ranging from 20-480 revealing AuNPs that have grown in diameter and are scattered randomly throughout the Au@UiO-66(Zr(O*n*Pr)) material. However, many AuNPs are distinctly on the surface of the UiO-66(Zr(O*n*Pr)) particles. For Au@UiO-66(Zr(O*n*Pr)) composites prepared with the acetic acid:Zr(O*n*Pr) ratio ranging from 120-480, depicted in Figures 6.15-6.18, the larger UiO-66(Zr(O*n*Pr)) particles support multiple AuNPs that are potentially within the UiO-66(Zr(O*n*Pr)) particles. Unfortunately, TEM is a two-dimensional technique so further analysis is necessary to confirm AuNP location. However, the display of potential confinement suggests that the UiO-66(Zr(O*n*Pr)) particle diameter is a significant factor for incorporating AuNPs, specifically that larger UiO-66(Zr(O*n*Pr)) particles are more likely to encase AuNPs. There are two potential explanations: (1) the AuNPs coordinate on missing linker defect sites which were suggested to occur at acetic acid:Zr(O*n*Pr) ratios exceeding 120 and/or (2) AuNP incorporation does not occur during nucleation (AuNP induced nucleation), but rather are encased within the particles during crystal growth, therefore, slower growth rates would effectively incorporate more AuNPs within the UiO-66(Zr(O*n*Pr)).

Furthermore, Figure 6.9 and Figures 6.19-6.21 portray the TEM images for the Au@UiO-66(Zr(O*n*Pr)) composites prepared by varying the AuNP capping agent and UiO-66(Zr(O*n*Pr)) modulator. Figure 6.9 shows that the use of AuNP-DDT/MUA and acetic acid results in a material with AuNPs 8.2 nm in diameter scattered throughout the

Au@UiO-66(Zr(O*n*Pr)) composites. In addition, there are several AuNPs that are definitively deposited on the surface of the UiO-66 particles. Alternatively, Au@UiO-66(Zr(O*n*Pr)) prepared with AuNP-DDT/MUA and a benzoic acid:Zr(O*n*Pr) ratio of 30, depicted in Figure 6.19, reveals a limited number of AuNPs 3.2 nm in diameter scattered throughout the UiO-66(Zr(O*n*Pr)) particles. From the obtained images, shown in Figure 6.19, no AuNPs are observed on the UiO-66 particles' surfaces; however, there is a limited number of AuNPs observed. The contrast between AuNPs 3 nm in diameter and UiO-66(Zr(O*n*Pr)) particles, even when deposited on the UiO-66(Zr(O*n*Pr)) surface, is limited. This will make detecting AuNPs confined within UiO-66(Zr(O*n*Pr)) particles using TEM a challenge. Therefore, the combination of a colorless filtrate, a brown powder (Figure 6.3n), and difficulty locating AuNPs in TEM suggests that the AuNPs do not aggregate and are potentially confined within the UiO-66 particles. However, further investigations are necessary to confirm this hypothesis.

Lastly, for Au@UiO-66(Zr(O*n*Pr)) synthesized with AuNP-PVP and both acetic acid and benzoic acid, the AuNP-PVP are decisively on the surface of the UiO-66(Zr(O*n*Pr)) particles. In addition, there was a significant number of AuNPs not retained in the Au@UiO-66(Zr(O*n*Pr)) composites for both modulators surmised by the pink filtrate. This is also suggested by from the pale brown and pink powders presented in Figure 6.3o and 6.3p. Huo et al. observed that competitive coordination of excess PVP inhibits the incorporation of the PVP-modified AuNPs in ZIF-8.[4] Additionally, most of the AuNPs were deposited on the ZIF-8 surface. Therefore, excess PVP conceivably remains in the AuNP solution resulting in competitive coordination which limits AuNP

incorporation. Thus, further analysis of AuNP-PVP is necessary to determine if excess PVP is present.

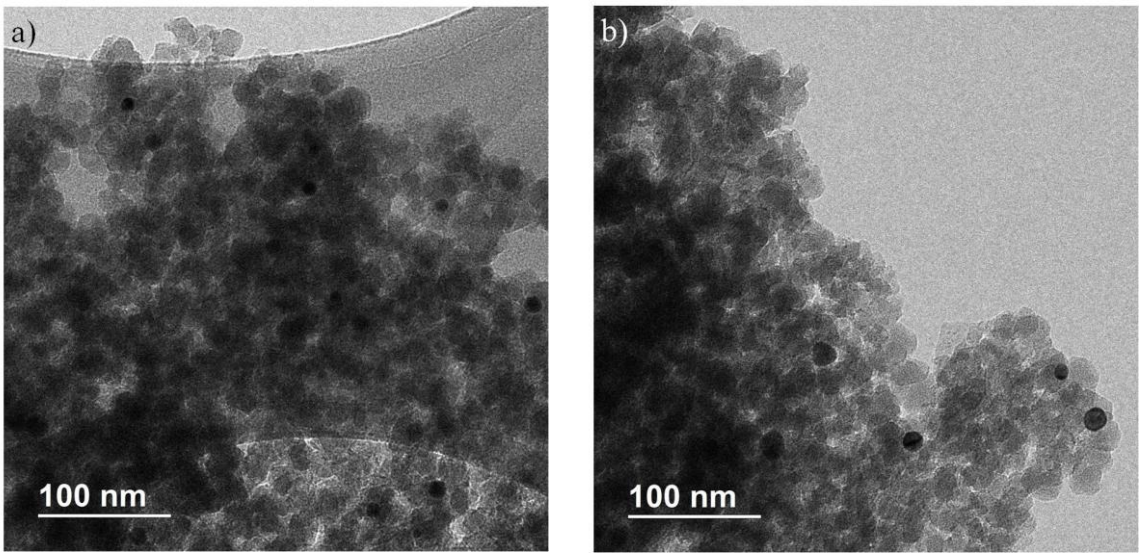

Figure 6.7: TEM images for Au@UiO-66(Zr(O*n*Pr)) prepared with a MeOH:DMF ratio of 0.0, an acetic acid:Zr(O*n*Pr) ratio of 30, and AuNP-DDT/MUA

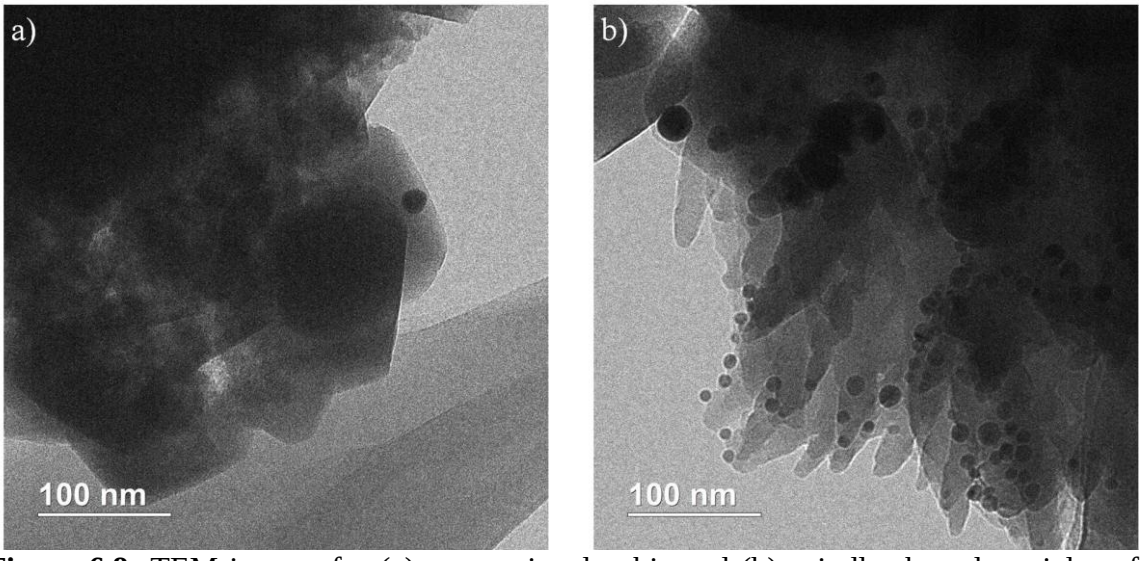

Figure 6.8: TEM images for (a) conventional cubic and (b) spindle-shaped particles of Au@UiO-66(Zr(O*n*Pr)) prepared with a MeOH:DMF ratio of 0.3, an acetic acid:Zr(O*n*Pr) ratio of 30, and AuNP-DDT/MUA

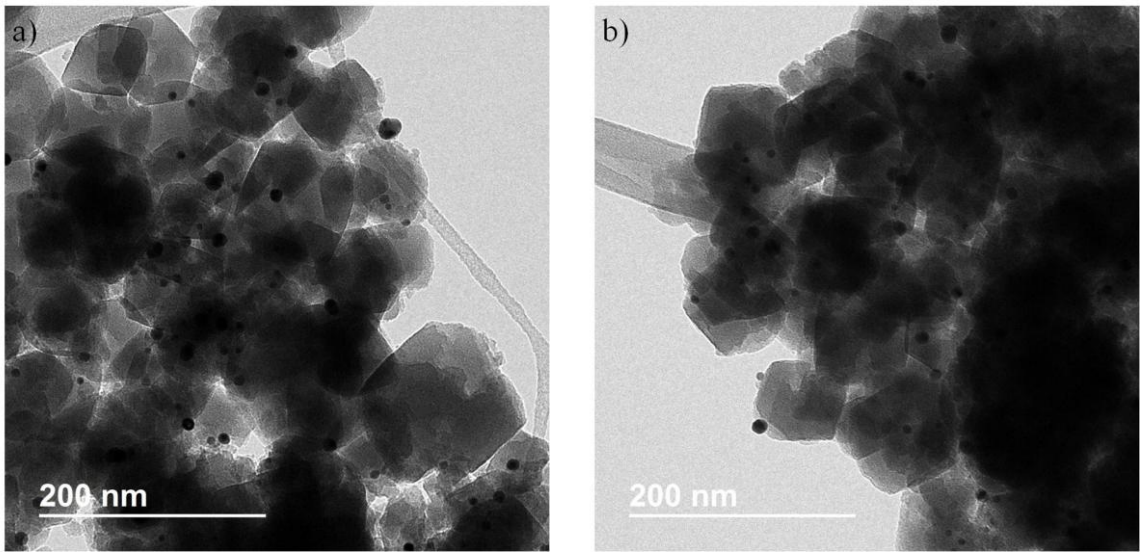

Figure 6.9: TEM images for Au@UiO-66(Zr(O*n*Pr)) prepared with a MeOH:DMF ratio of 1.9, an acetic acid:Zr(O*n*Pr) ratio of 30, and AuNP-DDT/MUA

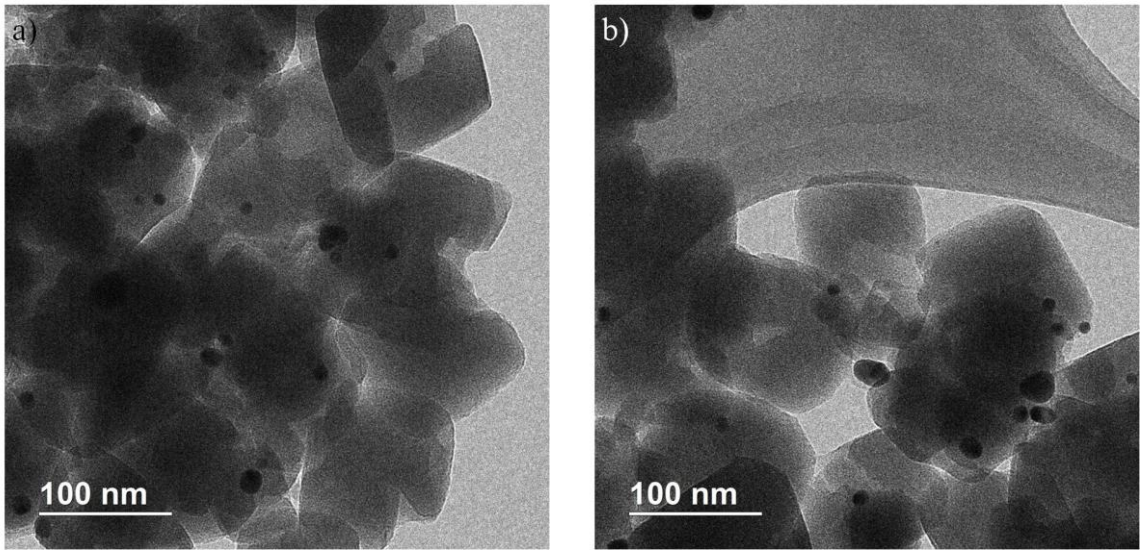

Figure 6.10: TEM images for Au@UiO-66(Zr(O*n*Pr)) prepared with a MeOH:DMF ratio of 4.8, an acetic acid:Zr(O*n*Pr) ratio of 30, and AuNP-DDT/MUA

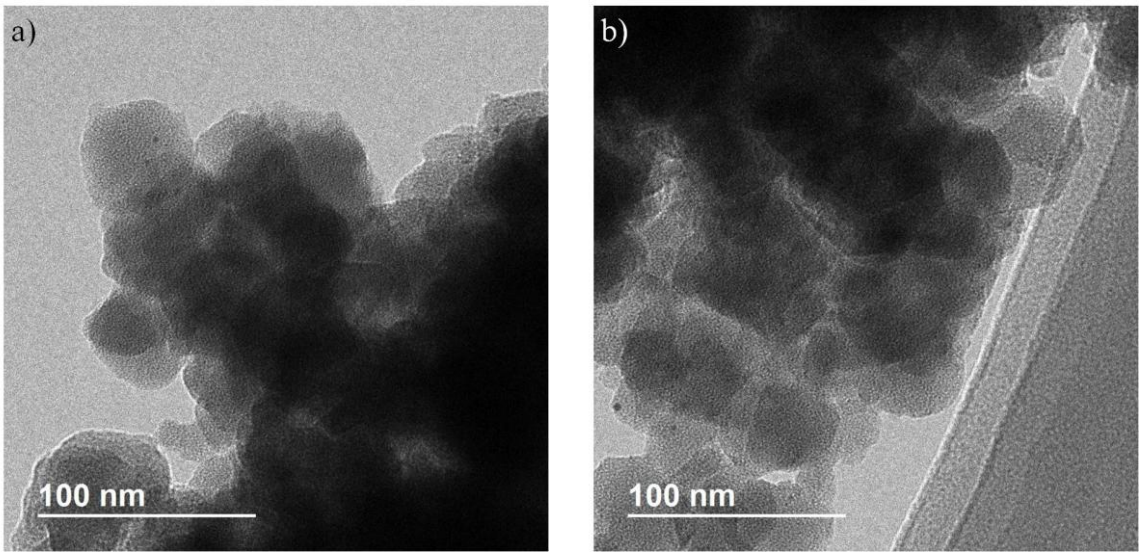

Figure 6.11: TEM images for Au@UiO-66(Zr(O*n*Pr)) prepared with a MeOH:DMF ratio of 1.9, an acetic acid:Zr(O*n*Pr) ratio of 15, and AuNP-DDT/MUA

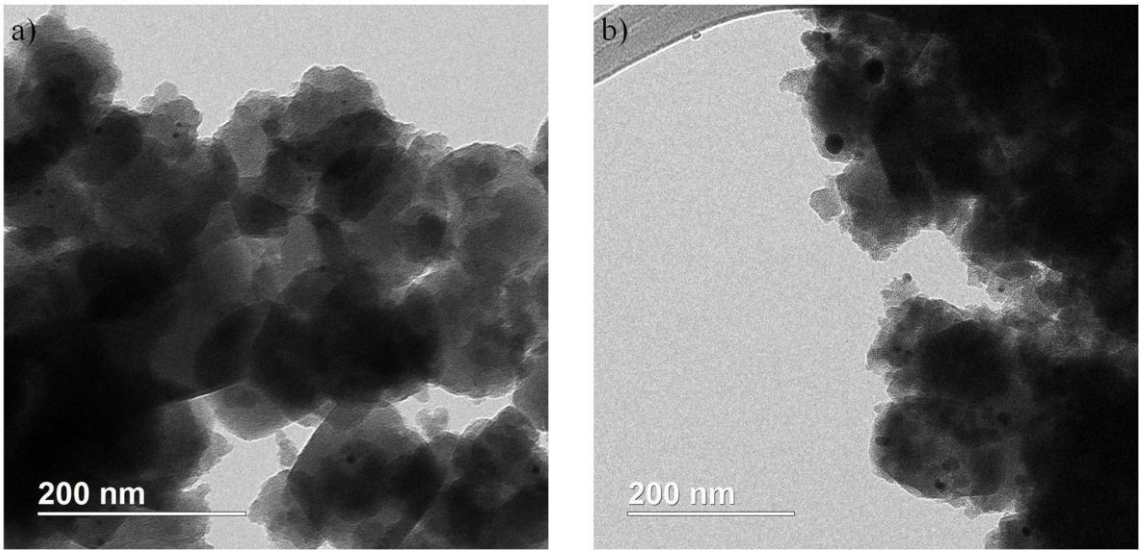

Figure 6.12: TEM images for Au@UiO-66(Zr(O*n*Pr)) prepared with a MeOH:DMF ratio of 1.9, an acetic acid:Zr(O*n*Pr) ratio of 20, and AuNP-DDT/MUA

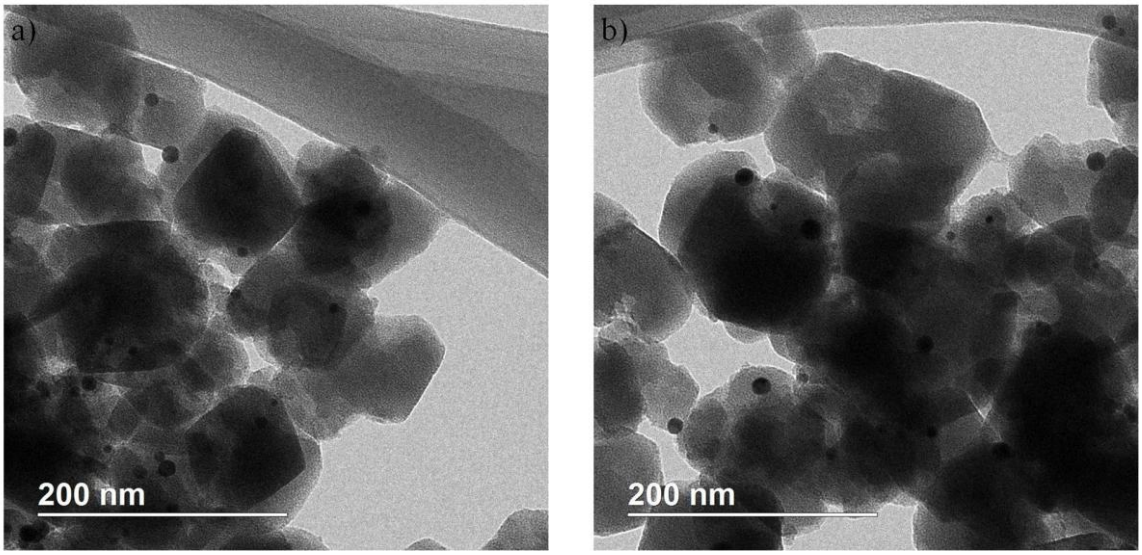

Figure 6.13: TEM images for Au@UiO-66(Zr(O*n*Pr)) prepared with a MeOH:DMF ratio of 1.9, an acetic acid:Zr(O*n*Pr) ratio of 25, and AuNP-DDT/MUA

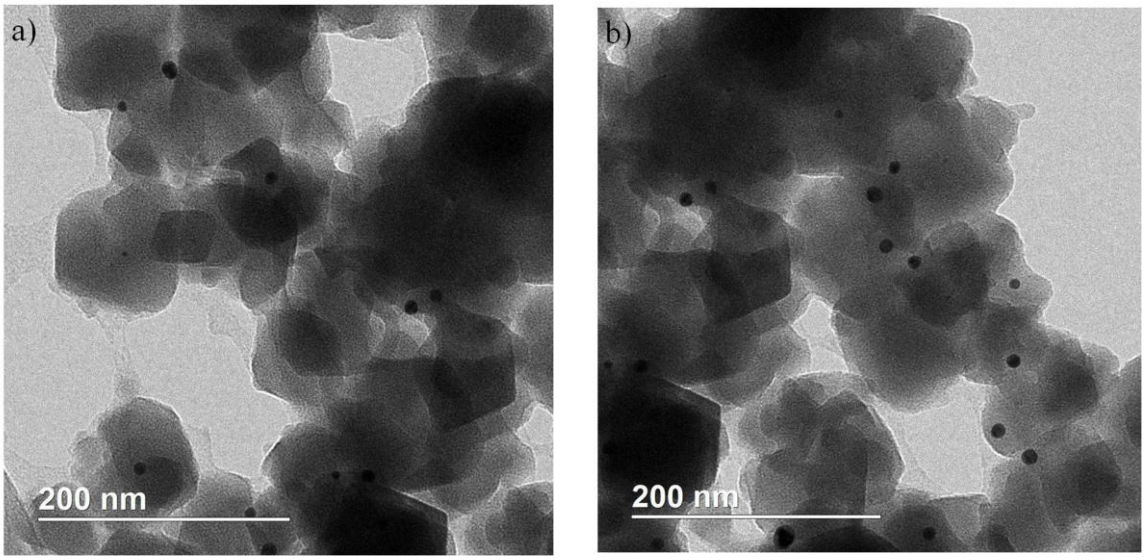

Figure 6.14: TEM images for Au@UiO-66(Zr(O*n*Pr)) prepared with a MeOH:DMF ratio of 1.9, an acetic acid:Zr(O*n*Pr) ratio of 60, and AuNP-DDT/MUA

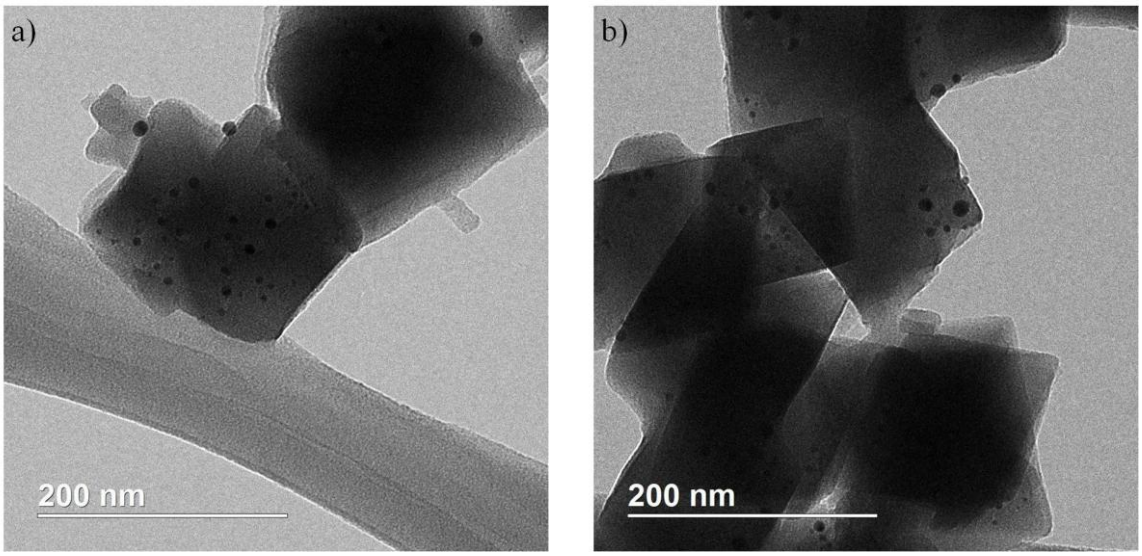

Figure 6.15: TEM images for Au@UiO-66(Zr(O*n*Pr)) prepared with a MeOH:DMF ratio of 1.9, an acetic acid:Zr(O*n*Pr) ratio of 120, and AuNP-DDT/MUA

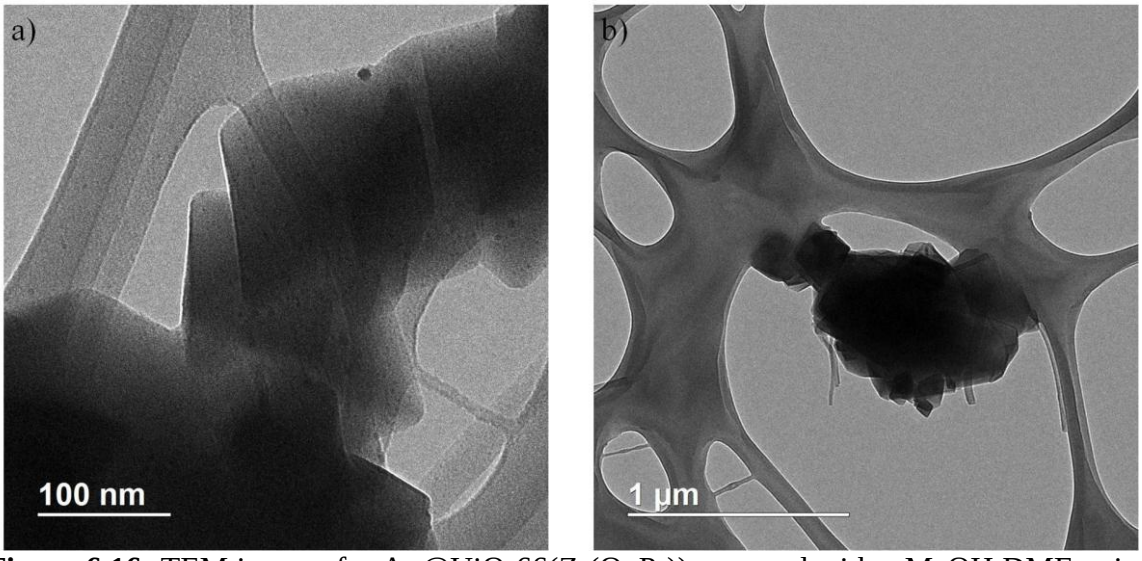

Figure 6.16: TEM images for Au@UiO-66(Zr(O*n*Pr)) prepared with a MeOH:DMF ratio of 1.9, an acetic acid:Zr(O*n*Pr) ratio of 180, and AuNP-DDT/MUA

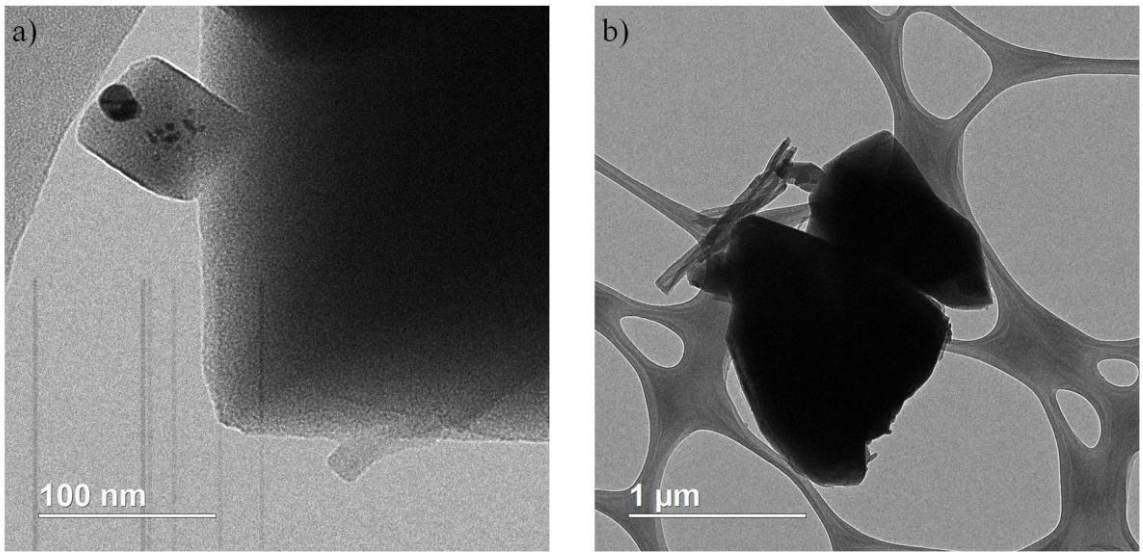

Figure 6.17: TEM images for Au@UiO-66(Zr(O*n*Pr)) prepared with a MeOH:DMF ratio of 1.9, an acetic acid:Zr(O*n*Pr) ratio of 240, and AuNP-DDT/MUA

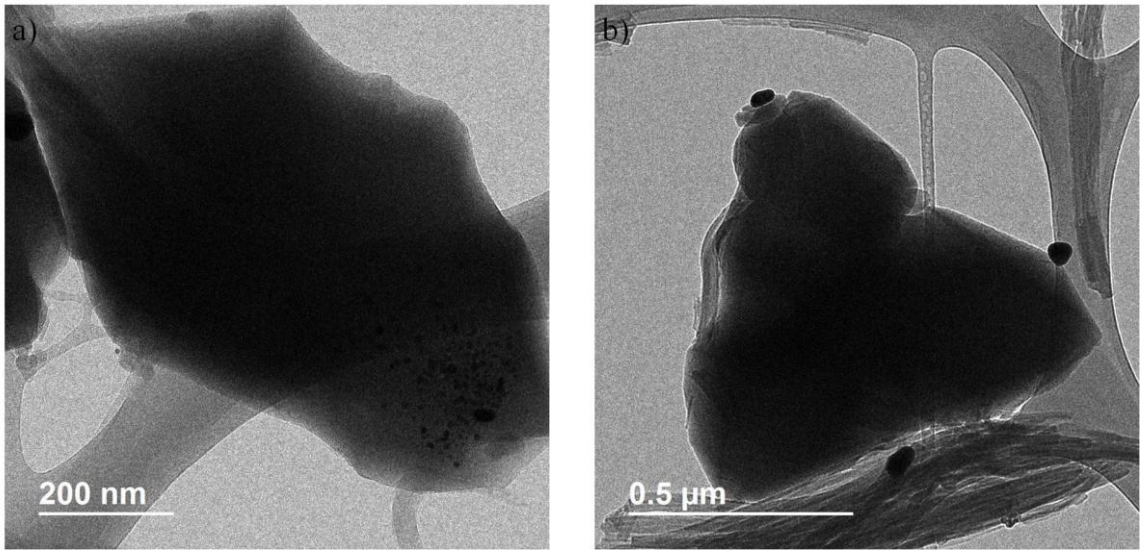

Figure 6.18: TEM images for Au@UiO-66(Zr(O*n*Pr)) prepared with a MeOH:DMF ratio of 1.9, an acetic acid:Zr(O*n*Pr) ratio of 480, and AuNP-DDT/MUA

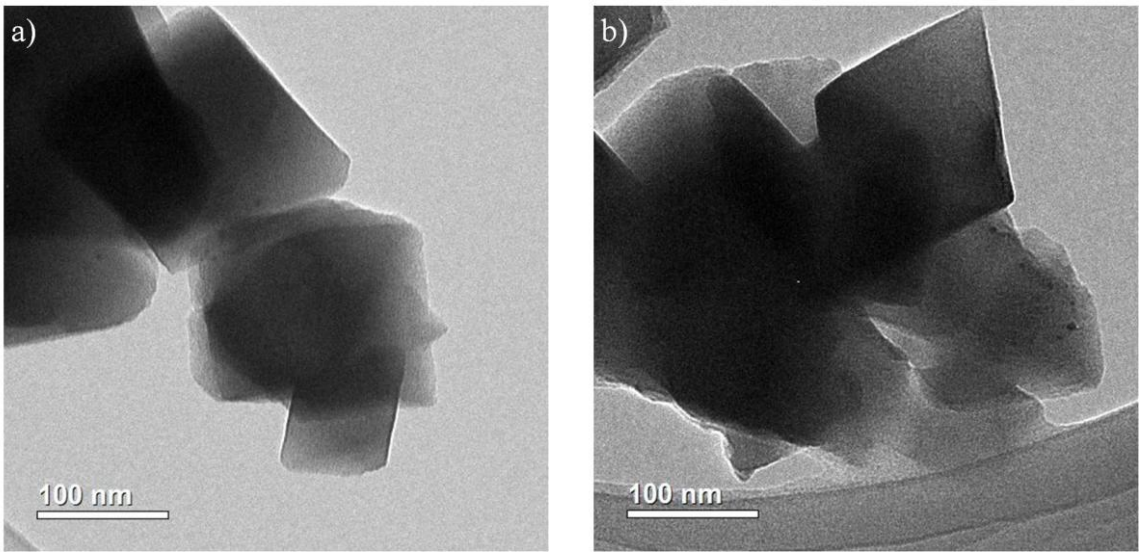

Figure 6.19: TEM images for Au@UiO-66(Zr(O*n*Pr)) prepared with a MeOH:DMF ratio of 1.9, a benzoic acid:Zr(O*n*Pr) ratio of 30, and AuNP-DDT/MUA

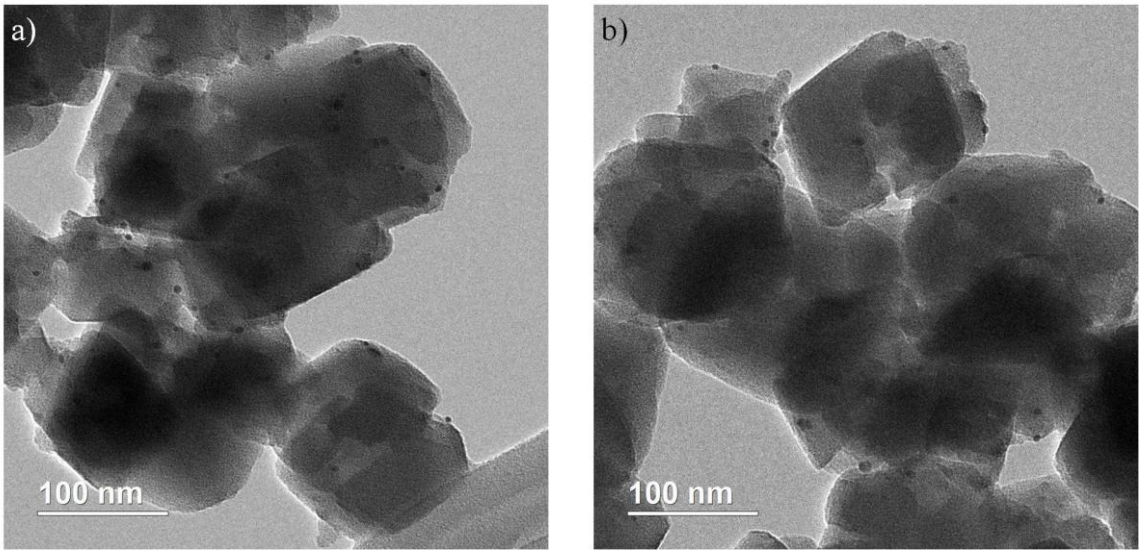

Figure 6.20: TEM images for Au@UiO-66(Zr(O*n*Pr)) prepared with a MeOH:DMF ratio of 1.9, an acetic acid:Zr(O*n*Pr) ratio of 30, and AuNP-PVP

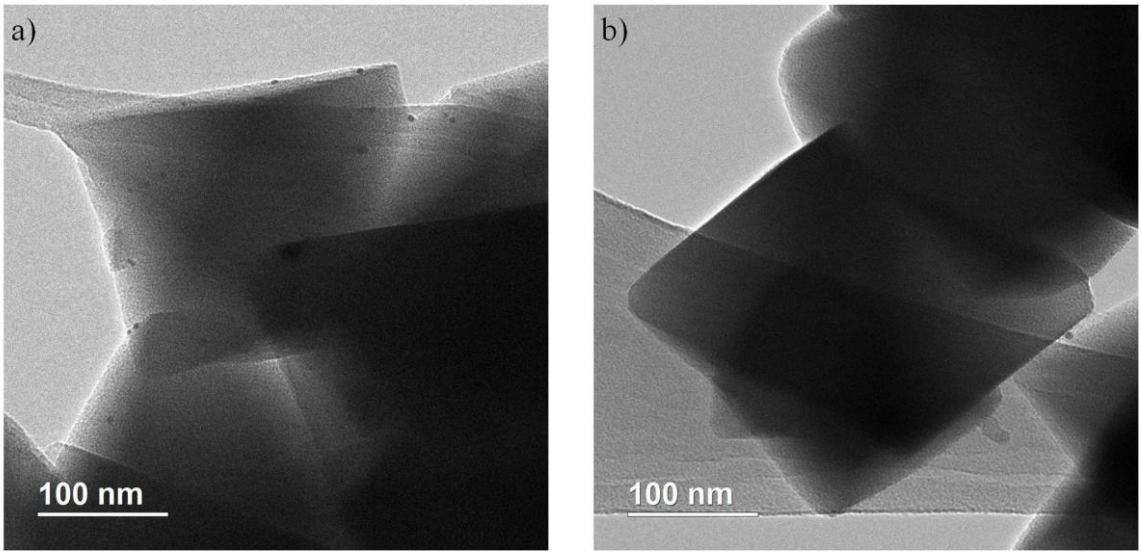

Figure 6.21: TEM images for Au@UiO-66(Zr(O*n*Pr)) prepared with a MeOH:DMF ratio of 1.9, a benzoic acid:Zr(O*n*Pr) ratio of 30, and AuNP-PVP

6.4 Conclusions

These studies show that the AuNP capping ligand and UiO-66 modulator have the most prominent effects on the Au@UiO-66(Zr(O*n*Pr)) properties such as AuNP diameter and location and UiO-66(Zr(O*n*Pr)) particle diameter and shape. Specifically, the choice of capping ligand significantly affects the propensity for the AuNPs to aggregate and grow. AuNP-DDT/MUA aggregate due to hydrogen bonding under the acidic conditions necessary for UiO-66 crystallization with acetic acid, whereas AuNP-PVP aggregation is not observed under acidic conditions. In addition, the modulator has a significant impact on the composite properties. Although increased concentrations of acetic acid resulted in AuNP-DDT/MUA aggregation and growth, the AuNPs were potentially confined within UiO-66(Zr(O*n*Pr)) particles. This confinement could be a product of the increased number of defect sites introduced during crystallization and/or the reduced crystal growth which encourages AuNP incorporation. Alternatively, substituting benzoic acid, which is known to introduce missing linker defect sites, as the modulator minimized AuNP-

DDT/MUA growth. However, AuNP-DDT/MUA location could not be established because only a limited number of AuNP-DDT/MUA were located using TEM. This could suggest that the 3 nm AuNPs are confined within the particles because the contrast of the small AuNPs within the zirconium-based MOF would be negligible. However, further investigations are necessary to confirm or reject this hypothesis. Additional studies for Au@UiO-66(Zr(O*n*Pr)) prepared with AuNP-DDT/MUA and benzoic acid should be performed including size selective catalysis or STEM tomography to further probe the AuNP size and location. Lastly, additional investigations of AuNP-PVP encapsulation in UiO-66(Zr(O*n*Pr)) should be implemented after confirming that AuNP-PVP is properly prepared.

6.5 References

1. Kitagawa, S.; Kitaura, R.; Noro, S., Functional porous coordination polymers. *Angewandte Chemie-International Edition* **2004,** *43* (18), 2334-2375.

2. Ferey, G., Hybrid porous solids: past, present, future. *Chemical Society Reviews* **2008,** *37* (1), 191-214.

3. Falcaro, P.; Ricco, R.; Yazdi, A.; Imaz, I.; Furukawa, S.; Maspoch, D.; Ameloot, R.; Evans, J. D.; Doonan, C. J., Application of metal and metal oxide nanoparticles@MOFs. *Coordination Chemistry Reviews* **2016,** *307*, 237-254.

4. Lu, G.; Li, S.; Guo, Z.; Farha, O. K.; Hauser, B. G.; Qi, X.; Wang, Y.; Wang, X.; Han, S.; Liu, X.; DuChene, J. S.; Zhang, H.; Zhang, Q.; Chen, X.; Ma, J.; Loo, S. C. J.; Wei, W. D.; Yang, Y.; Hupp, J. T.; Huo, F., Imparting functionality to a metal-organic framework material by controlled nanoparticle encapsulation. *Nature Chemistry* **2012,** *4* (4), 310-316.

5. Cavka, J. H.; Jakobsen, S.; Olsbye, U.; Guillou, N.; Lamberti, C.; Bordiga, S.; Lillerud, K. P., A new zirconium inorganic building brick forming metal organic frameworks with exceptional stability. *Journal of the American Chemical Society* **2008,** *130* (42), 13850-13851.

6. Schoenecker, P. M.; Carson, C. G.; Jasuja, H.; Flemming, C. J. J.; Walton, K. S., Effect of Water Adsorption on Retention of Structure and Surface Area of Metal-Organic Frameworks. *Industrial & Engineering Chemistry Research* **2012,** *51* (18), 6513-6519.

7. Biswas, S.; Van der Voort, P., A General Strategy for the Synthesis of Functionalised UiO-66 Frameworks: Characterisation, Stability and CO_2 Adsorption Properties. *European Journal of Inorganic Chemistry* **2013,** (12), 2154-2160.

8. Daniel, M. C.; Astruc, D., Gold nanoparticles: Assembly, supramolecular chemistry, quantum-size-related properties, and applications toward biology, catalysis, and nanotechnology. *Chemical Reviews* **2004,** *104* (1), 293-346.

9. Tulig, K.; Walton, K. S., An alternative UiO-66 synthesis for HCl-sensitive nanoparticle encapsulation. *RSC Advances* **2014,** *4* (93), 51080-51083.

10. Brust, M.; Walker, M.; Bethell, D.; Schiffrin, D. J.; Whyman, R., Synthesis of thiol-derivatised gold nanoparticles in a two-phase Liquid-Liquid system. *Journal of the Chemical Society-Chemical Communications* **1994,** (7), 801-802.

11. Hostetler, M. J.; Templeton, A. C.; Murray, R. W., Dynamics of place-exchange reactions on monolayer-protected gold cluster molecules. *Langmuir* **1999,** *15* (11), 3782-3789.

12. Liu, H. L.; Liu, Y. L.; Li, Y. W.; Tang, Z. Y.; Jiang, H. F., Metal-Organic Framework Supported Gold Nanoparticles as a Highly Active Heterogeneous Catalyst for Aerobic Oxidation of Alcohols. *Journal of Physical Chemistry C* **2010,** *114* (31), 13362-13369.

13. Tsunoyama, H.; Sakurai, H.; Negishi, Y.; Tsukuda, T., Size-specific catalytic activity of polymer-stabilized gold nanoclusters for aerobic alcohol oxidation in water. *Journal of the American Chemical Society* **2005,** *127* (26), 9374-9375.

14. Hostetler, M. J.; Wingate, J. E.; Zhong, C. J.; Harris, J. E.; Vachet, R. W.; Clark, M. R.; Londono, J. D.; Green, S. J.; Stokes, J. J.; Wignall, G. D.; Glish, G. L.; Porter, M. D.; Evans, N. D.; Murray, R. W., Alkanethiolate gold cluster molecules with core diameters from 1.5 to 5.2 nm: Core and monolayer properties as a function of core size. *Langmuir* **1998,** *14* (1), 17-30.

15. Zhang, W. N.; Lu, G.; Cui, C. L.; Liu, Y. Y.; Li, S. Z.; Yan, W. J.; Xing, C.; Chi, Y. R.; Yang, Y. H.; Huo, F. W., A Family of Metal-Organic Frameworks Exhibiting Size-Selective Catalysis with Encapsulated Noble-Metal Nanoparticles. *Advanced Materials* **2014,** *26* (24), 4056-4060.

16. Schaate, A.; Roy, P.; Godt, A.; Lippke, J.; Waltz, F.; Wiebcke, M.; Behrens, P., Modulated Synthesis of Zr-Based Metal-Organic Frameworks: From Nano to Single Crystals. *Chemistry-a European Journal* **2011,** *17* (24), 6643-6651.

17. Diring, S.; Furukawa, S.; Takashima, Y.; Tsuruoka, T.; Kitagawa, S., Controlled Multiscale Synthesis of Porous Coordination Polymer in Nano/Micro Regimes. *Chemistry of Materials* **2010,** *22* (16), 4531-4538.

18. Gutov, O. V.; Hevia, M. G.; Escudero-Adán, E. C.; Shafir, A., Metal–Organic Framework (MOF) Defects under Control: Insights into the Missing Linker Sites and Their Implication in the Reactivity of Zirconium-Based Frameworks. *Inorganic Chemistry* **2015,** *54* (17), 8396-8400.

19. Wu, H.; Chua, Y. S.; Krungleviciute, V.; Tyagi, M.; Chen, P.; Yildirim, T.; Zhou, W., Unusual and Highly Tunable Missing-Linker Defects in Zirconium Metal–Organic Framework UiO-66 and Their Important Effects on Gas Adsorption. *Journal of the American Chemical Society* **2013,** *135* (28), 10525-10532.

20. Johnson, S. R.; Evans, S. D.; Brydson, R., Influence of a terminal functionality on the physical properties of surfactant-stabilized gold nanoparticles. *Langmuir* **1998,** *14* (23), 6639-6647.

21. Su, C.-H.; Wu, P.-L.; Yeh, C.-S., pH Dependence of Interparticle Coupling for Gold Nanoparticle Assemblies Formation: Electrostatic Attraction and Hydrogen Bonding. *Bulletin of the Chemical Society of Japan* **2004,** *77* (1), 189-193.

22. Stock, N.; Biswas, S., Synthesis of Metal-Organic Frameworks (MOFs): Routes to Various MOF Topologies, Morphologies, and Composites. *Chemical Reviews* **2012,** *112* (2), 933-969.

23. Bustamante, E. L.; Fernandez, J. L.; Zamaro, J. M., Influence of the solvent in the synthesis of zeolitic imidazolate framework-8 (ZIF-8) nanocrystals at room temperature. *Journal of Colloid and Interface Science* **2014,** *424*, 37-43.

24. Tsuruoka, T.; Furukawa, S.; Takashima, Y.; Yoshida, K.; Isoda, S.; Kitagawa, S., Nanoporous Nanorods Fabricated by Coordination Modulation and Oriented Attachment Growth. *Angewandte Chemie-International Edition* **2009,** *48* (26), 4739-4743.

25. Umemura, A.; Diring, S.; Furukawa, S.; Uehara, H.; Tsuruoka, T.; Kitagawa, S., Morphology Design of Porous Coordination Polymer Crystals by Coordination Modulation. *Journal of the American Chemical Society* **2011,** *133* (39), 15506-15513.

26. Bauer, S.; Serre, C.; Devic, T.; Horcajada, P.; Marrot, J.; Ferey, G.; Stock, N., High-throughput assisted rationalization of the formation of metal organic

frameworks in the iron(III) aminoterephthalate solvothermal system. *Inorganic Chemistry* **2008,** *47* (17), 7568-7576.

27. Chen, D. M.; Zhang, X. P.; Shi, W.; Cheng, P., Tuning Two-Dimensional Layer to Three-Dimensional Pillar-Layered Metal-Organic Frameworks: Polycatenation and Interpenetration Behaviors. *Crystal Growth & Design* **2014,** *14* (12), 6261-6268.

28. Luan, Y.; Qi, Y.; Jin, Z.; Peng, X.; Gao, H.; Wang, G., Synthesis of a flower-like Zr-based metal-organic framework and study of its catalytic performance in the Mannich reaction. *RSC Advances* **2015,** *5* (25), 19273-19278.

CHAPTER 7

EXTENDING THE HCl-FREE SYNTHESIS TO INCLUDE UIO-66 ANALOGUES

7.1 Introduction

Metal-organic frameworks (MOFs) are nanoporous, crystalline materials constructed from metal or metal oxide nodes linked via organic moieties. The nearly infinite combinations of metal centers and organic ligand result in extensive structural diversity.[1, 2] Additional advantages include high surface areas and pore volumes, uniform pore size distributions, and chemical tunability.[3, 4] These properties make MOFs promising materials for applications such as gas storage and separation, drug delivery, imaging, air purification, and catalysis.[4-8] Unfortunately, many MOFs degrade under humid conditions, which severely limits the application perspective.[9] However, this limitation is currently being addressed. Specifically, investigations are being conducted to explore the underlying cause of the instability[9-11] and modify known water-stable MOFs for improved applicability via ligand functionalization and doping with nanoparticles.[12, 13]

UiO-66 is a well-studied zirconium-based MOF consisting of $Zr_6O_4(OH)_4$ connected by 1,4-benzenedicarboxylic acid (BDC). Its promise stems from its thermal stability up to 813K, mechanical and chemical resistance, stability in humid environments, and straightforward chemical tailorability.[12, 14, 15] UiO-66 has been prepared with a multitude of various functionalities via a direct substitution of the functionalized linker in the mother solution. Specifically, UiO-66-X, where X = {–H, –NH_2, –NO_2, –Naph, –Anth, –Cl_2, –Br, –CH_3, –$(CH_3)_2$, –COOH, –$(COOH)_2$, –OH, –$(OH)_2$,

–SO_3H, –SH, and –$(SH)_2$} have been prepared, and the physical properties evaluated.[12, 16-18] The addition of many of these pendant groups has shown enhanced capabilities towards target gas adsorption and removal, degradation of chemical warfare agents (CWAs), catalysis, and photocatalysis, demonstrating the potential of UiO-66 and its analogues.[16, 19-21]

UiO-66 and its analogues are typically prepared using zirconium chloride ($ZrCl_4$) as the metal precursor, which generates by-product HCl. Alternatively, Tulig et al. substituted zirconium propoxide (Zr(O*n*Pr)) as the metal precursor to eliminate by-product HCl and producing high quality parent UiO-66.[22] This synthesis allows for the inclusion of HCl-sensitive materials, such as nanoparticles, in the UiO-66 synthesis to prepare UiO-66 composites. Herein, this HCl-free synthesis procedure is extended to the UiO-66 family to determine the capabilities of the procedure for producing the functionalized versions of UiO-66 and to probe the underlying factors of the crystallization process. The amine functionalized analogue, UiO-66-NH_2, is an ideal starting material; it has been previously synthesized via the direct substitution of BDC-NH_2 and has shown promise for numerous applications such as gas separation, toxic industrial chemical (TIC) removal, and photocatalysis.[16, 23-25]

7.2 Experimental Methods

7.2.1 Material Synthesis

All chemicals were obtained commercially (Sigma Aldrich, VWR, and Fisher Scientific) and used without further purification. UiO-66-NH_2(Zr(O*n*Pr)) was prepared by stirring zirconium(IV) propoxide (Zr(O*n*Pr)), 2-aminobenzenedicarboxylic acid (BDC-

NH_2), methanol (MeOH), N,N'-dimethylformamide (DMF), and a specified modulator (acetic acid, benzoic acid, formic acid, trifluoroacetic acid (TFA), or hydrochloric acid (HCl)), illustrated in Figure 7.1, in a glass scintillation vial in a silicone oil bath. The product was filtered and washed three times with DMF and MeOH. Five synthesis parameters were varied: (1) time; (2) temperature; (3) H_2O:Zr(O*n*Pr) ratio; (4) MeOH:DMF ratio; and (4) modulator and modulator ratio. Tables 7.1 and 7.2 detail the conditions used for the UiO-66-NH_2(Zr(O*n*Pr)) synthesis variations.

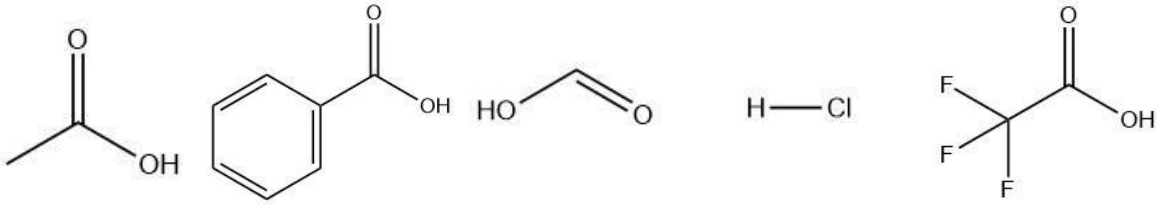

Acetic Acid | Benzoic Acid | Formic Acid | Hydrochloric Acid | Trifluoroacetic Acid (TFA)

Figure 7.1: Illustration of the modulators used to prepare UiO-66-NH_2(Zr(O*n*Pr))

Table 7.1: Synthesis conditions used to prepare UiO-66-NH_2(Zr(O*n*Pr)) at various times, temperatures, H_2O:Zr(O*n*Pr) ratios, and MeOH:DMF ratios

UiO-66-NH_2(Zr(O*n*Pr))	Zr(O*n*Pr) (mmol)	BDC-NH_2 (mmol)	MeOH (mmol)	DMF (mmol)	Acetic Acid (mmol)	DI H_2O (mmol)	Temp (K)	Time (h)
24 h, 393K, H_2O:Zr(O*n*Pr)=0, MeOH:DMF=1.9	0.227	0.454	86.5	45.4	6.81	0.0	393	24
48 h, 393K, H_2O:Zr(O*n*Pr)=0, MeOH:DMF=1.9	0.227	0.454	86.5	45.4	6.81	0.0	393	48
24 h, 373K, H_2O:Zr(O*n*Pr)=0, MeOH:DMF=1.9	0.227	0.454	86.5	45.4	6.81	0.0	373	24
24 h, 393K, H_2O:Zr(O*n*Pr)=6.1, MeOH:DMF=1.9	0.227	0.454	86.5	45.4	6.81	1.4	393	24
24 h, 393K, H_2O:Zr(O*n*Pr)=7.3, MeOH:DMF=1.9	0.227	0.454	86.5	45.4	6.81	1.7	393	24
24 h, 393K, H_2O:Zr(O*n*Pr)=0, MeOH:DMF=0	0.227	0.454	0.0	90.8	6.81	0.0	393	24
24 h, 393K, H_2O:Zr(O*n*Pr)=0, MeOH:DMF=4.8	0.227	0.454	123.6	25.9	6.81	0.0	393	24

Table 7.2: Synthesis conditions used to prepare UiO-66-NH_2(Zr(O*n*Pr)) with various modulators and modulator:Zr(O*n*Pr) ratio

Sample	Zr(O*n*Pr) (mmol)	BDC-NH_2 (mmol)	MeOH (mmol)	DMF (mmol)	Modulator (mmol)	Temp (K)	Time (h)
UiO-66-NH_2(Zr(O*n*Pr)) – Acetic Acid:Zr(O*n*Pr) = 15	0.227	0.454	86.5	45.4	Acetic Acid (3.41)	393	24
UiO-66-NH_2(Zr(O*n*Pr)) – Acetic Acid:Zr(O*n*Pr) = 30	0.227	0.454	86.5	45.4	Acetic Acid (6.81)	393	24
UiO-66-NH_2(Zr(O*n*Pr)) – Acetic Acid:Zr(O*n*Pr) = 60	0.227	0.454	86.5	45.4	Acetic Acid (13.62)	393	24
UiO-66-NH_2(Zr(O*n*Pr)) – Acetic Acid:Zr(O*n*Pr) = 120	0.227	0.454	86.5	45.4	Acetic Acid (27.24)	393	24
UiO-66-NH_2(Zr(O*n*Pr)) – Acetic Acid:Zr(O*n*Pr) = 240	0.227	0.454	86.5	45.4	Acetic Acid (54.48)	393	24
UiO-66-NH_2(Zr(O*n*Pr)) – Benzoic Acid:Zr(O*n*Pr) = 15	0.227	0.454	86.5	45.4	Benzoic Acid (3.41)	393	24
UiO-66-NH_2(Zr(O*n*Pr)) – Benzoic Acid:Zr(O*n*Pr) = 30	0.227	0.454	86.5	45.4	Benzoic Acid (6.81)	393	24
UiO-66-NH_2(Zr(O*n*Pr)) – Benzoic Acid:Zr(O*n*Pr) = 60	0.227	0.454	86.5	45.4	Benzoic Acid (13.62)	393	24
UiO-66-NH_2(Zr(O*n*Pr)) – Benzoic Acid:Zr(O*n*Pr) = 75	0.227	0.454	86.5	45.4	Benzoic Acid (17.03)	393	24
UiO-66-NH_2(Zr(O*n*Pr)) – Formic Acid:Zr(O*n*Pr) = 15	0.227	0.454	86.5	45.4	Formic Acid (3.41)	393	24
UiO-66-NH_2(Zr(O*n*Pr)) – Formic Acid:Zr(O*n*Pr) = 30	0.227	0.454	86.5	45.4	Formic Acid (6.81)	393	24
UiO-66-NH_2(Zr(O*n*Pr)) – Formic Acid:Zr(O*n*Pr) = 60	0.227	0.454	86.5	45.4	Formic Acid (13.62)	393	24
UiO-66-NH_2(Zr(O*n*Pr)) – Formic Acid:Zr(O*n*Pr) = 120	0.227	0.454	86.5	45.4	Formic Acid (27.24)	393	24
UiO-66-NH_2(Zr(O*n*Pr)) – Formic Acid:Zr(O*n*Pr) = 240	0.227	0.454	86.5	45.4	Formic Acid (54.48)	393	24
UiO-66-NH_2(Zr(O*n*Pr)) – TFA:Zr(O*n*Pr) = 15	0.227	0.454	86.5	45.4	TFA (3.41)	393	24
UiO-66-NH_2(Zr(O*n*Pr)) – TFA:Zr(O*n*Pr) = 30	0.227	0.454	86.5	45.4	TFA (6.81)	393	24
UiO-66-NH_2(Zr(O*n*Pr)) – TFA:Zr(O*n*Pr) = 60	0.227	0.454	86.5	45.4	TFA (13.62)	393	24
UiO-66-NH_2(Zr(O*n*Pr)) – TFA:Zr(O*n*Pr) = 120	0.227	0.454	86.5	45.4	TFA (27.24)	393	24
UiO-66-NH_2(Zr(O*n*Pr)) – TFA:Zr(O*n*Pr) = 240	0.227	0.454	86.5	45.4	TFA (54.48)	393	24
UiO-66-NH_2(Zr(O*n*Pr)) – HCl:Zr(O*n*Pr) = 4	0.227	0.454	86.5	45.4	TFA (0.91)	393	24
UiO-66-NH_2(Zr(O*n*Pr)) – HCl:Zr(O*n*Pr) = 30	0.227	0.454	86.5	45.4	TFA (6.81)	393	24
UiO-66-NH_2(Zr(O*n*Pr)) – HCl:Zr(O*n*Pr) = 60	0.227	0.454	86.5	45.4	TFA (13.62)	393	24
UiO-66-NH_2(Zr(O*n*Pr)) – HCl:Zr(O*n*Pr) = 120	0.227	0.454	86.5	45.4	TFA (27.24)	393	24
UiO-66-NH_2(Zr(O*n*Pr)) – HCl:Zr(O*n*Pr) = 240	0.227	0.454	86.5	45.4	TFA (54.48)	393	24

UiO-66-X(Zr(O*n*Pr)) was prepared, as documented in Table 7.3, by stirring Zr(O*n*Pr), the appropriate ligand, MeOH, DMF, and benzoic acid or TFA in a glass scintillation vial at 393 K for 24 h in a silicone oil bath. The product was filtered and washed three times with DMF and MeOH. The ligands used to prepare UiO-66-X include 1,4-benzenedicarboxylic acid (BDC); 1,4-benzenedicarboxylic acid, 2-nitro (BDC-NO_2); 1,4-naphthalenedicarboxylic acid (BDC-Naph); anthracene-9,10-dicarboxylic acid (BDC-Anth); 1,4-benzenedicarboxylic acid, 2,5-dichloro (BDC-Cl_2); 1,4-benzenedicarboxylic acid, 2-bromo (BDC-Br); 1,4-benzenedicarboxylic acid, 2,5-dimethyl (BDC-$(CH_3)_2$); 1,2,4-benzenetricarboxylic acid (BDC-COOH); 1,4-benzenedicarboxylic acid, 2-hydroxy (BDC-OH); and 1,4-benzenedicarboxylic acid, 2,5-dihydroxy (BDC-$(OH)_2$).

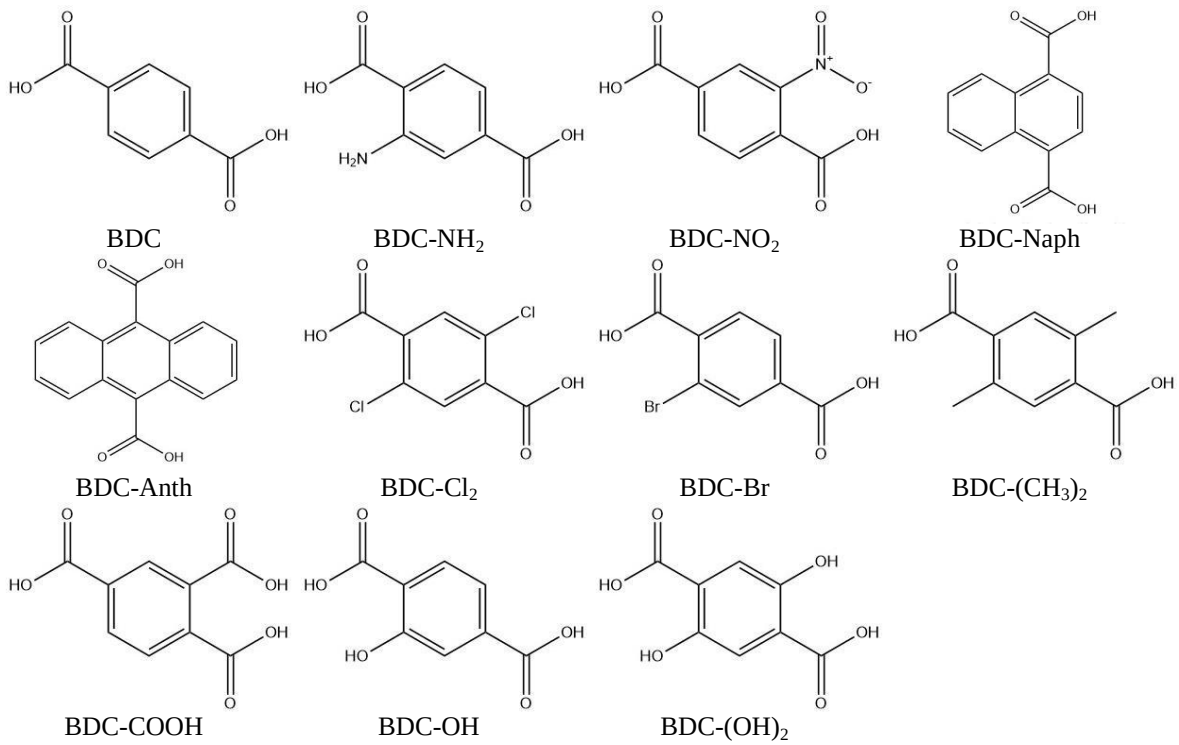

Figure 7.2: Illustration of the ligands used to prepare UiO-66-X(Zr(O*n*Pr))

Table 7.3: Synthesis conditions used to prepare UiO-66-X(Zr(O*n*Pr))

Sample	Zr(O*n*Pr) (mmol)	BDC-X (mmol)	MeOH (mmol)	DMF (mmol)	Modulator (mmol)	Temp (K)	Time (h)
UiO-66	0.227	0.454	86.5	45.4	Benzoic Acid (6.81)	393	24
UiO-66-NH_2	0.227	0.454	86.5	45.4	Benzoic Acid (6.81)	393	24
UiO-66-NO_2	0.227	0.454	86.5	45.4	Benzoic Acid (3.41)	393	24
UiO-66-Naph	0.227	0.454	86.5	45.4	Benzoic Acid (6.81)	393	24
UiO-66-Anth	0.227	0.454	86.5	45.4	Benzoic Acid (6.81)	393	24
UiO-66-Cl_2	0.227	0.454	86.5	45.4	Benzoic Acid (6.81)	393	24
UiO-66-Br	0.227	0.454	86.5	45.4	Benzoic Acid (6.81)	393	24
UiO-66-$(CH_3)_2$	0.227	0.454	86.5	45.4	Benzoic Acid (6.81)	393	24
UiO-66-COOH	0.227	0.454	86.5	45.4	Benzoic Acid (3.41)	393	24
UiO-66-OH	0.227	0.454	86.5	45.4	TFA (27.24)	393	24
UiO-66-$(OH)_2$	0.227	0.454	86.5	45.4	TFA (27.24)	393	24

Table 7.4: Synthesis conditions used to prepare UiO-66-OH(Zr(O*n*Pr)) and UiO-66-$(OH)_2$(Zr(O*n*Pr))

Sample	Yield (mg)	Zr(O*n*Pr) (mmol)	BDC-X (mmol)	MeOH (mmol)	DMF (mmol)	Modulator (mmol)	Temp (K)	Time (h)
UiO-66-OH(Zr(O*n*Pr)) – Benzoic Acid:Zr(OnPr)=30	0.0	0.227	0.454	86.5	45.4	Benzoic Acid (6.81)	393	24
UiO-66-OH(Zr(O*n*Pr)) – Benzoic Acid:Zr(OnPr)=15	1.9	0.227	0.454	86.5	45.4	Benzoic Acid (3.41)	393	24
UiO-66-OH(Zr(O*n*Pr)) – TFA:Zr(O*n*Pr)=120	33.9	0.227	0.454	86.5	45.4	TFA (27.24)	393	24
UiO-66-$(OH)_2$(Zr(O*n*Pr)) – Benzoic Acid:Zr(OnPr)=30	30.9	0.227	0.454	86.5	45.4	Benzoic Acid (6.81)	393	24
UiO-66-$(OH)_2$(Zr(O*n*Pr)) – Benzoic Acid:Zr(OnPr)=15	64.2	0.227	0.454	86.5	45.4	Benzoic Acid (3.41)	393	24
UiO-66-$(OH)_2$(Zr(O*n*Pr)) – TFA:Zr(O*n*Pr)=120	39.2	0.227	0.454	86.5	45.4	TFA (27.24)	393	24

7.2.2 Characterization

Powder X-ray diffraction (PXRD) patterns were obtained using a PANalytical X-ray diffractometer. Approximately 5 mg of sample were placed on a low background sample holder and scanned from 5-50°. The obtained diffractograms were compared to the simulated patterns to confirm that the UiO-66 structure was obtained.

Nitrogen sorption measurements at 77 K were performed using a Quantachrome Quadrasorb Evo volumetric analyzer. The isotherms were measured over a range of relative pressures from 0.003 to 0.990 using high purity nitrogen (99.998%) obtained from Airgas. Prior to the measurement, the samples were outgassed in a Quantachrome FloVac Degasser under dynamic vacuum at the following temperatures and times: (1) UiO-66(Zr(O*n*Pr)) was heated at 473 K for 16-18 h; (2) UiO-66-NH_2(Zr(O*n*Pr)), UiO-66-NO_2(Zr(O*n*Pr)), UiO-66-Naph(Zr(O*n*Pr)), and UiO-66-Anth(Zr(O*n*Pr)) were heated at 383 K for 16-18 h; and (3) UiO-66-COOH(Zr(O*n*Pr)), UiO-66-OH(Zr(O*n*Pr)), UiO-66-$(OH)_2$(Zr(O*n*Pr)), UiO-66-Cl_2(Zr(O*n*Pr)), UiO-66-Br(Zr(O*n*Pr)), and UiO-66-$(CH_3)_2$(Zr(O*n*Pr)) were heated at 338 K for 24 h.

Simulated nitrogen isotherms at 77 K were calculated using grand canonical Monte Carlo (GCMC) simulations with the nitrogen force field parameters taken from the TraPPE force field[26] and the Lennard-Jones potentials for the UiO-66 frameworks taken from the DREIDING[27] and universal force fields (UFF).[28] All simulations were performed using the RASPA simulation software.[29] The experimental and simulated surface areas were calculated using the Brunauer, Emmett, and Teller (BET) theory using relative pressures ranging from 0.005-0.03, and the total pore volume was calculated at a relative pressure (P/P_0) of 0.6.

Proton nuclear magnetic resonance (^{1}H NMR) spectroscopy was measured on a Varian Mercury Vx 300. The samples were prepared by suspending approximately 30 mg of UiO-66-NH_2 in 1 mL of 1M sodium hydroxide (NaOH) in deuterium oxide (D_2O). Transmission electron microscopy (TEM) images were acquired using the Hitachi

HT7700 operated at 120 keV. The samples were prepared by suspending less than 1 mg of sample in MeOH and dropcasting it on a lacy carbon copper grid.

7.3 Results and Discussion

7.3.1 UiO-66-NH_2(Zr(O*n*Pr))

The direct substitution of BDC-NH_2 in the UiO-66(Zr(O*n*Pr)) synthesis yields a crystalline material, depicted by the blue curve in Figure 7.4. However, the resulting BET surface area of 682 m^2/g (Table 7.5) is significantly lower than the simulated value of 934 m^2/g. This simulated BET surface area was calculated from a simulated nitrogen isotherm at 77 K (Figure 7.3) and satisfies all four of the consistency criteria.[30] Additionally, UiO-66-NH_2 has pores smaller than 1 nm suggesting that the BET surface area calculated is a true monolayer calculation.[31] Therefore, the simulated BET surface area of 934 m^2/g is an accurate assessment for UiO-66-NH_2. Based on this information, this alternative synthesis produces crystalline UiO-66-NH_2; however, the material porosity is reduced. Therefore, further investigations into the controlling synthetic factors were undertaken in order to determine the effect of the synthesis conditions on the material quality. Specifically, five parameters are examined: reaction time, reaction temperature, H_2O:Zr(O*n*Pr) ratio, MeOH:DMF ratio, and the acid used as a modulator and its concentration. Herein, the results will be grouped into three sections: (1) reaction time and temperature, H_2O:Zr(O*n*Pr) ratio, and MeOH:DMF ratio; (2) the acid used as a modulator; and (3) modulator:Zr(O*n*Pr) ratio.

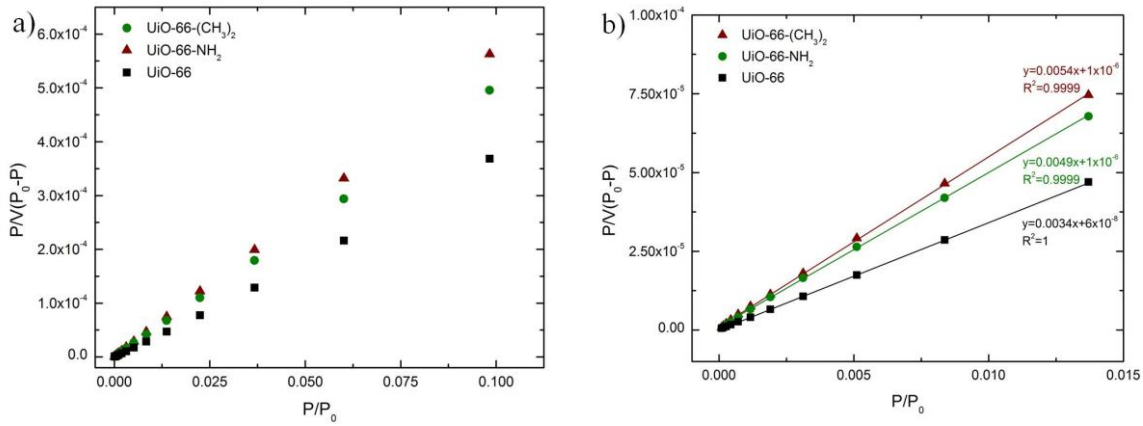

Figure 7.3: (a) Complete simulated nitrogen isotherms at 77 K and (b) BET theory fit for $0.001 \leq P/P_0 \leq 0.014$

7.3.1.1 Time, Temperature, H_2O:Zr(O*n*Pr) ratio, and MeOH:DMF ratio

Table 7.1 details the synthesis conditions used to examine the effect of reaction time, reaction temperature, H_2O:Zr(O*n*Pr) ratio, and MeOH:DMF ratio on the UiO-66-NH_2(Zr(O*n*Pr)) properties. Figure 7.4 demonstrates that the UiO-66-NH_2 crystal structure is obtained for all of the synthesis conditions used. In addition, Table 7.5 shows that the materials prepared with varied time, temperature, H_2O:Zr(O*n*Pr) ratio, and MeOH:DMF ratio have similar BET surface areas that are lower than the simulated value. Although these parameters often affect MOF properties, for the crystallization of UiO-66-NH_2 with Zr(O*n*Pr), the reaction time and temperature, H_2O:Zr(O*n*Pr) ratio, and MeOH:DMF ratio have an insignificant effect.

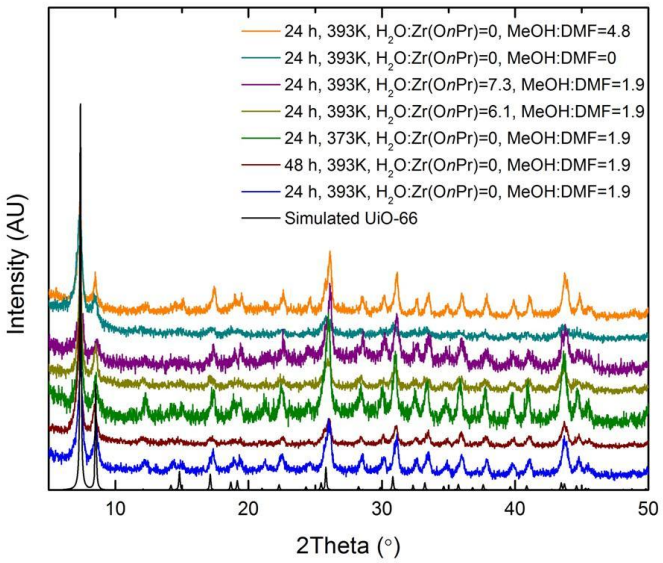

Figure 7.4: PXRD patterns for UiO-66-NH_2(Zr(O*n*Pr)) prepared by varying the time, temperature, H_2O:Zr(O*n*Pr) ratio, and MeOH:DMF ratio

Table 7.5: Porosity of UiO-66-NH_2(Zr(O*n*Pr)) prepared with varied time, temperature, H_2O:Zr(O*n*Pr) ratio, and MeOH:DMF ratio

UiO-66-NH_2(Zr(O*n*Pr))	BET Surface Area (m^2/g)	Total Pore Volume (cm^3/g)[a]
Simulated UiO-66-NH_2	934	-----
24 h, 393K, H_2O:Zr(O*n*Pr)=0, MeOH:DMF=1.9	682	0.30
48 h, 393K, H_2O:Zr(O*n*Pr)=0, MeOH:DMF=1.9	586	0.27
24 h, 373K, H_2O:Zr(O*n*Pr)=0, MeOH:DMF=1.9	619	0.30
24 h, 393K, H_2O:Zr(O*n*Pr)=6.1, MeOH:DMF=1.9	659	0.30
24 h, 393K, H_2O:Zr(O*n*Pr)=7.3, MeOH:DMF=1.9	671	0.34
24 h, 393K, H_2O:Zr(O*n*Pr)=0, MeOH:DMF=0.0	565	0.32
24 h, 393K, H_2O:Zr(O*n*Pr)=0, MeOH:DMF=4.8	493	0.24

[a]Measured at $P/P_0 = 0.6$

7.3.1.2 Acid Used As The Modulator

The coordination modulation method, or modulation, is an approach that incorporates an additive or modulator, typically with the same chemical functionality, introducing competition with the organic linker for coordinating with the metal ions. This competitive coordination regulates MOF crystallization establishing control over

morphology and size.[32-34] Figure 7.1 illustrates and Table 7.6 reports the pK_a of the five acids used as modulators in this work. These acids were chosen because they have been used as modulators for UiO-66 and its analogues.[12, 20, 33, 35] In addition, a constant modulator:Zr(O*n*Pr) ratio of 30:1 was used to probe the effect of the modulator structure on the UiO-66-NH_2(Zr(O*n*Pr)) properties. Figure 7.5 depicts the PXRD patterns for UiO-66-NH_2(Zr(O*n*Pr)) prepared with the various modulators. Acetic acid, benzoic acid, TFA, and HCl produce materials with the UiO-66-NH_2 structure; however, formic acid yields an amorphous powder. Additionally, Table 7.6 shows that benzoic acid produces highly porous UiO-66-NH_2(Zr(O*n*Pr)) with porosity comparable to the simulated value, whereas acetic acid, TFA, and HCl produce UiO-66-NH_2(Zr(O*n*Pr)) with reduced porosity.

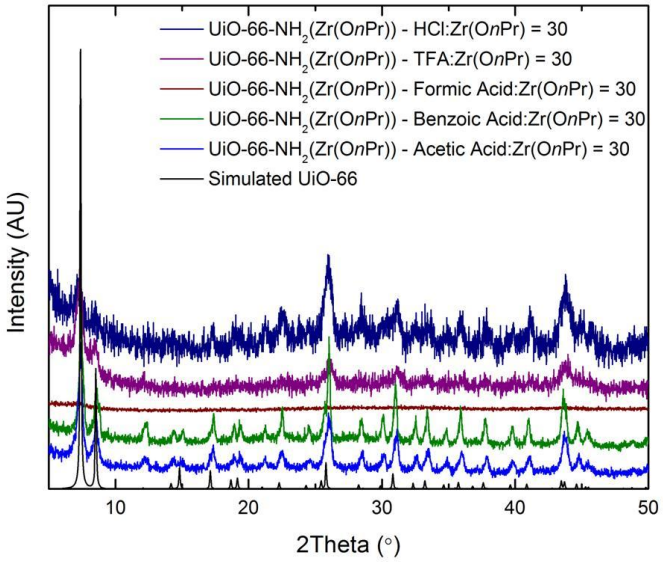

Figure 7.5: PXRD patterns for UiO-66-NH_2(Zr(O*n*Pr)) prepared with various modulator types with modulator:Zr(O*n*Pr) ratio of 30:1

Table 7.6: Porosity of UiO-66-NH_2(Zr(O*n*Pr)) with various modulators using modulator:Zr(O*n*Pr) ratio of 30

Material	Acid pK_a[36]	BET Surface Area (m^2/g)	Total Pore Volume (cm^3/g)[a]
Simulated	-----	934	-----
Acetic Acid	4.756	682	0.30
Benzoic Acid	4.204	998	0.43
Formic Acid	3.750	281	0.17
TFA	0.520	636	0.34
HCl	-7.000	672	0.32

[a]Measured at $P/P_0 = 0.6$

^{1}H NMR was used to further examine the material generated using benzoic acid. Figure 7.6 depicts the ^{1}H NMR spectra for UiO-66-NH_2(Zr(O*n*Pr)) synthesized with benzoic acid after it was activated at 383 K under vacuum for 18 h. There are characteristic peaks present for both BDC-NH_2 and benzoic acid. Specifically, the peaks at 7.12, 7.18, and 7.60 ppm are characteristic of the –H on the aromatic ring of BDC-NH_2, and the peaks at 7.4 and 7.77 ppm are characteristic of benzoic acid. Integration of these characteristic peaks reveals that 25% of BDC-NH_2 is replaced by benzoic acid in the UiO-66-NH_2(Zr(O*n*Pr)) structure. This revelation confirms that benzoic acid is acting as a modulating agent competing with BDC-NH_2 to coordinate with Zr^{4+} which suppresses the number of nuclei formed and enhances crystal growth. This theory is further supported by the well-defined UiO-66-NH_2(Zr(O*n*Pr)) particles seen in Figure 7.7a. In comparison, UiO-66-NH_2(Zr(O*n*Pr)) synthesized with acetic acid generates a combination of well-formed cubic UiO-66-NH_2(Zr(O*n*Pr)) particles and smaller amorphous particles, shown in Figure 7.7b. Therefore, using benzoic acid as the modulator produces crystalline, highly porous UiO-66-NH_2(Zr(O*n*Pr)) with well-defined particles by utilizing competitive coordination to control the nucleation rate and crystal growth. The authors theorize that benzoic acid is more effective because it has a similar

charge distribution compared with BDC-NH_2. This allows benzoic acid to effectively compete with BDC-NH_2 for the Zr^{4+} sites.

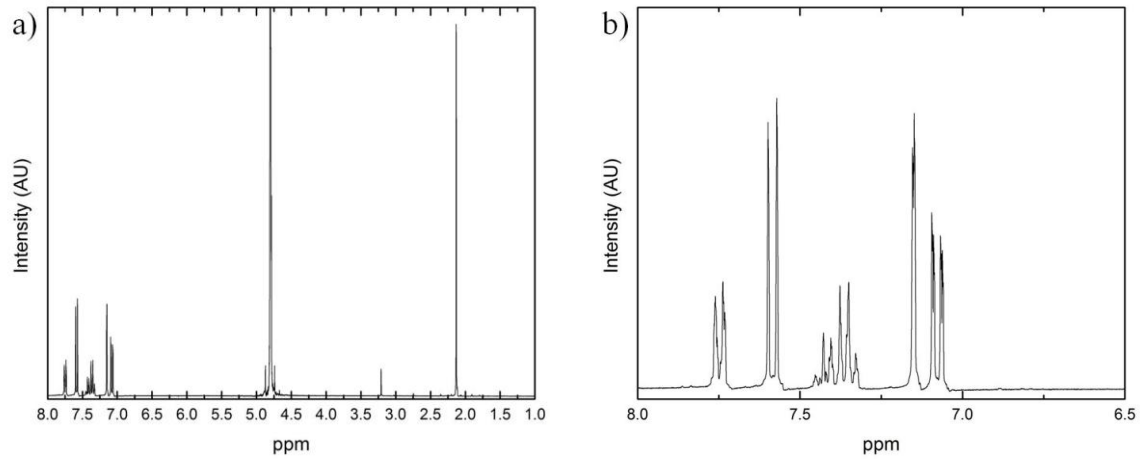

Figure 7.6: ^{1}H NMR for UiO-66-NH_2(Zr(O*n*Pr)) prepared with benzoic acid

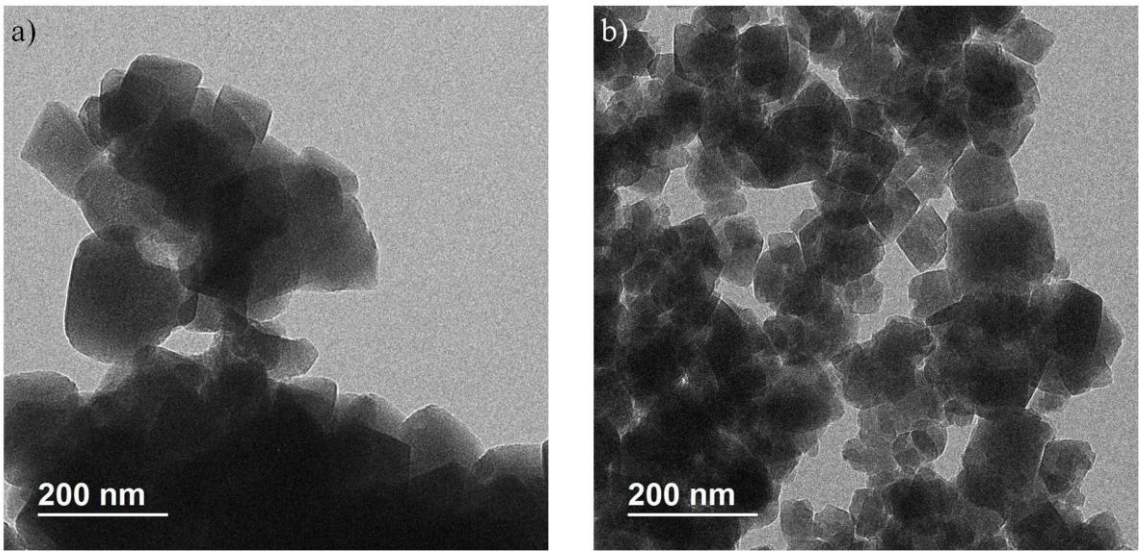

Figure 7.7: TEM images of UiO-66-NH_2(Zr(O*n*Pr)) prepared with (a) benzoic acid and (b) acetic acid

7.3.1.3 Modulator:Zr(O*n*Pr) Ratio

Table 7.2 details the synthesis conditions used to prepare UiO-66-NH_2(Zr(O*n*Pr)) with varying modulator:Zr(O*n*Pr) ratios. Figure 7.8 demonstrates that for acetic acid,

benzoic acid, TFA, and HCl, the UiO-66 structure is obtained for all modulator:Zr(O*n*Pr) ratios. However, formic acid:Zr(O*n*Pr) ratios less than and equal to 30:1 generate an amorphous powder and ratios of 60:1 and greater produce crystalline UiO-66-NH_2(Zr(O*n*Pr)). This suggests that increased formic acid:Zr(O*n*Pr) ratios are necessary to reduce the nucleation rate; a limitation that indicates two potential explanations: (1) increased formic acid concentrations are necessary to impede BDC-NH_2 coordination or (2) the reaction medium is sufficiently acidic to shift the deprotonation equilibrium of BDC-NH_2 to temper the nucleation rate. In addition, Figure 7.9 illustrates the effect of the modulator:Zr(O*n*Pr) ratio on the UiO-66-NH_2(Zr(O*n*Pr)) porosity. Increasing the modulator:Zr(O*n*Pr) ratio for acetic acid, formic acid, and benzoic acid has an insignificant effect on the crystalline material porosity. However, at benzoic acid:Zr(O*n*Pr) ratios exceeding 75:1, the synthesis ceases to yield material, there is zero product formed. This suggests that benzoic acid inhibits nucleation at high concentrations, potentially by completely coordinating all of the Zr^{4+} sites, therefore, prohibiting nucleation.

Notably, when the modulator:Zr(O*n*Pr) ratio of TFA and HCl is increased to 120:1 and 240:1, respectively, the UiO-66-NH_2(Zr(O*n*Pr)) BET surface area increases to be comparable to the simulated value. Table 7.6 shows that TFA and HCl are significantly more acidic than the other modulators. Therefore, increasing the modulator:Zr(O*n*Pr) ratio of TFA and HCl will substantially shift the equilibrium of deprotonated BDC-NH_2 resulting in more protonated BDC-NH_2, which will reduce the nucleation rate and yield higher quality materials. The weaker acids do not shift the equilibrium of deprotonated BDC-NH_2 as significantly, resulting in an abundance of

nuclei that cannot adequately grow to include an intricate pore system with high surface areas. Therefore, the preparation of high quality UiO-66-NH_2(Zr(O*n*Pr)) is dependent on the modulator, specifically, a combination of effective competitive coordination and acidity. For weak acids, the appropriate modulator must be used to effectively reduce the nucleation rate, whereas high concentrations of strong acids will adequately shift the deprotonation equilibrium of the linker subsequently reducing the nucleation rate and producing high quality UiO-66-NH_2(Zr(O*n*Pr)).

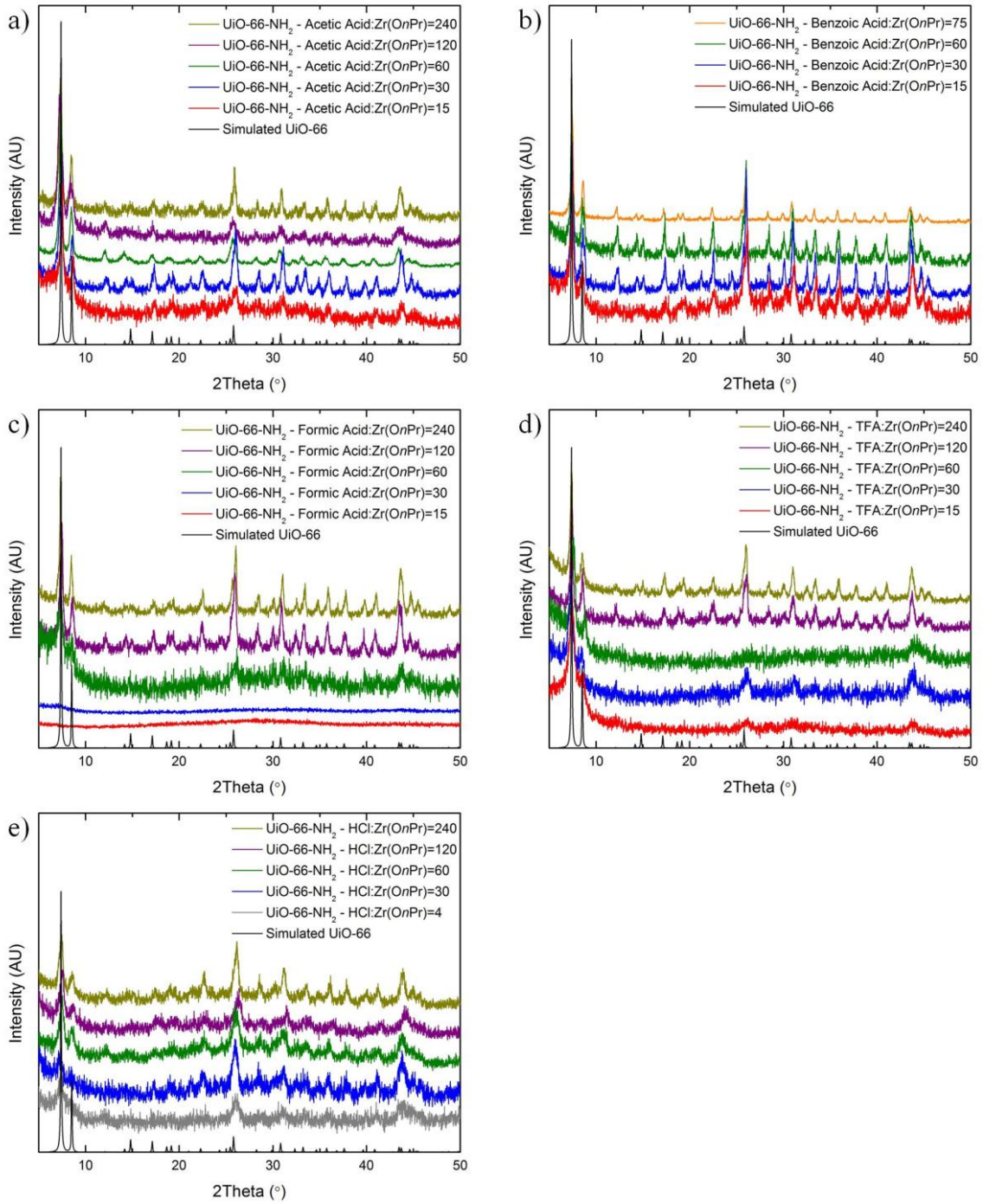

Figure 7.8: PXRD patterns for UiO-66-NH_2(Zr(O*n*Pr)) prepared using (a) acetic acid; (b) benzoic acid; (c) formic acid; (d) TFA; and (e) HCl

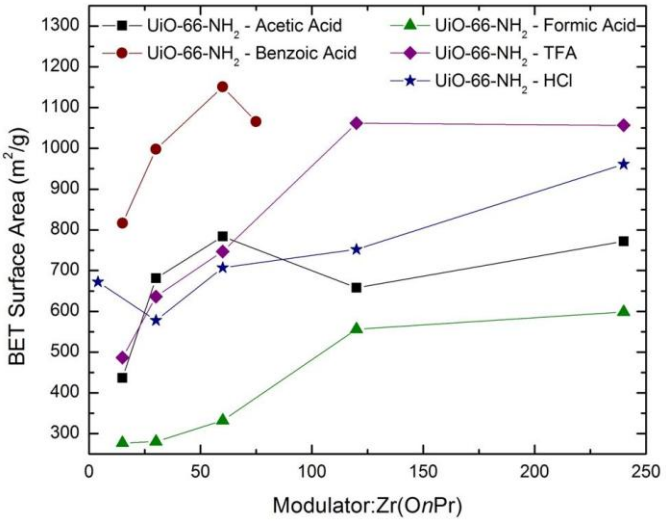

Figure 7.9: Modulator effect on UiO-66-NH_2(Zr(O*n*Pr)) porosity. The lines are to guide the eye only

7.3.2 UiO-66-X(Zr(O*n*Pr))

Based on the knowledge collected preparing UiO-66-NH_2(Zr(O*n*Pr)), the procedure was extended to the other UiO-66 analogues. Table 7.3 reports the synthesis conditions and Figure 7.2 illustrates the linkers used to prepare UiO-66-X(Zr(O*n*Pr)). Figure 7.10 shows that the UiO-66-X(Zr(O*n*Pr)) materials, where X = {–H, –NH_2, –NO_2, –Naph, –Anth, –Cl_2, –Br, –$(CH_3)_2$, –COOH, –OH, and –$(OH)_2$}, obtained the UiO-66 structure. Additionally, Table 7.7 reports that the porosity measurements for UiO-66-X(Zr(O*n*Pr)) are comparable to the simulated and literature values. The combination of PXRD and porosity measurements demonstrates that high quality UiO-66-X can be prepared without forming by-product HCl.

Notably, Table 7.3 reports that UiO-66-NO_2(Zr(O*n*Pr)) and UiO-66-COOH(Zr(O*n*Pr)) utilized a lower concentration of benzoic acid and that, for UiO-66-OH(Zr(O*n*Pr)) and UiO-66-$(OH)_2$(Zr(O*n*Pr)), TFA was used instead of benzoic acid. For UiO-66-NO_2(Zr(O*n*Pr)) and UiO-66-COOH(Zr(O*n*Pr)), a lower concentration of benzoic

acid was necessary to yield product. This suggests that benzoic acid strongly bound to the Zr^{4+} sites and could not be removed via linker exchange with BDC-NO_2 and BDC-COOH. The authors theorize that acidic functional groups result in a more acidic linker and, therefore, a weaker conjugate base. The weaker conjugate base cannot exchange with the coordinated benzoic acid as easily; therefore, lower concentrations of benzoic acid are necessary for BDC-NO_2 and BDC-COOH to be competitive with benzoic acid for coordination with the Zr^{4+} sites.

Alternatively, Table 7.4 reports the synthesis parameters and Figure 7.11 depicts the PXRD patterns for UiO-66-OH(Zr(O*n*Pr)) and UiO-66-$(OH)_2$(Zr(O*n*Pr)) produced under various preparation conditions. For UiO-66-OH(Zr(O*n*Pr)), utilizing benzoic acid:Zr(O*n*Pr) ratios of 30:1 and 15:1 result in poor yield (Table 7.4) and an amorphous material; however, using a TFA:Zr(O*n*Pr) ratio of 120:1 produces a crystalline material with the UiO-66 structure, as shown in Figure 7.11a. Additionally, Figure 7.11b shows that, for UiO-66-$(OH)_2$(Zr(O*n*Pr)), using benzoic acid:Zr(O*n*Pr) ratios of 30:1 and 15:1 produce a semi-crystalline material that is not UiO-66. However, substituting TFA for benzoic acid successfully produces UiO-66-$(OH)_2$(Zr(O*n*Pr)). This suggests that crystallization of UiO-66-OH(Zr(O*n*Pr)) and UiO-66-$(OH)_2$(Zr(O*n*Pr)) is controlled by the modulator acidity rather than competitive coordination. This is potentially due to benzoic acid acting as a structure directing agent (SDA) via competitive coordination, subsequently hindering the formation of UiO-66-$(OH)_2$(Zr(O*n*Pr)), whereas TFA controls nucleation by shifting the deprotonation equilibrium of the reaction.

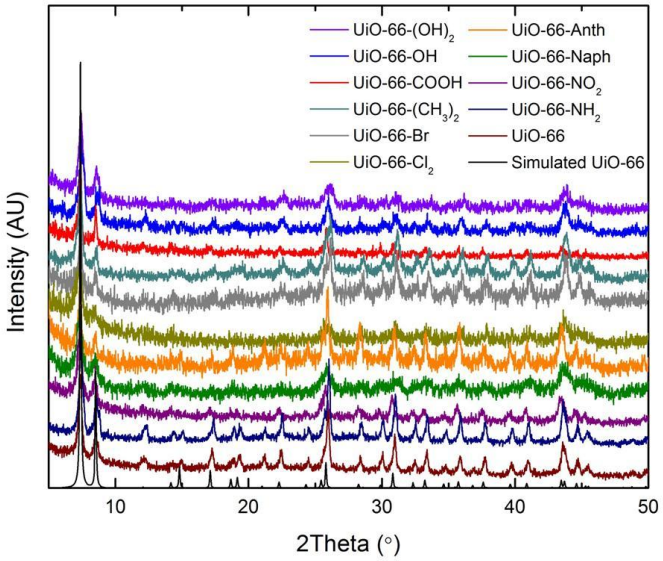

Figure 7.10: PXRD patterns for UiO-66-X(Zr(O*n*Pr))

Table 7.7: Porosity results for UiO-66-X(Zr(O*n*Pr))

Material	BET Surface Area (m^2/g)	Literature BET Surface Area (m^2/g)
UiO-66	1403	1334,[a] 1105[b]
UiO-66-NH_2	998	934,[a] 1123[b]
UiO-66-NO_2	832	792[b]
UiO-66-Naph	810	757[b]
UiO-66-Anth	612	627[c]
UiO-66-Cl_2	753	609[d]
UiO-66-Br	889	654[d]
UiO-66-$(CH_3)_2$	954	849,[a] 825[d]
UiO-66-COOH	805	842[d]
UiO-66-OH	1036	946,[e] 843[d]
UiO-66-$(OH)_2$	739	814,[e] 617[d]

[a]Simulated BET surface areas from this work
Experimental BET surface areas from [b]Walton et al.[23]; [c]Du et al.[18]; [e]Walton et al.[16]
Experimental Langmuir surface areas from [d]Van Der Voort et al.[12]

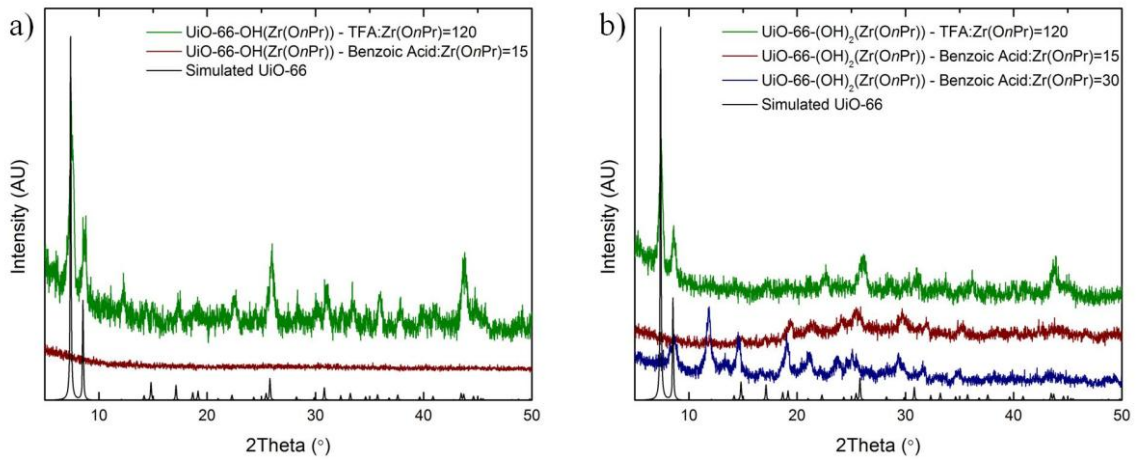

Figure 7.11: PXRD patterns for (a) UiO-66-OH(Zr(O*n*Pr)) and (b) UiO-66-$(OH)_2$(Zr(O*n*Pr)) prepared by varying the synthesis conditions

7.4 Conclusions

The preparation of UiO-66-X using Zr(O*n*Pr) appears to have a rapid nucleation rate requiring modulators to temper the nucleation rate and produce high quality UiO-66-X(Zr(O*n*Pr)) materials. Herein, UiO-66-NH_2(Zr(O*n*Pr)) is used to determine the effects of the modulator, specifically, the effect of the acid used as a modulator and the modulator:Zr(OnPr) ratio. At a constant modulator:Zr(O*n*Pr) ratio of 30:1, the dominating role of the acid is to competitively coordinate with the Zr^{4+} ions in order to regulate the nucleation rate. For UiO-66-NH_2(Zr(O*n*Pr)), only benzoic acid effectively controlled the nucleation rate which is suggested by the highly porous crystalline UiO-66-NH_2(Zr(O*n*Pr)) formed using benzoic acid. The other modulating acids produced materials with significantly reduced porosity.

In addition, the modulator:Zr(O*n*Pr) ratio was varied and the effect on the UiO-66-NH_2(Zr(O*n*Pr)) physical properties analyzed. The most significant effect is observed for TFA and HCl. When the modulator:Zr(O*n*Pr) ratio exceedes 120:1 and 240:1 for TFA and HCl, respectively, the UiO-66-NH_2(Zr(O*n*Pr)) porosity is improved and comparable

to the simulated porosity. Both TFA and HCl are strong acids capable of substantially shifting the deprotonation equilibrium of the linker, reducing the abundance of deprotonated BDC-NH_2, and diminishing the quantity of nuclei formed. Therefore, at moderate pH, a modulating agent that efficiently competes for coordination sites is necessary to regulate nucleation. Alternatively, using strong acids that can significantly reduce the pH of the reaction solution will shift the deprotonation equilibrium of the linker subsequently reducing the abundance of nuclei. Overall, the role of the acid is to regulate the nucleation rate via two mechanisms: (1) competitive coordination with Zr^{4+} ions and (2) shifting the deprotonation equilibrium of the linker by tuning the pH of the reaction medium.

Using this information, porous, crystalline UiO-66-X(Zr(O*n*Pr)), where X = {–H, –NH_2, –NO_2, –Naph, –Anth, –Cl_2, –Br, –$(CH_3)_2$, –COOH, –OH, and –$(OH)_2$}, was successfully prepared. This investigation has systematically probed the modulator effect on the formation of UiO-66-X(Zr(O*n*Pr)) and furthered the understanding of UiO-66-X crystallization. In addition, the preparation of UiO-66-X(Zr(O*n*Pr)), where X = {–H, –NH_2, –NO_2, –Naph, –Anth, –Cl_2, –Br, –$(CH_3)_2$, –COOH, –OH, and –$(OH)_2$}, has extended the HCl-free synthesis method to include many of the feasible analogues of UiO-66 and subsequently, augment the capabilities for designing HCl-sensitive UiO-66 composites with potential for gas storage and separation, catalysis, photocatalysis, and sensing.

7.5 References

1. The Cambridge Crystallographic Data Centre (CCDC).

2. Wilmer, C. E.; Leaf, M.; Lee, C. Y.; Farha, O. K.; Hauser, B. G.; Hupp, J. T.; Snurr, R. Q., Large-scale screening of hypothetical metal-organic frameworks. *Nature Chemistry* **2012,** *4* (2), 83-89.

3. Kitagawa, S.; Kitaura, R.; Noro, S., Functional porous coordination polymers. *Angewandte Chemie-International Edition* **2004,** *43* (18), 2334-2375.

4. Ferey, G., Hybrid porous solids: past, present, future. *Chemical Society Reviews* **2008,** *37* (1), 191-214.

5. Li, J.-R.; Kuppler, R. J.; Zhou, H.-C., Selective gas adsorption and separation in metal-organic frameworks. *Chemical Society Reviews* **2009,** *38* (5), 1477-1504.

6. Horcajada, P.; Chalati, T.; Serre, C.; Gillet, B.; Sebrie, C.; Baati, T.; Eubank, J. F.; Heurtaux, D.; Clayette, P.; Kreuz, C.; Chang, J. S.; Hwang, Y. K.; Marsaud, V.; Bories, P. N.; Cynober, L.; Gil, S.; Ferey, G.; Couvreur, P.; Gref, R., Porous metal-organic-framework nanoscale carriers as a potential platform for drug delivery and imaging. *Nature Materials* **2010,** *9* (2), 172-178.

7. DeCoste, J. B.; Peterson, G. W., Metal-Organic Frameworks for Air Purification of Toxic Chemicals. *Chemical Reviews* **2014,** *114* (11), 5695-5727.

8. Lee, J.; Farha, O. K.; Roberts, J.; Scheidt, K. A.; Nguyen, S. T.; Hupp, J. T., Metal-organic framework materials as catalysts. *Chemical Society Reviews* **2009,** *38* (5), 1450-1459.

9. Burtch, N. C.; Jasuja, H.; Walton, K. S., Water Stability and Adsorption in Metal-Organic Frameworks. *Chemical Reviews* **2014,** *114* (20), 10575-10612.

10. Jasuja, H.; Huang, Y.-g.; Walton, K. S., Adjusting the Stability of Metal-Organic Frameworks under Humid Conditions by Ligand Functionalization. *Langmuir* **2012,** *28* (49), 16874-16880.

11. Jasuja, H.; Burtch, N. C.; Huang, Y.-g.; Cai, Y.; Walton, K. S., Kinetic Water Stability of an Isostructural Family of Zinc-Based Pillared Metal-Organic Frameworks. *Langmuir* **2013,** *29* (2), 633-642.

12. Biswas, S.; Van der Voort, P., A General Strategy for the Synthesis of Functionalised UiO-66 Frameworks: Characterisation, Stability and CO_2 Adsorption Properties. *European Journal of Inorganic Chemistry* **2013,** (12), 2154-2160.

13. Falcaro, P.; Ricco, R.; Yazdi, A.; Imaz, I.; Furukawa, S.; Maspoch, D.; Ameloot, R.; Evans, J. D.; Doonan, C. J., Application of metal and metal oxide nanoparticles@MOFs. *Coordination Chemistry Reviews* **2016,** *307*, 237-254.

14. Cavka, J. H.; Jakobsen, S.; Olsbye, U.; Guillou, N.; Lamberti, C.; Bordiga, S.; Lillerud, K. P., A new zirconium inorganic building brick forming metal organic frameworks with exceptional stability. *Journal of the American Chemical Society* **2008,** *130* (42), 13850-13851.

15. Schoenecker, P. M.; Carson, C. G.; Jasuja, H.; Flemming, C. J. J.; Walton, K. S., Effect of Water Adsorption on Retention of Structure and Surface Area of Metal-Organic Frameworks. *Industrial & Engineering Chemistry Research* **2012,** *51* (18), 6513-6519.

16. Jasuja, H.; Peterson, G. W.; Decoste, J. B.; Browe, M. A.; Walton, K. S., Evaluation of MOFs for air purification and air quality control applications: Ammonia removal from air. *Chemical Engineering Science* **2015,** *124*, 118-124.

17. Hendrickx, K.; Vanpoucke, D. E. P.; Leus, K.; Lejaeghere, K.; Van Yperen-De Deyne, A.; Van Speybroeck, V.; Van Der Voort, P.; Hemelsoet, K., Understanding Intrinsic Light Absorption Properties of UiO-66 Frameworks: A Combined Theoretical and Experimental Study. *Inorganic Chemistry* **2015,** *54* (22), 10701-10710.

18. Pu, S.; Xu, L.; Sun, L.; Du, H., Tuning the optical properties of the zirconium-UiO-66 metal-organic framework for photocatalytic degradation of methyl orange. *Inorganic Chemistry Communications* **2015,** *52*, 50-52.

19. Katz, M. J.; Mondloch, J. E.; Totten, R. K.; Park, J. K.; Nguyen, S. T.; Farha, O. K.; Hupp, J. T., Simple and Compelling Biomimetic Metal-Organic Framework Catalyst for the Degradation of Nerve Agent Simulants. *Angewandte Chemie-International Edition* **2014,** *53* (2), 497-501.

20. Vermoortele, F.; Bueken, B.; Le Bars, G.; Van de Voorde, B.; Vandichel, M.; Houthoofd, K.; Vimont, A.; Daturi, M.; Waroquier, M.; Van Speybroeck, V.; Kirschhock, C.; De Vos, D. E., Synthesis Modulation as a Tool To Increase the Catalytic Activity of Metal-Organic Frameworks: The Unique Case of UiO-66(Zr). *Journal of the American Chemical Society* **2013,** *135* (31), 11465-8.

21. Shen, L.; Liang, R.; Luo, M.; Jing, F.; Wu, L., Electronic effects of ligand substitution on metal-organic framework photocatalysts: the case study of UiO-66. *Physical Chemistry Chemical Physics* **2015,** *17* (1), 117-121.

22. Tulig, K.; Walton, K. S., An alternative UiO-66 synthesis for HCl-sensitive nanoparticle encapsulation. *RSC Advances* **2014,** *4* (93), 51080-51083.

23. Cmarik, G. E.; Kim, M.; Cohen, S. M.; Walton, K. S., Tuning the Adsorption Properties of UiO-66 via Ligand Functionalization. *Langmuir* **2012,** *28* (44), 15606-15613.

24. DeCoste, J. B.; Browe, M. A.; Wagner, G. W.; Rossin, J. A.; Peterson, G. W., Removal of chlorine gas by an amine functionalized metal-organic framework via electrophilic aromatic substitution. *Chemical Communications* **2015,** *51* (62), 12474-12477.

25. Long, J.; Wang, S.; Ding, Z.; Wang, S.; Zhou, Y.; Huang, L.; Wang, X., Amine-functionalized zirconium metal-organic framework as efficient visible-light photocatalyst for aerobic organic transformations. *Chemical Communications* **2012,** *48* (95), 11656-11658.

26. Potoff, J. J.; Siepmann, J. I., Vapor-liquid equilibria of mixtures containing alkanes, carbon dioxide, and nitrogen. *Aiche Journal* **2001,** *47* (7), 1676-1682.

27. Mayo, S. L.; Olafson, B. D.; Goddard, W. A., DREIDING: a generic force field for molecular simulations. *Journal of Physical Chemistry* **1990,** *94* (26), 8897-8909.

28. Rappe, A. K.; Casewit, C. J.; Colwell, K. S.; Goddard, W. A.; Skiff, W. M., UFF, a full periodic table force field for molecular mechanics and molecular dynamics simulations. *Journal of the American Chemical Society* **1992,** *114* (25), 10024-10035.

29. Dubbeldam, D.; Calero, S.; Ellis, D. E.; Snurr, R. Q., RASPA: molecular simulation software for adsorption and diffusion in flexible nanoporous materials. *Molecular Simulation* **2016,** *42* (2), 81-101.

30. Rouquerol, J.; Llewellyn, P.; Rouquerol, F., Is the BET equation applicable to microporous adsorbents? In *Studies in Surface Science and Catalysis*, P.L. Llewellyn, F. R.-R. J. R.; Seaton, N., Eds. Elsevier: 2007; Vol. Volume 160, pp 49-56.

31. Gomez-Gualdron, D. A.; Moghadam, P. Z.; Hupp, J. T.; Farha, O. K.; Snurr, R. Q., Application of Consistency Criteria To Calculate BET Areas of Micro- And Mesoporous Metal-Organic Frameworks. *Journal of the American Chemical Society* **2016,** *138* (1), 215-224.

32. Tsuruoka, T.; Furukawa, S.; Takashima, Y.; Yoshida, K.; Isoda, S.; Kitagawa, S., Nanoporous Nanorods Fabricated by Coordination Modulation and Oriented Attachment Growth. *Angewandte Chemie-International Edition* **2009,** *48* (26), 4739-4743.

33. Schaate, A.; Roy, P.; Godt, A.; Lippke, J.; Waltz, F.; Wiebcke, M.; Behrens, P., Modulated Synthesis of Zr-Based Metal-Organic Frameworks: From Nano to Single Crystals. *Chemistry-a European Journal* **2011,** *17* (24), 6643-6651.

34. Diring, S.; Furukawa, S.; Takashima, Y.; Tsuruoka, T.; Kitagawa, S., Controlled Multiscale Synthesis of Porous Coordination Polymer in Nano/Micro Regimes. *Chemistry of Materials* **2010,** *22* (16), 4531-4538.

35. Katz, M. J.; Brown, Z. J.; Colon, Y. J.; Siu, P. W.; Scheidt, K. A.; Snurr, R. Q.; Hupp, J. T.; Farha, O. K., A facile synthesis of UiO-66, UiO-67 and their derivatives. *Chemical Communications* **2013,** *49* (82), 9449-9451.

36. Lide, D. R., *CRC Handbook of Chemistry and Physics*. 84 ed.; CRC: 2004.

CHAPTER 8

CONCLUSIONS AND RECOMMENDATIONS

The incorporation of metal nanoparticles in metal-organic frameworks (MOFs) produces composites that combine the unusual chemical and physical properties of the nanoparticles and MOFs to yield unprecedented performance for gas storage and separation, catalysis, and sensing.[1] Incorporation of metal nanoparticles via encapsulation presents numerous advantages, the most prominent being the capacity to incorporate nanomaterials of various sizes and shapes.[2] Therefore, the focus of this work was to introduce metal nanoparticles, such as gold nanoparticles (AuNPs), into stable MOFs, specifically UiO-66, using the encapsulation technique and to investigate the effect on the physical properties and adsorptive and catalytic capabilities of the composites.

8.1 Preparation of Au@UiO-66 via Encapsulation (Chapters 3 and 6)

Chapter 3 demonstrates an alternative UiO-66 synthesis procedure that substitutes zirconium propoxide (Zr(O*n*Pr)) for zirconium chloride ($ZrCl_4$) in order to remove by-product HCl. Due to the rapid nucleation rate, a modulating agent such as acetic acid or benzoic acid is necessary to introduce competitive coordination, which reduces the nucleation rate and enhances crystal growth to yield high-quality UiO-66(Zr(O*n*Pr)) particles. Additionally, HCl-sensitive AuNPs were added to the UiO-66(Zr(O*n*Pr)) mother solution and proven to be randomly dispersed throughout the Au@UiO-66(Zr(O*n*Pr)) composite. However, the AuNPs exhibit significant growth and many of the AuNPs are definitively deposited on the surface of the UiO-66(Zr(O*n*Pr))) particles.

Therefore, although this alternative synthesis procedure lays the groundwork for designing HCl-sensitive UiO-66 composites, there are limitations that must be overcome.

Chapter 6 endeavors to improve upon the Au@UiO-66(Zr(O*n*Pr)) synthesis procedure by controlling the AuNP diameter and location within UiO-66(Zr(O*n*Pr))) particles. Specifically, by investigating the effect of the solvent, modulator:Zr(O*n*Pr) ratio, modulator composition, and the functionality of the AuNP capping agent on the physical properties of the Au@UiO-66(Zr(O*n*Pr)) composites. These studies discovered that the AuNP diameter is dependent on the acetic acid:Zr(O*n*Pr) ratio, the UiO-66(Zr(O*n*Pr)) modulator composition, and the AuNP capping agent. Additionally, they show that the UiO-66(Zr(O*n*Pr)) particle geometry is affected by the solvent and the modulator ratios. However, the controlling factors for AuNP location are still speculative. Au@UiO-66(Zr(O*n*Pr)) prepared with an MeOH:DMF ratio of 1.9, 1-dodecanethiol (DDT) and 11-mercaptoundecanoic acid (MUA) as the AuNP capping agents, and a benzoic acid:Zr(O*n*Pr) of 30:1 produced a brown powder, colorless filtrate, and a limited number of discernible AuNPs 3 nm in diameter. This suggests that there are AuNPs confined within the UiO-66. The contrast between AuNPs 3 nm in diameter on the surface of UiO-66 particles is limited; therefore, if the AuNPs are confined within the UiO-66(Zr(O*n*Pr)) particles it would be very difficult to detect them. However, further investigation is necessary.

Future work should focus on determining the AuNP location in the Au@UiO-66(Zr(O*n*Pr)) composite previously described. STEM tomography may be capable of discerning AuNPs 3 nm in diameter when encased in UiO-66(Zr(O*n*Pr)). Alternatively, AuNP confinement within UiO-66(Zr(O*n*Pr)) can be confirmed using a catalytic reaction,

such as the reduction of nitrophenol, in the presence of large sulfur-based catalyst poisons, such as DDT. If the AuNPs are incorporated within the UiO-66(Zr(O*n*Pr)) particle, DDT will not affect the catalytic activity of the composite; however, if the AuNPs are mainly deposited on the surface of the UiO-66(Zr(O*n*Pr)) particles, then the activity will be significantly reduced. This exploitation of UiO-66(Zr(O*n*Pr)) molecular sieving will offer a bulk sample analysis of the location of the AuNPs within the Au@UiO-66(Zr(O*n*Pr)) composite. In addition, the Au@UiO-66(Zr(O*n*Pr)) samples prepared with AuNPs capped with polyvinylpyrrolidone (AuNP-PVP) should be reexamined. PVP capped nanomaterials have been successfully encapsulated in a variety of MOF structures, including UiO-66.[2, 3] Huo et al. showed that including excess PVP causes the nanoparticles to be filtered from the material and that the retained nanoparticles deposit on the MOF surface.[2] Therefore, the AuNP-PVP used in this work should be reanalyzed to determine if there is excess PVP in the material that could affect coordination.

Moving forward, this synthesis method should be extended to include AuNPs with diameters exceeding 5 nm to further probe the effect of NP diameter on the composite properties while also introducing the unusual AuNP optical properties which offer potential for sensing and photocatalysis applications.[4] In addition, this UiO-66(Zr(O*n*Pr)) composite preparation method should be extended to include other nanomaterials with various elemental compositions, sizes, and shapes. This will broaden the catalytic capabilities,[5-7] optical properties,[4, 8, 9] and magnetic capacity[10, 11] of the resulting composites providing fundamental knowledge of the synergistic effects and

effectively expanding the overall potential of MOF composites for specified applications.[12]

8.2 Oxygen Storage Capacity of MOFs (Chapter 4)

To the best of the authors' knowledge, Chapter 4 demonstrates the first evaluation of the oxygen storage capacity (OSC) of MOFs. AuNPs were deposited via colloidal deposition onto the surface of UiO-66, TiO_2, and ZrO_2 and the physical and catalytic properties were probed. Extensive characterization suggested that the AuNP factors such as weight percentage, diameter, and oxidation state were consistent for the three catalytic materials; therefore, the only variable was the catalyst support. Consistent with previous reports, Chapter 4 reveals a correlation between the OSC and the catalytic activity. Overall, AuNPs deposited on UiO-66 demonstrate an enhanced OSC, and subsequent CO oxidation activity, compared to AuNPs distributed on commercially available TiO_2 and ZrO_2. This is conceivably due to the unprecedented chemistry that evolves from the combination of metal nodes and organic linkers in MOFs and/or the introduction of defect sites during crystallization or activation.

This initial investigation into the OSC of MOFs shows that UiO-66 is capable of supplying active oxygen to the reaction. However, it is still unknown from where the active oxygen is supplied; it may be directly donated from the UiO-66 lattice or adsorbed and activated by the material. In order to understand the nature of the oxygen donating capabilities of UiO-66, isotopic OSC experiments on the Au on UiO-66 samples are recommended. Specifically, the author recommends using isotopic $^{18}O_2$ as the oxygen source to determine if oxygen is supplied directly from UiO-66 or adsorbed during the

calcination procedure. Based on these results, MOF selection as oxidation supports can be narrowed. Additionally, investigation into OSC should extend to other MOF systems that are stable under the experimental conditions, such as MIL-101 and MIL-100. MIL-101 and MIL-100 are good systems to evaluate because they are thermally, chemically, and mechanically stable and a metal substitution yields MIL-101(Cr, Fe)[13, 14] and MIL-100(Cr, Fe, Al, V)[15-18] which will offer insight into the metal impact on the OSC.

8.3 Effect of Preparation Method on Au@UiO-66 Properties (Chapter 5)

Chapter 5 utilized the Au@UiO-66(Zr(O*n*Pr)) system to probe the effect of the preparation method on the physical and catalytic properties of the composites. Three preparation methods were used: impregnation, encapsulation, and colloidal deposition. The samples prepared by colloidal deposition are used as a control system; briefly, AuNPs 2.4, 4.9, and 7.2 nm in diameter were deposited on the surface of the UiO-66 particles to probe the AuNP diameter effect for physical mixtures. The combination of TEM and CO oxidation suggests that the impregnation technique, Au@UiO-66(IMP), used herein produces a composite with the AuNPs randomly distributed on the UiO-66 particle surface. Alternatively, Au@UiO-66(ENC) demonstrates enhanced catalytic activity relative to the comparable physical mixture suggesting that the encapsulation technique introduces synergistic effects. Further investigation into the nature of the synergism via STEM tomography indicates that many of the AuNPs are deposited on the UiO-66 surface. However, others appear confined within the UiO-66 particles or UiO-66 aggregates. Unfortunately, the exact form of confinement is inconclusive, but either mode

of confinement will increase the surface area of contact between the AuNPs and UiO-66 and subsequently increases the number of AuNP-UiO-66 interface sites.

Notably, neither the impregnation or encapsulation technique herein is optimized to achieve its full potential, which is proven by the existence of AuNPs deposited on the UiO-66 surface. However, the encapsulation technique, even with its limitations, effectively introduces synergistic effects conveying that complete control of the encapsulation procedure would be beneficial.

Although AuNP growth was not the aim of this work, it can be exploited. During UiO-66 crystallization the AuNPs increased in size subsequently shifting the surface-plasmon resonance (SPR) of the nanoparticles into the visible range. SPR is a phenomenon that develops on the nanoscale when the nanoparticle surface electrons oscillate with a frequency within the visible light range. This generates a variation of colors that are dependent on the size, shape, and composition of the materials. Studies have shown that the addition of noble metal nanoparticles with pronounced SPR in the visible light region will enhance the photocatalytic capabilities of materials such as metal oxides when exposed to UV and visible light.[19, 20] Therefore, the author recommends evaluating the catalytic abilities of Au@UiO-66(Zr(O*n*Pr)) for photocatalytic oxidation or water splitting reactions.

8.4 UiO-66-X(Zr(O*n*Pr)) (Chapter 7)

Chapter 7 extends the HCl-free UiO-66 synthesis procedure to prepare UiO-66-X, where X = {–H, $–NH_2$, $–NO_2$, –Naph, –Anth, $–Cl_2$, –Br, $–(CH_3)_2$, –COOH, –OH, and $–(OH)_2$}. In addition, UiO-66-NH_2 was used to systematically study the effect of the acid

structure and concentration on UiO-66-NH_2(Zr(O*n*Pr)) properties. In summary, the role of the acid is two-fold: under moderately acidic conditions (pH ≈ 2-4), the dominating role of the acid is to competitively coordinate with the Zr^{4+} ions in order to regulate the nucleation rate and enhance crystal growth. However, increasing the modulator:Zr(O*n*Pr) ratio reveals that strong acids will shift the deprotonation equilibrium of BDC-NH_2 subsequently reducing the nucleation rate. Therefore, a benzoic acid:Zr(O*n*Pr) ratio of 30:1 or 15:1 and a trifluroroacetic acid (TFA):Zr(O*n*Pr) ratio of 120:1 are recommended when preparing UiO-66 analogues with Zr(O*n*Pr).

In addition, Chapter 7 examined a respectable variety of UiO-66-X materials, where BDC-X is commercially available; however, there are others that were not included in this study that could introduce unusual chemical properties. In particular, producing high-quality UiO-66-SO_3H has proven difficult using the previously reported synthesis procedure,[21] and the acidic functional group offers potential for acid-base interactions for the removal of basic gases. Therefore, the author recommends attempting to prepare high-quality UiO-66-SO_3H using Zr(O*n*Pr). In addition, investigating the encapsulation of HCl-sensitive AuNPs in UiO-66-X and probing the Au@UiO-66-X(Zr(O*n*Pr)) properties. The combination of AuNPs and organic functionality will potentially have a profound effect on the optical properties and photocatalytic capabilities of the composites.

In conclusion, we have made great strides into advancing the fundamental understanding of MOF composite preparation, specifically UiO-66 composites. However, further studies are necessary to fully understand the synergistic effects

introduced in the composites and to determine the synthesis procedures necessary to generate well-designed MOF composites.

8.5 References

1. Falcaro, P.; Ricco, R.; Yazdi, A.; Imaz, I.; Furukawa, S.; Maspoch, D.; Ameloot, R.; Evans, J. D.; Doonan, C. J., Application of metal and metal oxide nanoparticles@MOFs. *Coordination Chemistry Reviews* **2016,** *307*, 237-254.

2. Lu, G.; Li, S.; Guo, Z.; Farha, O. K.; Hauser, B. G.; Qi, X.; Wang, Y.; Wang, X.; Han, S.; Liu, X.; DuChene, J. S.; Zhang, H.; Zhang, Q.; Chen, X.; Ma, J.; Loo, S. C. J.; Wei, W. D.; Yang, Y.; Hupp, J. T.; Huo, F., Imparting functionality to a metal-organic framework material by controlled nanoparticle encapsulation. *Nature Chemistry* **2012,** *4* (4), 310-316.

3. Zhang, W. N.; Lu, G.; Cui, C. L.; Liu, Y. Y.; Li, S. Z.; Yan, W. J.; Xing, C.; Chi, Y. R.; Yang, Y. H.; Huo, F. W., A Family of Metal-Organic Frameworks Exhibiting Size-Selective Catalysis with Encapsulated Noble-Metal Nanoparticles. *Advanced Materials* **2014,** *26* (24), 4056-4060.

4. Eustis, S.; El-Sayed, M. A., Why gold nanoparticles are more precious than pretty gold: Noble metal surface plasmon resonance and its enhancement of the radiative and nonradiative properties of nanocrystals of different shapes. *Chemical Society Reviews* **2006,** *35* (3), 209-217.

5. Gang, L. Catalytic Oxidation of Ammonia to Nitrogen. Eindhoven University of Technology, Eindhoven, The Netherlands, 2002.

6. Narayanan, R.; El-Sayed, M. A., Catalysis with transition metal nanoparticles in colloidal solution: Nanoparticle shape dependence and stability. *Journal of Physical Chemistry B* **2005,** *109* (26), 12663-12676.

7. Lopez, N.; Janssens, T. V. W.; Clausen, B. S.; Xu, Y.; Mavrikakis, M.; Bligaard, T.; Norskov, J. K., On the origin of the catalytic activity of gold nanoparticles for low-temperature CO oxidation. *Journal of Catalysis* **2004,** *223* (1), 232-235.

8. Wiley, B. J.; Im, S. H.; Li, Z.-Y.; McLellan, J.; Siekkinen, A.; Xia, Y., Maneuvering the surface plasmon resonance of silver nanostructures through shape-controlled synthesis. *Journal of Physical Chemistry B* **2006,** *110* (32), 15666-15675.

9. Wiley, B. J.; Chen, Y. C.; McLellan, J. M.; Xiong, Y. J.; Li, Z. Y.; Ginger, D.; Xia, Y. N., Synthesis and optical properties of silver nanobars and nanorice. *Nano Letters* **2007,** *7* (4), 1032-1036.

10. Park, J. I.; Kang, N. J.; Jun, Y. W.; Oh, S. J.; Ri, H. C.; Cheon, J., Superlattice and magnetism directed by the size and shape of nanocrystals. *Chemphyschem* **2002,** *3* (6), 543-+.

11. Aslam, M.; Bhobe, R.; Alem, N.; Donthu, S.; Dravid, V. P., Controlled large-scale synthesis and magnetic properties of single-crystal cobalt nanorods. *Journal of Applied Physics* **2005,** *98* (7).

12. Xia, Y.; Xiong, Y.; Lim, B.; Skrabalak, S. E., Shape-Controlled Synthesis of Metal Nanocrystals: Simple Chemistry Meets Complex Physics? *Angewandte Chemie (International ed. in English)* **2009,** *48* (1), 60-103.

13. Ferey, G.; Mellot-Draznieks, C.; Serre, C.; Millange, F.; Dutour, J.; Surble, S.; Margiolaki, I., A chromium terephthalate-based solid with unusually large pore volumes and surface area. *Science* **2005,** *309* (5743), 2040-2042.

14. Taylor-Pashow, K. M. L.; Della Rocca, J.; Xie, Z. G.; Tran, S.; Lin, W. B., Postsynthetic Modifications of Iron-Carboxylate Nanoscale Metal-Organic Frameworks for Imaging and Drug Delivery. *Journal of the American Chemical Society* **2009,** *131* (40), 14261-+.

15. Ferey, G.; Serre, C.; Mellot-Draznieks, C.; Millange, F.; Surble, S.; Dutour, J.; Margiolaki, I., A hybrid solid with giant pores prepared by a combination of targeted chemistry, simulation, and powder diffraction. *Angewandte Chemie-International Edition* **2004,** *43* (46), 6296-6301.

16. Horcajada, P.; Surble, S.; Serre, C.; Hong, D. Y.; Seo, Y. K.; Chang, J. S.; Greneche, J. M.; Margiolaki, I.; Ferey, G., Synthesis and catalytic properties of MIL-100(Fe), an iron(III) carboxylate with large pores. *Chemical Communications* **2007,** (27), 2820-2822.

17. Volkringer, C.; Popov, D.; Loiseau, T.; Férey, G.; Burghammer, M.; Riekel, C.; Haouas, M.; Taulelle, F., Synthesis, Single-Crystal X-ray Microdiffraction, and NMR Characterizations of the Giant Pore Metal-Organic Framework Aluminum Trimesate MIL-100. *Chemistry of Materials* **2009,** *21* (24), 5695-5697.

18. Lieb, A.; Leclerc, H.; Devic, T.; Serre, C.; Margiolaki, I.; Mahjoubi, F.; Lee, J. S.; Vimont, A.; Daturi, M.; Chang, J.-S., MIL-100(V) – A mesoporous vanadium metal organic framework with accessible metal sites. *Microporous and Mesoporous Materials* **2012,** *157*, 18-23.

19. Chen, X.; Zhu, H.-Y.; Zhao, J.-C.; Zheng, Z.-T.; Gao, X.-P., Visible-light-driven oxidation of organic contaminants in air with gold nanoparticle catalysts on oxide supports. *Angewandte Chemie-International Edition* **2008,** *47* (29), 5353-5356.

20. Hou, W.; Cronin, S. B., A Review of Surface Plasmon Resonance-Enhanced Photocatalysis. *Advanced Functional Materials* **2013,** *23* (13), 1612-1619.

21. Jasuja, H.; Peterson, G. W.; Decoste, J. B.; Browe, M. A.; Walton, K. S., Evaluation of MOFs for air purification and air quality control applications: Ammonia removal from air. *Chemical Engineering Science* **2015,** *124*, 118-124.

APPENDIX A

ALTERNATIVE MIL-125 SYNTHESIS PROCEDURE

A.1 Introduction

MIL-125 is a titanium-based MOF consisting of $Ti_8O_8(OH)_4$ nodes linked via 1,4-benzenedicarboxylic acid (BDC) yielding a quasi-cubic, tetragonal structure (Figure A.1) with trapezoidal windows ranging from 5-7 Å. It collapses at temperatures exceeding 633K; however, it undergoes a phase transition between 563-623K.[1] In addition, TiO_2 is a well-studied catalytic support; specifically, AuNPs supported on TiO_2 is well known to be catalytically active towards CO oxidation under ambient conditions.[2, 3] Therefore, MIL-125 is an ideal MOF system to probe the capabilities of MOFs as catalyst supports.

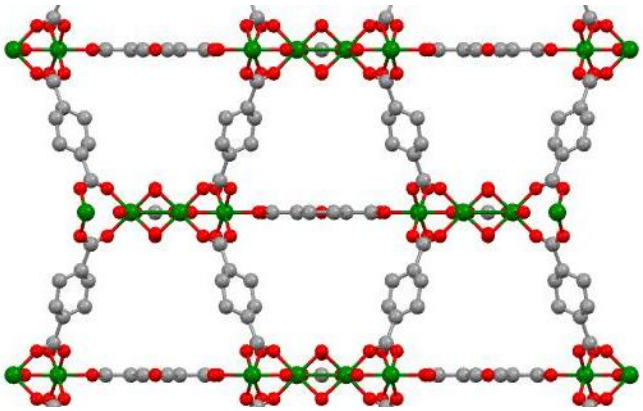

Figure A.1: MIL-125 structure illustration. Titanium atoms are green, oxygen atoms are red, and carbon atoms are gray

A.2 Experimental Methods

A.2.1 Material Synthesis

All chemicals were obtained commercially (Sigma-Aldrich and Fisher Scientific) and used as obtained. MIL-125(original) was synthesized as previously reported.[1] Briefly, titanium isopropoxide ($Ti(O^iPr)_4$), BDC, methanol, and N,N'-dimethylformamide (DMF) in a glass scintillation vial was stirred at 383 K for 24 h in an oil bath. The solution was allowed to cool to room temperature, then, filtered and washed with DMF three times and methanol three times. Alternative combinations of the precursors were also explored to tune the synthesis procedure (Table A.1).

Table A.1: MIL-125 synthesis conditions

Material	$Ti(O^iPr)$ (mmol)	BDC (mmol)	Acetic Acid (mmol)	MeOH (mmol)	DMF (mmol)
MIL-125(original)	1.00	1.50	0.00	12.36	58.12
MIL-125(a)	0.74	2.25	0.00	160.67	83.95
MIL-125(b)	0.74	2.25	24.48	160.67	83.95

AuNPs capped with 1-dodecanethiol (DDT) were prepared using a previously reported procedure.[4] A solution of tetraoctylammonium bromide (0.728 mmol) in toluene (40 mL) was added to a solution of gold(III) chloride trihydrate ($HAuCl_4 \cdot 3H_2O$) (0.314 mmol) in water (20 mL). The mixture was stirred for 30 min. Then, DDT (0.314 mmol) was added, followed by a solution of sodium borohydride ($NaBH_4$) (3.14 mmol) in water (10 mL). The solution was stirred vigorously for 3 h and washed with copious amounts of water. The organic phase was then separated and reduced to approximately 10 mL under vacuum at 298K. Next, 100 mL of methanol was added and the particles precipitated overnight. The solvent was decanted and the particles were washed twice more with

copious amounts of methanol. Finally, the DDT monolayer was place-exchanged with 11-mercaptoundecanoic acid (MUA) (0.154 mmol) and washed with toluene.[5]

A.2.2 Characterization

Powder X-ray diffraction (PXRD) patterns were obtained using a PANalytical X-ray diffractometer. Approximately 5 mg of sample were placed on a low background sample holder and scanned from 5-50°. The obtained diffractograms were compared to the simulated patterns to confirm that the MIL-125 structure was obtained. Nitrogen sorption measurements at 77 K were performed using a Quantachrome Quadrasorb SI volumetric analyzer. The isotherms were measured over a range of relative pressures from 0.003 to 0.990 using high purity nitrogen (99.998%) obtained from Airgas. Prior to the measurement, the samples were outgassed in a Quantachrome FloVac Degasser at 423 K under dynamic vacuum for approximately 18 h. The surface areas were calculated using the Brunauer, Emmett, and Teller (BET) theory using relative pressures ranging from 0.005-0.03 and the total pore volume was calculated at a relative pressure (P/P_0) of 0.6. Transmission Electron Microscopy (TEM) and Scanning Transmission Electron Microscopy-Energy Dispersive Spectroscopy (STEM-EDS) were used to analyze the original AuNPs and Au@MIL-125(b). Only Au@MIL-125(b) was further characterized because MIL-125(original) is not crystalline and Au@MIL-125(a) does not retain the AuNPs. The samples were prepared by suspending a less than 1 mg of sample in solution and dropcasting onto a lacy carbon coated copper grid. The AuNPs were analyzed using the JEOL 100CX operated at 100 keV. Au@MIL-125(b) was analyzed using the FEI Tecnai F30 operated at 300 keV and EDS spectra were acquired using the Oxford EDX

6763. The composition was measured at a specified point marked with a red circle and analyzed using TEM Imaging & Analysis (TIA) Software. The FEI Tecnai F30 is supported by funding DMR 0922776. Proton nuclear magnetic resonance (^{1}H NMR) spectroscopy was measured on a Varian Mercury Vx 300. The samples were prepared by suspending approximately 10 mg of AuNPs in 1 mL of dimethyl sulfoxide-d_6. ^{1}H NMR data were used to determine the composition of the organic monolayer on the AuNPs.

A.2.3 Adsorption and Catalysis

Single component adsorption isotherms were measured at 298 K from 0-20 bar using a Hiden Isochema IGA-001 microbalance. The samples were activated in-situ at 423 K under dynamic vacuum to remove excess solvent and water. CO oxidation experiments were performed using a lab-built packed bed reactor with the outlet connected to a Hiden DSMS. Approximately 25-40 mg of sample were packed into the sample cell with glass wool. Before the catalytic measurement, the material was purged with helium at 473 K overnight to remove excess solvent and water. After heating to the reaction temperature, 1% CO in air was passed through the system at a total flow rate of 50 mL/min.

A.3 Results

Figure A.2a shows that using the original synthesis procedure yields an amorphous material. However, by adjusting the synthesis parameters, crystalline MIL-125 is produced. Table A.2 also shows that the alternative MIL-125 procedure yields highly porous MIL-125 with BET surface areas comparable to the previously reported

material. In addition, CO_2 and CH_4 adsorption experiments were conducted to further confirm the quality of MIL-125 prepared under alternative synthesis conditions. The CO_2 uptake exhibited by MIL-125(b), depicted in Figure A.3a, is similar to previously reported values.[6] Lastly, a crucial limitation of MOFs is the material degradation in humid environments. A cursory evaluation of the stability of MIL-125 was performed by immersing MIL-125(b) in water for 24 h. Figure A.2b shows that after soaking in water for 24 h the crystal structure for MIL-125(b) degrades. Additionally, the BET surface area after soaking is 71 m^2/g which is a 96% loss showing that the crystal structure and porosity are completely degraded when soaked in water.

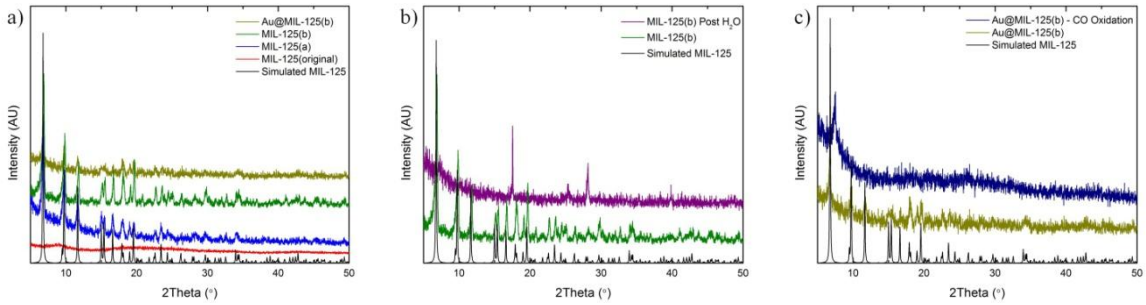

Figure A.2: PXRD patterns for MIL-125 samples (a) as synthesized, (b) after soaking in water for 24 h, and (c) after CO oxidation at 523K

Table A.2: Porosity measurements for various MIL-125 synthesis procedures

Material	BET Surface Area (m^2/g)	Total Pore Volume (cm^3/g)[a]
MIL-125(lit)	1550[1]	-----
MIL-125(original)	245	0.16
MIL-125(a)	1533	0.66
MIL-125(b)	1749	0.73
Au@MIL-125(b)	1277	0.55

[a]Measured at $P/P_0 = 0.6$

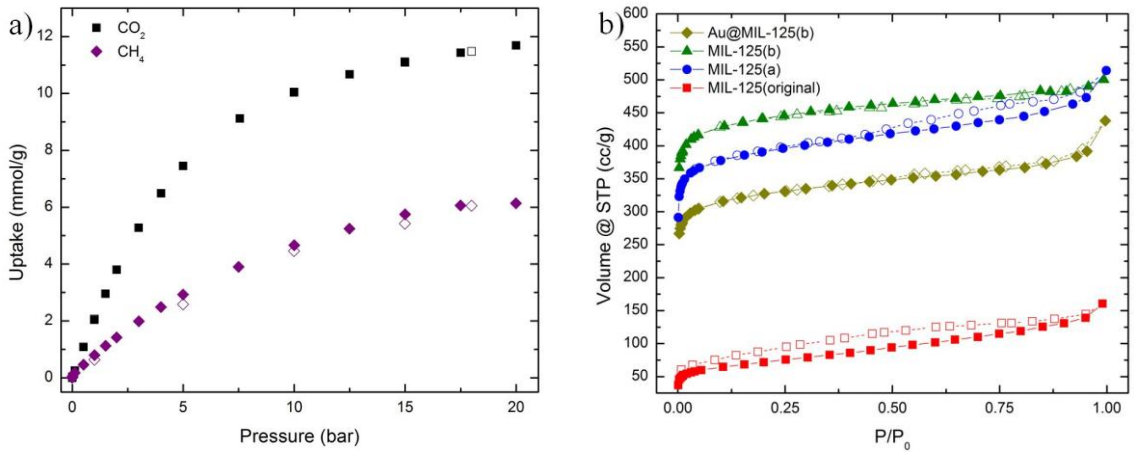

Figure A.3: (a) CO_2 and CH_4 sorption isotherms at 298 K for MIL-125(b) and (b) nitrogen sorption isotherms at 77 K for the various MIL-125 samples. The closed and open symbols represent adsorption and desorption, respectively

As previously mentioned, AuNPs deposited on TiO_2 is a well-studied system, specifically for CO oxidation.[2] Herein, preformed AuNPs were added to the MIL-125 mother solution. First, AuNPs 3.1±0.6 nm in diameter were prepared as previously reported.[4, 5] They are stabilized in solution using a mixed surface assembled monolayer (SAM) consisting of MUA and DDT in a 3:1 ratio. TEM is used to determine the AuNP diameter (Figure A.4a) and ^{1}H NMR confirms and quantifies the SAM on the AuNP surface (Figure A.4b). In Figure A.4b, the broad peaks are characteristic of ligands bound to a surface. The T_2 relaxation time accelerates when an organic is bound to a surface.[7] Therefore, the lack of coupling suggests that all of the ligands are bound to the AuNP surface. Additionally, the composition of the SAM is confirmed by analyzing the characteristic peak positions. DDT has a unique peak at 0.84 ppm associated with $–CH_3$ and MUA has a characteristic peak at 2.13 ppm for $–CH_2COOH$.

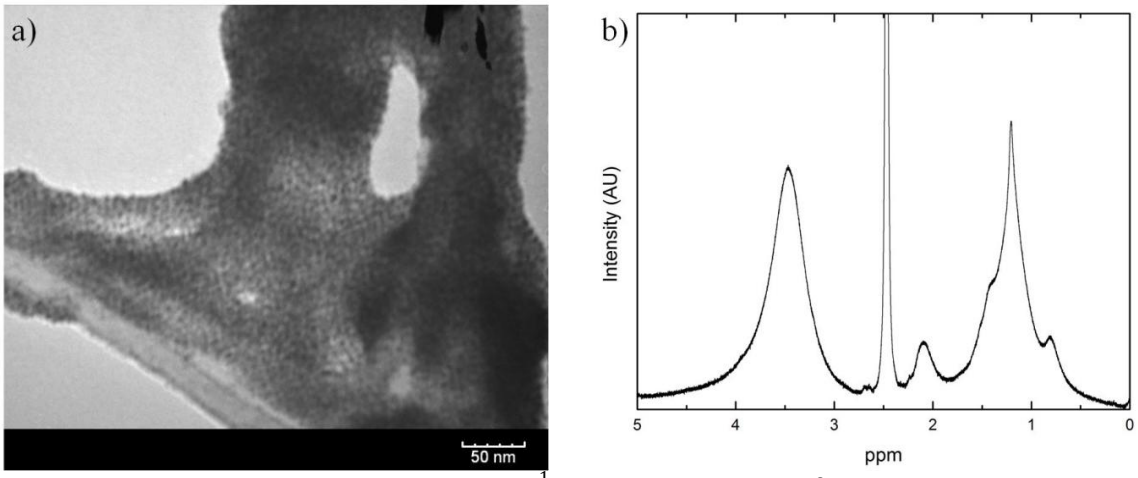

Figure A.4: (a) TEM image and (b) ^{1}H NMR spectra of as-synthesized AuNP-DDT/MUA

These preformed AuNPs were added to the MIL-125(a) and MIL-125(b) mother solutions to allow MIL-125 to grow around the AuNPs and the properties of the composite probed. The Au@MIL-125(b) procedure yielded a colorless filtrate and pink powder (Figure A.5). Whereas, MIL-125(a) produced a brown filtrate, indicating that the AuNPs are not a part of the material. In short, acetic acid is necessary in order for the AuNPs to be retained in MIL-125. One possible explanation is that acetic acid introduces more defects in MIL-125 which increases the potential open titanium sites for the functionalized AuNPs to coordinate. Figure A.2a and Table A.2 show that including AuNPs in the MIL-125 mother solution yields a highly porous material with the MIL-125 structure. The BET surface area for Au@MIL-125(b) is reduced compared to MIL-125(b) due to the increased density of the material that occurs when dense AuNPs are added to the material. The color change and retention of the MIL-125 structure suggests that, for Au@MIL-125, there are AuNPs incorporated somewhere in the material. TEM and STEM-EDS are used to probe the AuNP size, distribution, and composition. Figure A.6 shows TEM and STEM images of Au@MIL-125(b). Assuming that the dark

particles in Figure A.6a are the AuNPs (contrast in TEM is dependent on atomic number); the particles grow during the synthesis from the original 3.1 nm to approximately 6.9 nm. STEM-EDS was performed to confirm that the dark particles (which are bright in STEM mode) deposited randomly throughout the material are AuNPs. Table A.3 reports the composition of the material at the red dot in Figure A.6b. Based on STEM-EDS, the bright particles scattered throughout the material are not AuNPs. However, the point analysis could have been on an area that did not include AuNPs.

Figure A.5: Images of (a) MIL-125(b) and (b) Au@MIL-125(b)

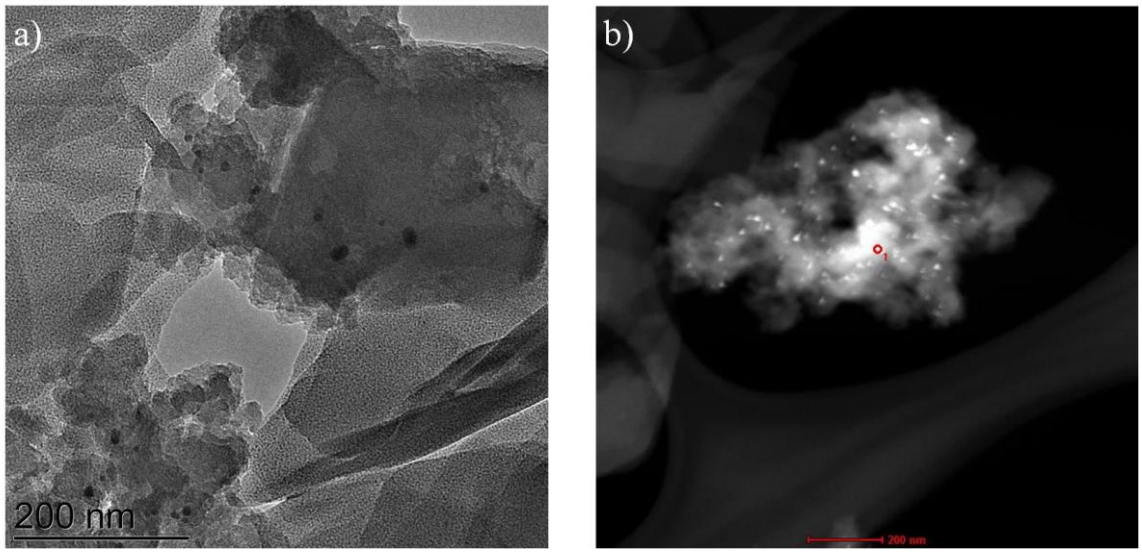

Figure A.6: (a) TEM and (b) STEM-EDS images of Au@MIL-125(b)

Table A.3: EDS analysis of Au@MIL-125(b) at red dot in Figure A.6

Element	Weight Percentage
C(K)	51.04
O(K)	19.96
Ti(K)	24.68
Cu(K)	4.31
Au(L)	0

CO oxidation at 523 K was performed to further probe the existence of AuNPs in Au@MIL-125(b). These composites were prepared using AuNPs with a mixed SAM of DDT and MUA. Removing this SAM is paramount for CO oxidation activity; the Au sites must be accessible. To determine the necessary activation conditions, two CO oxidation experiments were performed: the material was activated at (1) 423 K in helium for approximately 18 h, and (2) 423 K in helium for approximately 18 h, then calcined in air at 523 K for 2 h. Figure A.7 reports the catalytic activity of Au@MIL-125(b) for both activation conditions over time. For both activation procedures, CO_2 is produced; however, the activity is improved when the sample is calcined at 523K. Calcination could be necessary for several reasons: (1) to combust the SAM, effectively removing the ligands from the sample to free the AuNP active sites; (2) to oxide the AuNPs; or (3) to improve the interactions between the AuNPs and MIL-125 potentially by oxidizing open titanium sites. However, the reason for calcination was not probed further for this work. The catalytic capabilities of Au@MIL-125 suggest that there are AuNPs scattered throughout the material; however, the size and location cannot be verified. Lastly, to test the stability of the composite under reaction conditions, PXRD was performed on the sample after CO oxidation. Figure A.2c shows that the MIL-125 structure is not retained after CO oxidation at 523K.

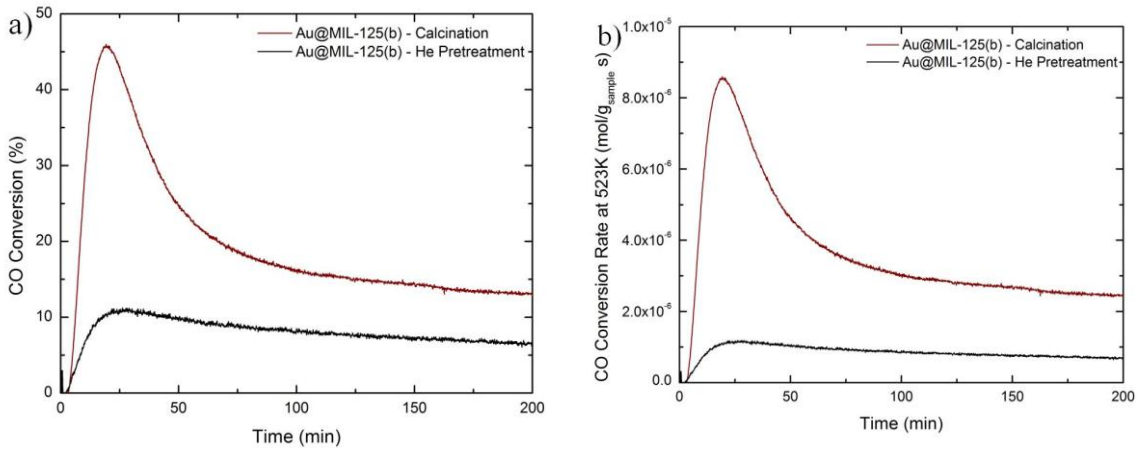

Figure A.7: (a) CO conversion and (b) reaction rate over time for Au@MIL-125(b) at 523 K for a sample activated under He flow at 423 K and a sample activated under He flow at 423 K then calcined in air at 523 K for 2 h

A.4 Conclusions

The synthesis for parent MIL-125 was tuned to produce highly porous, crystalline material. Additionally, preformed AuNPs were encapsulated in MIL-125 and the physical and catalytic capabilities of the material were probed. However, TEM was inconclusive when probing AuNP diameter because definitive proof of AuNPs was not obtained. Additionally, Au@MIL-125 degrades under the reaction conditions used to probe the catalytic capabilities of the material. Therefore, MIL-125 and Au@MIL-125 are not probed further.

A.5 References

1. Dan-Hardi, M.; Serre, C.; Frot, T.; Rozes, L.; Maurin, G.; Sanchez, C.; Ferey, G., A New Photoactive Crystalline Highly Porous Titanium(IV) Dicarboxylate. *Journal of the American Chemical Society* **2009,** *131* (31), 10857-+.

2. Haruta, M., Catalysis of gold nanoparticles deposited on metal oxides. *Cattech* **2002,** *6* (3), 102-115.

3. Comotti, M.; Li, W. C.; Spliethoff, B.; Schuth, F., Support effect in high activity gold catalysts for CO oxidation. *Journal of the American Chemical Society* **2006,** *128* (3), 917-924.

4. Brust, M.; Walker, M.; Bethell, D.; Schiffrin, D. J.; Whyman, R., Synthesis of thiol-derivatised gold nanoparticles in a two-phase Liquid-Liquid system. *Journal of the Chemical Society-Chemical Communications* **1994,** (7), 801-802.

5. Hostetler, M. J.; Templeton, A. C.; Murray, R. W., Dynamics of place-exchange reactions on monolayer-protected gold cluster molecules. *Langmuir* **1999,** *15* (11), 3782-3789.

6. Kim, S. N.; Kim, J.; Kim, H. Y.; Cho, H. Y.; Ahn, W. S., Adsorption/catalytic properties of MIL-125 and NH_2-MIL-125. *Catalysis Today* **2013,** *204*, 85-93.

7. Hostetler, M. J.; Wingate, J. E.; Zhong, C. J.; Harris, J. E.; Vachet, R. W.; Clark, M. R.; Londono, J. D.; Green, S. J.; Stokes, J. J.; Wignall, G. D.; Glish, G. L.; Porter, M. D.; Evans, N. D.; Murray, R. W., Alkanethiolate gold cluster molecules with core diameters from 1.5 to 5.2 nm: Core and monolayer properties as a function of core size. *Langmuir* **1998,** *14* (1), 17-30.

APPENDIX B

Au@ZIF-8

B.1 Introduction

ZIF-8 is a zinc-methylimidazole framework structure with a sodalite topology (illustrated in Figure B.1), a pore diameter of 11.6 Å, and a pore aperture diameter of 3.4 Å. It is thermally stable up to 823K, chemically stable, and hydrophobic.[1,2] In addition, ZIF-8 has been prepared utilizing numerous synthesis methods such as solvothermal, room temperature, electrochemical, sonochemical, microwave, and mechanochemical techniques and under a multitude of synthesis conditions.[1, 3-7] For instance, ZIF-8 has been effectively prepared at various temperatures, in assorted reaction media, and by altering the precursor ratios.[1, 3, 8, 9] Therefore, ZIF-8 is an ideal system to investigate the effect of the synthesis conditions on the physical properties of MOF composites.

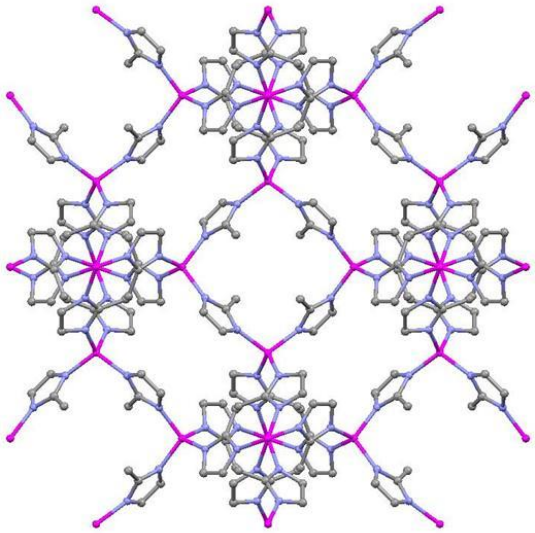

Figure B.1: ZIF-8 structure illustration. Zinc atoms are pink, nitrogen atoms are blue, and carbon atoms are gray

B.2 Materials and Methods

B.2.1 Material Synthesis

All chemicals were obtained commercially (Sigma-Aldrich, VWR, and Fisher Scientific) and used as obtained.

B.2.1.1 AuNP-DDT/MUA

AuNPs capped with 1-dodecanethiol (DDT) and 11-mercaptoundecanoic acid (MUA) were prepared using a two-step process: (1) the synthesis of DDT capped gold nanoparticles (AuNP-DDT) followed by (2) a ligand exchange with MUA. AuNP-DDT were prepared using a previously reported procedure.[10] A solution of tetraoctylammonium bromide (0.728 mmol) in toluene (40 mL) was mixed with a solution of gold(III) chloride trihydrate ($HAuCl_4 \cdot 3H_2O$) (0.314 mmol) in water (20 mL) and stirred for 30 min. Next, DDT (0.314 mmol) was added, and the mixture was stirred for 30 min. Finally, a solution of sodium borohydride ($NaBH_4$) (3.14 mmol) in water (10 mL) was added and the mixture is rigorously stirred for 3 h. The product was washed with de-ionized water, the organic phase separated, and the AuNP-DDT were precipitated three times from methanol (MeOH). The ligand exchange entailed stirring AuNP-DDT (3 mg/mL) and MUA (0.154 mmol) in toluene for 72 h and washing the product three times with toluene.[11] The resulting mixed ligand product will be referred to as AuNP-DDT/MUA throughout this work.

B.2.1.2 Au@ZIF-8: Molar Ratio of Precursors

Au@ZIF-8 was synthesized at room temperature for 24 h, as previously reported.[3] Briefly, two mixtures were prepared: (1) zinc nitrate hexahydrate ($Zn(NO_3)_2 \cdot 6H_2O$) was dissolved in 12.5 mL MeOH and (2) 2-methylimidazole (HMIM) and 1 mg AuNP-DDT/MUA dissolved in 12.5 mL MeOH were combined and stirred at room temperature for 24 h. The ratio of HMIM:$Zn(NO_3)_2 \cdot 6H_2O$ was varied to determine the effect of precursor ratio on the formation of Au@ZIF-8 composites. Table B.1 reports the two ratios probed in this work.

Table B.1: Synthesis parameters for Au@ZIF-8(HMIM:$Zn(NO_3)_2 \cdot 6H_2O$)

Material	$Zn(NO_3)_2 \cdot 6H_2O$ (mmol)	HMIM (mmol)
Au@ZIF-8(HMIM:$Zn(NO_3)_2$ = 4)	0.62	2.48
Au@ZIF-8(HMIM:$Zn(NO_3)_2$ = 1)	0.62	0.62

B.2.1.3 Au@ZIF-8: Precursor Addition Time

Au@ZIF-8 was synthesized at room temperature by adding the AuNPs at three different times using a procedure adapted from a previously reported ZIF-8 procedure.[3] The samples are denoted Au@ZIF-8(Zn), Au@ZIF-8(HMIM), and Au@ZIF-8(3min). Au@ZIF-8(Zn) was prepared by mixing 0.62 mmol of $Zn(NO_3)_2 \cdot 6H_2O$ and 1 mg of AuNP-DDT/MUA in 12.5 mL of MeOH for 10 min yielding a brown suspension. Then, of HMIM (2.47 mmol), dissolved in 12.5 mL of MeOH, was added. The mixture was stirred at room temperature for 24 h yielding a brown powder (Figure B.2b). Au@ZIF-8(HMIM) was synthesized by mixing HMIM (2.47 mmol) and 1 mg of AuNP-DDT/MUA in 12.5 mL of MeOH for 10 min yielding a brown solution. Then, the mixture was added to a solution of $Zn(NO_3)_2 \cdot 6H_2O$ (0.62 mmol) in 12.5 mL of MeOH.

The mixture was stirred at room temperature for 24 h yielding a purple powder (Figure B.2c). Au@ZIF-8(3min) was prepared by stirring a solution of $Zn(NO_3)_2 \cdot 6H_2O$ (0.62 mmol) in 12.5 mL MeOH and HMIM (2.47 mmol) in 12.5 mL MeOH for 3 min. Then, 1 mg of AuNP-DDT/MUA was added and the mixture was stirred at room temperature for 24 h yielding a purple powder (Figure B.2d).

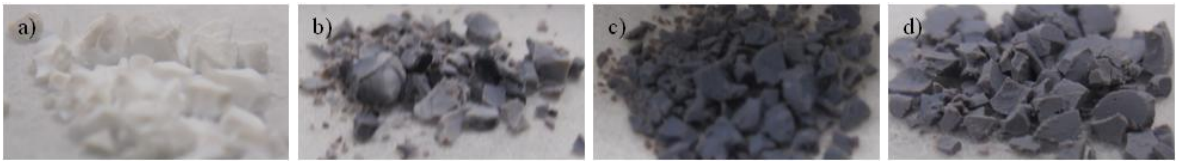

Figure B.2: Digital images of (a) ZIF-8, (b) Au@ZIF-8(Zn), (c) Au@ZIF-8(HMIM), and (d) Au@ZIF-8(3min)

B.2.1.4 Au@ZIF-8: Solvent Effect

ZIF-8 and Au@ZIF-8 were synthesized at room temperature using a variation of solvents and solvent mixtures listed in Table B.2. Briefly, two solutions were prepared: (1) $Zn(NO_3)_2 \cdot 6H_2O$ was dissolved in 12.5 mL solvent/solvent mixture and (2) HMIM with AuNP-DDT/MUA were dissolved in 12.5 mL solvent/solvent mixture. These solutions were combined and stirred at room temperature for 24 h. The resulting Au@ZIF-8 powders have a range of optical differences shown in Figure B.3.

Table B.2: Synthesis parameters for Au@ZIF-8(solvent)

Material	$Zn(NO_3)_2 \cdot 6H_2O$ (mmol)	HMIM (mmol)	MeOH (mmol)	EtOH (mmol)	DMF (mmol)	Acetone (mmol)
ZIF-8 (MeOH)	0.62	2.48	618	0	0	0
ZIF-8 (EtOH)	0.62	2.48	0	428	0	0
ZIF-8 (DMF)	0.62	2.48	0	0	323	0
ZIF-8 (Acetone)	0.62	2.48	0	0	0	340
ZIF-8 (MeOH:EtOH)	0.62	2.48	309	214	0	0
ZIF-8 (MeOH:DMF)	0.62	2.48	309	0	161	0
ZIF-8 (EtOH:DMF)	0.62	2.48	0	214	161	0
Au@ZIF-8 (MeOH)	0.62	2.48	618	0	0	0
Au@ZIF-8 (EtOH)	0.62	2.48	0	428	0	0
Au@ZIF-8 (DMF)	0.62	2.48	0	0	323	0
Au@ZIF-8 (Acetone)	0.62	2.48	0	0	0	340
Au@ZIF-8 (MeOH:EtOH)	0.62	2.48	309	214	0	0
Au@ZIF-8 (MeOH:DMF)	0.62	2.48	309	0	161	0
Au@ZIF-8 (EtOH:DMF)	0.62	2.48	0	214	161	0

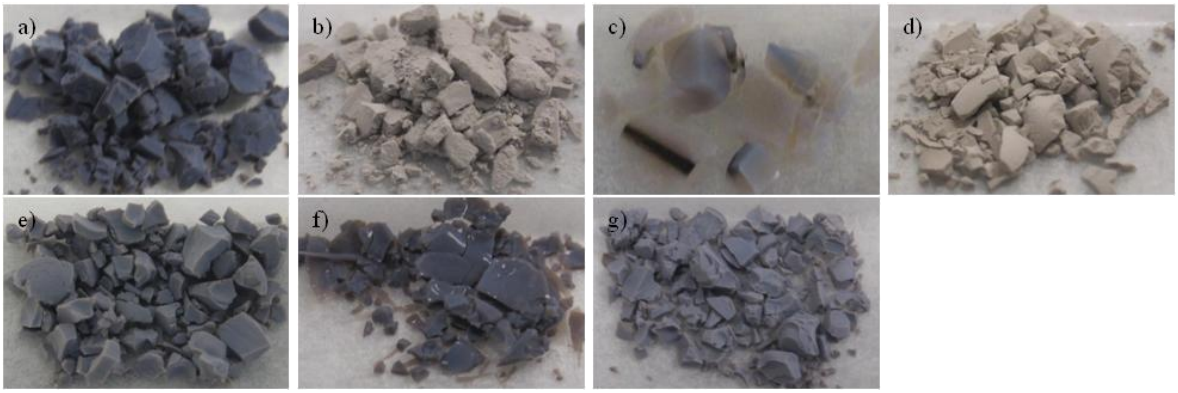

Figure B.3: Images of (a) Au@ZIF-8(MeOH), (b) Au@ZIF-8(EtOH), (c) Au@ZIF-8(DMF), (d) Au@ZIF-8(Acetone), (e) Au@ZIF-8(MeOH:EtOH), (f) Au@ZIF-8(MeOH:DMF), and (g) Au@ZIF-8(EtOH:DMF)

B.2.2 Characterization

Powder X-ray diffraction (PXRD) patterns were obtained using a PANalytical X-ray diffractometer. Approximately 10 mg of sample were deposited on a low background silica sample holder and scanned from 5-50°. A Quantachrome Quadrasorb SI volumetric analyzer collected nitrogen sorption data at 77K. The isotherms were measured over a relative pressure (P/P_0) range of 0.001-0.990 with high purity nitrogen (Airgas 99.998%).

Prior to the measurement, the samples were heated at 473 K for 16-18 h under vacuum using a Quantachrome FloVac Degasser. The specific surface areas were calculated using the Brunauer, Emmett, and Teller (BET) Theory using $0.005 \leq P/P_0 \leq 0.03$, and the total pore volume was calculated at $P/P_0 = 0.6$. TEM images were acquired using the JEOL 100CX operated at 100 keV, the Hitachi HT7700 operated at 120 keV, and the FEI Tecnai F30 operated at 300 keV. The FEI Tecnai F30 is supported by funding DMR 0922776. The samples were prepared by suspending less than 1 mg of sample in MeOH and dropcasting it on a lacy carbon copper grid. Proton nuclear magnetic resonance (^{1}H NMR) spectroscopy data were used to determine the composition of the organic monolayer on the AuNPs. ^{1}H NMR was measured on a Varian Mercury Vx 300. The samples were prepared by suspending approximately 10 mg of AuNP-DDT/MUA in 1 mL of dimethyl sulfoxide-d_6.

B.2.3 CO Oxidation

CO oxidation experiments were performed using a lab-built packed bed reactor with the outlet connected to a Hiden DSMS. Approximately 25-40 mg of sample were packed into the sample cell with glass wool. Before the catalytic measurement, the material was purged with helium at 473 K for 16-18 h to remove excess solvent and water. After heating/cooling to the reaction temperature, 1% CO in air passed through the system at a total flow rate of 50 mL/min.

B.3 Results and Discussion

B.3.1 Material Synthesis

B.3.1.1 AuNP-DDT/MUA

For the encapsulation of AuNPs in ZIF-8, preformed AuNPs are formed, and then added to the ZIF-8 mother solution. The TEM image depicted in Figure B.4a shows AuNP-DDT/MUA that are 3.1±0.6 nm in diameter. In addition, the ^{1}H NMR spectrum shown in Figure B.4b confirms that the AuNPs are stabilized in solution by a mixed surface assembled monolayer (SAM) consisting of MUA:DDT in a 3:1 ratio. The broad peaks in Figure B.4b are characteristic of ligands bound to a surface. The T_2 relaxation time accelerates when an organic is bound to a surface.[12] Therefore, the lack of coupling suggests that all of the ligands are bound to the AuNP surface. Additionally, the composition of the SAM is confirmed by analyzing the characteristic peak positions. DDT has a unique peak at 0.84 ppm associated with $–CH_3$, and MUA has a characteristic peak at 2.13 ppm for $–CH_2COOH$.

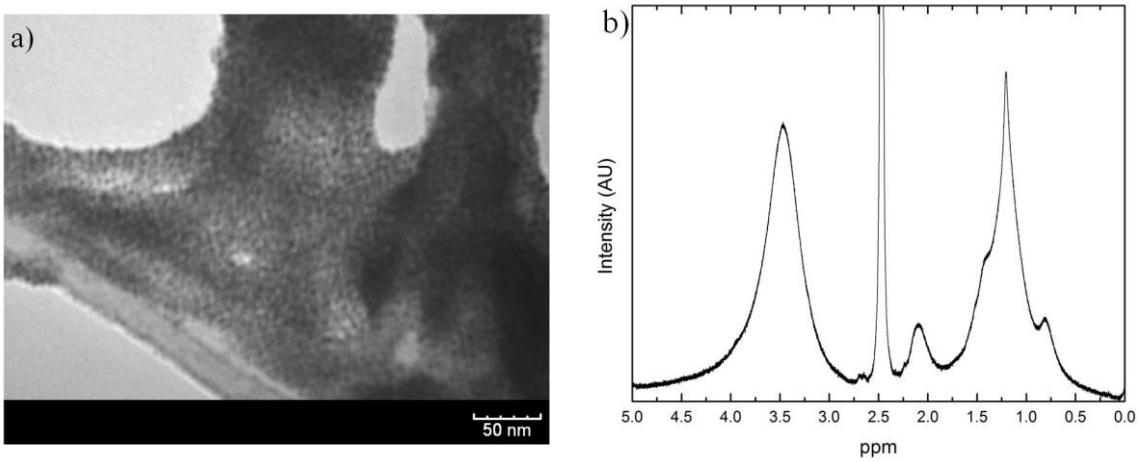

Figure B.4: (a) TEM image and (b) ^{1}H NMR spectra of as synthesized AuNP-DDT/MUA

B.3.1.2 Au@ZIF-8: Molar Ratio of Precursors

Table B.1 reports the synthesis conditions used to prepare Au@ZIF-8(HMIM:$Zn(NO_3)_2$). For this study, two ratios are used: HMIM:$Zn(NO_3)_2$ = 4 and HMIM:$Zn(NO_3)_2$ = 1. A major drawback of the HMIM:$Zn(NO_3)_2$ = 1 ratio is the low yield reported in Table B.3, which limits the material characterization. Notably, Au@ZIF-8(HMIM:$Zn(NO_3)_2$ = 4) begins nucleation within 3 min of the solution combination, whereas nucleation for Au@ZIF-8(HMIM:$Zn(NO_3)_2$ = 1) occurs after 10 min. Figure B.5 shows that the ZIF-8 structure is obtained when AuNPs are added to the ZIF-8 mother solution. Table B.3 shows that the AuNPs do not grow during the ZIF-8 crystallization with either HMIM:$Zn(NO_3)_2$ ratio. In addition, TEM images, depicted in Figure B.6, reveal two things: (1) the HMIM:$Zn(NO_3)_2$ ratio affects the ZIF-8 particle size, a lower ratio yields in larger crystals and (2) the HMIM:$Zn(NO_3)_2$ ratio affects the tentative AuNP-DDT/MUA location in ZIF-8. Specifically, Au@ZIF-8 (HMIM:$Zn(NO_3)_2$ = 4) has AuNPs scattered throughout the sample with particles potentially trapped within the ZIF-8 structure, whereas Au@ZIF-8 (HMIM:$Zn(NO_3)_2$ = 1) has clusters of AuNPs deposited on the surface of the ZIF-8 particles. A potential explanation of this phenomenon is that Au@ZIF-8 (HMIM:$Zn(NO_3)_2$ = 1) has a reduced nucleation rate and the AuNPs aggregate rapidly once $Zn(NO_3)_2$ is introduced. Therefore, AuNP aggregation occurs before ZIF-8 crystallization and the AuNP aggregates cannot effectively be incorporated into the ZIF-8 structure. This results in AuNP aggregates dispersed throughout the Au@ZIF-8 composite. Au@ZIF-8 is prepared with an HMIM:$Zn(NO_3)_2$ ratio of 4 throughout the rest of this work.

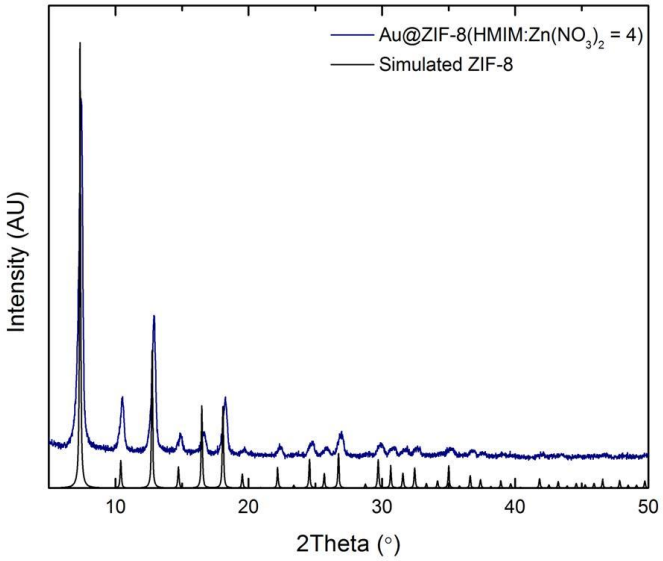

Figure B.5: PXRD patterns for Au@ZIF-8(HMIM:$Zn(NO_3)_2$ = 4)

Table B.3: AuNP diameter for Au@ZIF-8(HMIM:$Zn(NO_3)_2$)

Material	Yield (mg)	AuNP Diameter (nm)
Au@ZIF-8(HMIM:$Zn(NO_3)_2$ = 4)	42.5	2.0±0.7
Au@ZIF-8(HMIM:$Zn(NO_3)_2$ = 1)	3	2.2±0.7

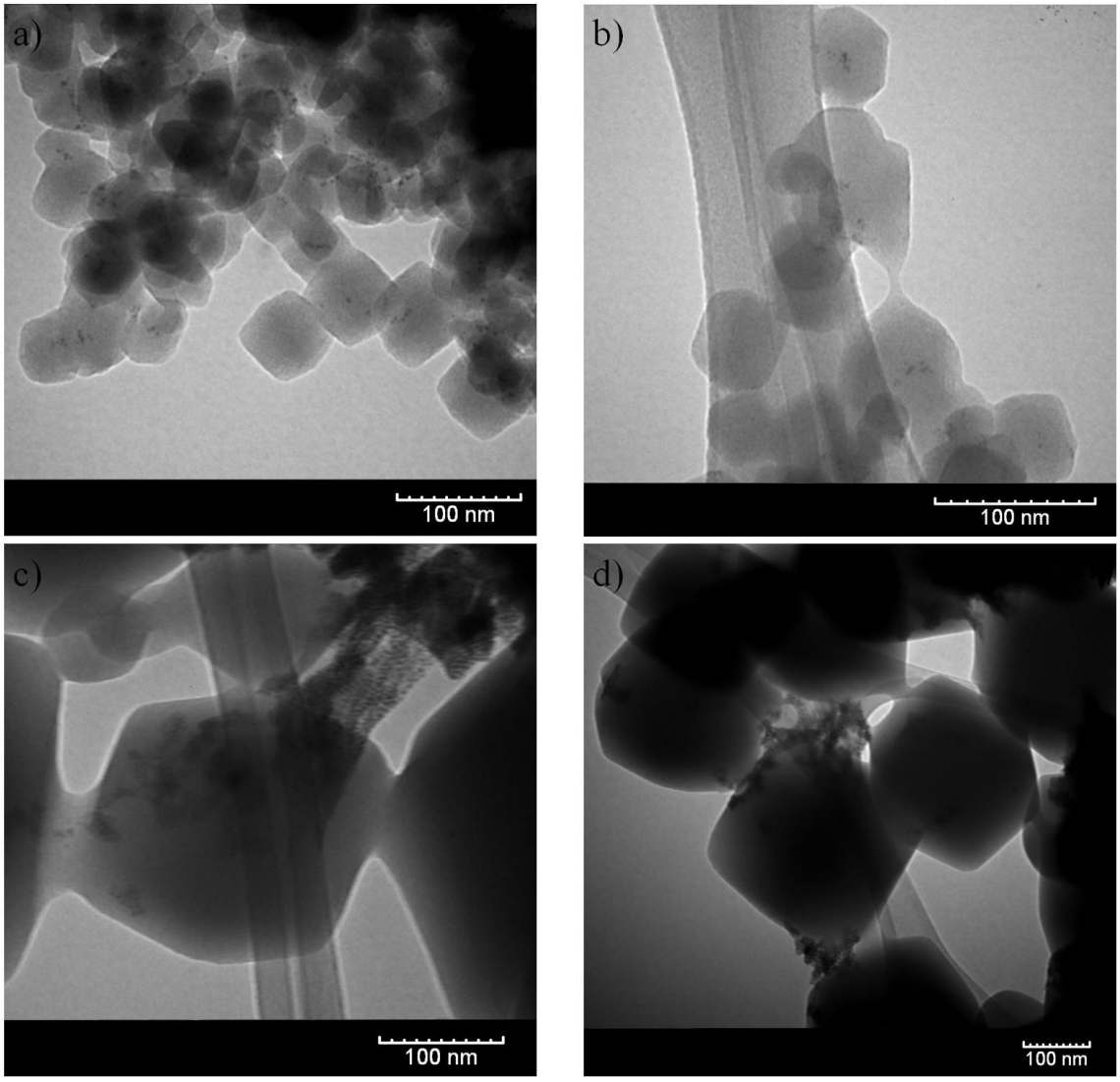

Figure B.6: TEM images for (a, b) Au@ZIF-8 (HMIM:$Zn(NO_3)_2$ = 4) and (c, d) Au@ZIF-8 (HMIM:$Zn(NO_3)_2$ = 1)

B.3.1.3 Au@ZIF-8: Precursor Addition Time

Au@ZIF-8 was prepared at room temperature with the AuNPs added to the reaction solution at three different reaction points. The AuNPs were added to the $Zn(NO_3)_2$ solution before it was combined with the HMIM; the HMIM solution before combining with the $Zn(NO_3)_2$ solution; and 3 min after the $Zn(NO_3)_2$ and HMIM solutions were combined, after the solution became turbid. These samples are denoted

Au@ZIF-8(Zn), Au@ZIF-8(HMIM), and Au@ZIF-8(3 min), respectively. When the AuNPs were added to the $Zn(NO_3)_2$ solution, a brown precipitate was formed which can be dissociated by adding acetic acid. This suggests that the –COOH groups on the AuNPs coordinated with the Zn^{2+} ions to create AuNP-COO-Zn aggregates. There is no brown precipitate observed when the AuNPs are premixed with HMIM. Figure B.7 shows that the ZIF-8 structure is formed for all three Au@ZIF-8 composites. Figure B.8 depicts TEM images for Au@ZIF-8(Zn), Au@ZIF-8(HMIM), and Au@ZIF-8(3 min) and Table B.4 reports that the AuNPs do not grow during the ZIF-8 crystallization. Figures B.8a and B.8b reveal that AuNP aggregates are dispersed throughout the Au@ZIF-8(Zn) material with many AuNPs on the surface of the ZIF-8 particles. This suggests that ZIF-8 does not preferentially grow from the AuNP-COO-Zn aggregates as seen for Au@HKUST-1.[13] In addition, Figures B.8c and B.8d show that AuNPs are randomly dispersed throughout Au@ZIF-8(HMIM). For Au@ZIF-8(HMIM), there are not any AuNPs that are obviously on the ZIF-8 surface; however, TEM is a two-dimensional technique so the exact location is not conclusive. Lastly, Figures B.8e and B.8f show that AuNP aggregates are scattered throughout the Au@ZIF-8(3 min) sample; some of the aggregates are merely on the ZIF-8 surface, whereas others are potentially confined in the ZIF-8 particles. However, the AuNPs in Au@ZIF-8(3 min) are not as well dispersed as the AuNPs in Au@ZIF-8(HMIM). Therefore, the AuNPs are added to the HMIM solution for the rest of this work.

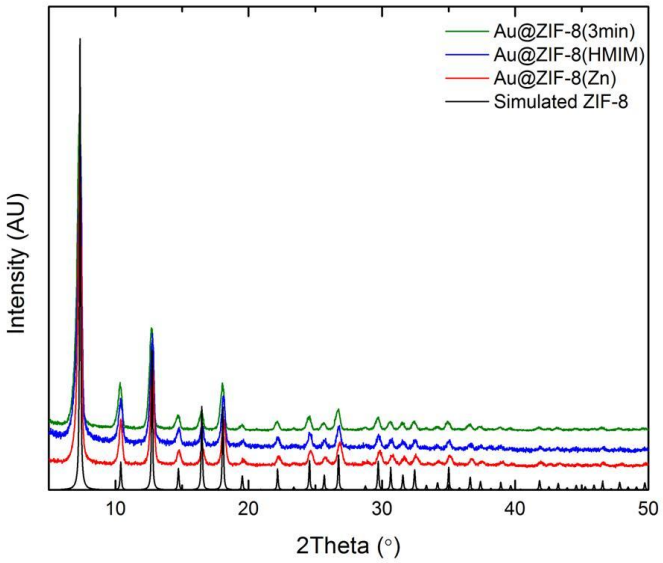

Figure B.7: PXRD patterns for Au@ZIF-8 with the AuNPs added to the mother solution at various times

Table B.4: AuNP diameter for Au@ZIF-8(AuNP Addition Time)

Material	Yield (mg)	AuNP Diameter (nm)
Au@ZIF-8(Zn)	48.2	2.1±0.9
Au@ZIF-8(HMIM)	47.9	2.0±0.7
Au@ZIF-8(3min)	36.8	2.1±0.6

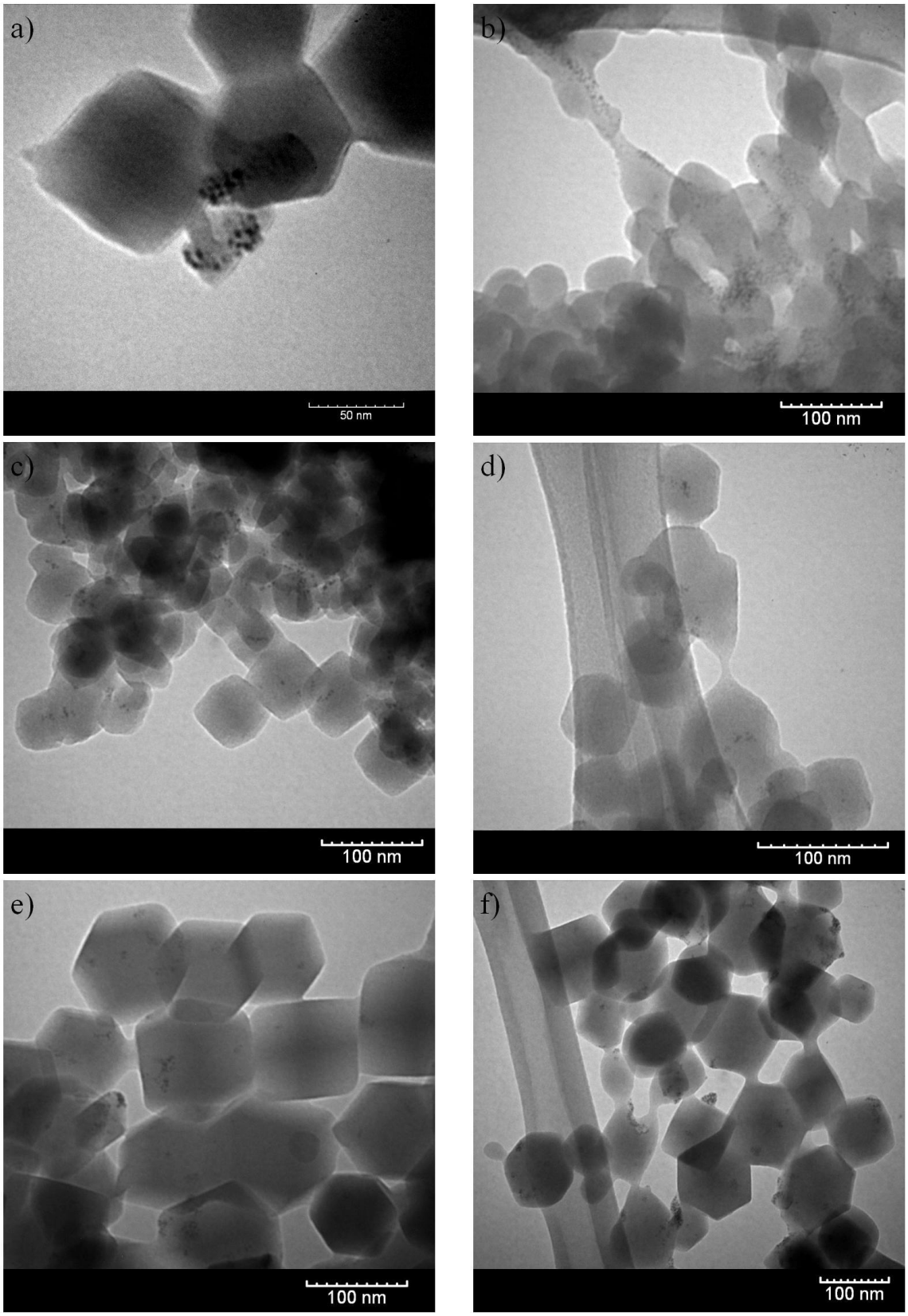

Figure B.8: TEM images for (a, b) Au@ZIF-8(Zn), (c, d) Au@ZIF-8(HMIM), and (e, f) Au@ZIF-8(3min)

B.3.1.4 Au@ZIF-8: Solvent Effect

Table B.2 details the synthesis conditions used to evaluate the solvent effect on the Au@ZIF-8 properties. Zamaro et al. have investigated the solvent effect on the ZIF-8 geometry discovering that varying the reaction medium results in particle size modulation, particle aggregation, and pill-shaped particles.[8] Herein, the effect on the Au@ZIF-8 properties is explored. PXRD patterns in Figure B.9 show that the ZIF-8 structure is obtained for ZIF-8 and Au@ZIF-8 materials prepared at room temperature in various solvent and solvent mixtures. Table B.5 shows that the solvent does not cause AuNP aggregation and growth, and Figures B.10-B.16 depict TEM images of Au@ZIF-8 prepared with the various solvents and solvent mixtures. Specifically, Figure B.10 shows that, for Au@ZIF-8(MeOH), there are AuNPs randomly dispersed among the ZIF-8 particles with none of the AuNPs obviously on the ZIF-8 surface. In addition, Figure B.11 reveals that Au@ZIF-8(EtOH) has many AuNPs deposited on the surface of the pill-shaped ZIF-8 particles. Also, Figure B.12 depicts TEM images of Au@ZIF-8(DMF); synthesizing with DMF produces ZIF-8 particles approximately 50 nm in diameter, however, no AuNPs are located. Figure B.13 reveals spherical aggregates of Au@ZIF-8(acetone) and AuNPs scattered randomly throughout ZIF-8 particles without any AuNPs distinctly located on the ZIF-8 surface. Lastly, TEM images, displayed in Figures B.14-B.16, show that solvent mixtures produce hexagonal ZIF-8 particles with AuNPs scattered throughout the material with several AuNPs definitively on the surface of the ZIF-8 particles.

In summary, the effects of the solvent on the ZIF-8 geometry as previously reported were observed.[8] In addition, AuNPs were dispersed randomly throughout the

Au@ZIF-8 materials, except when prepared with DMF, with definitively surface-based AuNPs detected with all solvents and mixtures except MeOH and acetone, which both generate ZIF-8 aggregates with AuNPs dispersed throughout.

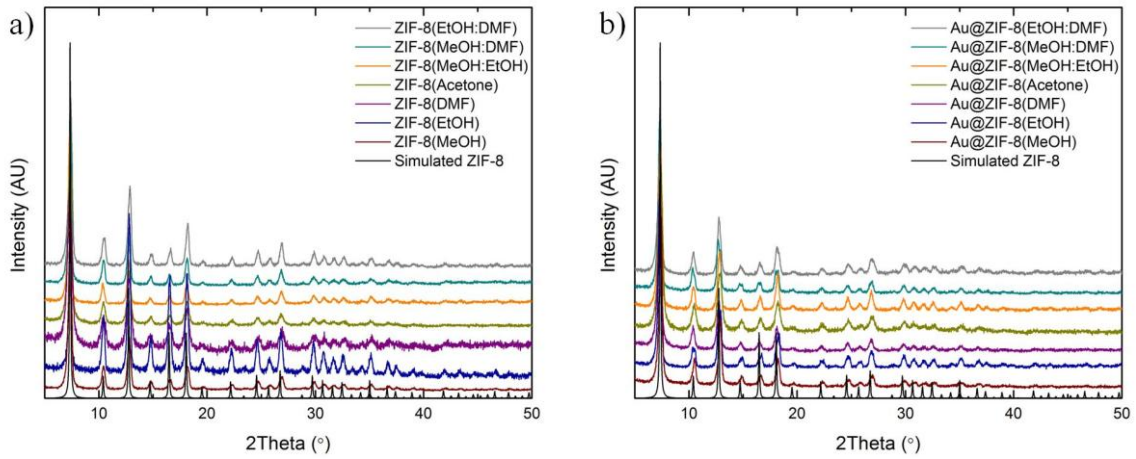

Figure B.9: PXRD patterns for (a) ZIF-8(solvent) and (b) Au@ZIF-8(solvent)

Table B.5: AuNP diameter for Au@ZIF-8(solvent)

Material	Yield (mg)	AuNP Diameter (nm)
Au@ZIF-8 (MeOH)	42.5	2.0±0.7
Au@ZIF-8 (EtOH)	38.3	2.8±1.6
Au@ZIF-8 (DMF)	10.2	-----
Au@ZIF-8 (Acetone)	65.0	1.5±0.4
Au@ZIF-8 (MeOH:EtOH)	45.6	2.0±0.6
Au@ZIF-8 (MeOH:DMF)	24.1	2.2±0.7
Au@ZIF-8 (EtOH:DMF)	43.7	2.1±0.7

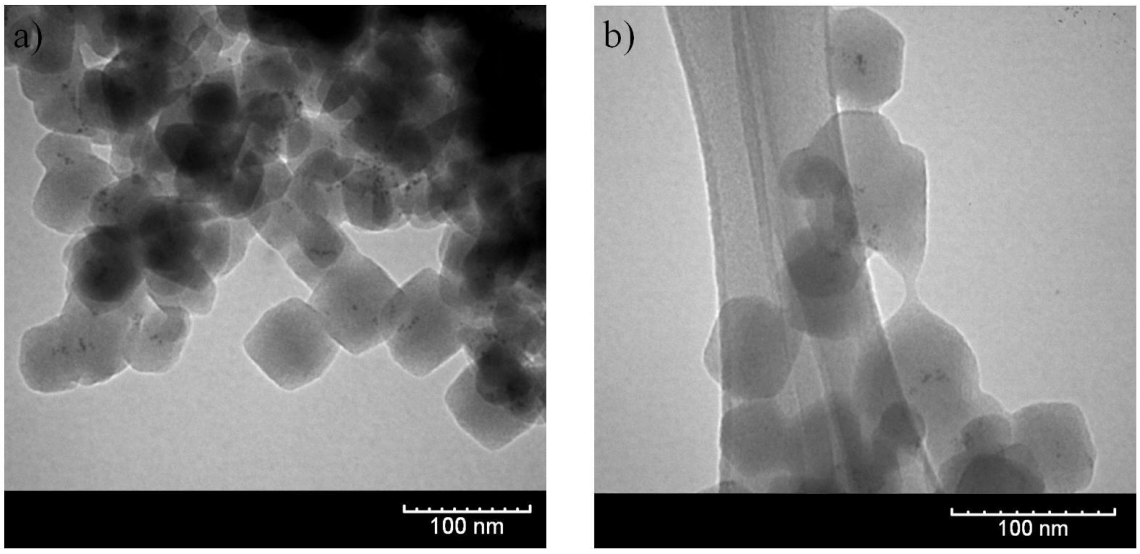

Figure B.10: TEM images for Au@ZIF-8(MeOH)

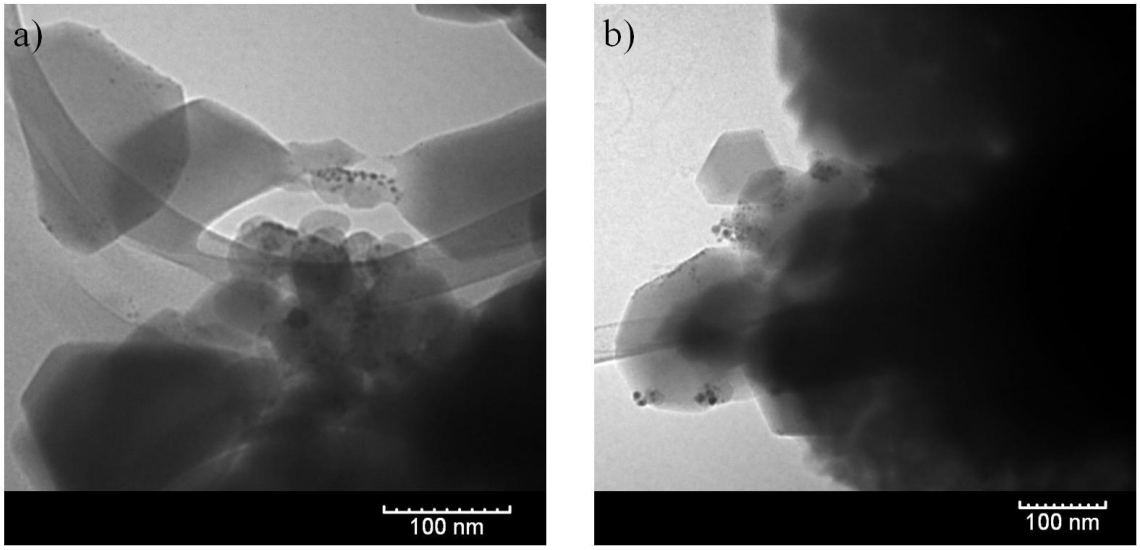

Figure B.11: TEM images for Au@ZIF-8(EtOH)

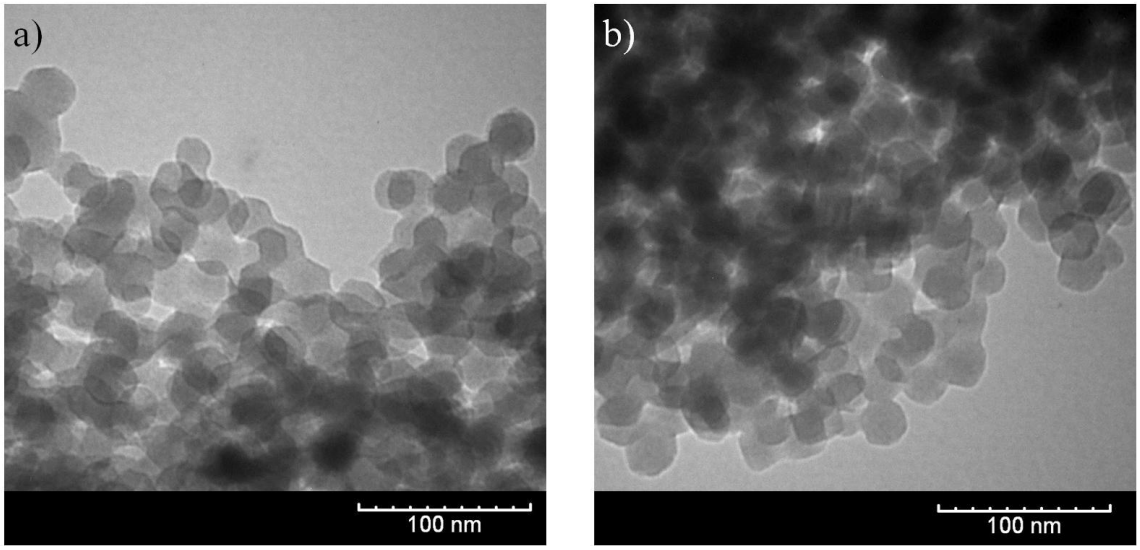

Figure B.12: TEM images for Au@ZIF-8(DMF)

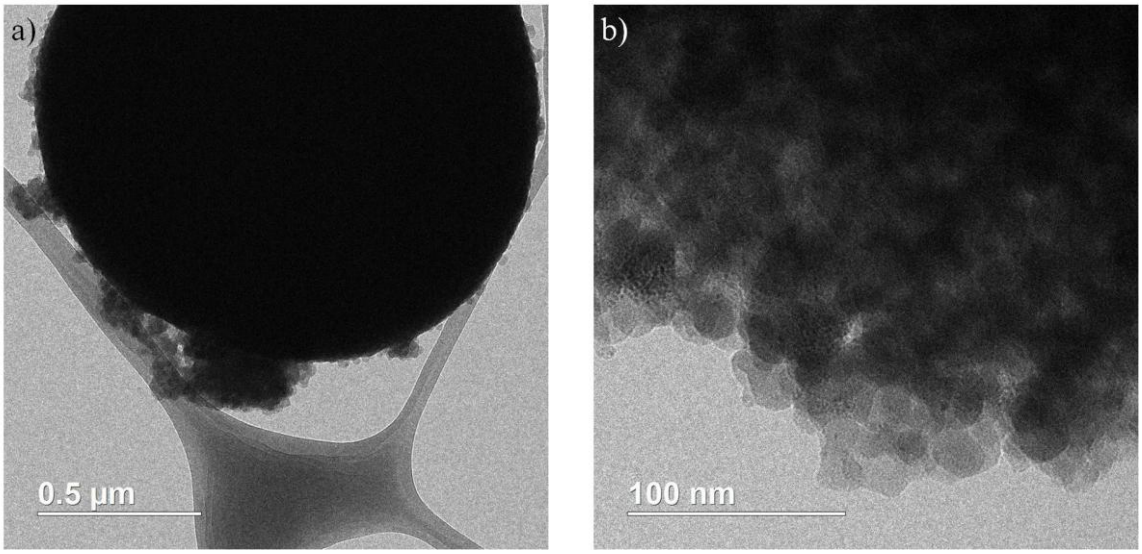

Figure B.13: TEM images for Au@ZIF-8(Acetone)

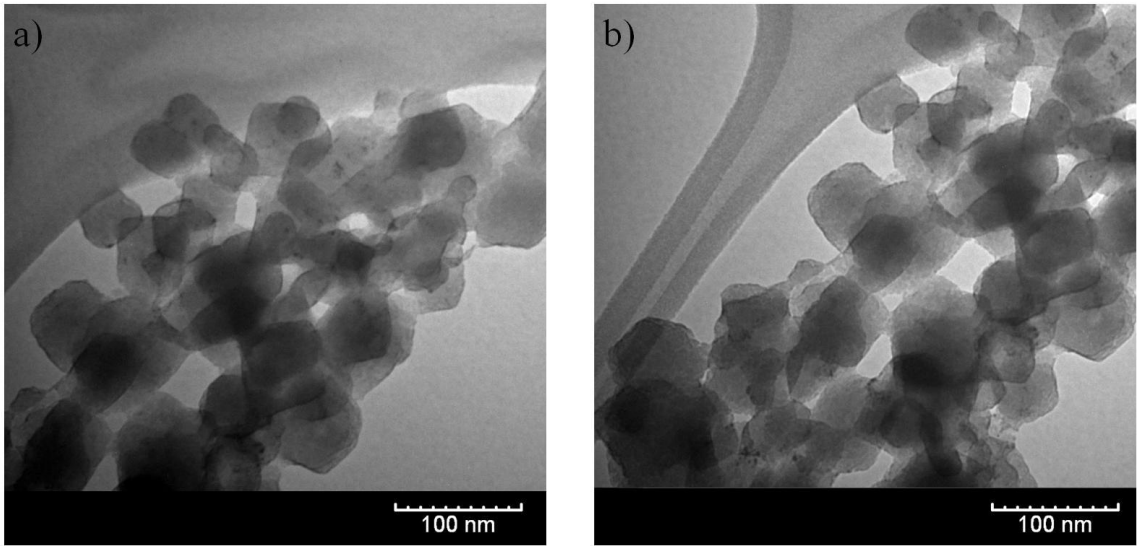

Figure B.14: TEM images for Au@ZIF-8(MeOH:EtOH)

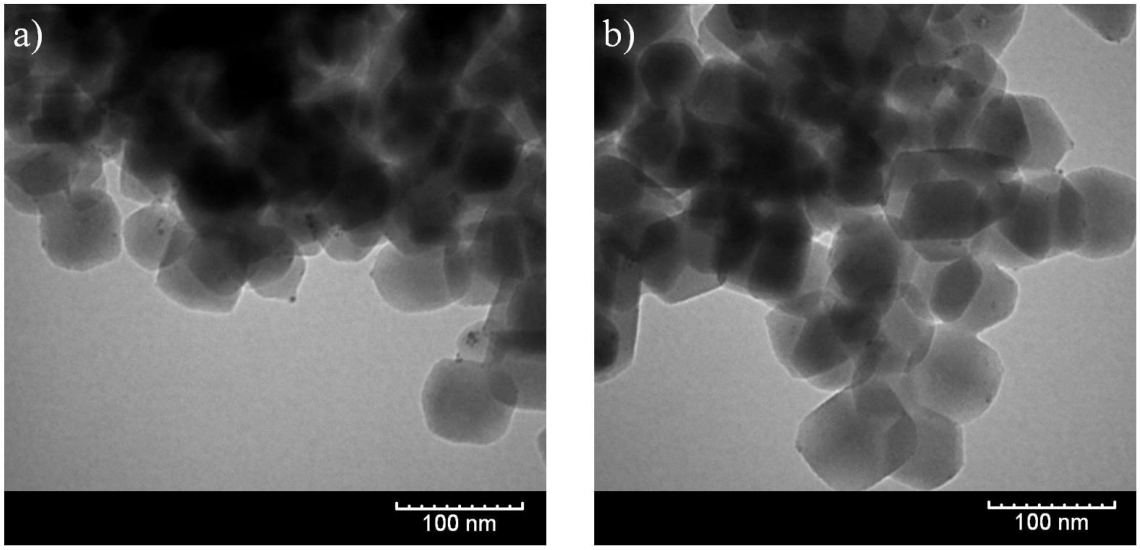

Figure B.15: TEM images for Au@ZIF-8(MeOH:DMF)

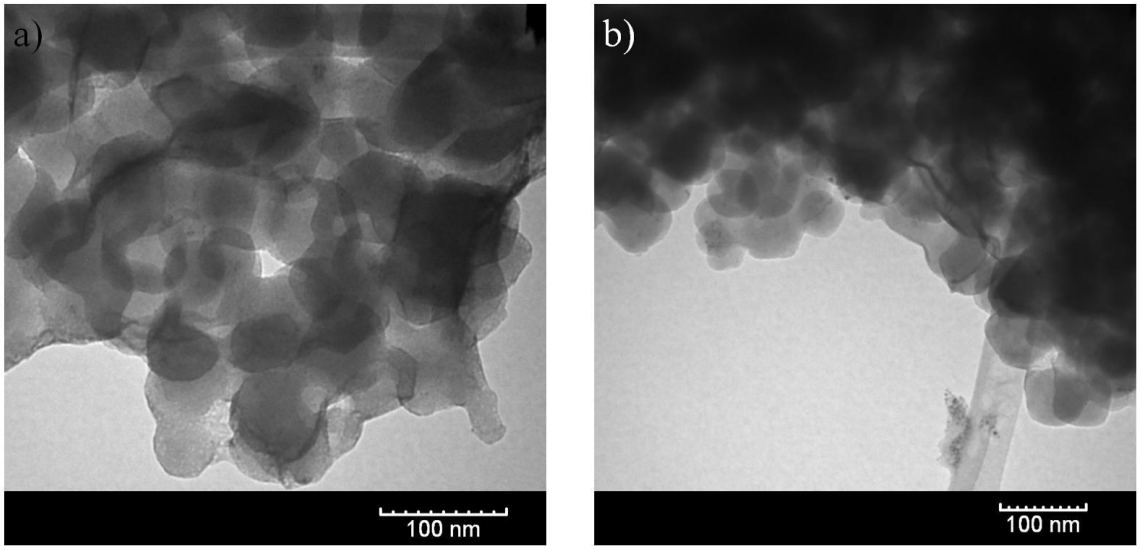

Figure B.16: TEM images for Au@ZIF-8(EtOH:DMF)

B.3.1.4 Au@ZIF-8: TEM Rotation

Based on the data obtained in the previous sections, Au@ZIF-8 was prepared in MeOH with an HMIM:$Zn(NO_3)_2$ ratio of 4 and the AuNPs were added to the HMIM solution. This sample was selected for further investigation into the AuNP location because TEM offered no definitive evidence that the AuNPs are located on the ZIF-8 particle surface. Specifically, the sample was rotated from -60-58° under the electron beam taking images in 2° increments, a technique known as TEM tomography. Figure B.17 presents the TEM images at 10° increments for Au@ZIF-8 rotated from -60-58°. The highlighted portion proves that there are AuNPs completely confined in the ZIF-8 particles; however, there are other AuNPs that are on the surface of the ZIF-8 particles.

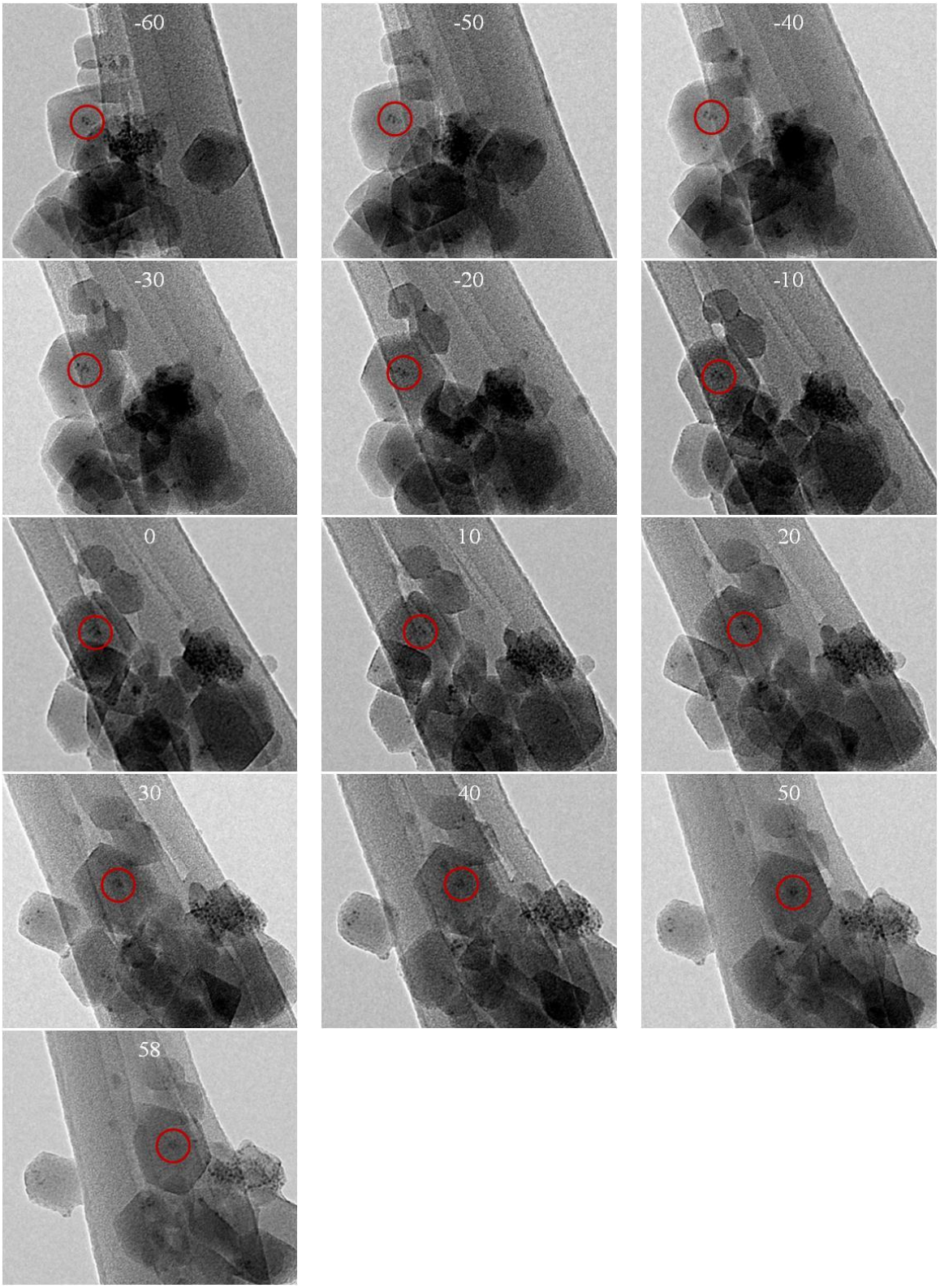

Figure B.17: TEM images of Au@ZIF-8 prepared in MeOH with HMIM:$Zn(NO_3)_2$ = 4 and the AuNPs added to the HMIM solution rotated from -60-58°

B.3.2 CO Oxidation

TEM tomography showed that Au@ZIF-8 prepared in MeOH with an HMIM:$Zn(NO_3)_2$ ratio of 4 successfully confines some of the AuNPs within the ZIF-8 particles. Therefore, this sample was used to test the catalytic capabilities of Au@ZIF-8 using CO oxidation as a probe reaction. In addition, a physical mixture, denoted Au on ZIF-8, was prepared via colloidal deposition. Prior to the CO oxidation study; the sample was activated in-situ via two procedures: (1) heating under helium flow at 523 K and (2) calcination in air at 523 K for 16-18 h. ZIF-8, Au on ZIF-8, and Au@ZIF-8 were inactive for CO oxidation at 523K. There are two theories. First, DDT and MUA cannot be adequately removed from the ZIF-8 pores via either activation. However, if that were the main limitation, then Au on ZIF-8 would have been active because DDT and MUA can be removed from the AuNP surface using either activation procedure. The second theory is that ZIF-8 cannot generate oxygen vacancy sites necessary to activate oxygen for CO oxidation.[14, 15]

B.4 Conclusions

Diverse variations of Au@ZIF-8 synthesis procedures were explored, specifically, the HMIM:$Zn(NO_3)_2$ ratio, the AuNP addition time, and the reaction solvent. Unfortunately, broader conclusions about the controlling factors of the synthesis conditions were not forthcoming. However, from these studies, the most effective combination was HMIM:$Zn(NO_3)_2$ = 4, AuNPs added to the HMIM solution, and MeOH as the solvent. Further analysis proved that there is partial confinement of the AuNPs in the ZIF-8 particles; however, there are many AuNPs also deposited on the ZIF-8 particle

surface. In addition, Au@ZIF-8 prepared via encapsulation under these conditions were inactive towards CO oxidation at temperatures as high as 523 K. Although this material is not effective for CO oxidation other catalytic reactions such as the reduction of nitroarenes[16] or hydrogenation reactions[17] could be explored.

B.5 References

1. Park, K. S.; Ni, Z.; Cote, A. P.; Choi, J. Y.; Huang, R.; Uribe-Romo, F. J.; Chae, H. K.; O'Keeffe, M.; Yaghi, O. M., Exceptional chemical and thermal stability of zeolitic imidazolate frameworks. *Proceedings of the National Academy of Sciences of the United States of America* **2006,** *103* (27), 10186-10191.

2. Kuesgens, P.; Rose, M.; Senkovska, I.; Froede, H.; Henschel, A.; Siegle, S.; Kaskel, S., Characterization of metal-organic frameworks by water adsorption. *Microporous and Mesoporous Materials* **2009,** *120* (3), 325-330.

3. Cravillon, J.; Nayuk, R.; Springer, S.; Feldhoff, A.; Huber, K.; Wiebcke, M., Controlling Zeolitic Imidazolate Framework Nano- and Microcrystal Formation: Insight into Crystal Growth by Time-Resolved In Situ Static Light Scattering. *Chemistry of Materials* **2011,** *23* (8), 2130-2141.

4. Joaristi, A. M.; Juan-Alcaniz, J.; Serra-Crespo, P.; Kapteijn, F.; Gascon, J., Electrochemical Synthesis of Some Archetypical Zn^{2+}, Cu^{2+}, and Al^{3+} Metal Organic Frameworks. *Crystal Growth & Design* **2012,** *12* (7), 3489-3498.

5. Seoane, B.; Zamaro, J. M.; Tellez, C.; Coronas, J., Sonocrystallization of zeolitic imidazolate frameworks (ZIF-7, ZIF-8, ZIF-11 and ZIF-20). *Crystengcomm* **2012,** *14* (9), 3103-3107.

6. Bao, Q. L.; Lou, Y. B.; Xing, T. T.; Chen, J. X., Rapid synthesis of zeolitic imidazolate framework-8 (ZIF-8) in aqueous solution via microwave irradiation. *Inorganic Chemistry Communications* **2013,** *37*, 170-173.

7. Beldon, P. J.; Fabian, L.; Stein, R. S.; Thirumurugan, A.; Cheetham, A. K.; Friscic, T., Rapid Room-Temperature Synthesis of Zeolitic Imidazolate Frameworks by Using Mechanochemistry. *Angewandte Chemie-International Edition* **2010,** *49* (50), 9640-9643.

8. Bustamante, E. L.; Fernandez, J. L.; Zamaro, J. M., Influence of the solvent in the synthesis of zeolitic imidazolate framework-8 (ZIF-8) nanocrystals at room temperature. *Journal of Colloid and Interface Science* **2014,** *424*, 37-43.

9. Cravillon, J.; Muenzer, S.; Lohmeier, S.-J.; Feldhoff, A.; Huber, K.; Wiebcke, M., Rapid Room-Temperature Synthesis and Characterization of Nanocrystals of a Prototypical Zeolitic Imidazolate Framework. *Chemistry of Materials* **2009,** *21* (8), 1410-1412.

10. Brust, M.; Walker, M.; Bethell, D.; Schiffrin, D. J.; Whyman, R., Synthesis of thiol-derivatised gold nanoparticles in a two-phase Liquid-Liquid system. *Journal of the Chemical Society-Chemical Communications* **1994,** (7), 801-802.

11. Hostetler, M. J.; Templeton, A. C.; Murray, R. W., Dynamics of place-exchange reactions on monolayer-protected gold cluster molecules. *Langmuir* **1999,** *15* (11), 3782-3789.

12. Hostetler, M. J.; Wingate, J. E.; Zhong, C. J.; Harris, J. E.; Vachet, R. W.; Clark, M. R.; Londono, J. D.; Green, S. J.; Stokes, J. J.; Wignall, G. D.; Glish, G. L.; Porter, M. D.; Evans, N. D.; Murray, R. W., Alkanethiolate gold cluster molecules with core diameters from 1.5 to 5.2 nm: Core and monolayer properties as a function of core size. *Langmuir* **1998,** *14* (1), 17-30.

13. Tsuruoka, T.; Kawasaki, H.; Nawafune, H.; Akamatsu, K., Controlled Self-Assembly of Metal-Organic Frameworks on Metal Nanoparticles for Efficient Synthesis of Hybrid Nanostructures. *Acs Applied Materials & Interfaces* **2011,** *3* (10), 3788-3791.

14. Haruta, M., When Gold Is Not Noble: Catalysis by Nanoparticles. *The Chemical Record* **2003,** *3* (2), 75-87.

15. Ishida, T.; Nagaoka, M.; Akita, T.; Haruta, M., Deposition of Gold Clusters on Porous Coordination Polymers by Solid Grinding and Their Catalytic Activity in Aerobic Oxidation of Alcohols. *Chemistry-a European Journal* **2008,** *14* (28), 8456-8460.

16. Li, S.; Zhang, W.; Huo, F., The structural and catalytic properties of nanoparticles@MOF composites: A case study of Au@ZIF-8 hybrid crystals. *Physica E-Low-Dimensional Systems & Nanostructures* **2015,** *69*, 56-60.

17. Goel, S.; Wu, Z.; Zones, S. I.; Iglesia, E., Synthesis and Catalytic Properties of Metal Clusters Encapsulated within Small-Pore (SOD, GIS, ANA) Zeolites. *Journal of the American Chemical Society* **2012,** *134* (42), 17688-17695.

APPENDIX C

SUPPLEMENTAL INFORMATION

C.1 Chapter 3: An Alternative UiO-66 Synthesis for HCl-Sensitive Nanoparticle Encapsulation

Reproduced (adapted) from Tulig, K.; Walton, K. S., An alternative UiO-66 synthesis for HCl-sensitive nanoparticle encapsulation. *RSC Advances* **2014,** *4* (93), 51080-51083.

C.1.1 Acetic Acid Effect on BET Surface Area

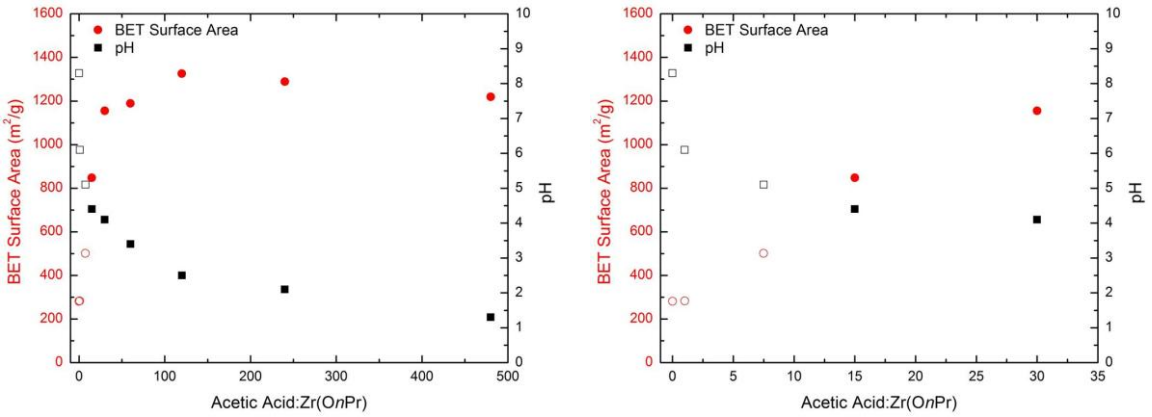

Figure C.1: Relationship between acetic acid:Zr(O*n*Pr) ratio, pH, and BET surface area. The close and open points represent crystalline and non-crystalline materials, respectively

Table C.1: Porosity of UiO-66(Zr(OnPr)) prepared with varied acetic acid:Zr(O*n*Pr)

Acetic Acid:Zr(O*n*Pr)	pH	BET Surface Area (m^2/g)	Total Pore Volume[a] (cm^3/g)
0	8.3	281	0.19
1	6.1	282	0.19
7.5	5.1	501	0.31
15	4.4	848	0.42
30	4.1	1155	0.51
60	3.4	1189	0.52
120	2.5	1326	0.55
240	2.1	1289	0.52
480	1.3	1220	0.52

[a]Measured at $P/P_0 = 0.6$

C.1.2 ^{1}H NMR

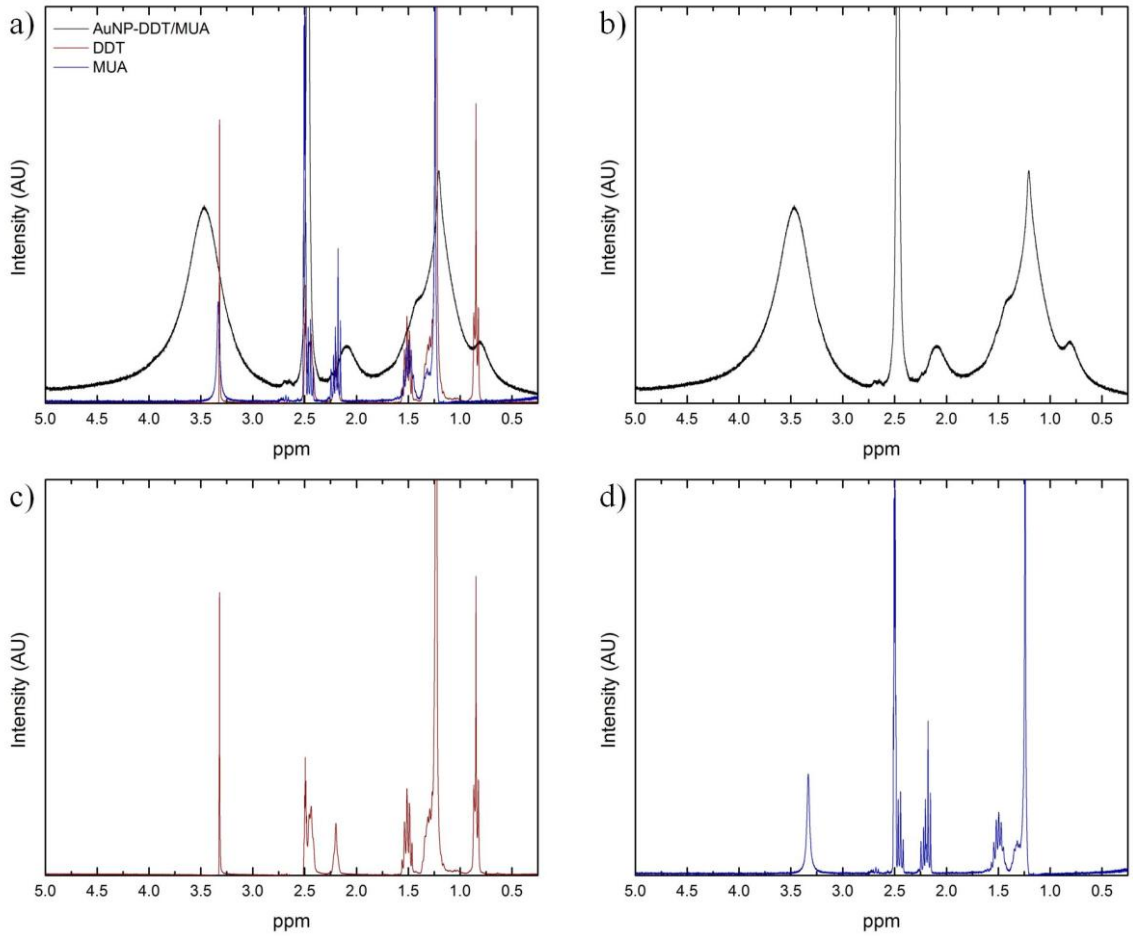

Figure C.2: ^{1}H NMR spectra for (a) AuNP-DDT/MUA, DDT, and MUA; (b) AuNP-DDT/MUA; (c) DDT; and (d) MUA

C.1.3 Nitrogen Sorption at 77K

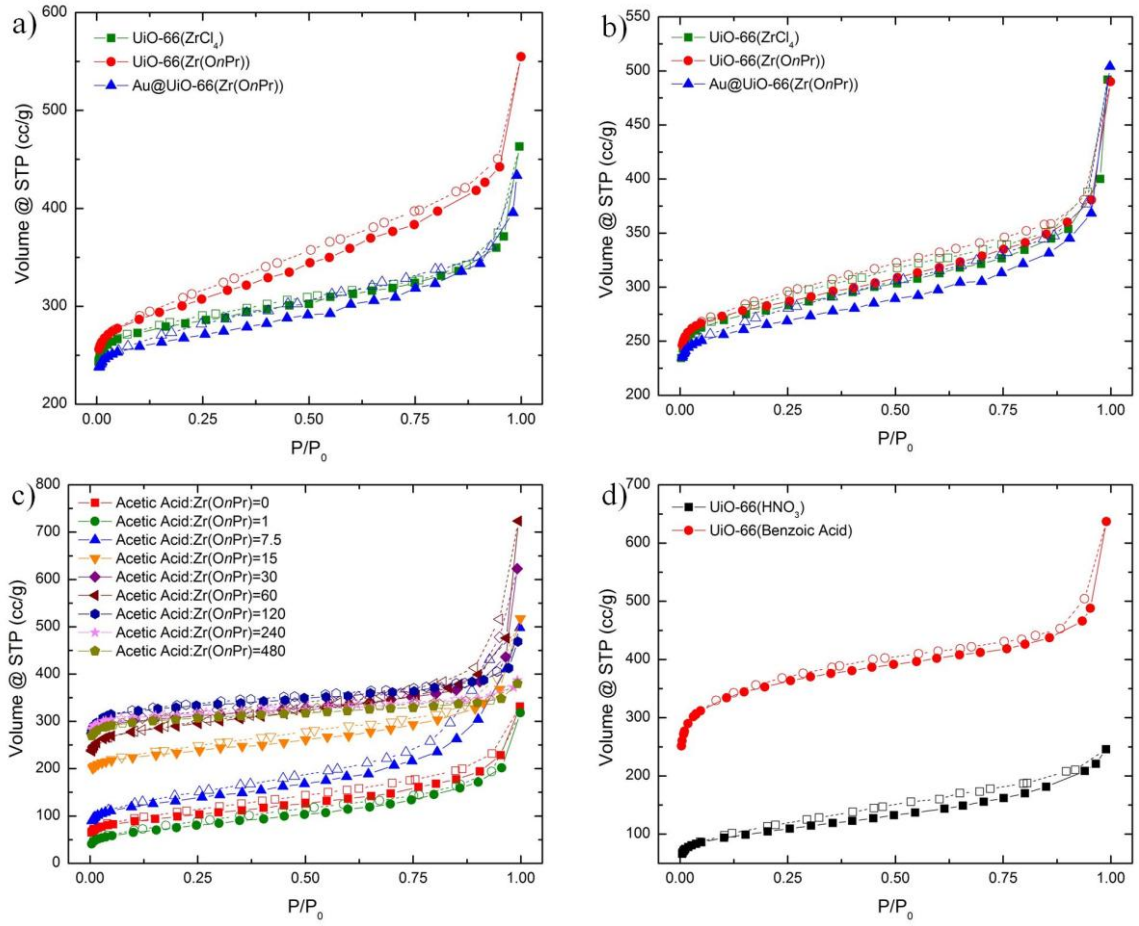

Figure C.3: Nitrogen sorption isotherms at 77 K for UiO-66($ZrCl_4$), UiO-66(Zr(O*n*Pr)), and Au@UiO-66(Zr(O*n*Pr)) (a) as-synthesized and (b) after soaking in water for 24 h; (c) UiO-66(Zr(O*n*Pr) prepared by varying the acetic acid:Zr(O*n*Pr) ratio; and (d) UiO-66(Zr(O*n*Pr) prepared using HNO_3 (black squares) and benzoic acid (red circles) as the modulator. Closed and open symbols represent adsorption and desorption curves, respectively

C.2 Chapter 4: Static Oxygen Storage Capacity and Catalytic Activity of Metal-Organic Framework Supported Gold Nanoparticles

C.2.1 Nitrogen Sorption at 77 K

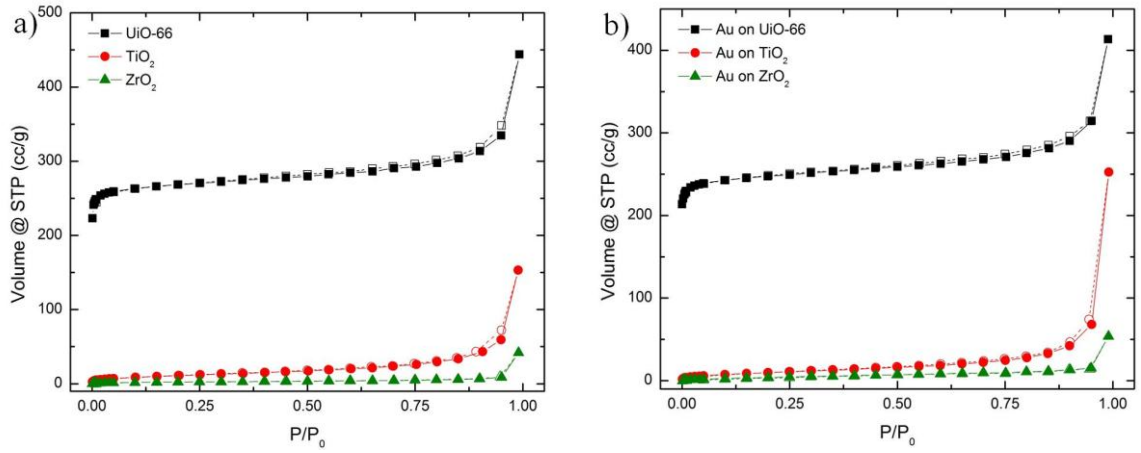

Figure C.4: Nitrogen sorption isotherms at 77 K for (a) parent supports and (b) supported AuNPs. Closed and open symbols represent adsorption and desorption curves, respectively

C.2.2 CO Oxidation

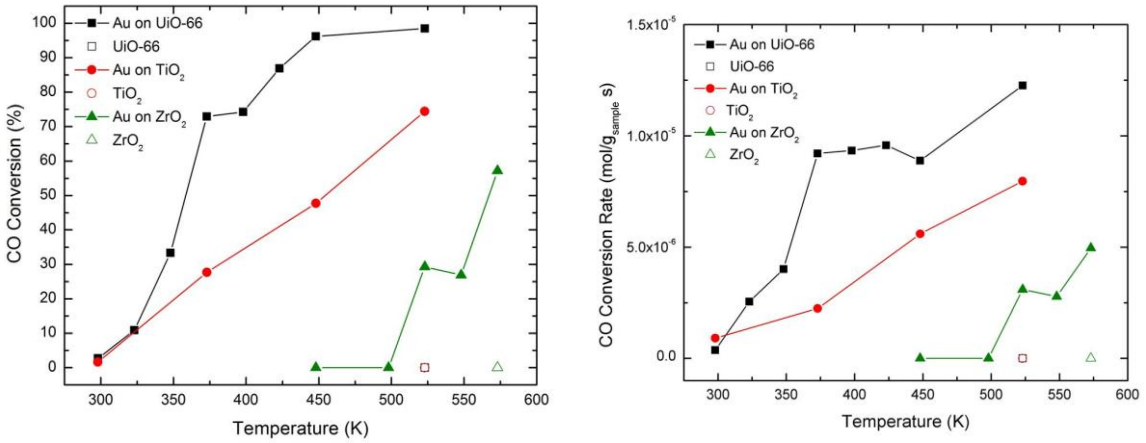

Figure C.5: (a) CO conversion and (b) reaction rate vs. temperature for Au on UiO-66 (black squares), Au on TiO_2 (red circles), and Au on ZrO_2 (green triangles). The lines are to guide the eye only

Table C.2: CO conversion versus temperature for Au on UiO-66, Au on TiO_2, and Au on ZrO_2

	CO Conversion (%)		
Temperature (K)	Au on UiO-66	Au on TiO_2	Au on ZrO_2
298	3	2	------
323	11	------	------
348	33	------	------
373	73	28	------
398	74	------	------
423	87	------	------
448	96	48	0
498	------	------	0
523	99	74	29
548	------	------	27
573	------	------	57

Table C.3: Conversion rate versus temperature for Au on UiO-66, Au on TiO_2, and Au on ZrO_2

	CO Conversion Rate ($mol/g_{sample}\ s$)		
Temperature (K)	Au on UiO-66	Au on TiO_2	Au on ZrO_2
298	$3.7x10^{-7}$	$9.1x10^{-7}$	-----
323	$2.5x10^{-6}$	-----	-----
348	$4.0x10^{-6}$	-----	-----
373	$9.2x10^{-6}$	$2.2x10^{-6}$	-----
398	$9.3x10^{-6}$	-----	-----
423	$9.6x10^{-6}$	-----	-----
448	$8.9x10^{-6}$	$5.6x10^{-6}$	0
498	-----	-----	0
523	$1.2x10^{-5}$	$8.0x10^{-6}$	$3.1x10^{-6}$
548	-----	-----	$2.8x10^{-6}$
573	-----	-----	$5.0x10^{-6}$

Table C.4: TOF versus temperature for Au on UiO-66, Au on TiO_2, and Au on ZrO_2

	TOF (s^{-1})		
Temperature (K)	Au on UiO-66	Au on TiO_2	Au on ZrO_2
298	0.7	0.2	-----
323	7.8	-----	-----
348	6.3	-----	-----
373	15.2	2.4	-----
398	15.8	-----	-----
423	13.7	-----	-----
448	10.9	8.5	0
498	-----	-----	0
523	19.9	11.1	4.0
548	-----	-----	3.4
573	-----	-----	5.5

C.2.3 Adsorption Equilibrium Isotherms

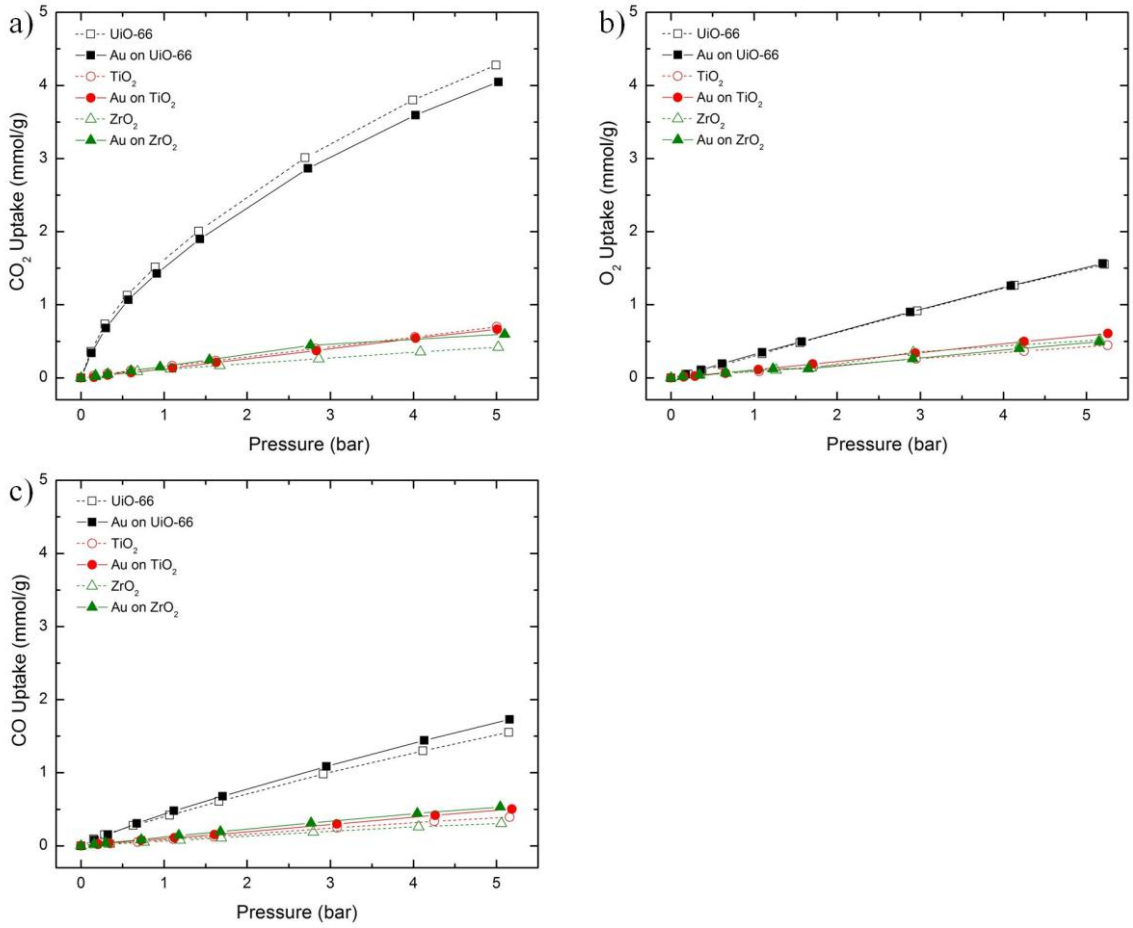

Figure C.6: (a) CO_2, (b) O_2, and (c) CO isotherms at 298K

Table C.5: CO_2 adsorption at 298 K for UiO-66 and Au on UiO-66

UiO-66		Au on UiO-66	
Pressure (bar)	CO_2 Uptake (mmol/g)	Pressure (bar)	CO_2 Uptake (mmol/g)
0.00	0.00	0.00	0.00
0.12	0.36	0.13	0.34
0.29	0.74	0.30	0.68
0.56	1.13	0.57	1.07
0.89	1.52	0.91	1.43
1.41	2.01	1.43	1.90
2.69	3.01	2.73	2.87
3.99	3.80	4.02	3.59
4.99	4.28	5.02	4.05

Table C.6: CO_2 adsorption at 298 K for TiO_2 and Au on TiO_2

TiO_2		Au on TiO_2	
Pressure (bar)	CO_2 Uptake (mmol/g)	Pressure (bar)	CO_2 Uptake (mmol/g)
0.00	0.00	0.00	0.00
0.16	0.03	0.16	0.01
0.32	0.06	0.32	0.04
0.60	0.10	0.60	0.07
1.10	0.17	1.10	0.14
1.62	0.23	1.63	0.21
2.83	0.40	2.83	0.37
4.02	0.56	4.03	0.54
5.00	0.70	5.01	0.67

Table C.7: CO_2 adsorption at 298 K for ZrO_2 and Au on ZrO_2

ZrO_2		Au on ZrO_2	
Pressure (bar)	CO_2 Uptake (mmol/g)	Pressure (bar)	CO_2 Uptake (mmol/g)
0.00	0.00	0.00	0.00
0.18	0.04	0.18	0.02
0.32	0.05	0.32	0.05
0.68	0.09	0.60	0.10
1.08	0.12	0.95	0.15
1.67	0.17	1.55	0.25
2.86	0.26	2.76	0.45
4.09	0.36	5.10	0.60
5.02	0.42		

Table C.8: O_2 adsorption at 298 K for UiO-66 and Au on UiO-66

UiO-66		Au on UiO-66	
Pressure (bar)	O_2 Uptake (mmol/g)	Pressure (bar)	O_2 Uptake (mmol/g)
0.00	0.00	0.00	0.00
0.21	0.05	0.18	0.05
0.38	0.10	0.36	0.11
0.62	0.18	0.62	0.20
1.10	0.33	1.10	0.35
1.55	0.48	1.57	0.50
2.96	0.92	2.88	0.90
4.13	1.27	4.09	1.26
5.21	1.55	5.19	1.57

Table C.9: O_2 adsorption at 298 K for TiO_2 and Au on TiO_2

TiO_2		Au on TiO_2	
Pressure (bar)	O_2 Uptake (mmol/g)	Pressure (bar)	O_2 Uptake (mmol/g)
0.00	0.00	0.00	0.00
0.15	0.01	0.16	0.02
0.29	0.03	0.29	0.02
0.66	0.06	0.65	0.07
1.06	0.09	1.05	0.11
1.71	0.15	1.71	0.19
2.95	0.26	2.94	0.34
4.25	0.37	4.25	0.50
5.26	0.44	5.26	0.61

Table C.10: O_2 adsorption at 298 K for ZrO_2 and Au on ZrO_2

ZrO_2		Au on ZrO_2	
Pressure (bar)	O_2 Uptake (mmol/g)	Pressure (bar)	O_2 Uptake (mmol/g)
0.00	0.00	0.00	0.00
0.14	0.02	0.14	0.02
0.35	0.04	0.34	0.04
0.66	0.06	0.66	0.07
1.26	0.11	1.23	0.12
1.69	0.14	1.65	0.12
2.92	0.35	2.91	0.26
4.20	0.45	4.19	0.40
5.16	0.52	5.15	0.49

Table C.11: CO adsorption at 298 K for UiO-66 and Au on UiO-66

UiO-66		Au on UiO-66	
Pressure (bar)	CO Uptake (mmol/g)	Pressure (bar)	CO Uptake (mmol/g)
0.00	0.00	0.00	0.00
0.15	0.09	0.16	0.08
0.28	0.15	0.32	0.16
0.63	0.28	0.67	0.31
1.07	0.42	1.12	0.48
1.66	0.61	1.71	0.68
2.91	0.98	2.95	1.09
4.11	1.30	4.13	1.44
5.14	1.55	5.16	1.73

Table C.12: CO adsorption at 298 K for TiO_2 and Au on TiO_2

TiO_2		Au on TiO_2	
Pressure (bar)	CO Uptake (mmol/g)	Pressure (bar)	CO Uptake (mmol/g)
0.00	0.00	0.00	0.00
0.21	0.02	0.21	0.03
0.36	0.03	0.34	0.04
0.68	0.05	0.72	0.08
1.11	0.09	1.12	0.11
1.60	0.13	1.61	0.15
3.08	0.25	3.08	0.30
4.25	0.33	4.26	0.42
5.16	0.39	5.18	0.50

Table C.13: CO adsorption at 298 K for ZrO_2 and Au on ZrO_2

ZrO_2		Au on ZrO_2	
Pressure (bar)	CO Uptake (mmol/g)	Pressure (bar)	CO Uptake (mmol/g)
0.00	0.00	0.00	0.00
0.16	0.01	0.16	0.03
0.34	0.02	0.30	0.04
0.76	0.05	0.72	0.09
1.19	0.08	1.18	0.14
1.69	0.11	1.68	0.19
2.80	0.19	2.77	0.31
4.06	0.26	4.05	0.44
5.06	0.31	5.05	0.53

C.3 Chapter 5: Evaluating the Effect of Preparation Method on Au@UiO-66 Properties

C.3.1 Nitrogen Sorption at 77K

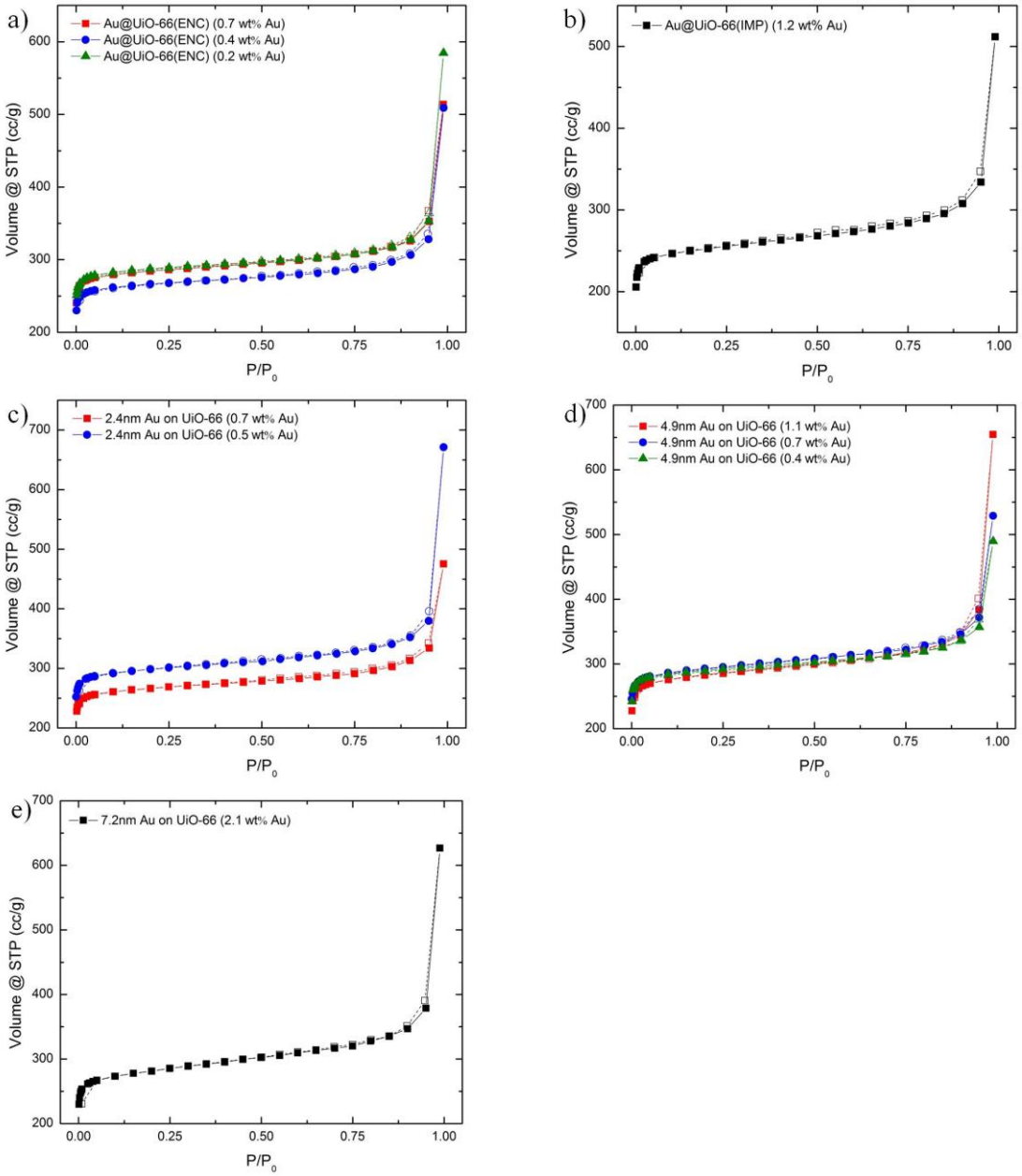

Figure C.7: Nitrogen sorption isotherms at 77 K for (a) Au@UiO-66(ENC); (b) Au@UiO-66(IMP); (c) 2.4 nm Au on UiO-66; (d) 4.9 nm Au on UiO-66; and (e) 7.2 nm Au on UiO-66 with various Au concentrations. Closed and open symbols represent adsorption and desorption curves, respectively

C.3.2 CO Oxidation

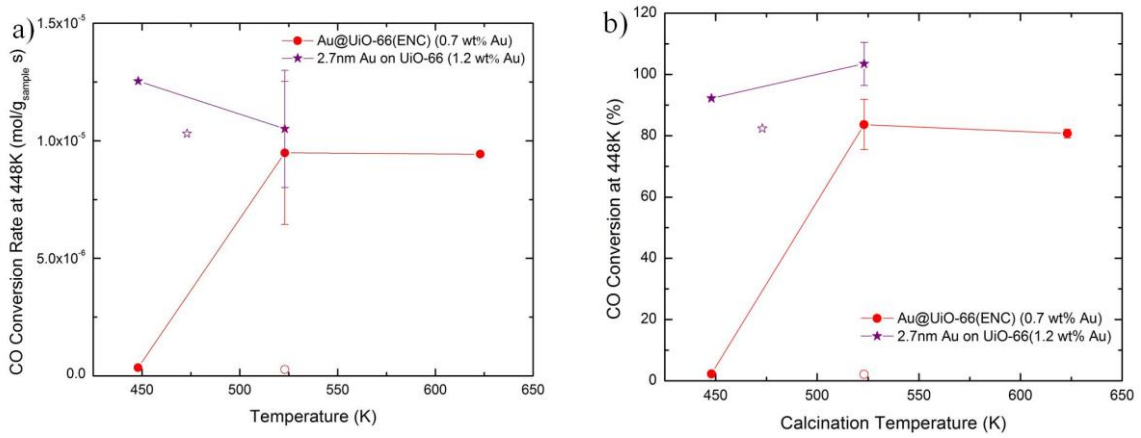

Figure C.8: Dependence of (a) CO conversion rate and (b) CO conversion at 448 K on calcination temperature. Closed and open symbols represent calcination in air and helium, respectively

Table C.14: Dependence of CO conversion rate and CO conversion at 448 K on calcination temperature

Material	CO Conversion Rate at 448 K (mol/g_{sample} s)	CO Conversion at 448 K (%)
Au@UiO-66(ENC)-He(523K)	$2.8x10^{-7}$	2.2
Au@UiO-66(ENC)-Air(448K)	$3.5x10^{-7}\pm0.3x10^{-7}$	2.3±0.5
Au@UiO-66(ENC)-Air(523K)	$9.5x10^{-6}\pm3.0x10^{-6}$	83.7±8.2
Au@UiO-66(ENC)-Air(623K)	$9.4x10^{-6}\pm0.1x10^{-6}$	80.8±1.4
2.7nm Au on UiO-66-He(473K)	$1.0x10^{-5}$	82.4
2.7nm Au on UiO-66-Air(448K)	$1.3x10^{-5}$	92.3
2.7nm Au on UiO-66-Air(523K)	$1.1x10^{-5}\pm0.3x10^{-5}$	103.5±7.0

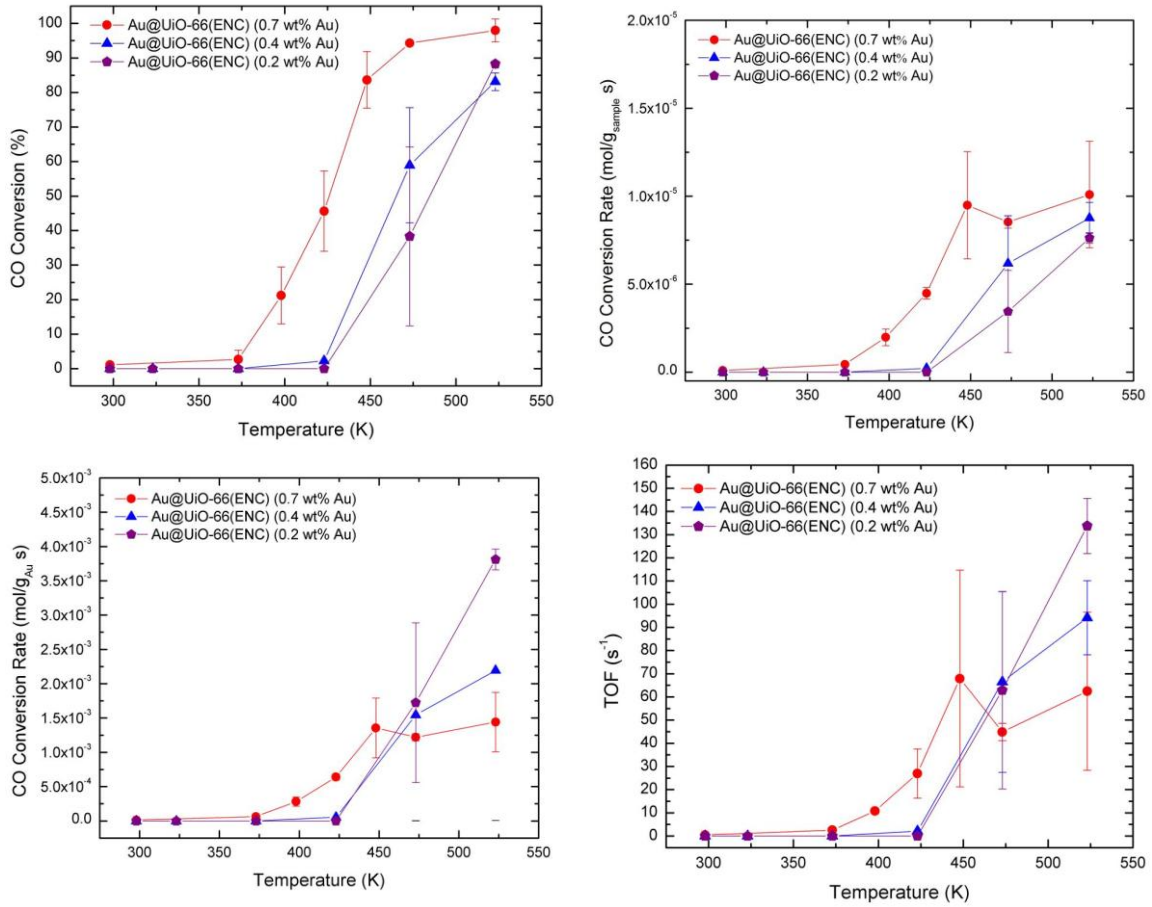

Figure C.9: Temperature dependence of CO conversion, CO conversion rate, and TOF over Au@UiO-66(ENC)

Table C.15: Temperature dependence of CO conversion over Au@UiO-66(ENC)

Temperature (K)	CO Conversion (%)		
	Au@UiO-66(ENC) (0.7 wt% Au)	Au@UiO-66(ENC) (0.4 wt% Au)	Au@UiO-66(ENC) (0.2 wt% Au)
298	1.1	0	0
323	-----	0	0
373	2.7±2.7	0	0
398	21.2±8.2	-----	-----
423	45.6±11.6	2.3	0
448	83.7±8.2	-----	-----
473	94.3±0.2	58.9±16.7	38.3±25.9
523	98.0±3.3	83.1±2.5	88.3±0.8

Table C.16: Temperature dependence of CO conversion rate over Au@UiO-66(ENC)

Temperature (K)	CO Conversion Rate (mol/g_{sample} s) Au@UiO-66(ENC) (0.7 wt% Au)	Au@UiO-66(ENC) (0.4 wt% Au)	Au@UiO-66(ENC) (0.2 wt% Au)
298	$9.6x10^{-8}$	0	0
323	-----	0	0
373	$4.4x10^{-7}$	0	0
398	$2.0x10^{-6}\pm0.5x10^{-6}$	-----	-----
423	$4.5x10^{-6}\pm0.3x10^{-6}$	$2.2x10^{-7}$	0
448	$9.5x10^{-6}\pm3.0x10^{-6}$	-----	-----
473	$8.5x10^{-6}\pm0.3x10^{-6}$	$6.2x10^{-6}\pm2.7x10^{-6}$	$3.4x10^{-6}\pm2.3x10^{-6}$
523	$1.0x10^{-5}\pm0.3x10^{-5}$	$8.8x10^{-6}\pm0.9x10^{-6}$	$7.6x10^{-6}\pm0.8x10^{-6}$

Table C.17: Temperature dependence of CO conversion rate over Au@UiO-66(ENC)

Temperature (K)	CO Conversion Rate (mol/g_{Au} s) Au@UiO-66(ENC) (0.7 wt% Au)	Au@UiO-66(ENC) (0.4 wt% Au)	Au@UiO-66(ENC) (0.2 wt% Au)
298	$1.4x10^{-5}$	0	0
323	-----	0	0
373	$6.3x10^{-5}$	0	0
398	$2.8x10^{-4}\pm0.7x10^{-4}$	-----	-----
423	$6.4x10^{-4}\pm0.5x10^{-4}$	$5.4x10^{-5}$	0
448	$1.4x10^{-3}\pm0.4x10^{-3}$	-----	-----
473	$1.2x10^{-3}\pm0.1x10^{-3}$	$1.5x10^{-3}\pm0.7x10^{-3}$	$1.7x10^{-3}\pm1.1x10^{-3}$
523	$1.4x10^{-3}\pm0.4x10^{-3}$	$2.2x10^{-3}\pm0.2x10^{-3}$	$3.8x10^{-3}\pm0.2x10^{-3}$

Table C.18: Temperature dependence of TOF over Au@UiO-66(ENC)

Temperature (K)	TOF (s^{-1}) Au@UiO-66(ENC) (0.7 wt% Au)	Au@UiO-66(ENC) (0.4 wt% Au)	Au@UiO-66(ENC) (0.2 wt% Au)
298	0.5	0	0
323	-----	0	0
373	2.5	0	0
398	10.8±0.9	-----	-----
423	27.0±10.6	2.1	0
448	67.9±46.7	-----	-----
473	44.9±3.8	66.5±39.0	62.9±42.5
523	62.4±34.1	94.2±16.0	133.8±11.9

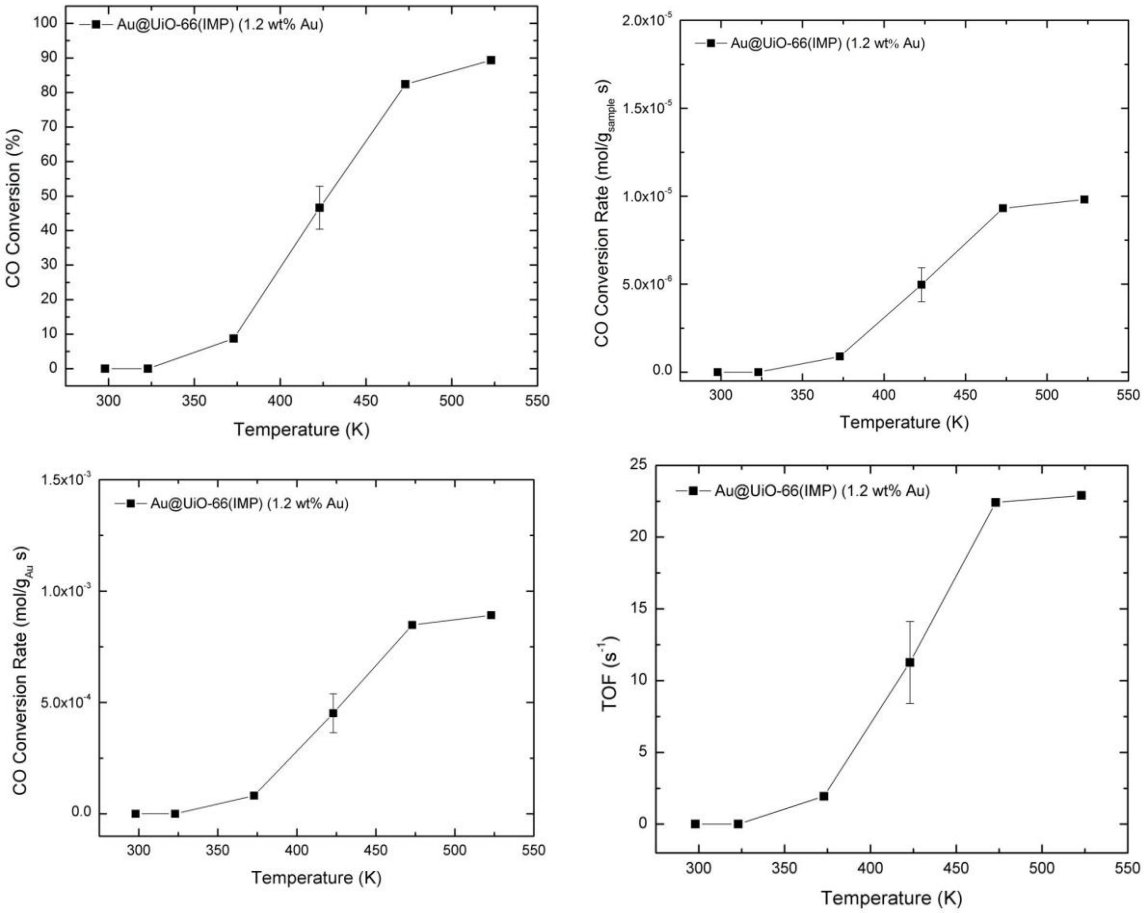

Figure C.10: Temperature dependence of CO conversion, CO conversion rate, and TOF over Au@UiO-66(IMP)

Table C.19: Temperature dependence of CO conversion, CO conversion rate, and TOF over Au@UiO-66(IMP)

	Au@UiO-66 (1.2 wt% Au)			
Temperature (K)	CO Conversion (%)	CO Conversion Rate (mol/g_{sample} s)	CO Conversion Rate (mol/g_{Au} s)	TOF (s^{-1})
298	0	0	0	0
323	0	0	0	0
373	8.7	$8.9x10^{-7}$	$8.1x10^{-5}$	1.9
423	46.6±6.3	$5.0x10^{-6}$±$1.0x10^{-6}$	$4.5x10^{-4}$±$0.9x10^{-4}$	11.3±2.8
473	82.4	$9.3x10^{-6}$	$8.5x10^{-4}$	22.4
523	89.3	$9.8x10^{-6}$	$8.9x10^{-4}$	22.9

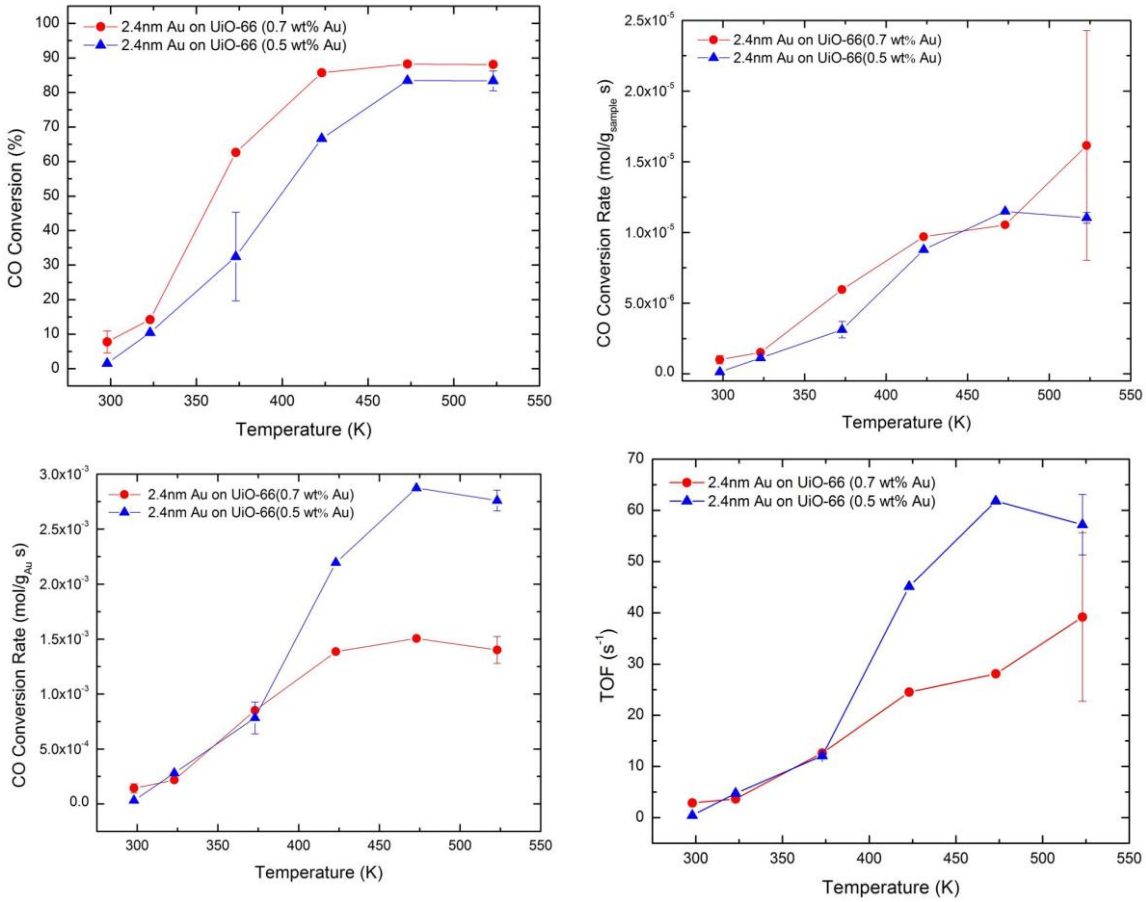

Figure C.11: Temperature dependence of CO conversion, CO conversion rate, and TOF over 2.4 nm Au on UiO-66

Table C.20: Temperature dependence of CO conversion and CO conversion rate over 2.4 nm Au on UiO-66

Temp (K)	CO Conversion (%)		CO Conversion Rate (mol/g_{sample} s)	
	2.4 nm Au on UiO-66 (0.7 wt% Au)	2.4 nm Au on UiO-66 (0.5 wt% Au)	2.4 nm Au on UiO-66 (0.7 wt% Au)	2.4 nm Au on UiO-66 (0.5 wt% Au)
298	7.8±3.2	1.5	$1.0x10^{-6}$±$0.3x10^{-6}$	$1.3x10^{-7}$
323	14.2	10.4	$1.5x10^{-6}$	$1.1x10^{-6}$
373	62.6	32.5±12.8	$6.0x10^{-6}$	$3.1x10^{-6}$±$0.6x10^{-6}$
423	85.7	66.7	$9.7x10^{-6}$	$8.8x10^{-6}$
473	88.2	83.4	$1.1x10^{-5}$	$1.1x10^{-5}$
523	88.1±0.4	83.4±2.9	$1.6x10^{-5}$±$0.8x10^{-5}$	$1.1x10^{-5}$±$0.4x10^{-6}$

Table C.21: Temperature dependence of CO conversion rate and TOF over 2.4 nm Au on UiO-66

Temp (K)	CO Conversion Rate (mol/g_{Au} s)		TOF (s^{-1})	
	2.4 nm Au on UiO-66 (0.7 wt% Au)	2.4 nm Au on UiO-66 (0.5 wt% Au)	2.4 nm Au on UiO-66 (0.7 wt% Au)	2.4 nm Au on UiO-66 (0.5 wt% Au)
298	$1.4x10^{-4}$±$0.4x10^{-4}$	$3.3x10^{-5}$	2.9±0.5	0.4
323	$2.2x10^{-4}$	$2.8x10^{-4}$	3.7	4.8
373	$8.5x10^{-4}$	$7.8x10^{-4}$±$1.4x10^{-4}$	12.6	12.1±0.4
423	$1.4x10^{-3}$	$2.2x10^{-3}$	24.5	45.1
473	$1.5x10^{-3}$	$2.9x10^{-3}$	28.1	61.8
523	$1.4x10^{-3}$±$0.1\ x10^{-3}$	$2.8x10^{-3}$±$0.1x10^{-3}$	39.2±16.5	57.2±5.9

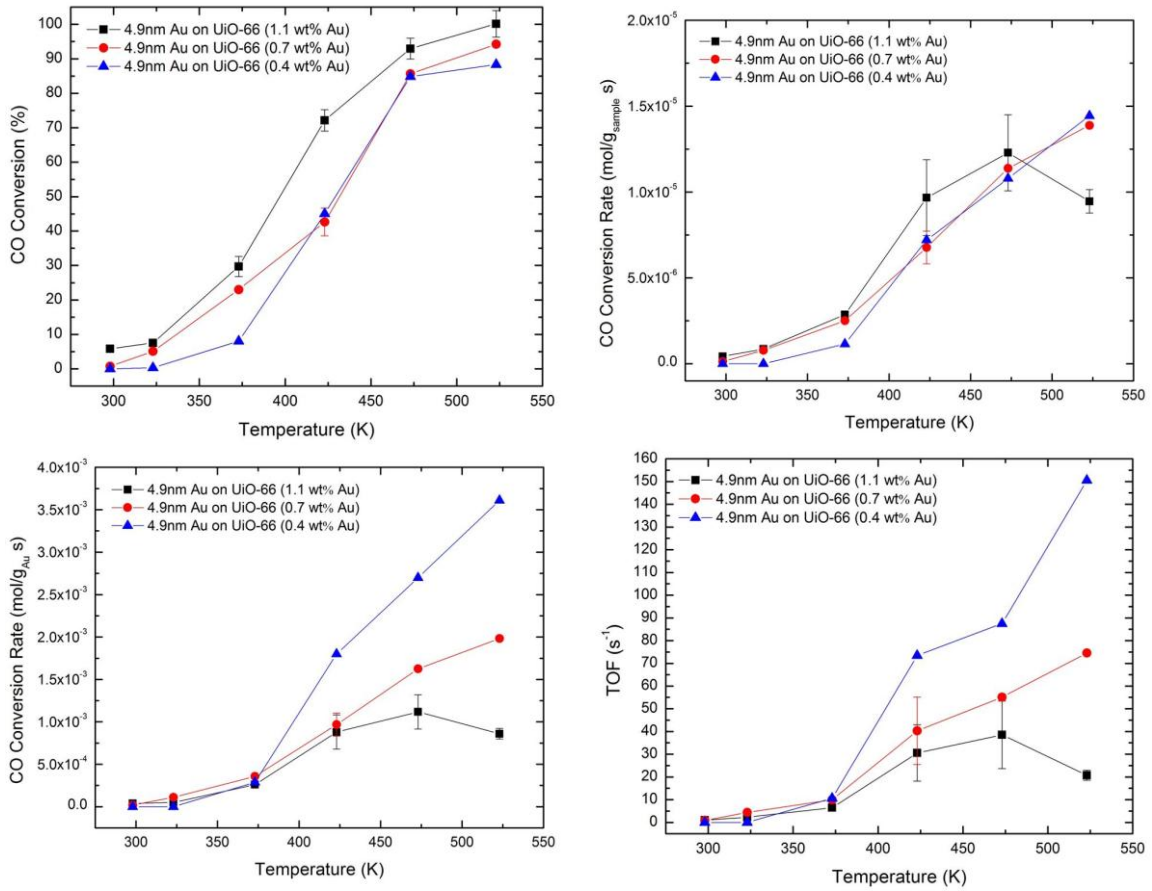

Figure C.12: Temperature dependence of CO conversion, CO conversion rate, and TOF over 4.9 nm Au on UiO-66

Table C.22: Temperature dependence of CO conversion over 4.9 nm Au on UiO-66

Temperature (K)	CO Conversion (%)		
	4.9nm Au on UiO-66 (1.1 wt% Au)	4.9nm Au on UiO-66 (0.7 wt% Au)	4.9nm Au on UiO-66 (0.4 wt% Au)
298	5.8±0.6	0.8	0
323	7.5	5.1	0.3
373	29.7±2.9	23.0	8.0
423	72.2±3.1	42.6±4.0	45.0
473	93.0±3.1	85.6	84.9
523	100.2±3.9	94.2	88.3

Table C.23: Temperature dependence of CO conversion rate over 4.9 nm Au on UiO-66

Temperature (K)	CO Conversion Rate (mol/g_{sample} s)		
	4.9nm Au on UiO-66 (1.1 wt% Au)	4.9nm Au on UiO-66 (0.7 wt% Au)	4.9nm Au on UiO-66 (0.4 wt% Au)
298	$4.3x10^{-7}±2.1x10^{-7}$	$1.3x10^{-7}$	0
323	$8.6x10^{-7}$	$7.8x10^{-7}$	0
373	$2.9x10^{-6}±0.9x10^{-7}$	$2.5x10^{-6}$	$1.2x10^{-6}$
423	$9.7x10^{-6}±2.2x10^{-6}$	$6.8x10^{-6}±1.0x10^{-6}$	$7.2x10^{-6}$
473	$1.2x10^{-5}±0.2x10^{-5}$	$1.1x10^{-5}$	$1.1x10^{-5}$
523	$9.5x10^{-6}±0.7x10^{-6}$	$1.4x10^{-5}$	$1.4x10^{-5}$

Table C.24: Temperature dependence of CO conversion rate over 4.9 nm Au on UiO-66

Temperature (K)	CO Conversion Rate (mol/g_{Au} s)		
	4.9nm Au on UiO-66 (1.1 wt% Au)	4.9nm Au on UiO-66 (0.7 wt% Au)	4.9nm Au on UiO-66 (0.4 wt% Au)
298	$3.9x10^{-5}±1.9x10^{-5}$	$1.9x10^{-5}$	0
323	$5.0x10^{-5}$	$1.1x10^{-4}$	0
373	$2.6x10^{-4}±0.8x10^{-5}$	$3.6x10^{-4}$	$2.9x10^{-4}$
423	$8.8x10^{-4}±2.0x10^{-4}$	$9.7x10^{-4}±1.3x10^{-4}$	$1.8x10^{-3}$
473	$1.1x10^{-3}±0.2x10^{-3}$	$1.6x10^{-3}$	$2.7x10^{-3}$
523	$8.6x10^{-4}±0.6x10^{-4}$	$2.0x10^{-3}$	$3.6x10^{-3}$

Table C.25: Temperature dependence of TOF over 4.9 nm Au on UiO-66

Temperature (K)	TOF (s^{-1})		
	4.9nm Au on UiO-66 (1.1 wt% Au)	4.9nm Au on UiO-66 (0.7 wt% Au)	4.9nm Au on UiO-66 (0.4 wt% Au)
298	1.0±0.4	0.8	0
323	2.3	4.4	0
373	6.5±1.0	10.0	10.6
423	30.6±12.4	40.3±14.8	73.5
473	38.5±14.9	55.1	87.5
523	20.7±2.2	74.5	150.6

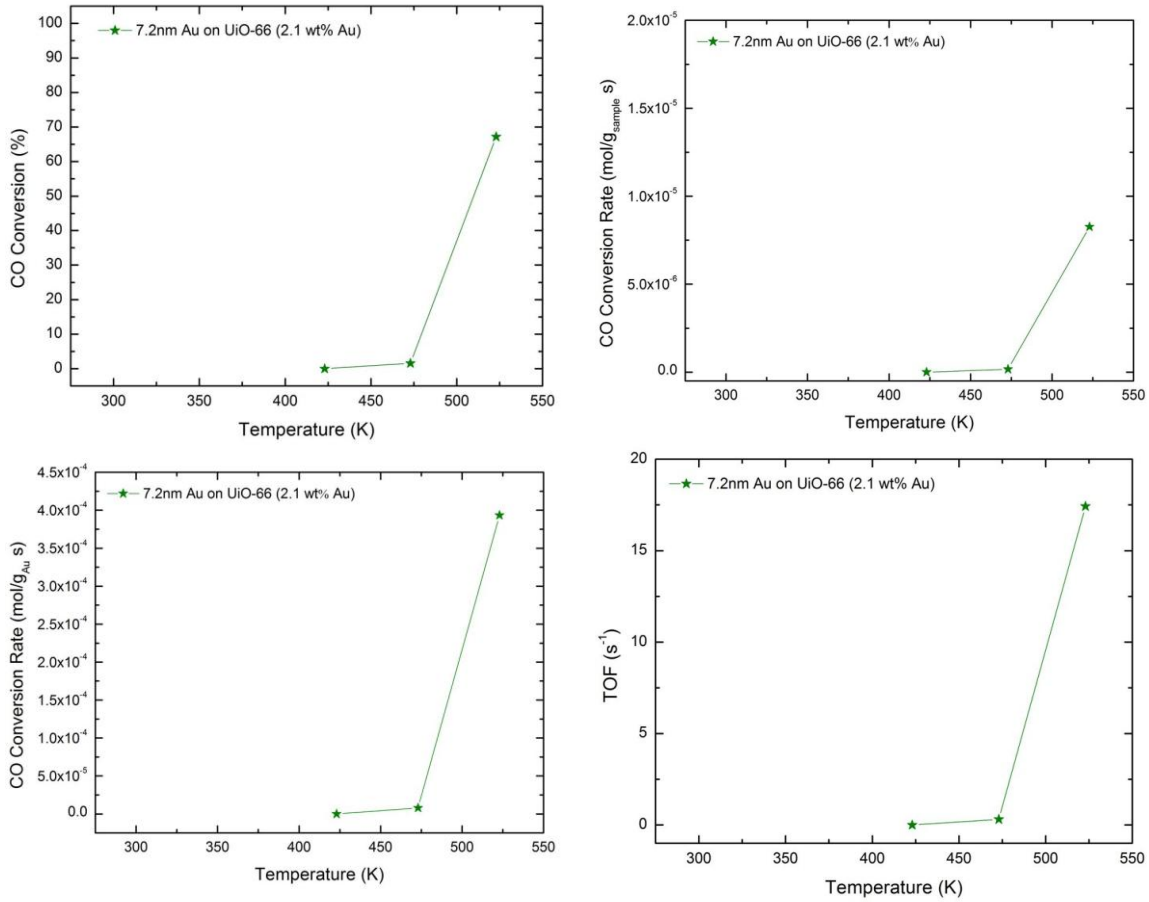

Figure C.13: Temperature dependence of CO conversion, CO conversion rate, and TOF over 7.2 nm Au on UiO-66

Table C.26: Temperature dependence of CO conversion, CO conversion rate, and TOF over 7.2 nm Au on UiO-66

	7.2 nm Au on UiO-66 (2.1 wt% Au)			
Temperature (K)	CO Conversion (%)	CO Conversion Rate (mol/g_{sample} s)	CO Conversion Rate (mol/g_{Au} s)	TOF (s^{-1})
423	0	0	0	0
473	1.6	$1.7x10^{-7}$	$8.0x10^{-6}$	0.3
523	67.2	$8.3x10^{-6}$	$3.9x10^{-4}$	17.4

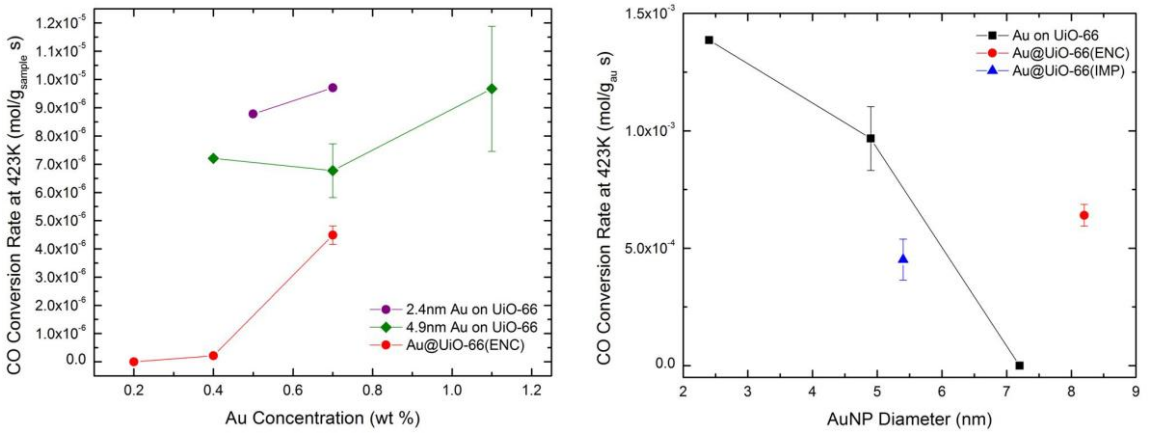

Figure C.14: Effect of AuNP concentration and diameter on catalytic activity. The lines are to guide the eyes only

Table C.27: Effect of AuNP concentration on CO conversion rate at 423K

Material	Au wt %	CO Conversion Rate at 423 K (mol/g_{sample} s)
2.4 nm Au on UiO-66	0.7	$9.7x10^{-6}$
	0.5	$8.8x10^{-6}$
4.9 nm Au on UiO-66	1.1	$9.7x10^{-6}\pm2.2x10^{-6}$
	0.7	$6.8x10^{-6}\pm1.0x10^{-6}$
	0.4	$7.2x10^{-6}$
Au@UiO-66(ENC)	0.7	$4.5x10^{-6}\pm0.3x10^{-6}$
	0.4	$2.2x10^{-7}$
	0.2	0.0

Table C.28: Effect of AuNP diameter on CO conversion rate at 423K

Material	AuNP Diameter (nm)	Au wt %	CO Conversion Rate at 423 K (mol/g_{Au} s)
Au on UiO-66	2.4±0.7	0.7	$1.4x10^{-3}$
	4.9±1.8	0.7	$9.7x10^{-4}\pm1.3x10^{-4}$
	7.2±3.9	2.1	0.0
Au@UiO-66(ENC)	8.2±3.1	0.7	$6.4x10^{-4}\pm0.5x10^{-4}$
Au@UiO-66(IMP)	5.4±2.8	1.2	$4.5x10^{-4}\pm0.9x10^{-4}$

C.4 Chapter 6: Tuning the Au@UiO-66 Encapsulation Procedure

C.4.1 ^{1}H NMR

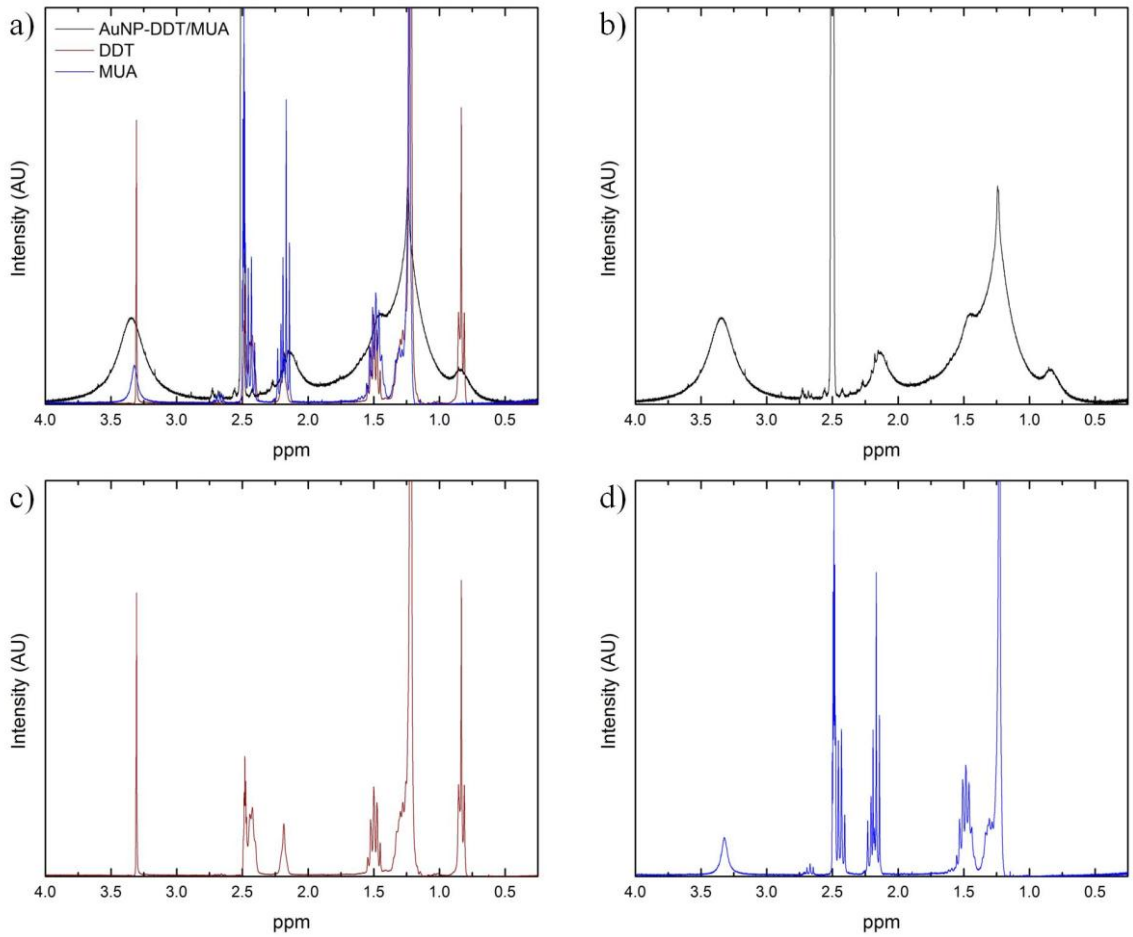

Figure C.15: ^{1}H NMR spectra for (a) AuNP-DDT/MUA, DDT, and MUA; (b) AuNP-DDT/MUA; (c) DDT; and (d) MUA

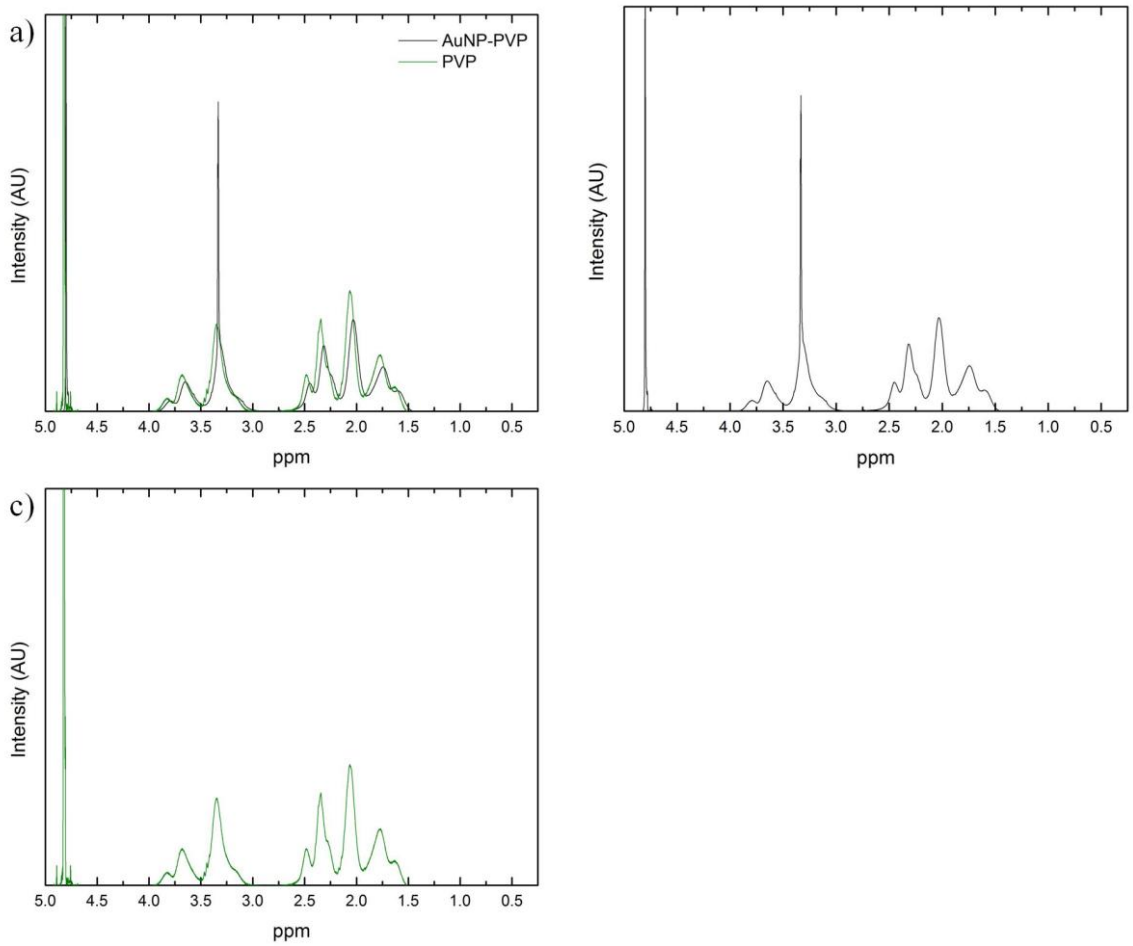

Figure C.16: ^{1}H NMR spectra for (a) AuNP-PVP and PVP; (b) AuNP-PVP; and (c) PVP

C.4.2 Nitrogen Sorption at 77K

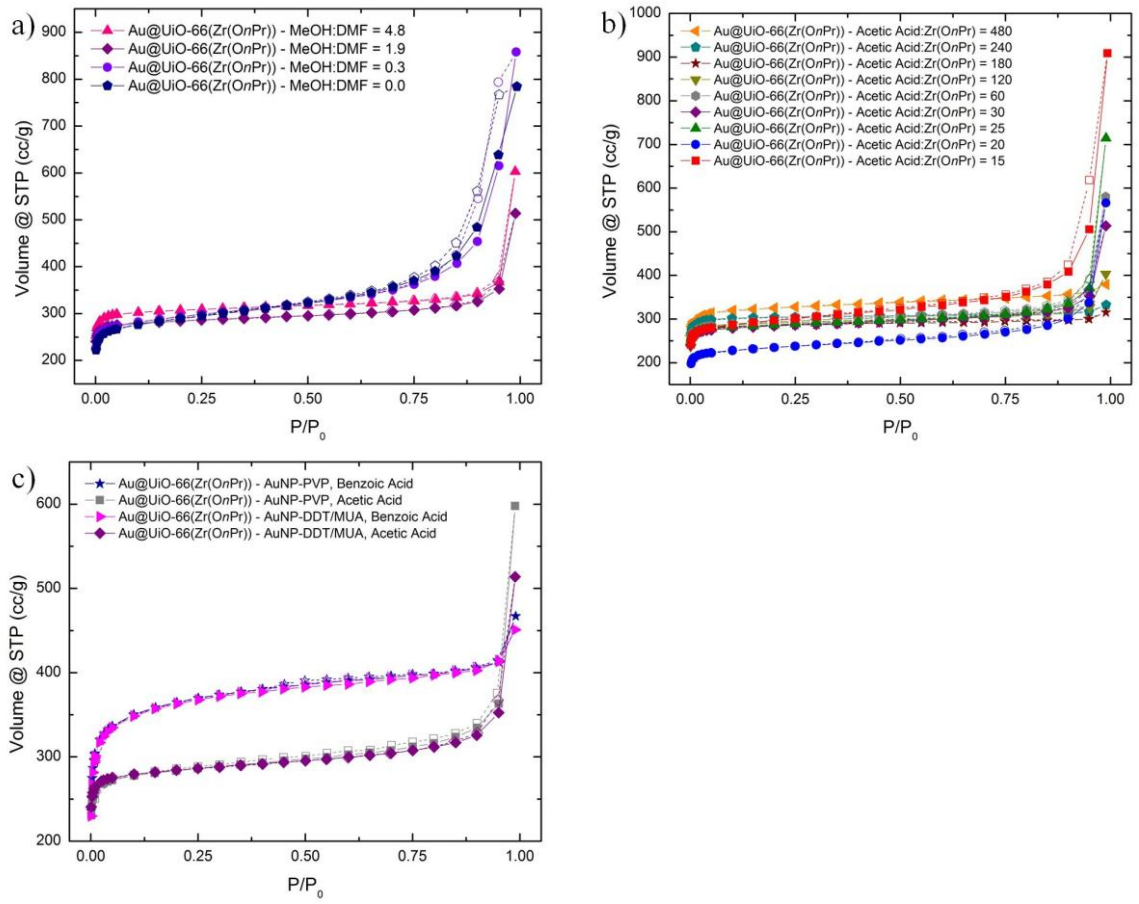

Figure C.17: Nitrogen sorption isotherms at 77 K for Au@UiO-66(Zr(O*n*Pr)) prepared with various (a) MeOH:DMF ratios; (b) acetic acid:Zr(O*n*Pr) ratios; and (c) AuNP capping agent and UiO-66(Zr(O*n*Pr)) modulator. Closed and open symbols represent adsorption and desorption curves, respectively

C.5 Chapter 7: Extending the HCl-Free Synthesis to Include UiO-66 Analogues

C.5.1 Modulator Effect on UiO-66-NH_2 (Zr(O*n*Pr)) Porosity

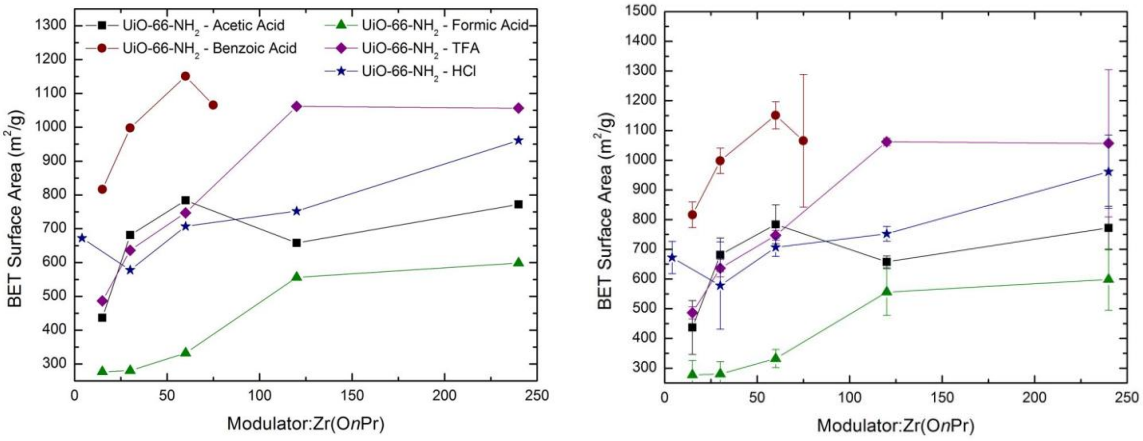

Figure C.18: Modulator effect on UiO-66-NH_2(Zr(O*n*Pr)) porosity

Table C.29: Modulator effect on UiO-66-NH_2(Zr(O*n*Pr)) porosity

Modulator: Zr(O*n*Pr)	UiO-66-NH_2 – Acetic Acid		UiO-66-NH_2 – Benzoic Acid		UiO-66-NH_2 – Formic Acid	
	BET Surface Area (m^2/g)	Total Pore Volume (cm^3/g)[a]	BET Surface Area (m^2/g)	Total Pore Volume (cm^3/g)[a]	BET Surface Area (m^2/g)	Total Pore Volume (cm^3/g)[a]
15	437±90	0.22±0.04	817±43	0.42±0.04	278±48	0.16±0.02
30	682±56	0.30±0.02	998±43	0.43±0.02	281±41	0.17±0.01
60	784±65	0.33±0.02	1151±46	0.45±0.01	332±30	0.18±0.01
75	-----	-----	1066±223	0.43±0.08	-----	-----
120	658±20	0.31±0.01	-----	-----	556±78	0.26±0.03
240	772±74	0.33±0.03	-----	-----	598±103	0.27±0.06

[a]Measured at $P/P_0 = 0.6$

Table C.30: Modulator effect on UiO-66-NH_2(Zr(O*n*Pr)) porosity

Modulator: Zr(O*n*Pr)	UiO-66-NH_2 – TFA		UiO-66-NH_2 – HCl	
	BET Surface Area (m^2/g)	Total Pore Volume (cm^3/g)[a]	BET Surface Area (m^2/g)	Total Pore Volume (cm^3/g)[a]
4	-----	-----	578±147	0.32±0.08
15	486±20	0.28±0.00	-----	-----
30	636±29	0.34±0.01	672±54	0.32±0.04
60	747±16	0.37±0.00	707±25	0.32±0.02
120	1061±12	0.48±0.00	752±29	0.33±0.02
240	1057±247	0.46±0.10	961±123	0.40±0.05

[a]Measured at $P/P_0 = 0.6$

C.5.2 ^{1}H NMR

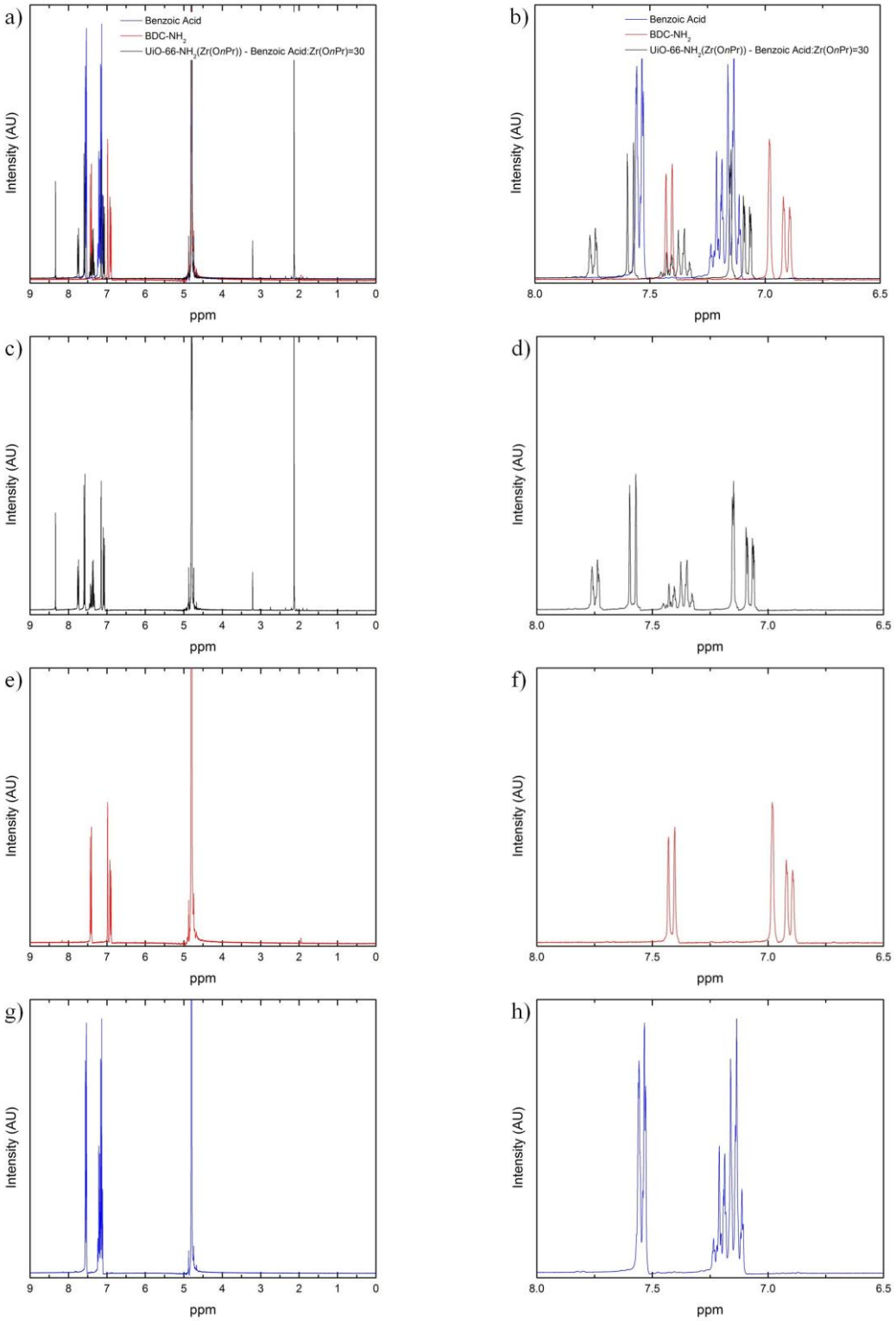

Figure C.19: ^{1}H NMR spectra for (a,b) UiO-66-NH_2(Zr(O*n*Pr)) – benzoic acid:Zr(O*n*Pr) = 30, BDC-NH_2, and benzoic acid; (c,d) UiO-66-NH_2(Zr(O*n*Pr)) – benzoic acid:Zr(O*n*Pr) = 30; (e,f) BDC-NH_2; and (g,h) benzoic acid

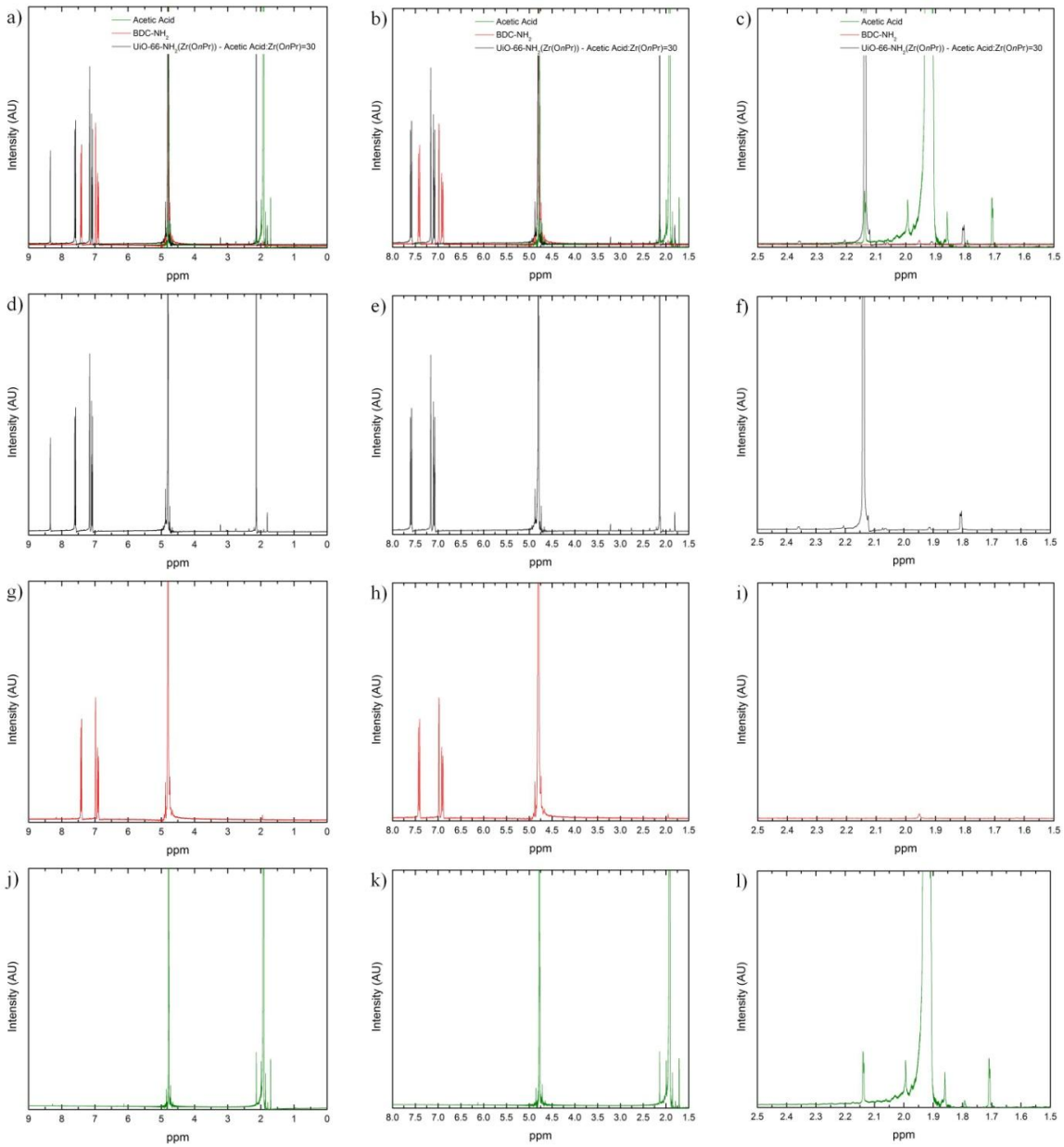

Figure C.20: ^{1}H NMR spectra for (a,b,c) UiO-66-NH_2(Zr(O*n*Pr)) – acetic acid:Zr(O*n*Pr) = 30, BDC-NH_2, and acetic acid; (d,e,f) UiO-66-NH_2(Zr(O*n*Pr)) – acetic acid:Zr(O*n*Pr) = 30; (g,h,i) BDC-NH_2; and (j,k,l) acetic acid

C.5.3 Nitrogen Sorption at 77 K

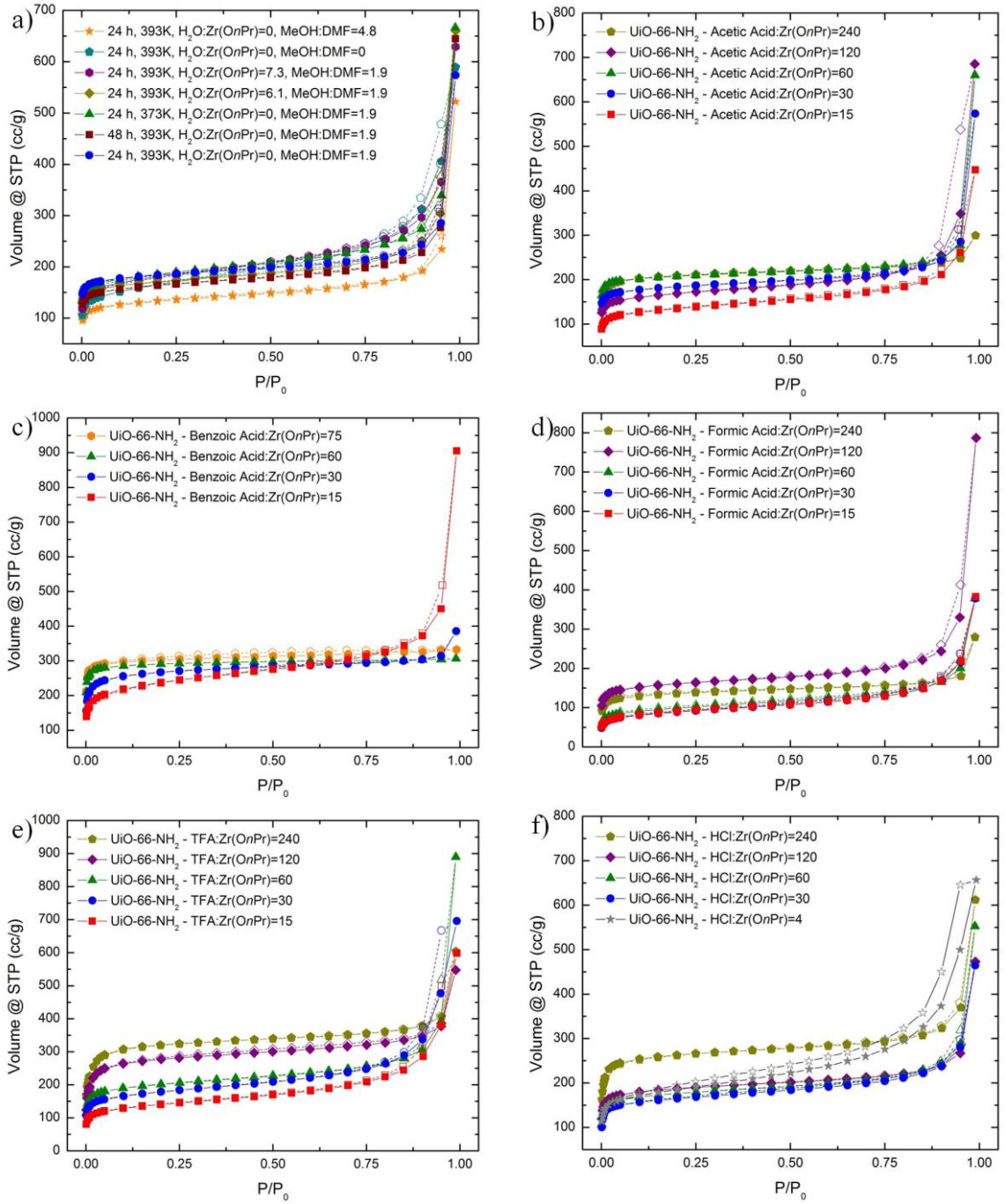

Figure C.21: Nitrogen sorption isotherms at 77 K for UiO-66-NH_2(Zr(O*n*Pr)) prepared with various (a) times, temperatures, H_2O:Zr(O*n*Pr) ratios, and MeOH:DMF ratios; (b) acetic acid:Zr(O*n*Pr) ratios; (c) benzoic acid:Zr(O*n*Pr) ratios; (d) formic acid:Zr(O*n*Pr) ratios; (e) TFA:Zr(O*n*Pr) ratios; and (f) HCl:Zr(O*n*Pr) ratios. Closed and open symbols represent adsorption and desorption curves, respectively

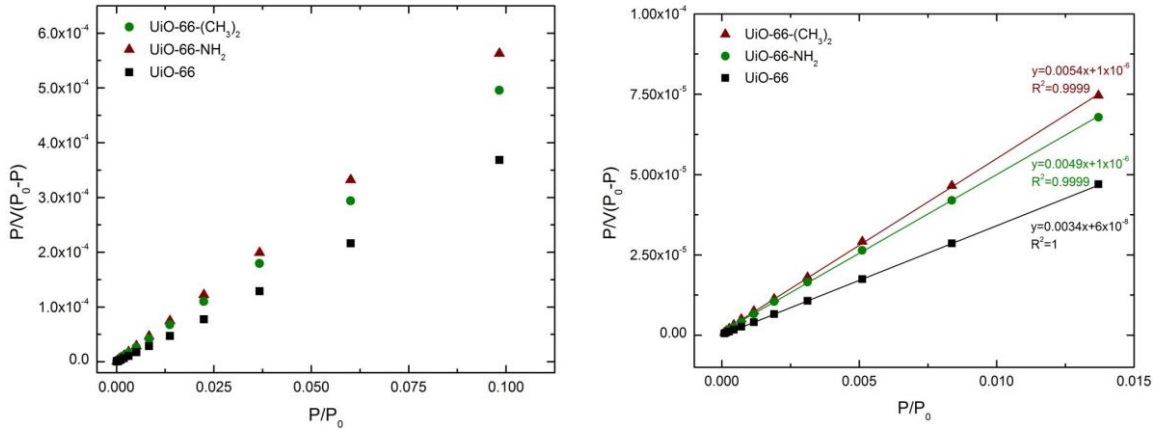

Figure C.22: Simulated nitrogen adsorption isotherms at 77 K for UiO-66, UiO-66-NH_2, and UiO-66-$(CH_3)_2$. The lines and equations show the BET fit

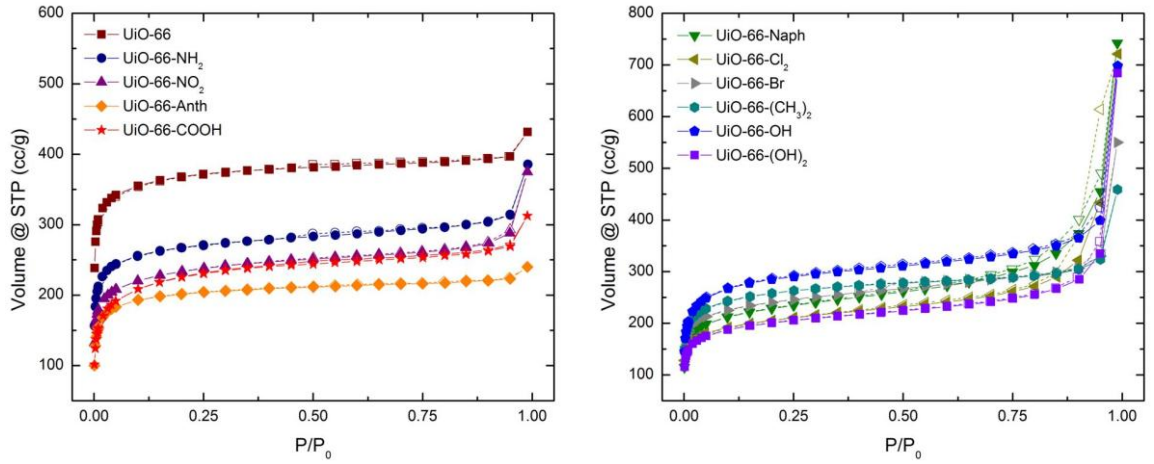

Figure C.23: Nitrogen sorption isotherms at 77 K for UiO-66-X(Zr(O*n*Pr)). Closed and open symbols represent adsorption and desorption curves, respectively

C.5.4 PXRD

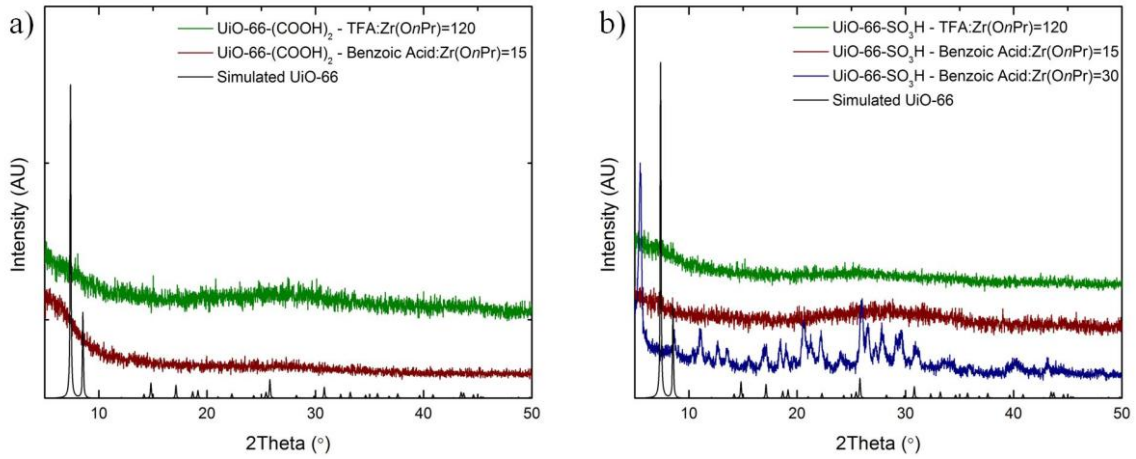

Figure C.24: PXRD patterns for (a) UiO-66-$(COOH)_2$ and (b) UiO-66-SO_3H

APPENDIX D

NP@MOF LITERATURE REVIEW

D.1 Impregnation

Table D.1: Overview of NP@MOF composites prepared using impregnation

NP	MOF[a]	Infiltration Method, precursor (solvent)[b]	Reduction/ Oxidation Conditions	Application[c]	Ref
Ag	MOF-5	S-IMP, $AgNO_3$ (EtOH)	UV irradiation	-----	
	MIL-101(Cr)	DSA, $AgNO_3$ (*n*-hexane/H_2O)	H_2(20%), 200°C, 4h	Cascade reactions (inactive)	1
			$NaBH_4$	Reduction of 4-nitrophenol	2
		S-IMP, $AgNO_3$ (MeOH)	$NaBH_4$	Dehydrogenation of formic acid	3
		S-IMP, $AgNO_3$ (CH_3CN)	$NaBH_4$	CO_2 capture/CO_2 conversion	4
	MIL-53(Al)	S-IMP, $AgNO_3$ (ethylene glycol)	Ethylene glycol	CO oxidation	5
	MIL-53(Al)-SH	S-IMP, $AgNO_3$ (H_2O)	$NaBH_4$	-----	6
	MIL-125	S-IMP, $AgNO_3$ (EtOH)	UV irradiation	Photocatalytic degradation of RhB	7
	MIL-125-NH_2	S-IMP, [$Ag(CH_3COO)$] (CH_3CN/H_2O)		Photocatalytic degradation of MB	8
	ZIF-8	S-IMP, $AgNO_3$ (MeOH)	$NaBH_4$	Dehydrogenation of formic acid (inactive)	9
				Reduction of 4-nitrophenol	10
	HKUST-1	S-IMP, $AgNO_3$ (H_2O/EtOH)	Cobalt-60 gamma irradiation	-----	11
	HKUST-1, MOF-508, MIL-68(In)	S-IMP, $AgNO_3$ (H_2O/EtOH)	EtOH	-----	12
	MOF-74(Ni)	S-IMP, $AgNO_3$ (EtOH)	MOF autoreduction	Noble gas adsorption	13
	[{$Ni(C_{10}H_{26}N_6)_3(bpdc)_3$]·$2C_5H_5N·6H_2O$, {[Ni(cyclam)]$_2$[BPTC]}$_n$·$2nH_2O$	S-IMP, $AgNO_3$ (MeOH)	MOF autoreduction	-----	14, 15
	Rb-CD-MOF, Cs-CD-MOF	S-IMP, $AgNO_3$ (CH_3CN)	MOF autoreduction	-----	16
Ag/AgCl	MIL-101(Cr)	S-IMP, $AgNO_3$ (H_2O)	HCl, UV irradiation	Photocatalytic degradation of RhB	17
AgI	UiO-66	S-IMP, $AgNO_3$ (H_2O)	KI	Photocatalytic degradation of RhB	18
Ag_2CO_3	UiO-66	S-IMP, $AgNO_3$ (H_2O)	$NaHCO_3$	Photocatalytic degradation of RhB	19
Ag_2O	Cu-BDC	S-IMP, $AgNO_3$ (H_2O)	$NaBH_4$, O_2 bubbled through H_2O	Photocatalytic degradation of Acid Blue 92	20
Ag_2S	MIL-125	S-IMP, $AgNO_3$,S_8 (CH_3CN/H_2O/EtOH)	UV irradiation	Photocatalytic reduction of aqueous Cr(IV)	21
Ag_1Pd_4	UiO-66-NH_2	S-IMP, $AgNO_3$ (H_2O)/$PdCl_2$ (H_2O)	$NaBH_4$	Hydrolysis of AB	22
				Dehydrogenation of formic acid	23
Ag/Pd	ZIF-8, MIL-101(Cr)	S-IMP, $AgNO_3$/$PdCl_4$ (MeOH)	$NaBH_4$	Dehydrogenation of formic acid	9, 24
Au	ZIF-8	S-IMP, $HAuCl_4$ (MeOH)	$NaBH_4$	Reduction of 4-nitrophenol	10
		CVD, Au(CO)Cl	H_2 (2 bar), 100°C	Oxidation of benzyl alcohol	25
		SG, $(CH_3)_2$Au(acac)	H_2 (10%), 230°C, 2.5h	CO oxidation	26
	{[Ni(cyclam)]$_2$[BPTC]}$_n$, $2nH_2O$	S-IMP, $NaAuCl_4$ (EtOH)	MOF autoreduction	-----	15

NP	MOF[a]	Infiltration Method, precursor (solvent)[b]	Reduction/ Oxidation Conditions	Application[c]	Ref
	Rb-CD-MOF, Cs-CD-MOF	S-IMP, $HAuCl_4$ (CH_3CN)	MOF autoreduction	-----	16
	ZIF-90	CVD, Au(CO)Cl	H_2 (2 bar), 130°C	Oxidation of benzyl alcohol	25
	MOF-1, MOF-2, MOF-3	S-IMP, $HAuCl_4$ (MeOH)	$NaBH_4$	Reduction of nitrophenol and 2,4-dinitrophenol	27
	MOF-5	SG, $(CH_3)_2Au(acac)$	H_2 (10%), 120°C, 2h	Oxidation of 1-phenylethanol	28
				Synthesis of dibenzylamine and N-alkylation of aniline	29
		CVD, $[(CH_3)Au(P(CH_3)_3)]$	H_2, 190°C, 2h	Oxidation of benzylalcohol	28, 30
		CVD, ClAuCO	H_2, 150°C		31
	MIL-101(Cr)	S-IMP $HAuCl_4/H_2O$	Reduction Sodium citrate	SERS	32
		DSA, $HAuCl_4$ (*n*-hexane/H_2O)	$NaBH_4$	Reduction of 4-nitrophenol	2
				Photocatalytic H_2 production (inactive)	33
	ED-MIL-101(Cr)	S-IMP, $HAuCl_4$ (H_2O)	$NaBH_4$		34
			H_2 (50%), 200°C	Dehydrogenation of formic acid (inactive)	35
	MIL-100(Fe)	S-IMP, $HAuCl_4$(H_2O)	EtOH	Degradation of pharmaceuticals and personal care products	36
		S-IMP, $HAuCl_4$(H_2O)	UV irradiation	Photocatalytic degradation of methyl orange and reduction of Cr(IV)	37
	CPL-1, CPL-2, MIL-53(Al), HKUST-1	SG $(CH_3)_2Au(acac)$	H_2 (10%), 120°C, 2h	CO oxidation (inactive) Oxidation of benzyl alcohol and 1-phenylethanol	28
	CPL-2	CVD $(CH_3)_2Au(acac)$	H_2 (10%), 120°C, 2h	Synthesis of dibenzylamine N-alkylation of aniline	29
	MIL-53(Al)	SG $(CH_3)_2Au(acac)$	H_2 (10%), 120°C, 2h	Synthesis of dibenzylamine N-alkylation of aniline	29
	UiO-66	S-IMP, $HAuCl_4$ (MeOH)	$NaBH_4$/Triethylamine/ H_2, 200°C, 2h	Oxidation of benzyl alcohol	38
		S-IMP, $HAuCl_4$ (octadecene/oleylamine)	Oleylamine	CO oxidation	39
		DSA, $HAuCl_4$ (*n*-hexane/H_2O)	$NaBH_4$	Oxidation of benzyl alcohol	40
	UiO-66-NH_2	S-IMP, $HAuCl_4$ (H_2O/EtOH)	$NaBH_4$	Oxidation of benzyl alcohol and reduction of nitrophenol	41
	IRMOF-3	S-IMP, $HAuCl_4$ (H_2O/EtOH)	$NaBH_4$	-----	41
	MIL-125	S-IMP $HAuCl_4$(MeOH)	MOF autoreduction	Photocatalysis: oxidation of benzylalcohol	42
	MIL-125-NH_2	S-IMP, $HAuCl_4$ (H_2O)	Sodium citrate	Electrocatalytic oxidation of hydrazine	43
Au_{11}	ZIF-8	S-IMP, $HAuCl_4$/PPh_3 (EtOH)	$NaBH_4$/calcine (150, 200, 300°C)	Oxidation of benzyl alcohol	44
$Au_{13}Ag_{12}$	MIL-101(Cr)	S-IMP, $HAuCl_4$/PPh_3 (EtOH)	$NaBH_4$/calcine (150°C)	Oxidation of benzyl alcohol	44

NP	MOF[a]	Infiltration Method, precursor (solvent)[b]	Reduction/ Oxidation Conditions	Application[c]	Ref
Au@Ag	ZIF-8	S-IMP, $AgNO_3$ (MeOH), $HAuCl_4$ (MeOH)	$NaBH_4$	Reduction of 4-nitrophenol	10
	Rb-CD-MOF, Cs-CD-MOF	S-IMP, $AgNO_3$ (CH_3CN), $HAuCl_4$ (CH_3CN)	MOF autoreduction	-----	16
Au/CdS	MIL-101(Cr)	DSA, $HAuCl_4$ (*n*-hexane/H_2O) S-IMP, $Cd(CH_3COO)_2$ (DMSO)	$NaBH_4$ DMSO	Photocatalytic H_2 production	33
Au/Pd	MIL-101(Cr), ED-MIL-101(Cr)	S-IMP, H_2PdCl_4/$HAuCl_4$ (H_2O)	H_2 (50%), 200°C	Dehydrogenation of formic acid	35
	MIL-101(Cr)	S-IMP, $PdCl_2$/$HAuCl_4$	$NaBH_4$	Reduction of 4-nitrophenol	2
		DSA, $PdCl_2$/$HAuCl_4$ (*n*-hexane/H_2O)	$NaBH_4$	Reduction of 4-nitrophenol	2
Au/Pt	ED-MIL-101(Cr)	S-IMP, H_2PtCl_6/$HAuCl_4$ (H_2O)	H_2 (50%), 200°C	Dehydrogenation of formic acid	35
Au/TiO_2	MOF-5	CVD, Ti(O*i*Pr)$_4$/ClAuCO	O_2 (4.5 vol%)/H_2	Oxidation of benzylalcohol	30
Au/ZnO	MOF-5	CVD, $(C_2H_5)_2Zn$/ClAuCO	O_2 (4.5 vol%)/H_2	Oxidation of benzylalcohol	30
C@Pd	ZIF-8	S-IMP, $PdCl_2$/glucose (H_2O)	H_2 (5%), 300°C, 2h	Hydrogenation of olefins	45
CdS	MIL-125	S-IMP, $CdCl_2$/S_8 (EtOH)	UV irradiation	Photocatalytic reduction of aqueous Cr(IV)	21
	UiO-66	S-IMP, $Cd(CH_3COO)_2$ (DMSO)	DMSO	Photocatalytic H_2 generetion	46
	MIL-100(Fe)	S-IMP, $Cd(CH_3COO)_2$ (DMSO)	DMSO	Photocatalytic oxidation of benzene alcohol	47
	MIL-100(Cr)	S-IMP, $Cd(CH_3COO)_2$ (DMSO)	DMSO	Photocatalytic degradation of nitrite	48
				Photocatalytic H_2 production	33
CdSe	UiO-66	S-IMP, ($CdCl_2$) (EtOH)	H_2Se	Photocatalytic degradation of RhB	49
CeO_2	MIL-100(Fe)	S-IMP, $Ce(NO_3)_3$ (EtOH)	N_2, 250°C, 2 h	SCR of NO_x with NH_3	50
Co	MIL-101(Cr)	DSA, $CoCl_2$ (*n*-hexane/H_2O)	$NaBH_4$	Dehydrogenation of AB	51, 52
Co_3O_4	MIL-101(Cr)	DSA, $Co(NO_3)_2$ (*n*-hexane/H_2O)	Air, 150°C,	Photocatalytic water oxidation	53
CoAgPd	MIL-101(Cr)	S-IMP, $CoCl_2$, $AgNO_3$, H_2PdCl_4 (H_2O)	$NaBH_4$	Dehydrogenation of formic acid	54
Cu	MOF-5	CVD, $[(\eta^5\text{-}C_5H_5)Cu(P(CH_3)_3]$	H_2, 150°C, 1 h	-----	31
		CVD, $[(C_5H_5)Cu(P(CH_3)_3)]$/ $[[(C_5H_5)Cu(CN^tBu)]$	UV irradiation/H_2, 220°C, 5h	Methanol synthesis	55
	MIL-101(Cr)	DSA, $Cu(NO_3)_2$ (*n*-hexane/H_2O)	$NaBH_4$	Dehydrogenation of AB	51
		S-IMP, $Cu(NO_3)_2$ (H_2O)	$NaBH_4$	CO_2 adsorption	56
			Microwave irradiation	Reduction of 4-nitrophenol	57
	MOF-177	CVD, $Cu(\eta^5\text{-}C_5H_5)(P(CH_3)_3)]_2$/$[Cu(\eta^5\text{-}C_5H_5)(CNtBu)]_2$	H_2, 220°C, 5h	-----	58
	ZIF-8	S-IMP, $CuSO_4$ (H_2O)	$NaBH_4$	Sensing	59
Cu/Co	MIL-101(Cr)	DSA, $Cu(NO_3)_2$/$CoCl_2$ (*n*-hexane/H_2O)	$NaBH_4$	Dehydrogenation of AB	51
Cu/ZnO	MOF-5	CVD $Zn(C_2H_6)_2$/$[(C_5H_5)Cu(P(CH_3)_3)]$	H_2, 220°C, 5h	Methanol synthesis	55
Cu_2O	{[Zn(Himdc)$(bipy)_{0.5}$]·DMF}	S-IMP, $CuSO_4$ (H_2O)	Hydrazine	Huisgen 1,3-dipolar cycloaddition	60
CuS	MIL-125	S-IMP, $CuCl_2$,S_8 (EtOH)	UV irradiation	Photocatalytic reduction of aqueous Cr(IV)	21
Fe_3O_4	MIL-101(Cr)	S-IMP, $FeCl_2$/$FeCl_3$ (H_2O)	NH_3 solution	Oxidation of benzyl alcohol	61

NP	MOF[a]	Infiltration Method, precursor (solvent)[b]	Reduction/ Oxidation Conditions	Application[c]	Ref
		DSA, $FeCl_2/FeCl_3$ (H_2O)	NH_3 solution	Adsorption of anionic dyes	62
	MIL-101(Cr), MIL-53(Cr)	S-IMP, $FeNO_3$ (H_2O)	Air, 200°C, 4h	Photocatalytic oxidation of dye X-3B	63
GaN	ZIF-8	CVD, $[(CH_3)_3NGaH_3]$	NH_3 (2 bar), 150°C, 24 h and vacuum, 200°C, 24h	-----	64
In_2S_3	MIL-125	S-IMP, $In(NO_3)_3$ (EtOH)	CH_3CSNH_2	Photocatalytic degradation of tetracycline	65
α-MnO_2	MIL-101(Cr)	S-IMP, $MnSO_4/KMnO_4$ (H_2O)		Electrocatalytic oxygen reduction reaction and oxygen evolution reaction	66
ε-MnO_2	MOF(Fe)	S-IMP, $Mn(NO_3)_2$ (H_2O)	Air, 110°C	Oxygen reduction reaction	67
MoS_2	MIL-125	S-IMP, $(NH_4)_2MoS_4$ (EtOH)	UV irradiation	Photocatalytic reduction of aqueous Cr(IV)	21
MoS_2/CdS	UiO-66	S-IMP, $Cd(CH_3COO)_2$ (DMSO) $(NH_4)_2MoS_4$ (H_2O/EtOH)	UV irradiation	Photocatalytic H_2 generation	46
$NaAlH_4$	HKUST-1	S-IMP, $NaAlH_4$ (THF)	Vacuum, 100°C	H_2 storage	68
Ni	MesMOF-1	CVD, $[Ni(\eta^5\text{-}C_5H_5)_2]$	H_2, 95°C, 5h	Hydrogenolysis of nitrobenzene Hydrogenation of styrene	69
	UiO-67-BPyDC	S-IMP, $Ni(NO_3)_2$ (DMF)	$NaBH_4$	Hydrogenation of nitrobenzene	70
	MIL-101(Cr)	S-IMP, $NiCl_2$ (H_2O)	$NaBH_4$	H_2 generation from hydrazine	71
		S-IMP, $Ni(NO_3)_2$ (H_2O)	$NaBH_4$	CO_2 adsorption	56
	MIL-125-NH_2	IW-IMP, ($NiCl_2$) (MeOH)	$NaBH_4$	Photocatalytic reduction of aromatic alcohols	72
	MIL-96, ZIF-8	S-IMP, $NiCl_2$ (H_2O)	$NaBH_4$	Catalytic hydrogen generation from hydrazine	73
	ZIF-8	S-IMP, $NiCl_2$ (MeOH)	$NaBH_4$	Dehydrogenation of AB	74
NiO	MIL-101(Cr)	ALD, $[Ni(\eta^5\text{-}C_5H_5)_2]$	O_2 (1.5torr), 150°C, 270s	CO oxidation	75
Ni/Pt	MIL-96	S-IMP, $NiCl_2/K_2PtCl_6$ (H_2O)	$NaBH_4$	Catalytic hydrogen generation from hydrazine	73
Ni/Rh	ZIF-8	S-IMP, $NiCl_2/RhCl_3$ (H_2O)	$NaBH_4$	Catalytic hydrogen generation from hydrazine	76
		S-IMP, $NiCl_2/RhCl_3$ (MeOH)	$NaBH_4$	Dehydrogenation of AB	74
	MIL-101(Cr)	S-IMP, $NiCl_2/RhCl_3$ (H_2O)	$NaBH_4$	H_2 generation from hydrazine	71
Pd	MIL-101(Cr)	DSA, $PdNO_3$/ H_2PdCl_2 (*n*-hexane/H_2O)	H_2/AB	Cascade reactions, hydrodeoxygenation of vanillin, dehydrogenation of AB	1, 52, 77, 78
		DSA, $PdCl_2$ (*n*-hexane/H_2O)	$NaBH_4$	Reduction of 4-nitrophenol	2
		S-IMP, $PdCl_2$	$NaBH_4$	Reduction of 4-nitrophenol	2
		S-IMP, $PdCl_4$ (MeOH)	$NaBH_4$	Dehydrogenation of formic acid	3
		S-IMP, H_2PdCl_4 (H_2O)	$NaBH_4$	Sonogashira Coupling Hydrogenation of phenol	79 80

NP	MOF[a]	Infiltration Method, precursor (solvent)[b]	Reduction/ Oxidation Conditions	Application[c]	Ref
				Degradation of AB	24
		S-IMP, $Pd(NO_3)_2$ (H_2O)	H_2, 200°C, 4h	Arylation of indoles	81
		S-IMP, $Pd(NO_3)_2$ (DMF)	H_2, 200°C, 2h	Suzuki–Miyaura cross-coupling and Ullmann homocoupling reactions	82
		IW-IMP, $Pd(acac)_2$ (acetone/DMF)	CO (40%)/ H_2 (10%)	CO oxidation	83
		IW-IMP, $Pd(acac)_2$ ($CHCl_3$)	H_2 (10 vol%), 200°C, 2h	Hydrogenation of 2,3,5-trimethylbenzoquinone	84
		IW-IMP, $Pd(NO_3)_2$ (DMF)	H_2, 200°C, 2h	Synthesis of methyl isobutyl ketone	85
		Sol-Gel $PdCl_2$/PVA/$NaBH_4$ (MeOH)	H_2, 200°C, 2h	VOC Adsorption H_2 storage	86
		CVD, $[(\eta^5\text{-}C_5H_5)Pd(\eta^3\text{-}C_3H_5)]$	H_2 (5-110 bar), 21-220°C	Reduction of propiophenone	87
			H_2 (50 bar), 70°C, 20h	Reduction of benzenophone	88
				Dehydrogenation of alcohols	89
	ED-MIL-101(Cr)	S-IMP, $PdCl_2$ (H_2O)	$NaBH_4$	Heck reaction	34
		S-IMP, H_2PdCl_4 (H_2O)	H_2 (50%), 200°C	Dehydrogenation of formic acid	35
	MIL-101(Cr)-NH_2	S-IMP, $PdCl_2$	$NaBH_4$	Suzuki-Miyaura cross coupling reaction	90-92
		S-IMP, $PdCl_2(MeCN)_2$ (CH_2Cl_2)	$NaBH_4$	C-H activation and halogenation reactions	93
		S-IMP, $Pd(OAc)_2$ (ethylene glycol)	Ethylene glycol	Oxidative amination of aldehydes	94
	MIL-101(Cr)-SO_3H	IW-IMP, $Pd(acac)_2$ ($CHCl_3$)	H_2 (10 vol%), 200°C, 2h	Hydrodeoxygenation of vanillin	95
	MIL-100(Fe)	S-IMP, H_2PdCl_4(H_2O)	EtOH	Degradation of pharmaceuticals and personal care products	36
		S-IMP, H_2PdCl_4(H_2O)	UV irradiation	Photocatalytic degradation of methyl orange and reduction of Cr(IV)	37
	MIL-100(Al)	S-IMP, H_2PdCl_4 (H_2O)	H_2, 280°C, 6 h	H_2 storage	96
	MIL-53(Al), MIL-53(Al)-NH_2	IW-IMP, $Pd(acac)_2$ ($CHCl_3$)	H_2, 150°C, 2h	Hydrogenation of diphenylacetylene	97
	MOF-5	CVD, $[(\eta^5\text{-}C_5H_5)Pd(\eta^3\text{-}C_3H_3)]$	H_2, 23°C, 30min	-----	31
			UV irradiation	-----	98
		S-IMP, $Pd(OAc)_2$ (DMF)		CO oxidation	99
		IW-IMP, $Pd(acac)_2$ ($CHCl_3$)	H_2, 150-200°C, 1h	Hydrogenation of styrene, 1-octene, and *cis*-cyclooctene	100
	MOF-5(BDC)(BDC-NH_2)	S-IMP, $Pd(OAc)_2$ (DMF)		CO oxidation	99
	MIL-125	S-IMP, H_2PdCl_2 (MeOH)	MOF Autoreduction	Photocatalytic oxidation of benzylalcohol	42
	MIL-125-NH_2	S-IMP, $PdCl_2$ (MeOH)	Hydrazine	Suzuki-Miyaura cross coupling reaction	101
	ZIF-8	S-IMP, $PdCl_4$ (MeOH)	$NaBH_4$	Dehydrogenation of formic acid	9
		S-IMP, $PdCl_2$ (H_2O)	H_2 (5%), 300°C, 2h	Hydrogenation of olefins	45
		S-IMP, $Pd(NO_3)_2$ (H_2O)	H_2, 200°C, 12h	Hydrogenation of cinnamaldehyde	102
		CVD, $Pd(C_3H_5)(C_5H_5)$	H_2 (10^5 Pa), 23°C, 1h	Suzuki cross-coupling reaction	103

NP	MOF[a]	Infiltration Method, precursor (solvent)[b]	Reduction/ Oxidation Conditions	Application[c]	Ref
		IW-IMP, H_2PdCl_2 (H_2O)	H_2 (20%), 200°C, 4h	MOF-derived porous carbon Catalytic biofuel upgrade	104
	ZIF-8-COOH	S-IMP, $PdCl_2$ (CH_3CN)	H_2, 150°C, 5h	Hydrogenation of diene	105
	MOF-177	CVD, $Pd(C_3H_5)(C_5H_5)$	UV irradiation, 3.5h	-----	58
	$[\{[Ni(cyclam)]_2(mtb)\}_n]\cdot 8nH_2O\cdot 4nDMF$	S-IMP, $Pd(NO_3)_2$ (CH_3CN)	MOF autoreduction	-----	106
	SNU-3	S-IMP, $Pd(NO_3)_2$ (CH_3CN)	MOF autoreduction	H_2 storage	107
	HKUST-1	S-IMP, $Pd(acac)_2$ (H_2O)	AB	Dehydrogenation of AB	108
	MIL-53(Al), MIL-53(Al)-NH_2	S-IMP, H_2PdCl_4 (H_2O)	$NaBH_4$	Suzuki-Miyaura cross coupling reaction	109
	MIL-88B(Fe)	S-IMP, H_2PdCl_4 (MeOH)	$NaBH_4$	Reduction of nitrophenol	110
	MIL-88B(Fe)-NH_2	S-IMP, Na_2PdCl_4 (MeOH)	$NaB(OAc)_3$	C-H activation and halogenation reactions	93
	MIL-88B(Cr)-NH_2	S-IMP, Na_2PdCl_2 (MeOH)	$NaBH_4$	Oxidation of secondary benzylic alcohols	111
	UiO-66	S-IMP, $Pd(OAc)_2$ (MeOH)	MeOH	Suzuki-Miyaura	112,
		S-IMP, H_2PdCl_4 (H_2O)	$NaBH_4$	cross coupling reaction	113
	UiO-66, UiO-67	CVD, $Pd(C_3H_5)(C_5H_5)$	UV irradiation,	Hydrogenation of ketones to alcohols	114
	UiO-66-NH_2	S-IMP, $PdCl_2$ (MeOH)	Na(OAc)	Suzuki-Miyaura cross coupling reaction	115
		S-IMP, $Pd(OAc)_2$ (methylene chloride)	H_2 (10%), 200°C, 2h	Tandem Oxidation-Acetalization Reaction of benzylalcohols	116
		Hydrothermal IMP, PVP/$PdCl_2$/NaI (H_2O), 180°C		Photcatalytic reduction of Cr(IV)	117
	UiO-67-BPyDC	S-IMP, $PdCl_2(CH_3CN)_2$ (DMF)	$NaBH_4$	Hydrogenation of nitrobenzene	70
	Cu-TDPAT	IW-IMP, $Pd(acac)_2$ (DEF)	H_2, 150-200°C, 1h	H_2 storage	118
	DUT-67(Zr)	S-IMP, $PdCl_2$ (DMF)	$NaBH_4$	Suzuki cross-coupling reaction Hydrogenation of nitrobenzene	119
	MOF-1, MOF-2(Zn), MOF-2(Cd), MOF-3	S-IMP, $PdCl_2$ (MeOH)	$NaBH_4$	Heck-coupling and hydrogenation reactions	120
Pd/Ag	MIL-101(Cr)	DSA, $PdNO_3/AgNO_3$ (*n*-hexane/H_2O) IW-IMP, $PdNO_3/AgNO_3$ (H_2O)	H_2 (20%), 200°C, 4h	Cascade reaction	1
Pd/Ni	UiO-67-BPyDC	S-IMP, $PdCl_2(CH_3CN)_2/Ni(NO_3)_2$ (DMF)	$NaBH_4$	Hydrogenation of nitrobenzene	70
Pd/TiO_2	MIL-101(Cr)	CVD, $[Ti(O^iP)_4]/[(\eta^5\text{-}C_5H_5)Pd(\eta^3\text{-}C_3H_5)]$	H_2O, 80°C/H_2 (50 bar), 70°C, 20h	Dehydrogenation of alcohols	89
Pd@Co	MIL-101(Cr)	DSA, $H_2PdCl_2/CoCl_2$ (*n*-hexane/H_2O)	AB	Dehydrogenation of AB	52
Pt	MIL-101(Cr)	IW-IMP, $Pt(acac)_2$ (acetone/DMF)	40% CO, 10% H_2, 50% He	Catalysis: CO oxidation	83
		S-IMP, H_2PtCl_6 (EtOH)	H_2 (2%), 100°C	Hydrogenation of 1-octene, 1-hexadecene, benzonitrile, and linoleic acid	121
		S-IMP, H_2PtCl_6 (EtOH)	Na(formate)	Hydrogenation of benzaldehyde and nitrobenzene	122

NP	MOF[a]	Infiltration Method, precursor (solvent)[b]	Reduction/ Oxidation Conditions	Application[c]	Ref
		S-IMP, H_2PtCl_6/PVA (H_2O)	$NaBH_4$	Hydrogenation of nitroarenes	123
	ED-MIL-101(Cr)	S-IMP, H_2PtCl_6 (H_2O)	$NaBH_4$	-----	34
			H_2 (50%), 200°C	Dehydrogenation of formic acid	35
	MIL-101(Al)-NH_2	S-IMP, H_2PtCl_6 (MeOH)	$NaBH_4$	Hydrogenation of cinnamaldehyde	124
	MIL-101(Cr)-NH_2	S-IMP, H_2PtCl_4 (H_2O)	H_2, 200°C, 2h	Photocatalytic H_2 generation from H_2O	125
	MIL-100(Fe)	S-IMP, H_2PtCl_6 (MeOH)	$NaBH_4$	Hydrogenation of cinnamaldehyde	124
		S-IMP, H_2PtCl_6(H_2O)	EtOH	Degradation of pharmaceuticals and personal care products	36
		S-IMP, H_2PtCl_6(H_2O)	UV irradiation	Photocatalytic degradation of methyl orange and reduction of Cr(IV)	37
	MIL-125	S-IMP, H_2PtCl_6 (MeOH)	MOF Autoreduction	Photocatalytic oxidation of benzylalcohol	42
	MIL-125-NH_2	S-IMP, H_2PtCl_6 (MeOH)	UV irradiation	Photocatalytic H_2 generation	126
		DSA, K_2PtCl_4 (*n*-hexane/H_2O)	UV irradiation	Photoelectrochemical H_2 generation	127
	UiO-66	S-IMP, H_2PtCl_6 (H_2O)	Ascorbic acid	Photocatalytic H_2 generation	128
		S-IMP, H_2PtCl_6 (MeOH)	UV irradiation	Photocatalytic H_2 generation	129
	UiO-66, UiO-66-NH_2	S-IMP K_2PtCl_4/H_2O	H_2 (10%), 200°C, 1h	Hydrogenation of cinnamaldehyde	130
	MOF-177	CVD, $[(CH_3)_3Pt(C_5(CH_3)_5]$	H_2 (100 bar), 100°C, 24h	H_2 storage Oxidation of alcohols	131
	MOF-5	IW-IMP, $[Pt(NH_3)_4]Cl_2$ (H_2O)		Oxidation of vanillyl and piperonyl alcohols	132
	IRMOF-8, Cu-TDPAT	IW-IMP, $Pt(acac)_2$ (DMF)	H_2, 300°C, 2h	H_2 adsorption	133
	MIL-96	S-IMP K_2PtCl_6/H_2O	$NaBH_4$	Catalytic hydrogen generation from hydrazine	73
Pt/Pd	MIL-101(Cr)	IW-IMP, $Pd(acac)_2$ (acetone/DMF)	CO (40%)/H_2 (10%)	CO oxidation	83
Pt@Pd	MIL-101(Cr)	IW-IMP, $Pt(acac)_2$ (acetone/DMF)	CO (40%)/H_2 (10%), CO (40%)/H_2 (10%)	CO oxidation	83
Rh	ZIF-8	S-IMP, $RhCl_3/H_2O$	$NaBH_4$	Hydrogen generation from hydrazine	76
		S-IMP, $NiCl_2/RhCl_3$ (MeOH)	$NaBH_4$	Dehydrogenation of AB	74
	MIL-101(Cr)	S-IMP, $RhCl_3$ (H_2O)	$NaBH_4$	H_2 generation from hydrazine	71
	S-MIL-101(Cr)	S-IMP, $RhCl_3$ (H_2O)	$NaBH_4$	Hydrogenation of phenol	134
Ru	MIL-101(Cr)	S-IMP, $RuCl_3$ (H_2O)	H_2 (50%), 200°C	Dehydrogenation of formic acid (inactive)	35
	MOF-5	CVD, [Ru(cod)-(cot)]	H_2	-----	98, 135
	MIL-96	S-IMP, $RuCl_3$ (H_2O)	$NaBH_4$	Dehydrogenation of AB	136
	La-BTC	Supercritical CO_2, $RuCl_3$ (MeOH/CO_2)		Hydrogenation of cyclohexene and benzene	137
	La-BTC	S-IMP, $RuCl_3$ (H_2O)	H_2, 220°C, 2h	Hydrogenation of cyclohexene and benzene	137
	UiO-66, UiO-67, Zr_6-NDC, MIL-140A, MIL-140B, MIL-140C	S-IMP, $RuCl_3$ (H_2O)	Hydrazine	Hydrogenation of furfural	138
Ru/Pd	MIL-101(Cr)	S-IMP, $H_2PdCl_4/RuCl_3$ (H_2O)	H_2 (50%), 200°C	Dehydrogenation of formic acid	35

NP	MOF[a]	Infiltration Method, precursor (solvent)[b]	Reduction/ Oxidation Conditions	Application[c]	Ref
Ru/Pt	MOF-5	CVD, [Ru(cod)(cot)]/ [Pt(cod)(CH_3)$_2$]	H_2 (1 bar), 25°C, 10min	-----	139
TiO_2	MOF-5	CVD, [Ti(O^iPr)$_4$]	O_2 (4.5 vol %), 220°C, 8h	-----	140
	MIL-101(Cr)	CVD, [Ti(O^iP)$_4$]	H_2O, 80°C/H_2 (50 bar), 70°C, 20h	Dehydrogenation of alcohols	89
ZnO	MOF-5	CVD, [Zn(C_2H_5)$_2$]	Exposed to ambient air	Methanol synthesis	55
	ZIF-8	CVD [Zn(C_2H_5)$_2$]	O_2 (5 vol%), 25-150°C, 6h	-----	141

[a]MOF systems: (Rb,Cs)-CD-MOF with CD = cyclodextrin; CPL-1 = [Cu_2(PZDC)$_2$(PYZ)]; CPL-2 = [Cu_2(PZDC)$_2$(BPy)]; DUT-67 = [$Zr_6O_6(OH)_2$(TDC)$_4$(CH_3COO)$_2$]; HKUST-1 = [Cu_3(BTC)$_2$]; IRMOF-3 = [Zn_4O(BDC-NH_2)$_3$]; IRMOF-8 = [Zn_4O(NDC)$_3$]; mesMOF-1 = [Tb_{16}(TATB)$_{16}$]; MIL-53(Al) = [Al(OH)(BDC)]; MIL-53(Al)-NH_2 = [Al(OH)(BDC-NH_2)]; MIL-68(In) = [In(OH)(BDC)]; MIL-88B(Fe) = [Fe_3O(BDC)$_3$L] with L = (Cl^{1-}, OH^{1-}); MIL-88B(Fe)-NH_2 = [Fe_3O(BDC-NH_2)$_3$L] with L = (Cl^{1-}, OH^{1-}); MIL-88B(Cr)-NH_2 = [Cr_3O(BDC-NH_2)$_3$X] with X = (Cl^-, OH^-); MIL-96 = [$Al_{12}O(OH)_{18}(H_2O)_3$($Al_2$($OH$)$_4$)(BTC)$_6$]; MIL-100(Al) = [$Al_3L_3(BTC)_3$] with L = ($H_2O$, O^{2-}, F^-); MIL-101(Cr) = [Cr_3L_3(BDC)$_3$] with L = (H_2O, O^{2-}, F^-); MIL-101(Cr)-NH_2 = [Cr_3L_3(BDC-NH_2)$_3$] with L = (H_2O, O^{2-}, F^-); ED-MIL-101(Cr) = [Cr_3L_3(BDC)$_3$] with L = (H_2O, O^{2-}, F^-) and ED = ethylenediamine; MIL-125 = [TiO_8(OH)$_4$(BDC)$_6$]; MIL-125-NH_2 = [TiO_8(OH)$_4$(BDC-NH_2)$_6$]; MIL-140A = [ZrO(BDC)]; MIL-140B = [ZrO(NDC)]; MIL-140C = [ZrO(BPDC)]; MOF-1 = [Zn(PIP)(BPy)]; MOF-2(Zn) = [Zn(PIP)(BPE)]; MOF-2(Cd) = [Cd(PIP)(BPE)]; MOF-2 = [Zn(PIP)(BPE)]; MOF-3 = [Zn(PIP)(BPB)]; MOF-5 = [Zn_4O(BDC)$_3$]; MOF-74(Ni) = [Ni_2(DOBDC)]; MOF-177 = [Zn_4O(BTB)$_3$]; MOF-508 = [Zn_2(BDC)$_2$(BPy)]; SNU-3 = [Zn_3(NTB)$_2$]; UiO-66 = [Zr_6O_4(OH)$_4$(BDC)$_6$]; UiO-66-NH_2 = [Zr_6O_4(OH)$_4$(BDC-NH_2)$_6$]; UiO-67-BPyDC = [Zr_6O_4(OH)$_4$(BPyDC)$_6$]; ZIF-8 = [Zn(MeIM)$_2$]; ZIF-8-COOH = [Zn(MeIMDC)$_2$]; ZIF-90 = [Zn(ICA)$_2$]; Zr_6(NDC) = [Zr_6O_4(OH)$_4$(NDC)$_6$]; Linkers: BDC = 1,4-benzenedicarboxylic acid; BDC-NH_2 = 2-amino-1,4-benzenedicarboxylic acid; BPy = 4,4′-bipyridine; BPyDC = 2,2′-bipyridine-5,5′-dicarboxylate; BPB = 1,4-bis(pyridine-4-yl)benzene; BPDC = 4,4’-biphenyldicaboxylate; BPE = 1,2-bis(pyridine-4-yl)ethane; BPTC = 1,1’-biphenyl-2,2’,6,6’-tetracarboxylic acid; BTB = 1,3,5-benzenetribenzoic acid; BTC = 1,3,5-benzenetricarboxylic acid; cyclam = 1,4,8,11-tetraazacyclotetradecane; DOBDC = 2,5-hydroxy-1,4-benzenedicarboxylic acid; Himdc = 4,5-imidazoledicarboxylic acid; ICA = imidazolate-2-carboxyaldehyde; MeIM = 2-methylimidazole; MeIMDC = 2-methyl-1H-imidazole-4,5-dicarboxylic acid; MTB = methanetetrabenzoate; NDC = naphthalene-2,6-dicarboxylate; NTB = 4,4’,4”-nitrilotrisbenzoate; PIP = 5-(prop-2-yn-1-yloxy) isopthalic acid; PYZ = pyrazine; PZDC = pyrazine-2,3-dicarboxylate; TATB = triazine-1,3,5-tribenzoic acid; TDC = 2,5-thiophenedicarboxylic acid; TDPAT = 2,4,6-tris(3,5-dicarboxylphenylamino)-1,3,5-triazine;
[b]Preparation methods: S-IMP = solution impregnation; DSA = double solvents approach; IW-IMP = incipient wetness impregnation; CVD = chemical vapour deposition; ALD = atomic layer deposition; SG = solid grinding; Precursors: acac = bis(acetylacetonato; cod = 1,5-cyclooctadiene; cot = 1,3,5-cycloocatriene; PDA = polydopamine; PVA = poly(vinyl alcohol); PVP = poly(vinylpyrrolidinone)
[c]SCR = selective catalytic reduction; VOC = volatile organic compound; RhB = rhodamine blue; MB = methylene blue; AB = ammonia borane

D.2 Encapsulation

Table D.2: Overview of NP@MOF composites prepared using encapsulation

Metal	MOF[a]	MOF Synthesis (Conditions)[b]	Nanomaterial Type (size)[c]	Nanomaterial capping ligand	Application[d]	Ref
Ag	ZIF-8	RT	NP	MPA	Reduction of 1-nitrophenol	142
		MW (200°C, 1.5h)	NP (≈20nm)	PVP	Reduction of 1-nitrophenol	143
		RT (24h)	NC	PVP	-----	144, 145
		RT (12h)	NW (90-120nm)	PVP	Solar-driven butanol separation	146
	ZIF-90	RT (10min)	NP (3nm)	ICA	Sensing	147
Ag/Pd	MIL-101(Fe)	ST (140°C, 12h)	NP (40nm)	PVP	Dehydrogenation of formic acid	148
Au	ZIF-8	RT	NP (1-3nm)	MPA, DDT/MUA	Reduction of 1-nitrophenol	142
		RT	NP (3, 13nm)	PVP	-----	144, 145, 149, 150
		RT (24h)	NP (15, 25, 30nm)	PVP	Synthesis of Au@NPC	151
		RT (24h)	NP (13nm)	PVP	Reduction of nitroarenes	152
		RT (24h)	NP (2nm, 6nm)	PVP	Selective hydrogenation	153
		RT (12h)	NP (50nm), Nanostar (80nm)	PDA	-----	154
		ST (50°C, 2h)	NP (15, 50nm), NR	PVP	Photocatalytic oxidation of benzyl alcohol	120
		RT	NR	PVP	-----	150, 155
		RT (24h)	NW	PVP	-----	145
	ZIF-67	RT (24h)	NP (13nm)	PVP	-----	145
	$[Al(OH)(ndc)]_n$	MW (180°C, 60s)	NR (aspect ratio≈4)	PEG-SH	Light-induced molecular release	156
	MIL-100(Fe)	ST (70°C, 30min cycles)	NP (60nm)	MAA	Reduction of 4-nitrophenol	157
		US (RT, 10min)	NP (50nm)	PVP	SERS	158
	MIL-101(Cr)	ST (220°C, 8h/150°C, 12h)	NP (2.4, 6.4nm)	PVP, glucose	Aerobic oxidation of alcohols	159
	$MIL-125-NH_2$	ST (150°C, 15 h)	NP (2.1nm)	PVP	Synthesis of Au/TiO_2	160
	HKUST-1	ST (80°C, overnight)	NP (13 nm)	Citrate	-----	161, 162
		ST (70°C, 24h)	NP (9.5nm)	MUA	-----	126
	UiO-66	ST (100°C, 12h)	NP (50nm), Nanostar (80nm)	PDA	-----	154
	$UiO-66-NH_2$	ST (120°C, 24h)	NP (15nm)	PVP	Photocatalysis	163
	MOF-5	ST (140°C, 3h)	NP (30-54nm)	PVP	SERS	164
		RT	NR	MUA	SERS	165
	IRMOF-9	ST (80°C, 12h)	NR	MUA	SERS	166
	Eu-BTB	ST (25°C, 2h)	NP (5nm)	None	Detection of TNT	167
	Zn/Fe-BDC	ST (100°C, 6h)	NC (50-100nm)	PVP	-----	168
$Au-Fe_3O_4$	MIL-100(Fe)	ST (70°C, 30min cycles)	NP (Au: 3-5nm)	MAA	Reduction of 4-nitrophenol	169
Co_3O_4	MOF-5	ST (100°C, 6h)	NP (60nm)	PVP	Degradation of 4-chlorophenol	170
CdSe	ZIF-8	RT	NP (4nm)	PVP	-----	144, 149
	Eu-BTB	ST (25°C, 2h)	NP		Detection of TNT	171

Metal	MOF[a]	MOF Synthesis (Conditions)[b]	Nanomaterial Type (size)[c]	Nanomaterial capping ligand	Application[d]	Ref
CdSe-CdS-ZnS/ $Zn_3(PO_4)_2 \cdot 4H_2O$ (α-Hopeite, Desert Rose Microparticles)	MOF-5	ST (95°C, 3h)	NP (4.58nm)/ MS	None	-----	172
CdTe	ZIF-8	RT (24h)	NP (2.8nm) organized as nanochains	PVP	-----	144
CeO_2	ZIF-67	RT (1h)	NW	None	-----	173
B-FeOOH	ZIF-8	RT (24h)	NR (22 x 160nm)	PVP	-----	144
Fe_3O_4	ZIF-8	RT	NP (8nm)	PVP	-----	144, 149
		US (RT, 5min)	NP (≈160nm)	None	Mass spectroscopy	174
		RT (10min)	NP (10nm)	Citrate	Knoevenagel condensation	136
		ST (50°C, 3h)	NP (600nm)	Citrate	Knoevenagel condensation	175, 176
		ST (70°C, 20min)	NP (380nm)	None	Adsorption of MB	177
		RT (cycles)	NP	None	Arsenic adsorption	178
		RT (12h)	NP	PDA	-----	154
	MIL-53(Al)	ST (140°C, 72h)	NP	None	Removal of lead	179
	MIL-100(Fe)	ST (70°C, 30min cycles)	NP	MAA	Chromatographyand extraction	180-182
		ST (70°C, 30min cycles)	NP (250nm)	MAA	Reduction of *p*-nitrophenol	183
					Degradation of methyl blue	184
		ST (130°C, 3days)	NP	MAA	Removal of methyl red from H_2O	185
		ST (70°C, 30min cycles)	NP (5-8nm)	COOH	-----	186
	MIL-101(Fe)	ST (110°C, 24h)	NP	PAA	Oxidation of alcohols	187
	MIL-101(Cr)	ST (218°C, 18h)	NP (200nm)	Citrate	-----	188
		ST (218°C, 18h)	NP (25nm)	None	Removal of textile dyes	189
		ST (218°C, 18h)	NP	-COOH, $-NH_2$, C	Estrogen adsorption	190
	HKUST-1	Refluxed (12h)	NP	None	-----	191
		ST (70°C, 30min)	NP (200nm)	PDA	Enzyme digestion	192
		ST (70°C, 4h)	NR	None	Drug delivery	193
		ST (70°C, 1 h cycles)	NP	MAA	Knoevenagel condensation	194
	IRMOF-3	ST (100°C, 4h)	NP	None	Drug delivery	195
	UiO-66	ST (100°C, 12h)	NP	PDA	-----	154
	HKUST-1, Cr-BTC	RT (30min cycles)	NP	-COOH	-----	196
	DUT-4, DUT-5	ST (110°C, 24h), ST (180°C, 24h)	NP	None	-----	191
α-Fe_3O_4	ZIF-8	RT	NC, Nano-peanut	PVP	-----	155
Fe_3O_4/Graphite oxide	UiO-66	ST (85°C, 24h)		Polydopamine	-----	197
Fe_3O_4@SiO_2	ZIF-8	RT	NP (300-350nm)	None	-----	198
		RT	NP (160-165 nm)	None	Knoevenagel condensation	199
	HKUST-1	US (RT, 120min)	NP (160-170nm)	TA	Pechman reaction	200
	MIL-53(Al)	ST (220°C, 72h)	NP	None	Friedel-Crafts acylation	201
	MIL-101(V)	ST (90°C, 24h)	NP	APTMS	Oxidation of norborene	202
	UiO-66	ST (120°C, 24h)	MS (≈150nm)	-COOH	Chromatography	203
	$^2{}_\infty[Ln_2Cl_6(BPy)_3] \cdot 3BPy$, $[LnCl_3(Py)_4] \cdot 0.5Py$ (Ln = Eu, Tb)	MC, ST (90°C, 36h)	MS (20μm)	None	Sensing	204

Metal	MOF[a]	MOF Synthesis (Conditions)[b]	Nanomaterial Type (size)[c]	Nanomaterial capping ligand	Application[d]	Ref
Graphite Oxide	MIL-101(Cr)	ST	Powder	None	*n*-alkane adsorption, H_2O adsorption, CO_2/CH_4 separation, acetone adsorption	205-209
					Lithium ion battery	210
	HKUST-1	US, ST	Powder	None	NH_3, NO_2, H_2S, CO_2 adsorption, H_2 storage, and NH_3 sensing	211-219
		ST (60°C, 1h)		None	CO_2 capture	220
	ZIF-8	RT (24h)	Powder	None	-----	221
		RT		None	Electrochemical properties	222, 223
					H_2 storage	224
		RT (24h)	Powder	None	Biosensor	225
	MOF-5	ST	Powder	None	NH_3, NO_2, H_2S, CO_2 adsorption	214, 226-228
	MIL-100(Fe)	ST	Powder	None	NH_3, NO_2, H_2S, CO_2 adsorption	214, 229
	MOF-253	US, ST	Powder	None	Oxidation of ethylbenzene	230
	MIL-53(Fe)	ST (150°C, 3days)	Powder	None	Photodegradation of methyl blue	231
	MIL-125-NH_2	ST(120°C, 48h)	Powder	None	Photodegradation of methyl blue	232
	UiO-66	ST (120°C, 24h)	Powder	None	CO_2 capture	233
$Li(Li_{0.17}Ni_{0.20}Co_{0.05}Mn_{0.58})O_2$	MOF-74(Mn)	ST (80°C, 2h)	Powder (100-200nm)	None	Lithium-ion batteries	234
$NaYF_4$	ZIF-8	RT (24h)	NP (24nm), NR (50 x 310nm)	PVP	-----	144
β-$NaYF_4$:Yb^{3+}/Er^{3+} (UCNP)	MIL-100(Fe)	RT (40min)	NP (30nm)	PVP	Targeted drug delivery and cell imaging	235
	MIL-101(Fe)-NH_2	ST (40°C, 2.5h)	NP(41nm)	PVP	Luminescent/magnetic targeted imaging	236
	HKUST-1	ST (75°C, 4h)	NP	PAA	Sensing	237
N-$K_2Ti_4O_9$	UiO-66	ST (120°C, 24h)	NF (100-350nm)	None	Photocatalytic degradation of RhB	238
Pd	UiO-66	ST (120°C, 24h)	NP (3.9nm)	PVP	-----	145
	ZIF-8	Emulsion (RT, 24h)	NC (20nm)	PVP	Hydrogenation of olefins	239
		RT (24h)	NP	PVP	Reduction of *p*-nitrophenol	240
		RT	NC (17 nm, 7 nm)	PVP	Hydrogenation of olefins	241
	ZIF-L	RT (48 h)	NP (3nm)	PVP	Hydrogenation of alkenes	242
					Reduction of p-nitrophenol and p-aminophenol	243
	IRMOF-3	ST (100°C, 240min)	NP (35nm)	PVP	Cascade reactions	244
Pd/Cu_2O	ZIF-8	RT (24h)	NP (Pd: 20nm, 60nm)	PVP, CTAB	Hydrogenation of ethylene, cyclohexene, and cyclooctene	245
Pd/SiO_2	ZIF-8	RT (2h)	NP (Pd: 4-5nm)	PVP	Hydrogenation of alkenes	246
Pd@SiO_2	ZIF-8, ZIF-67	RT	NP	PVP	Hydrogenation of alkenes	247
Pd/ZnO	ZIF-8	ST (50°C, 2h)	NP (Pd: 5nm)	PVP	Hydrogenation of alkenes	248
Pd@ZnO	ZIF-8	RT (1h)	NC (Pd: 26nm)	None	Hydrogenation of alkenes	249

Metal	MOF[a]	MOF Synthesis (Conditions)[b]	Nanomaterial Type (size)[c]	Nanomaterial capping ligand	Application[d]	Ref
Pd/ $Zn_3(PO_4)_2 \cdot 4H_2O$ (α-Hopeite, Desert Rose Microparticles)	MOF-5	ST (95°C, 3h)	NP (85nm)/MS	None	-----	172
PS	ZIF-8	RT (24h)	NP (180nm)	PVP	-----	144
Pt	ZIF-8	RT (24h)	NP (2 .5, 3.3, 4.1nm)	PVP	CO oxidation	144
			NP (2-3 nm)	PVP, naked	Hydrogenation of alkenes and alkynes	145, 250, 251
			NP (2.9nm)	PVP	-----	149
	ZIF-8, SALEM-2	RT(24h), ST(100°C, 4 days)	NP(3 nm)	PVP	Hydrogenation of alkenes	252
	UiO-66	ST (120°C, 48h)	NP (2-3nm)	PVP	Electrocatalytic oxidation of H_2O_2	253
	UiO-66, UiO-66-SO_3H, UiO-66-NH_3^+, UiO-66-SO_3H/NH_3^+	ST (120°C, 24h)	NP (2.5nm)	PVP	Hydrogenative conversion of methylcyclopentane	254, 255
	UiO-66, UiO-67	ST	NP (2-3nm)	PVP	Hydrogenation of olefins, reduction of 4-nitrophenol, CO oxidation	256
	UiO-66-NH_2, MIL-53(Fe)-NH_2	ST	NP (2.9nm)	PVP	-----	256
	MOF-801	ST (120°C, 24h)	NP (2.5nm)	PVP	Hydrogenative conversion of methylcyclopentane	254
Pt/Au	HKUST-1	ST (80°C, overnight)	NP (≈50nm)	Citrate	Hydrogenation of olefins	161
Pt/Graphite oxide	MIL-101(Cr), HKUST-1	ST (220°C, 8h), ST (100°C, 4h)	NP (Pt: 3.5nm)	None	H_2 storage	257, 258
Pt/MIL-100(Fe)	MIL-100(Fe)	ST (70°C, 30min)	NP (Pt: 3nm)	None	Hydrogenation of cinnamaldehyde	124
Pt/MIL-101(Al)-NH_2	MIL-101(Al)-NH_2	ST (70°C, 30min)	NP (Pt: 3nm)	None	Hydrogenation of cinnamaldehyde	124
Pt@SiO_2	ZIF-8, ZIF-67	RT	NP	PVP	Hydrogenation of alkenes	247
Pt/ $Zn_3(PO_4)_2 \cdot 4H_2O$ (α-Hopeite, Desert Rose Microparticles)	MOF-5	ST (95°C, 3h)	NP (145nm)/MS	None	-----	172
S/Graphite oxide	MIL-101(Cr)	ST (95°C, 12h)		None	Lithium sulfur batteries	259
Si	HKUST-1	RT (20s cycles)	NW	-COOH	-----	260
SiO_2	MOF-5	ST (95°C, 2h)	NP (197, 153, 197nm)	-NH_2, -COOH, -OH	-----	261
	ZIF-8	ST (70°C, 15min)	MS (3μm)	-COOH	HPLC	262
		ST (150°C, 2h)	NP (460nm)	-COOH	Cu^{2+} sensing	263
		MC (30min)	NP	None	Lithium-ion batteries	264
		RT	NP, NR (aspect ratio ≈ 2.5-3)	PVP	-----	155
		RT (12h)	NP	PDA	-----	154
	HKUST-1	RT (30min cycles)	MS	-COOH	Fluorine ion storage and separation	196
		RT (5min cycles)	MS	-COOH	HPLC	265
	Cr-BTC	RT (30min cycles)	MS	-COOH	-----	196
	UiO-66	ST (120°C, 24h)	MS	None, -NH_2	HPLC	266, 267
SiO_2@Fe_3O_4	MOF-5	RT (180min)	NP	None	Friedel-Crafts alkylation	199

Metal	MOF[a]	MOF Synthesis (Conditions)[b]	Nanomaterial Type (size)[c]	Nanomaterial capping ligand	Application[d]	Ref
TiO_2	MOF-74(Mg)	ST (110°C 72h)	NP	None	Photocatalytic reduction of CO_2	[268]
	ZIF-8	RT (24 h)	NP	None	Photocatalytic reduction of CO_2	[268]
Zn_2GeO_4	ZIF-8	RT (2h)	NR(20-30nm x 200-300nm)	None	Photocatalytic reduction of CO_2	[269]
ZnO	Cu-TCPP	ST (80°C, 24h)	NR(100-200nm)	None	Light induced photocurrent	[270]
	ZIF-8	ST (70°C, 5h)	NR(1.5μm)	None	H_2O_2 sensing	[271]
		ST (70°C, 5h)	NP(300nm)	None	Photocatalytic degradation of methyl blue	[272]
$Zn_3(PO_4)_2{\cdot}4H_2O$ (α-Hopeite, Desert Rose Microparticles)	MOF-5	ST (95°C, 3h)	MS	None	-----	[172]

[a]MOF systems: DUT-4 = [Al(OH)(ndc)]; DUT-5 = [Al(OH)(BPDC)]; HKUST-1 = [$Cu_3(BTC)_2$]; IRMOF-3 = [$Zn_4O(BDC\text{-}NH_2)_3$]; IRMOF-9 = [$Zn_4O(BPDC)_3$]; MIL-53(Fe) = [Fe(OH)(BDC)]; MIL-53(Fe)-NH_2 = [Fe(OH)(BDC-NH_2)]; MIL-100(Fe) = [$Fe_3L_3(BTC)_3$] with L = (H_2O, O^{2-}, F^-); MIL-101(Cr) = [$Cr_3L_3(BDC)_3$] with L = (H_2O, O^{2-}, F^-); MIL-101(Fe) = [$Fe_3L_3(BDC)_3$] with L = (H_2O, O^{2-}, F^-); MIL-101(V) = [$V_3L_3(BDC)_3$] with L = (H_2O, O^{2-}, F^-); MOF-5 = [$Zn_4O(BDC)_3$]; MOF-74(Mg) = [Mg(DOBDC)]; MOF-74(Mn) = [Mn(DOBDC)]; MOF-253 = [Al(OH)(BPyDC)]; MOF-801 = [[$Zr_6O_4(OH)_4(fum)_6$]; SALEM-2 = [$Zn(IM)_2$]; UiO-66 = [$Zr_6O_4(OH)_4(BDC)_6$]; UiO-66-NH_2 = [$Zr_6O_4(OH)_4(BDC\text{-}NH_2)_6$]; UiO-67 = [$Zr_6O_4(OH)_4(BPDC)_6$]; ZIF-8 = [$Zn(MeIM)_2$]; ZIF-67 = [$Co(MeIM)_2$]; ZIF-90 = [$Zn(ICA)_2$]; ZIF-L = [$Zn(MeIM)_2$]; Linkers: BDC = 1,4-benzenedicarboxylic acid; BDC-NH_2 = 2-amino-1,4-benzenedicarboxylic acid; BPy = 4,4′-bipyridine; BPDC = 4,4'-biphenyldicaboxylate; BPyDC = 2,2′-bipyridine-5,5′-dicarboxylic acid; BTB = 1,3,5-tris(4-carboxyphenyl) benzene; BTC = 1,3,5-benzenetricarboxylic acid; DOBDC = 2,5-dihydroxytherephalic acid; fum = fumerate; ICA = imidazole-2-carboxaldehyde; IM = imidazole; MeIM = 2-methylimidazole; ndc = 1,4-naphthalene dicarboxylate; Py = pyridine; TCPP = tetrakis(4-carboxyphenyl)porphyrin

[b]Synthesis techniques: MC = mechanochemical; MW = microwave; RT = room temperature; ST = solvothermal; US = ultrasonic

[c]Nanomaterial type: NC = nanocube; NP = nanoparticle; NR = nanorod; NW = nanowire; MS = microspheres; Capping ligands: APTMS = 3-aminopropyltrimethoxysilane; CTAB = hexadecyltrimethylammonium bromide; DDT = 1-dodecanethiol; MAA = mercaptoacetic acid; MPA = 3-mercaptopropionic acid; MUA = 11-mercaptoundecanoic acid; PAA = polyacrylic acid; PEG-SH = thiolated polyethylene glycol; PVP = poly(vinylpyrrolidinone); TA = thioglycolic acid

[d]HPLC= High Performance Liquid Chromatography; MB = methylene blue; NPC = N-doped porous carbon; RhB = rhodamine blue; SERS = surface enhanced raman spectroscopy; TNT = trinitrotoluene

D.3 References

1. Chen, Y.-Z.; Zhou, Y.-X.; Wang, H.; Lu, J.; Uchida, T.; Xu, Q.; Yu, S.-H.; Jiang, H.-L., Multifunctional PdAg@MIL-101 for One-Pot Cascade Reactions: Combination of Host-Guest Cooperation and Bimetallic Synergy in Catalysis. *Acs Catalysis* **2015,** *5* (4), 2062-2069.

2. Liu, Y.; Jia, S.-Y.; Wu, S.-H.; Li, P.-L.; Liu, C.-J.; Xu, Y.-M.; Qin, F.-X., Synthesis of highly dispersed metallic nanopartides inside the pores of MIL-101(Cr) via the new double solvent method. *Catalysis Communications* **2015,** *70*, 44-48.

3. Dai, H.; Cao, N.; Yang, L.; Su, J.; Luo, W.; Cheng, G., AgPd nanoparticles supported on MIL-101 as high performance catalysts for catalytic dehydrogenation of formic acid. *Journal of Materials Chemistry A* **2014,** *2* (29), 11060-11064.

4. Liu, X.-H.; Ma, J.-G.; Niu, Z.; Yang, G.-M.; Cheng, P., An Efficient Nanoscale Heterogeneous Catalyst for the Capture and Conversion of Carbon Dioxide at

Ambient Pressure. *Angewandte Chemie-International Edition* **2015,** *54* (3), 988-991.

5. Qian, X.; Zhong, Z.; Yadian, B.; Wu, J.; Zhou, K.; Teo, J. S.-k.; Chen, L.; Long, Y.; Huang, Y., Loading MIL-53(Al) with Ag nanoparticles: Synthesis, structural stability and catalytic properties. *International Journal of Hydrogen Energy* **2014,** *39* (26), 14496-14502.

6. Cheng, X.; Liu, M.; Zhang, A.; Hu, S.; Song, C.; Zhang, G.; Guo, X., Size-controlled silver nanoparticles stabilized on thiol-functionalized MIL-53(Al) frameworks. *Nanoscale* **2015,** *7* (21), 9738-9745.

7. Guo, H.; Guo, D.; Zheng, Z.; Weng, W.; Chen, J., Visible-light photocatalytic activity of Ag@MIL-125(Ti) microspheres. *Applied Organometallic Chemistry* **2015,** *29* (9), 618-623.

8. Abdelhameed, R. M.; Simoes, M. M. Q.; Silva, A. M. S.; Rocha, J., Enhanced Photocatalytic Activity of MIL-125 by Post-Synthetic Modification with Cr-III and Ag Nanoparticles. *Chemistry-a European Journal* **2015,** *21* (31), 11072-11081.

9. Dai, H.; Xia, B.; Wen, L.; Du, C.; Su, J.; Luo, W.; Cheng, G., Synergistic catalysis of AgPd@ZIF-8 on dehydrogenation of formic acid. *Applied Catalysis B-Environmental* **2015,** *165*, 57-62.

10. Jiang, H.-L.; Akita, T.; Ishida, T.; Haruta, M.; Xu, Q., Synergistic Catalysis of Au@Ag Core-Shell Nanoparticles Stabilized on Metal-Organic Framework. *Journal of the American Chemical Society* **2011,** *133* (5), 1304-1306.

11. He, L.; Dumee, L. F.; Liu, D.; Velleman, L.; She, F.; Banos, C.; Davies, J. B.; Kong, L., Silver nanoparticles prepared by gamma irradiation across metal-organic framework templates. *RSC Advances* **2015,** *5* (14), 10707-10715.

12. Houk, R. J. T.; Jacobs, B. W.; El Gabaly, F.; Chang, N. N.; Talin, A. A.; Graham, D. D.; House, S. D.; Robertson, I. M.; Allendorf, M. D., Silver Cluster Formation, Dynamics, and Chemistry in Metal-Organic Frameworks. *Nano Letters* **2009,** *9* (10), 3413-3418.

13. Liu, J.; Strachan, D. M.; Thallapally, P. K., Enhanced noble gas adsorption in Ag@MOF-74Ni. *Chemical Communications* **2014,** *50* (4), 466-468.

14. Moon, H. R.; Kim, J. H.; Suh, M. P., Redox-active porous metal-organic framework producing silver nanoparticles from Ag^{I} ions at room temperature. *Angewandte Chemie-International Edition* **2005,** *44* (8), 1261-1265.

15. Suh, M. P.; Moon, H. R.; Lee, E. Y.; Jang, S. Y., A redox-active two-dimensional coordination polymer: Preparation of silver and gold nanoparticles and crystal dynamics on guest removal. *Journal of the American Chemical Society* **2006,** *128* (14), 4710-4718.

16. Wei, Y.; Han, S.; Walker, D. A.; Fuller, P. E.; Grzybowski, B. A., Nanoparticle Core/Shell Architectures within MOF Crystals Synthesized by Reaction Diffusion. *Angewandte Chemie-International Edition* **2012,** *51* (30), 7435-7439.

17. Gao, S.; Feng, T.; Feng, C.; Shang, N.; Wang, C., Novel visible-light-responsive Ag/AgCl@MIL-101 hybrid materials with synergistic photocatalytic activity. *Journal of Colloid and Interface Science* **2016,** *466*, 284-290.

18. Sha, Z.; Sun, J.; Chan, H. S. O.; Jaenicke, S.; Wu, J., Enhanced Photocatalytic Activity of the AgI/UiO-66(Zr) Composite for RhodamineB Degradation under Visible-Light Irradiation. *Chempluschem* **2015,** *80* (8), 1321-1328.

19. Sha, Z.; Chan, H. S. O.; Wu, J., Ag_2CO_3/UiO-66(Zr) composite with enhanced visible-light promoted photocatalytic activity for dye degradation. *Journal of Hazardous Materials* **2015,** *299*, 132-140.

20. Mohaghegh, N.; Kamrani, S.; Tasviri, M.; Elahifard, M.; Gholami, M., Nanoporous Ag_2O photocatalysts based on copper terephthalate metal-organic frameworks. *Journal of Materials Science* **2015,** *50* (13), 4536-4546.

21. Wang, H.; Yuan, X.; Wu, Y.; Chen, X.; Leng, L.; Zeng, G., Photodeposition of metal sulfides on titanium metal-organic frameworks for excellent visible-light-driven photocatalytic Cr(VI) reduction. *RSC Advances* **2015,** *5* (41), 32531-32535.

22. Shang, N. Z.; Feng, C.; Gao, S. T.; Wang, C., Ag/Pd nanoparticles supported on amine-functionalized metal-organic framework for catalytic hydrolysis of ammonia borane. *International Journal of Hydrogen Energy* **2016,** *41* (2), 944-950.

23. Gao, S. T.; Liu, W. H.; Feng, C.; Shang, N. Z.; Wang, C., A Ag-Pd alloy supported on an amine-functionalized UiO-66 as an efficient synergetic catalyst for the dehydrogenation of formic acid at room temperature. *Catalysis Science & Technology* **2016,** *6* (3), 869-874.

24. Dai, H. M.; Su, J.; Hu, K.; Luo, W.; Cheng, G. Z., Pd nanoparticles supported on MIL-101 as high-performance catalysts for catalytic hydrolysis of ammonia borane. *International Journal of Hydrogen Energy* **2014,** *39* (10), 4947-4953.

25. Esken, D.; Turner, S.; Lebedev, O. I.; Van Tendeloo, G.; Fischer, R. A., Au@ZIFs: Stabilization and Encapsulation of Cavity-Size Matching Gold

Clusters inside Functionalized Zeolite Imidazolate Frameworks, ZIFs. *Chemistry of Materials* **2010,** *22* (23), 6393-6401.

26. Jiang, H. L.; Liu, B.; Akita, T.; Haruta, M.; Sakurai, H.; Xu, Q., Au@ZIF-8: CO Oxidation over Gold Nanoparticles Deposited to Metal-Organic Framework. *Journal of the American Chemical Society* **2009,** *131* (32), 11302-+.

27. Gole, B.; Sanyal, U.; Mukherjee, P. S., A smart approach to achieve an exceptionally high loading of metal nanoparticles supported by functionalized extended frameworks for efficient catalysis. *Chemical Communications* **2015,** *51* (23), 4872-4875.

28. Ishida, T.; Nagaoka, M.; Akita, T.; Haruta, M., Deposition of Gold Clusters on Porous Coordination Polymers by Solid Grinding and Their Catalytic Activity in Aerobic Oxidation of Alcohols. *Chemistry-a European Journal* **2008,** *14* (28), 8456-8460.

29. Ishida, T.; Kawakita, N.; Akita, T.; Haruta, M., One-pot N-alkylation of primary amines to secondary amines by gold clusters supported on porous coordination polymers. *Gold Bulletin* **2009,** *42* (4), 267-274.

30. Muller, M.; Turner, S.; Lebedev, O. I.; Wang, Y. M.; van Tendeloo, G.; Fischer, R. A., Au@MOF-5 and Au/MO_x@MOF-5 (M = Zn, Ti; x=1, 2): Preparation and Microstructural Characterisation. *European Journal of Inorganic Chemistry* **2011,** (12), 1876-1887.

31. Hermes, S.; Schroter, M. K.; Schmid, R.; Khodeir, L.; Muhler, M.; Tissler, A.; Fischer, R. W.; Fischer, R. A., Metal@MOF: Loading of highly porous coordination polymers host lattices by metal organic chemical vapor deposition. *Angewandte Chemie-International Edition* **2005,** *44* (38), 6237-6241.

32. Hu, Y. L.; Liao, J.; Wang, D. M.; Li, G. K., Fabrication of Gold Nanoparticle-Embedded Metal-Organic Framework for Highly Sensitive Surface-Enhanced Raman Scattering Detection. *Analytical Chemistry* **2014,** *86* (8), 3955-3963.

33. Wang, Y.; Zhang, Y.; Jiang, Z.; Jiang, G.; Zhao, Z.; Wu, Q.; Liu, Y.; Xu, Q.; Duan, A.; Xu, C., Controlled fabrication and enhanced visible-light photocatalytic hydrogen production of Au@CdS/MIL-101 heterostructure. *Applied Catalysis B-Environmental* **2016,** *185*, 307-314.

34. Hwang, Y. K.; Hong, D. Y.; Chang, J. S.; Jhung, S. H.; Seo, Y. K.; Kim, J.; Vimont, A.; Daturi, M.; Serre, C.; Ferey, G., Amine grafting on coordinatively unsaturated metal centers of MOFs: Consequences for catalysis and metal encapsulation. *Angewandte Chemie-International Edition* **2008,** *47* (22), 4144-4148.

35. Gu, X. J.; Lu, Z. H.; Jiang, H. L.; Akita, T.; Xu, Q., Synergistic Catalysis of Metal-Organic Framework-Immobilized Au-Pd Nanoparticles in Dehydrogenation of Formic Acid for Chemical Hydrogen Storage. *Journal of the American Chemical Society* **2011,** *133* (31), 11822-11825.

36. Liang, R.; Luo, S.; Jing, F.; Shen, L.; Qin, N.; Wu, L., A simple strategy for fabrication of Pd@MIL-100(Fe) nanocomposite as a visible-light-driven photocatalyst for the treatment of pharmaceuticals and personal care products (PPCPs). *Applied Catalysis B: Environmental* **2015,** *176–177*, 240-248.

37. Liang, R.; Jing, F.; Shen, L.; Qin, N.; Wu, L., M@MIL-100(Fe) (M = Au, Pd, Pt) nanocomposites fabricated by a facile photodeposition process: Efficient visible-light photocatalysts for redox reactions in water. *Nano Research* **2015,** *8* (10), 3237-3249.

38. Leus, K.; Concepcion, P.; Vandichel, M.; Meledina, M.; Grirrane, A.; Esquivel, D.; Turner, S.; Poelman, D.; Waroquier, M.; Van Speybroeck, V.; Van Tendeloo, G.; Garcia, H.; Van Der Voort, P., Au@UiO-66: a base free oxidation catalyst. *RSC Advances* **2015,** *5* (29), 22334-22342.

39. Wu, R.; Qian, X.; Zhou, K.; Liu, H.; Yadian, B.; Wei, J.; Zhu, H.; Huang, Y., Highly dispersed Au nanoparticles immobilized on Zr-based metal-organic frameworks as heterostructured catalyst for CO oxidation. *Journal of Materials Chemistry A* **2013,** *1* (45), 14294-14299.

40. Zhu, J.; Wang, P. C.; Lu, M., Selective oxidation of benzyl alcohol under solvent-free condition with gold nanoparticles encapsulated in metal-organic framework. *Applied Catalysis a-General* **2014,** *477*, 125-131.

41. Luan, Y.; Qi, Y.; Gao, H.; Zheng, N.; Wang, G., Synthesis of an amino-functionalized metal-organic framework at a nanoscale level for gold nanoparticle deposition and catalysis. *Journal of Materials Chemistry A* **2014,** *2* (48), 20588-20596.

42. Shen, L.; Luo, M.; Huang, L.; Feng, P.; Wu, L., A Clean and General Strategy To Decorate a Titanium Metal Organic Framework with Noble-Metal Nanoparticles for Versatile Photocatalytic Applications. *Inorganic Chemistry* **2015,** *54* (4), 1191-1193.

43. Han, Y.; Han, L.; Zhang, L.; Dong, S., Ultrasonic synthesis of highly dispersed Au nanoparticles supported on Ti-based metal-organic frameworks for electrocatalytic oxidation of hydrazine. *Journal of Materials Chemistry A* **2015,** *3* (28), 14669-14674.

44. Liu, L.; Song, Y.; Chong, H.; Yang, S.; Xiang, J.; Jin, S.; Kang, X.; Zhang, J.; Yu, H.; Zhu, M., Size-confined growth of atom-precise nanoclusters in metal-organic frameworks and their catalytic applications. *Nanoscale* **2016,** *8* (3), 1407-1412.

45. Zhou, W.; Zou, B.; Zhang, W.; Tian, D.; Huang, W.; Huo, F., Synthesis of stable heterogeneous catalysts by supporting carbon-stabilized palladium nanoparticles on MOFs. *Nanoscale* **2015,** *7* (19), 8720-8724.

46. Shen, L.; Luo, M.; Liu, Y.; Liang, R.; Jing, F.; Wu, L., Noble-metal-free MoS_2 co-catalyst decorated UiO-66/CdS hybrids for efficient photocatalytic H_2 production. *Applied Catalysis B-Environmental* **2015,** *166*, 445-453.

47. Ke, F.; Wang, L. H.; Zhu, J. F., Facile fabrication of CdS-metal-organic framework nanocomposites with enhanced visible-light photocatalytic activity for organic transformation. *Nano Research* **2015,** *8* (6), 1834-1846.

48. He, J.; Yang, H.; Chen, Y.; Yan, Z.; Zeng, Y.; Luo, Z.; Gao, W.; Wang, J., Solar Light Photocatalytic Degradation of Nitrite in Aqueous Solution Over CdS Embedded on Metal-Organic Frameworks. *Water Air and Soil Pollution* **2015,** *226* (6).

49. Gan, H.; Wang, Z.; Li, H.; Wang, Y.; Sun, L.; Li, Y., CdSe QDs@ UIO-66 composite with enhanced photocatalytic activity towards RhB degradation under visible-light irradiation. *Rsc Advances* **2016,** *6* (7), 5192-5197.

50. Wang, P.; Sun, H.; Quan, X.; Chen, S., Enhanced catalytic activity over MIL-100(Fe) loaded ceria catalysts for the selective catalytic reduction of NO_x with NH_3 at low temperature. *Journal of Hazardous Materials* **2016,** *301*, 512-521.

51. Li, J.; Zhu, Q.-L.; Xu, Q., Non-noble bimetallic CuCo nanoparticles encapsulated in the pores of metal-organic frameworks: synergetic catalysis in the hydrolysis of ammonia borane for hydrogen generation. *Catalysis Science & Technology* **2015,** *5* (1), 525-530.

52. Chen, Y.-Z.; Xu, Q.; Yu, S.-H.; Jiang, H.-L., Tiny Pd@Co Core-Shell Nanoparticles Confined inside a Metal-Organic Framework for Highly Efficient Catalysis. *Small* **2015,** *11* (1), 71-76.

53. Han, J.; Wang, D.; Du, Y.; Xi, S.; Hong, J.; Yin, S.; Chen, Z.; Zhou, T.; Xu, R., Metal-organic framework immobilized cobalt oxide nanoparticles for efficient photocatalytic water oxidation. *Journal of Materials Chemistry A* **2015,** *3* (41), 20607-20613.

54. Cao, N.; Tan, S. Y.; Luo, W.; Hu, K.; Cheng, G. Z., Ternary CoAgPd Nanoparticles Confined Inside the Pores of MIL-101 as Efficient Catalyst for Dehydrogenation of Formic Acid. *Catalysis Letters* **2016,** *146* (2), 518-524.

55. Muller, M.; Hermes, S.; Kaehler, K.; van den Berg, M. W. E.; Muhler, M.; Fischer, R. A., Loading of MOF-5 with Cu and ZnO nanoparticles by gas-phase infiltration with organometallic precursors: properties of Cu/ZnO@MOF-5 as catalyst for methanol synthesis. *Chemistry of Materials* **2008,** *20* (14), 4576-4587.

56. Montazerolghaem, M.; Aghamiri, S. F.; Tangestaninejad, S.; Talaie, M. R., A metal-organic framework MIL-101 doped with metal nanoparticles (Ni & Cu) and its effect on CO_2 adsorption properties. *Rsc Advances* **2016,** *6* (1), 632-640.

57. Wu, F.; Qiu, L. G.; Ke, F.; Jiang, X., Copper nanoparticles embedded in metal-organic framework MIL-101(Cr) as a high performance catalyst for reduction of aromatic nitro compounds. *Inorganic Chemistry Communications* **2013,** *32*, 5-8.

58. Muller, M.; Lebedev, O. I.; Fischer, R. A., Gas-phase loading of $Zn_4O(btb)_2$ (MOF-177) with organometallic CVD-precursors: inclusion compounds of the type $[L_nM]_a$@MOF-177 and the formation of Cu and Pd nanoparticles inside MOF-177. *Journal of Materials Chemistry* **2008,** *18* (43), 5274-5281.

59. Shi, L.; Zhu, X.; Liu, T.; Zhao, H.; Lan, M., Encapsulating Cu nanoparticles into metal-organic frameworks for nonenzymatic glucose sensing. *Sensors and Actuators B: Chemical* **2016,** *227*, 583-590.

60. Jayaramulu, K.; Suresh, V. M.; Maji, T. K., Stabilization of Cu_2O nanoparticles on a 2D metal-organic framework for catalytic Huisgen 1,3-dipolar cycloaddition reaction. *Dalton Transactions* **2015,** *44* (1), 83-86.

61. Saikia, M.; Bhuyan, D.; Saikia, L., Facile synthesis of Fe_3O_4 nanoparticles on metal organic framework MIL-101(Cr): characterization and catalytic activity. *New Journal of Chemistry* **2015,** *39* (1), 64-67.

62. Jiang, Z.; Li, Y., Facile synthesis of magnetic hybrid Fe_3O_4/MIL-101 via heterogeneous coprecipitation assembly for efficient adsorption of anionic dyes. *Journal of the Taiwan Institute of Chemical Engineers* **2016,** *59*, 373-379.

63. Qin, L.; Li, Z.; Xu, Z.; Guo, X.; Zhang, G., Organic-acid-directed assembly of iron-carbon oxides nanoparticles on coordinatively unsaturated metal sites of MIL-101 for green photochemical oxidation. *Applied Catalysis B-Environmental* **2015,** *179*, 500-508.

64. Esken, D.; Turner, S.; Wiktor, C.; Kalidindi, S. B.; Van Tendeloo, G.; Fischer, R. A., GaN@ZIF-8: Selective Formation of Gallium Nitride Quantum Dots inside a Zinc Methylimidazolate Framework. *Journal of the American Chemical Society* **2011,** *133* (41), 16370-16373.

65. Wang, H.; Yuan, X.; Wu, Y.; Zeng, G.; Dong, H.; Chen, X.; Leng, L.; Wu, Z.; Peng, L., In situ synthesis of In_2S_3@MIL-125(Ti) core–shell microparticle for the removal of tetracycline from wastewater by integrated adsorption and visible-light-driven photocatalysis. *Applied Catalysis B: Environmental* **2016,** *186*, 19-29.

66. Yin, F.; Li, G.; Wang, H., Hydrothermal synthesis of α-MnO_2/MIL-101(Cr) composite and its bifunctional electrocatalytic activity for oxygen reduction/evolution reactions. *Catalysis Communications* **2014,** *54*, 17-21.

67. Wang, H.; Yin, F.; Chen, B.; Li, G., Synthesis of an ε-MnO_2/metal-organic-framework composite and its electrocatalysis towards oxygen reduction reaction in an alkaline electrolyte. *Journal of Materials Chemistry A* **2015,** *3* (31), 16168-16176.

68. Bhakta, R. K.; Herberg, J. L.; Jacobs, B.; Highley, A.; Behrens, R.; Ockwig, N. W.; Greathouse, J. A.; Allendorf, M. D., Metal-Organic Frameworks As Templates for Nanoscale $NaAlH_4$. *Journal of the American Chemical Society* **2009,** *131* (37), 13198-+.

69. Park, Y. K.; Choi, S. B.; Nam, H. J.; Jung, D. Y.; Ahn, H. C.; Choi, K.; Furukawa, H.; Kim, J., Catalytic nickel nanoparticles embedded in a mesoporous metal-organic framework. *Chemical Communications* **2010,** *46* (18), 3086-3088.

70. Chen, L.; Chen, X.; Liu, H.; Li, Y., Encapsulation of Mono- or Bimetal Nanoparticles Inside Metal-Organic Frameworks via In situ Incorporation of Metal Precursors. *Small* **2015,** *11* (22), 2642-2648.

71. Zhao, P.; Cao, N.; Luo, W.; Cheng, G., Nanoscale MIL-101 supported RhNi nanoparticles: an efficient catalyst for hydrogen generation from hydrous hydrazine. *Journal of Materials Chemistry A* **2015,** *3* (23), 12468-12475.

72. Fu, Y.; Sun, L.; Yang, H.; Xu, L.; Zhang, F.; Zhu, W., Visible-light-induced aerobic photocatalytic oxidation of aromatic alcohols to aldehydes over Ni-doped NH2-MIL-125(Ti). *Applied Catalysis B: Environmental* **2016,** *187*, 212-217.

73. Wen, L.; Du, X.; Su, J.; Luo, W.; Cai, P.; Cheng, G., Ni-Pt nanoparticles growing on metal organic frameworks (MIL-96) with enhanced catalytic activity for hydrogen generation from hydrazine at room temperature. *Dalton Transactions* **2015,** *44* (13), 6212-6218.

74. Xia, B.; Liu, C.; Wu, H.; Luo, W.; Cheng, G., Hydrolytic dehydrogenation of ammonia borane catalyzed by metal-organic framework supported bimetallic RhNi nanoparticles. *International Journal of Hydrogen Energy* **2015,** *40* (46), 16391-16397.

75. Jeong, M.-G.; Kim, D. H.; Lee, S.-K.; Lee, J. H.; Han, S. W.; Park, E. J.; Cychosz, K. A.; Thommes, M.; Hwang, Y. K.; Chang, J.-S.; Kim, Y. D., Decoration of the internal structure of mesoporous chromium terephthalate MIL-101 with NiO using atomic layer deposition. *Microporous and Mesoporous Materials* **2016,** *221*, 101-107.

76. Xia, B.; Cao, N.; Dai, H.; Su, J.; Wu, X.; Luo, W.; Cheng, G., Bimetallic Nickel-Rhodium Nanoparticles Supported on ZIF-8 as Highly Efficient Catalysts for Hydrogen Generation from Hydrazine in Alkaline Solution. *Chemcatchem* **2014,** *6* (9), 2549-2552.

77. Aijaz, A.; Zhu, Q.-L.; Tsumori, N.; Akita, T.; Xu, Q., Surfactant-free Pd nanoparticles immobilized to a metal-organic framework with size- and location-dependent catalytic selectivity. *Chemical Communications* **2015,** *51* (13), 2577-2580.

78. Yang, Q.; Chen, Y.-Z.; Wang, Z. U.; Xu, Q.; Jiang, H.-L., One-pot tandem catalysis over Pd@MIL-101: boosting the efficiency of nitro compound hydrogenation by coupling with ammonia borane dehydrogenation. *Chemical Communications* **2015,** *51* (52), 10419-10422.

79. Annapurna, M.; Parsharamulu, T.; Reddy, P. V.; Suresh, M.; Likhar, P. R.; Kantam, M. L., Nano palladium supported on high-surface-area metal-organic framework MIL-101: an efficient catalyst for Sonogashira coupling of aryl and heteroaryl bromides with alkynes. *Applied Organometallic Chemistry* **2015,** *29* (4), 234-239.

80. Zhang, D.; Guan, Y.; Hensen, E. J. M.; Chen, L.; Wang, Y., Porous MOFs supported palladium catalysts for phenol hydrogenation: A comparative study on MIL-101 and MIL-53. *Catalysis Communications* **2013,** *41* (0), 47-51.

81. Huang, Y. B.; Lin, Z. J.; Cao, R., Palladium Nanoparticles Encapsulated in a Metal-Organic Framework as Efficient Heterogeneous Catalysts for Direct C2 Arylation of Indoles. *Chemistry-a European Journal* **2011,** *17* (45), 12706-12712.

82. Yuan, B. Z.; Pan, Y. Y.; Li, Y. W.; Yin, B. L.; Jiang, H. F., A Highly Active Heterogeneous Palladium Catalyst for the Suzuki-Miyaura and Ullmann Coupling Reactions of Aryl Chlorides in Aqueous Media. *Angewandte Chemie-International Edition* **2010,** *49* (24), 4054-4058.

83. Aijaz, A.; Akita, T.; Tsumori, N.; Xu, Q., Metal-Organic Framework-Immobilized Polyhedral Metal Nanocrystals: Reduction at Solid-Gas Interface, Metal Segregation, Core-Shell Structure, and High Catalytic Activity. *Journal of the American Chemical Society* **2013,** *135* (44), 16356-16359.

84. Zhao, X. M.; Jin, Y.; Zhang, F. M.; Zhong, Y. J.; Zhu, W. D., Catalytic hydrogenation of 2,3,5-trimethylbenzoquinone over Pd nanoparticles confined in the cages of MIL-101(Cr). *Chemical Engineering Journal* **2014,** *239*, 33-41.

85. Pan, Y. Y.; Yuan, B. Z.; Li, Y. W.; He, D. H., Multifunctional catalysis by Pd@MIL-101: one-step synthesis of methyl isobutyl ketone over palladium nanoparticles deposited on a metal-organic framework. *Chemical Communications* **2010,** *46* (13), 2280-2282.

86. Qin, W.; Cao, W.; Liu, H.; Li, Z.; Li, Y., Metal-organic framework MIL-101 doped with palladium for toluene adsorption and hydrogen storage. *RSC Advances* **2014,** *4* (5), 2414-2420.

87. Hermannsdofer, J.; Kempe, R., Selective Palladium-Loaded MIL-101 Catalysts. *Chemistry-a European Journal* **2011,** *17* (29), 8071-8077.

88. Hermannsdorfer, J.; Friedrich, M.; Kempe, R., Colloidal Size Effect and Metal-Particle Migration in M@MOF/PCP Catalysis. *Chemistry-a European Journal* **2013,** *19* (41), 13652-13657.

89. Tilgner, D.; Friedrich, M.; Hermannsdoerfer, J.; Kempe, R., Titanium Dioxide Reinforced Metal-Organic Framework Pd Catalysts: Activity and Reusability Enhancement in Alcohol Dehydrogenation Reactions and Improved Photocatalytic Performance. *Chemcatchem* **2015,** *7* (23), 3916-3922.

90. Pascanu, V.; Yao, Q. X.; Gomez, A. B.; Gustafsson, M.; Yun, Y. F.; Wan, W.; Samain, L.; Zou, X. D.; Martin-Matute, B., Sustainable Catalysis: Rational Pd Loading on MIL-101Cr-NH_2 for More Efficient and Recyclable Suzuki-Miyaura Reactions. *Chemistry-a European Journal* **2013,** *19* (51), 17483-17493.

91. Pascanu, V.; Hansen, P. R.; Gomez, A. B.; Ayats, C.; Platero-Prats, A. E.; Johansson, M. J.; Pericas, M. A.; Martin-Matute, B., Highly Functionalized Biaryls via Suzuki-Miyaura Cross-Coupling Catalyzed by Pd@MOF under Batch and Continuous Flow Regimes. *Chemsuschem* **2015,** *8* (1), 123-130.

92. Carson, F.; Pascanu, V.; Gomez, A. B.; Zhang, Y.; Platero-Prats, A. E.; Zou, X. D.; Martin-Matute, B., Influence of the Base on Pd@MIL-101-NH_2(Cr) as Catalyst for the Suzuki-Miyaura Cross-Coupling Reaction. *Chemistry-a European Journal* **2015,** *21* (30), 10896-10902.

93. Pascanu, V.; Carson, F.; Solano, M. V.; Su, J.; Zou, X. D.; Johansson, M. J.; Martin-Matute, B., Selective Heterogeneous C-H Activation/Halogenation Reactions Catalyzed by Pd@MOF Nanocomposites. *Chemistry-a European Journal* **2016,** *22* (11), 3729-3737.

94. Saikia, M.; Saikia, L., Palladium nanoparticles immobilized on an amine-functionalized MIL-101(Cr) as a highly active catalyst for oxidative amination of aldehydes. *Rsc Advances* **2016,** *6* (18), 14937-14947.

95. Zhang, F.; Jin, Y.; Fu, Y.; Zhong, Y.; Zhu, W.; Ibrahim, A. A.; El-Shall, M. S., Palladium nanoparticles incorporated within sulfonic acid-functionalized MIL-101(Cr) for efficient catalytic conversion of vanillin. *Journal of Materials Chemistry A* **2015,** *3* (33), 17008-17015.

96. Zlotea, C.; Campesi, R.; Cuevas, F.; Leroy, E.; Dibandjo, P.; Volkringer, C.; Loiseau, T.; Ferey, G.; Latroche, M., Pd Nanoparticles Embedded into a Metal-Organic Framework: Synthesis, Structural Characteristics, and Hydrogen Sorption Properties. *Journal of the American Chemical Society* **2010,** *132* (9), 2991-2997.

97. Stakheev, A. Y.; Isaeva, V. I.; Markov, P. V.; Turova, O. V.; Mashkovskii, I. S.; Kapustin, G. I.; Saifutdinov, B. R.; Kustov, L. M., Novel catalysts for selective hydrogenation of Ca parts per thousand C bond based on Pd nanoparticles immobilized in phenylenecarboxylate frameworks (NH_2)-MIL-53(Al). *Russian Chemical Bulletin* **2015,** *64* (2), 284-290.

98. Turner, S.; Lebedev, O. I.; Schroder, F.; Esken, D.; Fischer, R. A.; Van Tendeloo, G., Direct imaging of loaded metal-organic framework materials (metal@MOF-5). *Chemistry of Materials* **2008,** *20* (17), 5622-5627.

99. Kleist, W.; Maciejewski, M.; Baiker, A., MOF-5 based mixed-linker metal-organic frameworks: Synthesis, thermal stability and catalytic application. *Thermochimica Acta* **2010,** *499* (1-2), 71-78.

100. Sabo, M.; Henschel, A.; Froede, H.; Klemm, E.; Kaskel, S., Solution infiltration of palladium into MOF-5: synthesis, physisorption and catalytic properties. *Journal of Materials Chemistry* **2007,** *17* (36), 3827-3832.

101. Puthiaraj, P.; Ahn, W.-S., Highly active palladium nanoparticles immobilized on NH_2-MIL-125 as efficient and recyclable catalysts for Suzuki-Miyaura cross coupling reaction. *Catalysis Communications* **2015,** *65*, 91-95.

102. Zhao, Y.; Liu, M.; Fan, B.; Chen, Y.; Lv, W.; Lu, N.; Li, R., Pd nanoparticles supported on ZIF-8 as an efficient heterogeneous catalyst for the selective hydrogenation of cinnamaldehyde. *Catalysis Communications* **2014,** *57*, 119-123.

103. Zhang, M.; Gao, Y.; Li, C.; Liang, C., Chemical vapor deposition of $Pd(C_3H_5)(C_5H_5)$ for the synthesis of reusable Pd@ZIF-8 catalysts for the Suzuki coupling reaction. *Chinese Journal of Catalysis* **2015,** *36* (4), 588-594.

104. Chen, Y.-Z.; Cai, G.; Wang, Y.; Xu, Q.; Yu, S.-H.; Jiang, H.-L., Palladium nanoparticles stabilized with N-doped porous carbons derived from metal-organic

frameworks for selective catalysis in biofuel upgrade: the role of catalyst wettability. *Green Chemistry* **2016,** *18* (5), 1212-1217.

105. Jia, X.; Wang, S.; Fan, Y., A novel strategy for producing highly dispersed Pd particles on ZIF-8 through the occupation and unoccupation of carboxyl groups and its application in selective diene hydrogenation. *Journal of Catalysis* **2015,** *327*, 54-57.

106. Cheon, Y. E.; Suh, M. P., Multifunctional fourfold interpenetrating diamondoid network: Gas separation and fabrication of palladium nanoparticles. *Chemistry-a European Journal* **2008,** *14* (13), 3961-3967.

107. Cheon, Y. E.; Suh, M. P., Enhanced Hydrogen Storage by Palladium Nanoparticles Fabricated in a Redox-Active Metal-Organic Framework. *Angewandte Chemie-International Edition* **2009,** *48* (16), 2899-2903.

108. Gulcan, M.; Zahmakiran, M.; Ozkar, S., Palladium(0) nanoparticles supported on metal organic framework as highly active and reusable nanocatalyst in dehydrogenation of dimethylamine-borane. *Applied Catalysis B-Environmental* **2014,** *147*, 394-401.

109. Huang, Y. B. A.; Zheng, Z. L.; Liu, T. F.; Lu, J.; Lin, Z. J.; Li, H. F.; Cao, R., Palladium nanoparticles supported on amino functionalized metal-organic frameworks as highly active catalysts for the Suzuki-Miyaura cross-coupling reaction. *Catalysis Communications* **2011,** *14* (1), 27-31.

110. Islam, D. A.; Acharya, H., Magnetically separable palladium nanocluster supported iron based metal-organic framework (MIL-88B) catalyst in efficient hydrogenation reactions. *RSC Advances* **2015,** *5* (58), 46583-46588.

111. Pascanu, V.; Gomez, A. B.; Ayats, C.; Platero-Prats, A. E.; Carson, F.; Su, J.; Yao, Q.; Pericas, M. A.; Zou, X.; Martin-Matute, B., Double-Supported Silica-Metal-Organic Framework Palladium Nanocatalyst for the Aerobic Oxidation of Alcohols under Batch and Continuous Flow Regimes. *Acs Catalysis* **2015,** *5* (2), 472-479.

112. Pourkhosravani, M.; Dehghanpour, S.; Farzaneh, F., Palladium Nanoparticles Supported on Zirconium Metal Organic Framework as an Efficient Heterogeneous Catalyst for the Suzuki-Miyaura Coupling Reaction. *Catalysis Letters* **2016,** *146* (2), 499-508.

113. Dong, W. H.; Feng, C.; Zhang, L.; Shang, N. Z.; Gao, S. T.; Wang, C.; Wang, Z., Pd@UiO-66: An Efficient Catalyst for Suzuki-Miyaura Coupling Reaction at Mild Condition. *Catalysis Letters* **2016,** *146* (1), 117-125.

114. Luz, I.; Roesler, C.; Epp, K.; Llabres i Xamena, F. X.; Fischer, R. A., Pd@UiO-66-Type MOFs Prepared by Chemical Vapor Infiltration as Shape-Selective Hydrogenation Catalysts. *European Journal of Inorganic Chemistry* **2015,** (23), 3904-3912.

115. Kardanpour, R.; Tangestaninejad, S.; Mirkhani, V.; Moghadam, M.; Mohammadpoor-Baltork, I.; Khosropour, A. R.; Zadehahmadi, F., Highly dispersed palladium nanoparticles supported on amino functionalized metal-organic frameworks as an efficient and reusable catalyst for Suzuki cross-coupling reaction. *Journal of Organometallic Chemistry* **2014,** *761*, 127-133.

116. Li, X.; Guo, Z.; Xiao, C.; Goh, T. W.; Tesfagaber, D.; Huang, W., Tandem Catalysis by Palladium Nanoclusters Encapsulated in Metal-Organic Frameworks. *Acs Catalysis* **2014,** *4* (10), 3490-3497.

117. Shen, L.; Wu, W.; Liang, R.; Lin, R.; Wu, L., Highly dispersed palladium nanoparticles anchored on UiO-66(NH_2) metal-organic framework as a reusable and dual functional visible-light-driven photocatalyst. *Nanoscale* **2013,** *5* (19), 9374-9382.

118. Wang, C.-Y.; Gray, J. L.; Gong, Q.; Zhao, Y.; Li, J.; Klontzas, E.; Psofogiannakis, G.; Froudakis, G.; Lueking, A. D., Hydrogen Storage with Spectroscopic Identification of Chemisorption Sites in Cu-TDPAT via Spillover from a Pt/Activated Carbon Catalyst. *Journal of Physical Chemistry C* **2014,** *118* (46), 26750-26763.

119. Zhuang, G.-l.; Bai, J.-q.; Tan, L.; Huang, H.-l.; Gao, Y.-f.; Zhong, X.; Zhong, C.-l.; Wang, J.-g., Preparation and catalytic properties of Pd nanoparticles supported on micro-crystal DUT-67 MOFs. *RSC Advances* **2015,** *5* (41), 32714-32719.

120. Gole, B.; Sanyal, U.; Banerjee, R.; Mukherjee, P. S., High Loading of Pd Nanoparticles by Interior Functionalization of MOFs for Heterogeneous Catalysis. *Inorganic Chemistry* **2016,** *55* (5), 2345-2354.

121. Khajavi, H.; Stil, H. A.; Kuipers, H.; Gascon, J.; Kapteijn, F., Shape and Transition State Selective Hydrogenations Using Egg-Shell Pt-MIL-101(Cr) Catalyst. *Acs Catalysis* **2013,** *3* (11), 2617-2626.

122. Pan, H.; Li, X.; Yu, Y.; Li, J.; Hu, J.; Guan, Y.; Wu, P., Pt nanoparticles entrapped in mesoporous metal-organic frameworks MIL-101 as an efficient catalyst for liquid-phase hydrogenation of benzaldehydes and nitrobenzenes. *Journal of Molecular Catalysis a-Chemical* **2015,** *399*, 1-9.

123. Du, W.; Chen, G.; Nie, R.; Li, Y.; Hou, Z., Highly dispersed Pt in MIL-101: An efficient catalyst for the hydrogenation of nitroarenes. *Catalysis Communications* **2013,** *41* (0), 56-59.

124. Liu, H.; Chang, L.; Chen, L.; Li, Y., Nanocomposites of Platinum/Metal-Organic Frameworks Coated with Metal-Organic Frameworks with Remarkably Enhanced Chemoselectivity for Cinnamaldehyde Hydrogenation. *Chemcatchem* **2016,** *8* (5), 946-951.

125. Wen, M.; Mori, K.; Kamegawa, T.; Yamashita, H., Amine-functionalized MIL-101(Cr) with imbedded platinum nanoparticles as a durable photocatalyst for hydrogen production from water. *Chemical Communications* **2014,** *50* (79), 11645-11648.

126. Horiuchi, Y.; Toyao, T.; Saito, M.; Mochizuki, K.; Iwata, M.; Higashimura, H.; Anpo, M.; Matsuoka, M., Visible-Light-Promoted Photocatalytic Hydrogen Production by Using an Amino-Functionalized Ti(IV) Metal-Organic Framework. *Journal of Physical Chemistry C* **2012,** *116* (39), 20848-20853.

127. Hou, C. T.; Xu, Q.; Wang, Y. J.; Hu, X. Y., Synthesis of Pt@NH_2-MIL-125(Ti) as a photocathode material for photoelectrochemical hydrogen production. *RSC Advances* **2013,** *3* (43), 19820-19823.

128. He, J.; Wang, J.; Chen, Y.; Zhang, J.; Duan, D.; Wang, Y.; Yan, Z., A dye-sensitized Pt@UiO-66(Zr) metal-organic framework for visible-light photocatalytic hydrogen production. *Chemical Communications* **2014,** *50* (53), 7063-7066.

129. Yuan, Y.-P.; Yin, L.-S.; Cao, S.-W.; Xu, G.-S.; Li, C.-H.; Xue, C., Improving photocatalytic hydrogen production of metal-organic framework UiO-66 octahedrons by dye-sensitization. *Applied Catalysis B-Environmental* **2015,** *168*, 572-576.

130. Guo, Z. Y.; Xiao, C. X.; Maligal-Ganesh, R. V.; Zhou, L.; Goh, T. W.; Li, X. L.; Tesfagaber, D.; Thiel, A.; Huang, W. Y., Pt Nanoclusters Confined within Metal Organic Framework Cavities for Chemoselective Cinnamaldehyde Hydrogenation. *Acs Catalysis* **2014,** *4* (5), 1340-1348.

131. Proch, S.; Herrmannsdorfer, J.; Kempe, R.; Kern, C.; Jess, A.; Seyfarth, L.; Senker, J., Pt@MOF-177: Synthesis, Room-Temperature Hydrogen Storage and Oxidation Catalysis. *Chemistry-a European Journal* **2008,** *14* (27), 8204-8212.

132. Tarasov, A. L.; Kustov, L. M.; Isaeva, V. I.; Kalenchuk, A. N.; Mishin, I. V.; Kapustin, G. I.; Bogdan, V. I., Platinum-containing catalyst supported on a metal-organic framework structure in the selective oxidation of benzyl alcohol derivatives into aldehydes. *Kinetics and Catalysis* **2011,** *52* (2), 273-276.

133. Wang, C.-Y.; Gong, Q.; Zhao, Y.; Li, J.; Lueking, A. D., Stability and hydrogen adsorption of metal-organic frameworks prepared via different catalyst doping methods. *Journal of Catalysis* **2014,** *318*, 128-142.

134. Ertas, I. E.; Gulcan, M.; Bulut, A.; Yurderi, M.; Zahmakiran, M., Rhodium nanoparticles stabilized by sulfonic acid functionalized metal-organic framework for the selective hydrogenation of phenol to cyclohexanone. *Journal of Molecular Catalysis a-Chemical* **2015,** *410*, 209-220.

135. Schroeder, F.; Esken, D.; Cokoja, M.; van den Berg, M. W. E.; Lebedev, O. I.; van Tendeloo, G.; Walaszek, B.; Buntkowsky, G.; Limbach, H. H.; Chaudret, B.; Fischer, R. A., Ruthenium nanoparticles inside porous $Zn_4O(bdc)_3$ by hydrogenolysis of adsorbed Ru(cod)(cot) : A solid-state reference system for surfactant-stabilized ruthenium colloids. *Journal of the American Chemical Society* **2008,** *130* (19), 6119-6130.

136. Wen, L.; Su, J.; Wu, X.; Cai, P.; Luo, W.; Cheng, G., Ruthenium supported on MIL-96: An efficient catalyst for hydrolytic dehydrogenation of ammonia borane for chemical hydrogen storage. *International Journal of Hydrogen Energy* **2014,** *39* (30), 17129-17135.

137. Zhao, Y. J.; Zhang, J. L.; Song, J. L.; Li, J. S.; Liu, J. L.; Wu, T. B.; Zhang, P.; Han, B. X., Ru nanoparticles immobilized on metal-organic framework nanorods by supercritical CO_2-methanol solution: highly efficient catalyst. *Green Chemistry* **2011,** *13* (8), 2078-2082.

138. Yuan, Q. Q.; Zhang, D. M.; van Haandel, L.; Ye, F. Y.; Xue, T.; Hensen, E. J. M.; Guan, Y. J., Selective liquid phase hydrogenation of furfural to furfuryl alcohol by Ru/Zr-MOFs. *Journal of Molecular Catalysis a-Chemical* **2015,** *406*, 58-64.

139. Schroder, F.; Henke, S.; Zhang, X. N.; Fischer, R. A., Simultaneous Gas-Phase Loading of MOF-5 with Two Metal Precursors: towards Bimetallics@MOF. *European Journal of Inorganic Chemistry* **2009,** (21), 3131-3140.

140. Muller, M.; Zhang, X. N.; Wang, Y. M.; Fischer, R. A., Nanometer-sized titania hosted inside MOF-5. *Chemical Communications* **2009,** (1), 119-121.

141. Esken, D.; Noei, H.; Wang, Y. M.; Wiktor, C.; Turner, S.; Van Tendeloo, G.; Fischer, R. A., ZnO@ZIF-8: stabilization of quantum confined ZnO nanoparticles by a zinc methylimidazolate framework and their surface structural characterization probed by CO_2 adsorption. *Journal of Materials Chemistry* **2011,** *21* (16), 5907-5915.

142. Li, Z.; Zeng, H. C., Surface and Bulk Integrations of Single-Layered Au or Ag Nanoparticles onto Designated Crystal Planes {110} or {100} of ZIF-8. *Chemistry of Materials* **2013,** *25* (9), 1761-1768.

143. Ohhashi, T.; Tsuruoka, T.; Matsuyama, T.; Takashima, Y.; Nawafune, H.; Minami, H.; Akamatsu, K., Metal nanocrystal/metal-organic framework core/shell nanostructure from selective self-assembly induced by localization of metal ion precursors on nanocrystal surface. *Journal of Colloid and Interface Science* **2015,** *451*, 212-215.

144. Lu, G.; Li, S.; Guo, Z.; Farha, O. K.; Hauser, B. G.; Qi, X.; Wang, Y.; Wang, X.; Han, S.; Liu, X.; DuChene, J. S.; Zhang, H.; Zhang, Q.; Chen, X.; Ma, J.; Loo, S. C. J.; Wei, W. D.; Yang, Y.; Hupp, J. T.; Huo, F., Imparting functionality to a metal-organic framework material by controlled nanoparticle encapsulation. *Nature Chemistry* **2012,** *4* (4), 310-316.

145. Zhang, W.; Liu, Y.; Lu, G.; Wang, Y.; Li, S.; Cui, C.; Wu, J.; Xu, Z.; Tian, D.; Huang, W.; DuCheneu, J. S.; Wei, W. D.; Chen, H.; Yang, Y.; Huo, F., Mesoporous Metal-Organic Frameworks with Size-, Shape-, and Space-Distribution-Controlled Pore Structure. *Advanced Materials* **2015,** *27* (18), 2923-+.

146. Liu, X.; He, L.; Zheng, J.; Guo, J.; Bi, F.; Ma, X.; Zhao, K.; Liu, Y.; Song, R.; Tang, Z., Solar-Light-Driven Renewable Butanol Separation by Core-Shell Ag@ZIF-8 Nanowires. *Advanced Materials* **2015,** *27* (21), 3273-3277.

147. Dai, C.; Yang, C.-X.; Yan, X.-P., Ratiometric Fluorescent Detection of Phosphate in Aqueous Solution Based on Near Infrared Fluorescent Silver Nanoclusters/Metal–Organic Shell Composite. *Analytical Chemistry* **2015,** *87* (22), 11455-11459.

148. Ke, F.; Wang, L.; Zhu, J., An efficient room temperature core-shell AgPd@MOF catalyst for hydrogen production from formic acid. *Nanoscale* **2015,** *7* (18), 8321-8325.

149. Zhang, W.; Lu, G.; Li, S. Z.; Liu, Y. Y.; Xu, H. B.; Cui, C. L.; Yan, W. J.; Yang, Y. H.; Huo, F. W., Controlled incorporation of nanoparticles in metal-organic framework hybrid thin films. *Chemical Communications* **2014,** *50* (33), 4296-4298.

150. Chen, L. Y.; Peng, Y.; Wang, H.; Gua, Z. Z.; Duana, C. Y., Synthesis of Au@ZIF-8 single- or multi-core-shell structures for photocatalysis. *Chemical Communications* **2014,** *50* (63), 8651-8654.

151. Yang, J.; Zhao, F.; Zeng, B., Well-defined gold nanoparticle@N-doped porous carbon prepared from metal nanoparticle@metal-organic frameworks for electrochemical sensing of hydrazine. *RSC Advances* **2016,** *6* (28), 23403-23410.

152. Li, S.; Zhang, W.; Huo, F., The structural and catalytic properties of nanoparticles@MOF composites: A case study of Au@ZIF-8 hybrid crystals. *Physica E-Low-Dimensional Systems & Nanostructures* **2015,** *69*, 56-60.

153. Stephenson, C. J.; Whitford, C. L.; Stair, P. C.; Farha, O. K.; Hupp, J. T., Chemoselective Hydrogenation of Crotonaldehyde Catalyzed by an Au@ZIF-8 Composite. *Chemcatchem* **2016,** *8* (4), 855-860.

154. Zhou, J.; Wang, P.; Wang, C.; Goh, Y. T.; Fang, Z.; Messersmith, P. B.; Duan, H., Versatile Core-Shell Nanoparticle@Metal-Organic Framework Nanohybrids: Exploiting Mussel-Inspired Polydopamine for Tailored Structural Integration. *Acs Nano* **2015,** *9* (7), 6951-6960.

155. Sindoro, M.; Granick, S., Voids and Yolk-Shells from Crystals That Coat Particles. *Journal of the American Chemical Society* **2014,** *136* (39), 13471-13473.

156. Khaletskaya, K.; Reboul, J.; Meilikhov, M.; Nakahama, M.; Diring, S.; Tsujimoto, M.; Isoda, S.; Kim, F.; Kamei, K.-i.; Fischer, R. A.; Kitagawa, S.; Furukawa, S., Integration of Porous Coordination Polymers and Gold Nanorods into Core-Shell Mesoscopic Composites toward Light-Induced Molecular Release. *Journal of the American Chemical Society* **2013,** *135* (30), 10998-11005.

157. Ke, F.; Zhu, J. F.; Qiu, L. G.; Jiang, X., Controlled synthesis of novel Au@MIL-100(Fe) core-shell nanoparticles with enhanced catalytic performance. *Chemical Communications* **2013,** *49* (13), 1267-1269.

158. Liao, J.; Wang, D.; Liu, A.; Hu, Y.; Li, G., Controlled stepwise-synthesis of core-shell Au@MIL-100 (Fe) nanoparticles for sensitive surface-enhanced Raman scattering detection. *Analyst* **2015,** *140* (24), 8165-8171.

159. Liu, H. L.; Liu, Y. L.; Li, Y. W.; Tang, Z. Y.; Jiang, H. F., Metal-Organic Framework Supported Gold Nanoparticles as a Highly Active Heterogeneous Catalyst for Aerobic Oxidation of Alcohols. *Journal of Physical Chemistry C* **2010,** *114* (31), 13362-13369.

160. Khaletskaya, K.; Pougin, A.; Medishetty, R.; Rosler, C.; Wiktor, C.; Strunk, J.; Fischer, R. A., Fabrication of Gold/Titania Photocatalyst for CO_2 Reduction Based on Pyrolytic Conversion of the Metal-Organic Framework NH_2-MIL-125(Ti) Loaded with Gold Nanoparticles. *Chemistry of Materials* **2015,** *27* (21), 7248-7257.

161. Liu, Y. Y.; Zhang, W. N.; Li, S. Z.; Cui, C. L.; Wu, J.; Chen, H. Y.; Huo, F. W., Designable Yolk-Shell Nanoparticle@MOF Petalous Heterostructures. *Chemistry of Materials* **2014,** *26* (2), 1119-1125.

162. Tsuruoka, T.; Kawasaki, H.; Nawafune, H.; Akamatsu, K., Controlled Self-Assembly of Metal-Organic Frameworks on Metal Nanoparticles for Efficient Synthesis of Hybrid Nanostructures. *Acs Applied Materials & Interfaces* **2011,** *3* (10), 3788-3791.

163. Gu, Z.; Chen, L.; Duan, B.; Luo, Q.; Liu, J.; Duan, C., Synthesis of Au@UiO-66(NH_2) structures by small molecule-assisted nucleation for plasmon-enhanced photocatalytic activity. *Chemical Communications* **2016,** *52* (1), 116-119.

164. He, L.; Liu, Y.; Liu, J.; Xiong, Y.; Zheng, J.; Liu, Y.; Tang, Z., Core-Shell Noble-Metal@Metal-Organic-Framework Nanoparticles with Highly Selective Sensing Property. *Angewandte Chemie-International Edition* **2013,** *52* (13), 3741-3745.

165. Sugikawa, K.; Nagata, S.; Furukawa, Y.; Kokado, K.; Sada, K., Stable and Functional Gold Nanorod Composites with a Metal–Organic Framework Crystalline Shell. *Chemistry of Materials* **2013,** *25* (13), 2565-2570.

166. Sugikawa, K.; Furukawa, Y.; Sada, K., SERS-Active Metal-Organic Frameworks Embedding Gold Nanorods. *Chemistry of Materials* **2011,** *23* (13), 3132-3134.

167. Kaur, R.; Paul, A. K.; Deep, A., Nanocomposite of europium organic framework and quantum dots for highly sensitive chemosensing of trinitrotoluene. *Forensic Science International* **2014,** *242*, 88-93.

168. Lu, J.; Zhou, W.; Wang, L.; Jia, J.; Ke, Y.; Yang, L.; Zhou, K.; Liu, X.; Tang, Z.; Li, L.; Chen, S., Core–Shell Nanocomposites Based on Gold Nanoparticle@Zinc–Iron-Embedded Porous Carbons Derived from Metal–Organic Frameworks as Efficient Dual Catalysts for Oxygen Reduction and Hydrogen Evolution Reactions. *ACS Catalysis* **2016,** *6* (2), 1045-1053.

169. Ke, F.; Wang, L.; Zhu, J., Multifunctional Au-Fe_3O_4@MOF core-shell nanocomposite catalysts with controllable reactivity and magnetic recyclability. *Nanoscale* **2015,** *7* (3), 1201-1208.

170. Zeng, T.; Zhang, X.; Wang, S.; Niu, H.; Cai, Y., Spatial Confinement of a Co_3O_4 Catalyst in Hollow Metal-Organic Frameworks as a Nanoreactor for Improved Degradation of Organic Pollutants. *Environmental Science & Technology* **2015,** *49* (4), 2350-2357.

171. Kaur, R.; Paul, A. K.; Deep, A., Highly sensitive chemosensing of trinitrotoluene with europium organic framework/gold nanoparticle composite. *Inorganic Chemistry Communications* **2014,** *43*, 118-120.

172. Falcaro, P.; Hill, A. J.; Nairn, K. M.; Jasieniak, J.; Mardel, J. I.; Bastow, T. J.; Mayo, S. C.; Gimona, M.; Gomez, D.; Whitfield, H. J.; Ricco, R.; Patelli, A.; Marmiroli, B.; Amenitsch, H.; Colson, T.; Villanova, L.; Buso, D., A new method

to position and functionalize metal-organic framework crystals. *Nature Communications* **2011,** *2*.

173. Wang, X.; Zhao, S.; Zhang, Y.; Wang, Z.; Feng, J.; Song, S.; Zhang, H., CeO_2 nanowires self-inserted into porous Co_3O_4 frameworks as high-performance "noble metal free" hetero-catalysts. *Chemical Science* **2016,** *7* (2), 1109-1114.

174. Lin, Z.; Bian, W.; Zheng, J.; Cai, Z., Magnetic metal-organic framework nanocomposites for enrichment and direct detection of small molecules by negative-ion matrix-assisted laser desorption/ionization time-of-flight mass spectrometry. *Chemical Communications* **2015,** *51* (42), 8785-8788.

175. Schejn, A.; Mazet, T.; Falk, V.; Balan, L.; Aranda, L.; Medjahdi, G.; Schneider, R., Fe_3O_4@ZIF-8: magnetically recoverable catalysts by loading Fe_3O_4 nanoparticles inside a zinc imidazolate framework. *Dalton Transactions* **2015,** *44* (22), 10136-10140.

176. Zhang, T.; Zhang, X.; Yan, X.; Kong, L.; Zhang, G.; Liu, H.; Qiu, J.; Yeung, K. L., Synthesis of Fe_3O_4@ZIF-8 magnetic core-shell microspheres and their potential application in a capillary microreactor. *Chemical Engineering Journal* **2013,** *228*, 398-404.

177. Zheng, J.; Cheng, C.; Fang, W. J.; Chen, C.; Yan, R. W.; Huai, H. X.; Wang, C. C., Surfactant-free synthesis of a Fe_3O_4@ZIF-8 core-shell heterostructure for adsorption of methylene blue. *Crystengcomm* **2014,** *16* (19), 3960-3964.

178. Zou, Z.; Wang, S.; Jia, J.; Xu, F.; Long, Z.; Hou, X., Ultrasensitive determination of inorganic arsenic by hydride generation-atomic fluorescence spectrometry using Fe_3O_4@ZIF-8 nanoparticles for preconcentration. *Microchemical Journal* **2016,** *124*, 578-583.

179. Zhao, F.-b.; Song, N.-z.; Ning, W.-k.; Jia, Q., Synthesis of Magnetic Metal Organic Framework Fe_3O_4@NH_2-MIL-53(Al) Materials and Application to the Adsorption of Lead. *Spectroscopy and Spectral Analysis* **2015,** *35* (9), 2439-2443.

180. Chen, X.; Ding, N.; Zang, H.; Yeung, H.; Zhao, R.-S.; Cheng, C.; Liu, J.; Chan, T. W. D., Fe_3O_4@MOF core-shell magnetic microspheres for magnetic solid-phase extraction of polychlorinated biphenyls from environmental water samples. *Journal of Chromatography A* **2013,** *1304*, 241-245.

181. Khezeli, T.; Daneshfar, A., Dispersive micro-solid-phase extraction of dopamine, epinephrine and norepinephrine from biological samples based on green deep eutectic solvents and Fe_3O_4@MIL-100 (Fe) core-shell nanoparticles grafted with pyrocatechol. *RSC Advances* **2015,** *5* (80), 65264-65273.

182. Chen, Y.; Xiong, Z.; Peng, L.; Gan, Y.; Zhao, Y.; Shen, J.; Qian, J.; Zhang, L.; Zhang, W., Facile Preparation of Core-Shell Magnetic Metal Organic Framework Nanoparticles for the Selective Capture of Phosphopeptides. *Acs Applied Materials & Interfaces* **2015,** *7* (30), 16338-16347.

183. Zhang, H.-j.; Qi, S.-d.; Niu, X.-y.; Hu, J.; Ren, C.-l.; Chen, H.-l.; Chen, X.-g., Metallic nanoparticles immobilized in magnetic metal-organic frameworks: preparation and application as highly active, magnetically isolable and reusable catalysts. *Catalysis Science & Technology* **2014,** *4* (9), 3013-3024.

184. Zhao, H.; Qian, L.; Lv, H.; Wang, Y.; Zhao, G., Introduction of a Fe_3O_4 Core Enhances the Photocatalytic Activity of MIL-100(Fe) with Tunable Shell Thickness in the Presence of H_2O_2. *Chemcatchem* **2015,** *7* (24), 4148-4155.

185. Dadfarnia, S.; Shabani, A. M. H.; Moradi, S. E.; Emami, S., Methyl red removal from water by iron based metal-organic frameworks loaded onto iron oxide nanoparticle adsorbent. *Applied Surface Science* **2015,** *330*, 85-93.

186. Yu, S.; Wan, J.; Chen, K., A facile synthesis of superparamagnetic Fe_3O_4 supraparticles@MIL-100 (Fe) core-shell nanostructures: Preparation, characterization and biocompatibility. *Journal of Colloid and Interface Science* **2016,** *461*, 173-178.

187. Jin, Z.; Luan, Y.; Yang, M.; Tang, J.; Wang, J.; Gao, H.; Lu, Y.; Wang, G., Imparting magnetic functionality to iron-based MIL-101 via facile Fe_3O_4 nanoparticle encapsulation: an efficient and recoverable catalyst for aerobic oxidation. *RSC Advances* **2015,** *5* (96), 78962-78970.

188. Wei, J.-P.; Qiao, B.; Song, W.-J.; Chen, T.; Li, F.; Li, B.-Z.; Wang, J.; Han, Y.; Huang, Y.-F.; Zhou, Z.-J., Synthesis of magnetic framework composites for the discrimination of Escherichia coli at the strain level. *Analytica Chimica Acta* **2015,** *868*, 36-44.

189. Huang, Y.-F.; Wang, Y.-Q.; Zhao, Q.-S.; Li, Y.; Zhang, J.-M., Facile in situ hydrothermal synthesis of Fe_3O_4@MIL-101 composites for removing textile dyes. *RSC Advances* **2014,** *4* (89), 47921-47924.

190. Huang, Y.-F.; Liu, M.; Wang, Y.-Q.; Li, Y.; Zhang, J.-M.; Huo, S.-H., Hydrothermal synthesis of functionalized magnetic MIL-101 for magnetic enrichment of estrogens in environmental water samples. *RSC Advances* **2016,** *6* (19), 15362-15369.

191. Lohe, M. R.; Gedrich, K.; Freudenberg, T.; Kockrick, E.; Dellmann, T.; Kaskel, S., Heating and separation using nanomagnet-functionalized metal-organic frameworks. *Chemical Communications* **2011,** *47* (11), 3075-3077.

192. Zhao, M.; Zhang, X.; Deng, C., Rational synthesis of novel recyclable Fe_3O_4@MOF nanocomposites for enzymatic digestion. *Chemical Communications* **2015,** *51* (38), 8116-8119.

193. Ke, F.; Yuan, Y.-P.; Qiu, L.-G.; Shen, Y.-H.; Xie, A.-J.; Zhu, J.-F.; Tian, X.-Y.; Zhang, L.-D., Facile fabrication of magnetic metal-organic framework nanocomposites for potential targeted drug delivery. *Journal of Materials Chemistry* **2011,** *21* (11), 3843-3848.

194. Zhang, Y.; Zhang, J.; Tian, M.; Chu, G.; Quan, C., Fabrication of amino-functionalized Fe_3O_4@$Cu_3(BTC)_2$ for heterogeneous Knoevenagel condensation. *Chinese Journal of Catalysis* **2016,** *37* (3), 420-427.

195. Ray Chowdhuri, A.; Bhattacharya, D.; Sahu, S. K., Magnetic nanoscale metal organic frameworks for potential targeted anticancer drug delivery, imaging and as an MRI contrast agent. *Dalton Transactions* **2016,** *45* (7), 2963-2973.

196. Zhang, N.; Zhu, B.; Peng, F.; Yu, X.; Jia, Y.; Wang, J.; Kong, L.; Jin, Z.; Luo, T.; Liu, J., Synthesis of metal-organic-framework related core-shell heterostructures and their application to ion enrichment in aqueous conditions. *Chemical Communications* **2014,** *50* (57), 7686-7689.

197. Zhao, M.; Zhang, X.; Deng, C., Facile synthesis of hydrophilic magnetic graphene@metal-organic framework for highly selective enrichment of phosphopeptides. *RSC Advances* **2015,** *5* (45), 35361-35364.

198. Zhang, T.; Lin, L.; Zhang, X.; Liu, H.; Yan, X.; Qiu, J.; Yeung, K. L., Synthesis and characterization of ZIF-8@SiO_2@Fe_3O_4 core@double-shell microspheres with noble metal nanoparticles sandwiched between two shell layers. *Materials Letters* **2015,** *148*, 17-21.

199. Li, Q.; Jiang, S.; Ji, S.; Ammar, M.; Zhang, Q.; Yan, J., Synthesis of magnetically recyclable ZIF-8@SiO_2@Fe_3O_4 catalysts and their catalytic performance for Knoevenagel reaction. *Journal of Solid State Chemistry* **2015,** *223*, 65-72.

200. Li, Q.; Jiang, S.; Ji, S.; Shi, D.; Yan, J.; Huo, Y.; Zhang, Q., Magnetically Recyclable Cu-BTC@$SiO_2Fe_3O_4$ Catalysts and Their Catalytic Performance for the Pechmann Reaction. *Industrial & Engineering Chemistry Research* **2014,** *53* (39), 14948-14955.

201. Jiang, S.; Yan, J.; Habimana, F.; Ji, S., Preparation of magnetically recyclable MIL-53(Al)@SiO_2@Fe_3O_4 catalysts and their catalytic performance for Friedel–Crafts acylation reaction. *Catalysis Today* **2016,** *264*, 83-90.

202. Farzaneh, F.; Sadeghi, Y., Immobilized V-MIL-101 on modified Fe_3O_4 nanoparticles as heterogeneous catalyst for epoxidation of allyl alcohols and alkenes. *Journal of Molecular Catalysis a-Chemical* **2015,** *398*, 275-281.

203. Zhang, W.; Yan, Z.; Gao, J.; Tong, P.; Liu, W.; Zhang, L., Metal-organic framework UiO-66 modified magnetite@silica core-shell magnetic microspheres for magnetic solid-phase extraction of domoic acid from shellfish samples. *Journal of Chromatography A* **2015,** *1400*, 10-18.

204. Wehner, T.; Mandel, K.; Schneider, M.; Sextl, G.; Muller-Buschbaum, K., Superparamagnetic Luminescent MOF@Fe_3O_4/SiO_2 Composite Particles for Signal Augmentation by Magnetic Harvesting as Potential Water Detectors. *Acs Applied Materials & Interfaces* **2016,** *8* (8), 5445-5452.

205. Sun, X.; Li, Y.; Xi, H.; Xia, Q., Adsorption performance of a MIL-101(Cr)/graphite oxide composite for a series of n-alkanes. *RSC Advances* **2014,** *4* (99), 56216-56223.

206. Yan, J.; Yu, Y.; Ma, C.; Xiao, J.; Xia, Q.; Li, Y.; Li, Z., Adsorption isotherms and kinetics of water vapor on novel adsorbents MIL-101(Cr)@GO with super-high capacity. *Applied Thermal Engineering* **2015,** *84*, 118-125.

207. Zhou, X.; Huang, W.; Miao, J.; Xia, Q.; Zhang, Z.; Wang, H.; Li, Z., Enhanced separation performance of a novel composite material GrO@MIL-101 for CO_2/CH_4 binary mixture. *Chemical Engineering Journal* **2015,** *266*, 339-344.

208. Zhou, X.; Huang, W. Y.; Shi, J.; Zhao, Z. X.; Xia, Q. B.; Li, Y. W.; Wang, H. H.; Li, Z., A novel MOF/graphene oxide composite GrO@MIL-101 with high adsorption capacity for acetone. *Journal of Materials Chemistry A* **2014,** *2* (13), 4722-4730.

209. Ahmed, I.; Khan, N. A.; Jhung, S. H., Graphite Oxide/Metal-Organic Framework (MIL-101): Remarkable Performance in the Adsorptive Denitrogenation of Model Fuels. *Inorganic Chemistry* **2013,** *52* (24), 14155-14161.

210. Li, G. H.; Li, F. C.; Yang, H.; Cheng, F. Y.; Xu, N.; Shi, W.; Cheng, P., Graphene oxides doped MIL-101(Cr) as anode materials for enhanced electrochemistry performance of lithium ion battery. *Inorganic Chemistry Communications* **2016,** *64*, 63-66.

211. Bashkova, S.; Bandosz, T. J., Effect of surface chemical and structural heterogeneity of copper-based MOF/graphite oxide composites on the adsorption of ammonia. *Journal of Colloid and Interface Science* **2014,** *417*, 109-114.

212. Ebrahim, A. M.; Jagiello, J.; Bandosz, T. J., Enhanced reactive adsorption of H_2S on Cu-BTC/S- and N-doped GO composites. *Journal of Materials Chemistry A* **2015,** *3* (15), 8194-8204.

213. Liu, S.; Sun, L.; Xu, F.; Zhang, J.; Jiao, C.; Li, F.; Li, Z.; Wang, S.; Wang, Z.; Jiang, X.; Zhou, H.; Yang, L.; Schick, C., Nanosized Cu-MOFs induced by graphene oxide and enhanced gas storage capacity. *Energy & Environmental Science* **2013,** *6* (3), 818-823.

214. Petit, C.; Bandosz, T. J., Engineering the surface of a new class of adsorbents: Metal-organic framework/graphite oxide composites. *Journal of Colloid and Interface Science* **2015,** *447*, 139-151.

215. Petit, C.; Mendoza, B.; Bandosz, T. J., Reactive Adsorption of Ammonia on Cu-Based MOF/Graphene Composites. *Langmuir* **2010,** *26* (19), 15302-15309.

216. Petit, C.; Huang, L.; Jagiello, J.; Kenvin, J.; Gubbins, K. E.; Bandosz, T. J., Toward Understanding Reactive Adsorption of Ammonia on Cu-MOF/Graphite Oxide Nanocomposites. *Langmuir* **2011,** *27* (21), 13043-13051.

217. Travlou, N. A.; Singh, K.; Rodriguez-Castellon, E.; Bandosz, T. J., Cu-BTC MOF-graphene-based hybrid materials as low concentration ammonia sensors. *Journal of Materials Chemistry A* **2015,** *3* (21), 11417-11429.

218. Zhao, Y. X.; Seredych, M.; Zhong, Q.; Bandosz, T. J., Superior Performance of Copper Based MOF and Aminated Graphite Oxide Composites as CO_2 Adsorbents at Room Temperature. *Acs Applied Materials & Interfaces* **2013,** *5* (11), 4951-4959.

219. Zhao, Y. X.; Seredych, M.; Jagiello, J.; Zhong, Q.; Bandosz, T. J., Insight into the mechanism of CO_2 adsorption on Cu-BTC and its composites with graphite oxide or aminated graphite oxide. *Chemical Engineering Journal* **2014,** *239*, 399-407.

220. Bian, Z. J.; Xu, J.; Zhang, S. P.; Zhu, X. M.; Liu, H. L.; Hu, J., Interfacial Growth of Metal Organic Framework/Graphite Oxide Composites through Pickering Emulsion and Their CO_2 Capture Performance in the Presence of Humidity. *Langmuir* **2015,** *31* (26), 7410-7417.

221. Chen, B.; Zhu, Y.; Xia, Y., Controlled in situ synthesis of graphene oxide/zeolitic imidazolate framework composites with enhanced CO_2 uptake capacity. *RSC Advances* **2015,** *5* (39), 30464-30471.

222. Luanwuthi, S.; Krittayavathananon, A.; Srimuk, P.; Sawangphruk, M., In situ synthesis of permselective zeolitic imidazolate framework-8/graphene oxide composites: rotating disk electrode and Langmuir adsorption isotherm. *RSC Advances* **2015,** *5* (58), 46617-46623.

223. Yang, L.; Tang, B.; Wu, P., Metal-organic framework-graphene oxide composites: a facile method to highly improve the proton conductivity of PEMs operated under low humidity. *Journal of Materials Chemistry A* **2015,** *3* (31), 15838-15842.

224. Zhou, H.; Zhang, J.; Zhang, J.; Yan, X.; Shen, X.; Yuan, A., High-capacity room-temperature hydrogen storage of zeolitic imidazolate framework/graphene oxide promoted by platinum metal catalyst. *International Journal of Hydrogen Energy* **2015,** *40* (36), 12275-12285.

225. Fan, Z.; Wang, J.; Nie, Y.; Ren, L.; Liu, B.; Liu, G., Metal-Organic Frameworks/Graphene Oxide Composite: A New Enzymatic Immobilization Carrier for Hydrogen Peroxide Biosensors. *Journal of the Electrochemical Society* **2016,** *163* (3), B32-B37.

226. Petit, C.; Bandosz, T. J., MOF-graphite oxide nanocomposites: surface characterization and evaluation as adsorbents of ammonia. *Journal of Materials Chemistry* **2009,** *19* (36), 6521-6528.

227. Petit, C.; Bandosz, T. J., Enhanced Adsorption of Ammonia on Metal-Organic Framework/Graphite Oxide Composites: Analysis of Surface Interactions. *Advanced Functional Materials* **2010,** *20* (1), 111-118.

228. Zhao, Y.; Ding, H.; Zhong, Q., Synthesis and characterization of MOF-aminated graphite oxide composites for CO_2 capture. *Applied Surface Science* **2013,** *284* (0), 138-144.

229. Petit, C.; Bandosz, T. J., Synthesis, Characterization, and Ammonia Adsorption Properties of Mesoporous Metal-Organic Framework (MIL(Fe))-Graphite Oxide Composites: Exploring the Limits of Materials Fabrication. *Advanced Functional Materials* **2011,** *21* (11), 2108-2117.

230. Qiu, X.; Wang, X.; Li, Y., Controlled growth of dense and ordered metal-organic framework nanoparticles on graphene oxide. *Chemical Communications* **2015,** *51* (18), 3874-3877.

231. Zhang, Y.; Li, G.; Lu, H.; Lv, Q.; Sun, Z., Synthesis, characterization and photocatalytic properties of MIL-53(Fe)-graphene hybrid materials. *RSC Advances* **2014,** *4* (15), 7594-7600.

232. Huang, L.; Liu, B., Synthesis of a novel and stable reduced graphene oxide/MOF hybrid nanocomposite and photocatalytic performance for the degradation of dyes. *RSC Advances* **2016,** *6* (22), 17873-17879.

233. Cao, Y.; Zhao, Y. X.; Lv, Z. J.; Song, F. J.; Zhong, Q., Preparation and enhanced CO_2 adsorption capacity of UiO-66/graphene oxide composites. *Journal of Industrial and Engineering Chemistry* **2015,** *27*, 102-107.

234. Qiao, Q.-Q.; Li, G.-R.; Wang, Y.-L.; Gao, X.-P., To enhance the capacity of Li-rich layered oxides by surface modification with metal-organic frameworks (MOFs) as cathodes for advanced lithium-ion batteries. *Journal of Materials Chemistry A* **2016,** *4* (12), 4440-4447.

235. Deng, K.; Hou, Z.; Li, X.; Li, C.; Zhang, Y.; Deng, X.; Cheng, Z.; Lin, J., Aptamer-Mediated Up-conversion Core/MOF Shell Nanocomposites for Targeted Drug Delivery and Cell Imaging. *Scientific Reports* **2015,** *5*.

236. Li, Y. T.; Tang, J. L.; He, L. C.; Liu, Y.; Liu, Y. L.; Chen, C. Y.; Tang, Z. Y., Core-Shell Upconversion Nanoparticle@Metal-Organic Framework Nanoprobes for Luminescent/Magnetic Dual-Mode Targeted Imaging. *Advanced Materials* **2015,** *27* (27), 4075-4080.

237. Guo, T.; Deng, Q.; Fang, G.; Gu, D.; Yang, Y.; Wang, S., Upconversion fluorescence metal-organic frameworks thermo-sensitive imprinted polymer for enrichment and sensing protein. *Biosensors and Bioelectronics* **2016,** *79*, 341-346.

238. Li, S.; Wang, X.; Chen, Q.; He, Q.; Lv, M.; Liu, X.; Lv, J.; Wei, F., Synthesis and photocatalytic activity of N-$K_2Ti_4O_9$/UiO-66 composites. *RSC Advances* **2015,** *5* (66), 53198-53206.

239. Yang, Y.; Wang, F.; Yang, Q.; Hu, Y.; Yan, H.; Chen, Y.-Z.; Liu, H.; Zhang, G.; Lu, J.; Jiang, H.-L.; Xu, H., Hollow Metal-Organic Framework Nanospheres via Emulsion-Based Interfacial Synthesis and Their Application in Size-Selective Catalysis. *Acs Applied Materials & Interfaces* **2014,** *6* (20), 18163-18171.

240. Wang, C.; Zhang, H.; Feng, C.; Gao, S.; Shang, N.; Wang, Z., Multifunctional Pd@MOF core-shell nanocomposite as highly active catalyst for p-nitrophenol reduction. *Catalysis Communications* **2015,** *72*, 29-32.

241. Yang, Q. H.; Xu, Q.; Yu, S. H.; Jiang, H. L., Pd Nanocubes@ZIF-8: Integration of Plasmon-Driven Photothermal Conversion with a Metal-Organic Framework for Efficient and Selective Catalysis. *Angewandte Chemie-International Edition* **2016,** *55* (11), 3685-3689.

242. Xue, S.; Jiang, H.; Zhong, Z.; Low, Z.-X.; Chen, R.; Xing, W., Palladium nanoparticles supported on a two-dimensional layered zeolitic imidazolate framework-L as an efficient size-selective catalyst. *Microporous and Mesoporous Materials* **2016,** *221*, 220-227.

243. Jiang, H.; Xue, S. L.; Liu, Y. F.; Chen, R. Z.; Xing, W. H., Controllable synthesis of Pd@ZIF-L catalysts by an assembly method. *Rsc Advances* **2016,** *6* (26), 21337-21344.

244. Zhao, M. T.; Deng, K.; He, L. C.; Liu, Y.; Li, G. D.; Zhao, H. J.; Tang, Z. Y., Core-Shell Palladium Nanoparticle@Metal-Organic Frameworks as Multifunctional Catalysts for Cascade Reactions. *Journal of the American Chemical Society* **2014,** *136* (5), 1738-1741.

245. Kuo, C. H.; Tang, Y.; Chou, L. Y.; Sneed, B. T.; Brodsky, C. N.; Zhao, Z. P.; Tsung, C. K., Yolk-Shell Nanocrystal@ZIF-8 Nanostructures for Gas-Phase Heterogeneous Catalysis with Selectivity Control. *Journal of the American Chemical Society* **2012,** *134* (35), 14345-14348.

246. Lin, L.; Zhang, T.; Zhang, X.; Liu, H.; Yeung, K. L.; Qiu, J., New Pd/SiO_2@ZIF-8 Core-Shell Catalyst with Selective, Antipoisoning, and Antileaching Properties for the Hydrogenation of Alkenes. *Industrial & Engineering Chemistry Research* **2014,** *53* (27), 10906-10913.

247. Xi, B.; Tan, Y. C.; Zeng, H. C., A General Synthetic Approach for Integrated Nanocatalysts of Metal-Silica@ZIFs. *Chemistry of Materials* **2016,** *28* (1), 326-336.

248. Lin, L.; Zhang, T.; Liu, H.; Qiu, J.; Zhang, X., In situ fabrication of a perfect Pd/ZnO@ZIF-8 core-shell microsphere as an efficient catalyst by a ZnO support-induced ZIF-8 growth strategy. *Nanoscale* **2015,** *7* (17), 7615-7623.

249. Li, F.-L.; Li, H.-X.; Lang, J.-P., Fabrication of yolk-shell Pd@ZIF-8 nanoparticles with excellent catalytic size-selectivity for the hydrogenation of olefins. *CrystEngComm* **2016,** *18* (10), 1760-1767.

250. Wang, P.; Zhao, J.; Li, X.; Yang, Y.; Yang, Q.; Li, C., Assembly of ZIF nanostructures around free Pt nanoparticles: efficient size-selective catalysts for hydrogenation of alkenes under mild conditions. *Chemical Communications* **2013,** *49* (32), 3330-3332.

251. Stephenson, C. J.; Hupp, J. T.; Farha, O. K., Pt@ZIF-8 composite for the regioselective hydrogenation of terminal unsaturations in 1,3-dienes and alkynes. *Inorganic Chemistry Frontiers* **2015,** *2* (5), 448-452.

252. Stephenson, C. J.; Hupp, J. T.; Farha, O. K., Postassembly Transformation of a Catalytically Active Composite Material, Pt@ZIF-8, via Solvent-Assisted Linker Exchange. *Inorganic Chemistry* **2016,** *55* (4), 1361-1363.

253. Xu, Z.; Yang, L.; Xu, C., Pt@UiO-66 Heterostructures for Highly Selective Detection of Hydrogen Peroxide with an Extended Linear Range. *Analytical Chemistry* **2015,** *87* (6), 3438-3444.

254. Na, K.; Choi, K. M.; Yaghi, O. M.; Somorjai, G. A., Metal Nanocrystals Embedded in Single Nanocrystals of MOFs Give Unusual Selectivity as Heterogeneous Catalysts. *Nano Letters* **2014,** *14* (10), 5979-5983.

255. Choi, K. M.; Na, K.; Somorjai, G. A.; Yaghi, O. M., Chemical Environment Control and Enhanced Catalytic Performance of Platinum Nanoparticles Embedded in Nanocrystalline Metal-Organic Frameworks. *Journal of the American Chemical Society* **2015,** *137* (24), 7810-7816.

256. Zhang, W. N.; Lu, G.; Cui, C. L.; Liu, Y. Y.; Li, S. Z.; Yan, W. J.; Xing, C.; Chi, Y. R.; Yang, Y. H.; Huo, F. W., A Family of Metal-Organic Frameworks Exhibiting Size-Selective Catalysis with Encapsulated Noble-Metal Nanoparticles. *Advanced Materials* **2014,** *26* (24), 4056-4060.

257. Zhang, J.; Liu, X.; Zhou, H.; Yan, X.; Liu, Y.; Yuan, A., Pt-doped graphene oxide/MIL-101 nanocomposites exhibiting enhanced hydrogen uptake at ambient temperature. *RSC Advances* **2014,** *4* (55), 28908-28913.

258. Zhou, H.; Liu, X. Q.; Zhang, J.; Yan, X. F.; Liu, Y. J.; Yuan, A. H., Enhanced room-temperature hydrogen storage capacity in Pt-loaded graphene oxide/HKUST-1 composites. *International Journal of Hydrogen Energy* **2014,** *39* (5), 2160-2167.

259. Bao, W.; Zhang, Z.; Qu, Y.; Zhou, C.; Wang, X.; Li, J., Confine sulfur in mesoporous metal-organic framework @ reduced graphene oxide for lithium sulfur battery. *Journal of Alloys and Compounds* **2013,** *582*, 334-340.

260. Liu, N.; Yao, Y.; Cha, J. J.; McDowell, M. T.; Han, Y.; Cui, Y., Functionalization of silicon nanowire surfaces with metal-organic frameworks. *Nano Research* **2012,** *5* (2), 109-116.

261. Buso, D.; Nairn, K. M.; Gimona, M.; Hill, A. J.; Falcaro, P., Fast Synthesis of MOF-5 Microcrystals Using Sol-Gel SiO_2 Nanoparticles. *Chemistry of Materials* **2011,** *23* (4), 929-934.

262. Fu, Y. Y.; Yang, C. X.; Yan, X. P., Fabrication of ZIF-8@SiO_2 Core-Shell Microspheres as the Stationary Phase for High-Performance Liquid Chromatography. *Chemistry-a European Journal* **2013,** *19* (40), 13484-13491.

263. Song, Y.; Hu, D.; Liu, F.; Chen, S.; Wang, L., Fabrication of fluorescent SiO_2@zeolitic imidazolate framework-8 nanosensor for Cu^{2+} detection. *Analyst* **2015,** *140* (2), 623-629.

264. Han, Y.; Qi, P.; Feng, X.; Li, S.; Fu, X.; Li, H.; Chen, Y.; Zhou, J.; Li, X.; Wang, B., In Situ Growth of MOFs on the Surface of Si Nanoparticles for Highly Efficient Lithium Storage: Si@MOF Nanocomposites as Anode Materials for Lithium-Ion Batteries. *Acs Applied Materials & Interfaces* **2015,** *7* (4), 2178-2182.

265. Qin, W.; Silvestre, M. E.; Kirschhoefer, F.; Brenner-Weiss, G.; Franzreb, M., Insights into chromatographic separation using core-shell metal-organic frameworks: Size exclusion and polarity effects. *Journal of Chromatography A* **2015,** *1411*, 77-83.

266. Yan, Z.; Zheng, J.; Chen, J.; Tong, P.; Lu, M.; Lin, Z.; Zhang, L., Preparation and evaluation of silica-UIO-66 composite as liquid chromatographic stationary phase for fast and efficient separation. *Journal of Chromatography A* **2014,** *1366*, 45-53.

267. Zhang, X.; Han, Q.; Ding, M., One-pot synthesis of UiO-66@SiO_2 shell-core microspheres as stationary phase for high performance liquid chromatography. *RSC Advances* **2015,** *5* (2), 1043-1050.

268. Wang, M.; Wang, D.; Li, Z., Self-assembly of CPO-27-Mg/TiO_2 nanocomposite with enhanced performance for photocatalytic CO_2 reduction. *Applied Catalysis B-Environmental* **2016,** *183*, 47-52.

269. Liu, Q.; Low, Z.-X.; Li, L.; Razmjou, A.; Wang, K.; Yao, J.; Wang, H., ZIF-8/Zn_2GeO_4 nanorods with an enhanced CO_2 adsorption property in an aqueous medium for photocatalytic synthesis of liquid fuel. *Journal of Materials Chemistry A* **2013,** *1* (38), 11563-11569.

270. Rahimi, R.; Shariatinia, S.; Zargari, S.; Berijani, M. Y.; Ghaffarinejad, A.; Shojaie, Z. S., Synthesis, characterization, and photocurrent generation of a new nanocomposite based Cu-TCPP MOF and ZnO nanorod. *RSC Advances* **2015,** *5* (58), 46624-46631.

271. Zhan, W.-w.; Kuang, Q.; Zhou, J.-z.; Kong, X.-j.; Xie, Z.-x.; Zheng, L.-s., Semiconductor@Metal-Organic Framework Core-Shell Heterostructures: A Case of ZnO@ZIF-8 Nanorods with Selective Photoelectrochemical Response. *Journal of the American Chemical Society* **2013,** *135* (5), 1926-1933.

272. Yu, B.; Wang, F. F.; Dong, W. B.; Hou, J.; Lu, P. C.; Gong, J. B., Self-template synthesis of core-shell ZnO@ZIF-8 nanospheres and the photocatalysis under UV irradiation. *Materials Letters* **2015,** *156*, 50-53.